INFORMATION TO USERS

This manuscript has been reproduced from the microfilm master. UMI films the text directly from the original or copy submitted. Thus, some thesis and dissertation copies are in typewriter face, while others may be from any type of computer printer.

The quality of this reproduction is dependent upon the quality of the copy submitted. Broken or indistinct print, colored or poor quality illustrations and photographs, print bleedthrough, substandard margins, and improper alignment can adversely affect reproduction.

In the unlikely event that the author did not send UMI a complete manuscript and there are missing pages, these will be noted. Also, if unauthorized copyright material had to be removed, a note will indicate the deletion.

Oversize materials (e.g., maps, drawings, charts) are reproduced by sectioning the original, beginning at the upper left-hand corner and continuing from left to right in equal sections with small overlaps.

Photographs included in the original manuscript have been reproduced xerographically in this copy. Higher quality 6" x 9" black and white photographic prints are available for any photographs or illustrations appearing in this copy for an additional charge. Contact UMI directly to order.

NOTE TO USERS

This reproduction is the best copy available.

University of Alberta

Plume Sampling of a Flare in Crosswind:

Structure and Combustion Efficiency

by

Pascal Poudenx (C)

A thesis submitted to the Faculty of Graduate Studies and Research in partial fulfilment

of the requirements for the degree of Master of Science.

Department of Mechanical Engineering

Edmonton, Alberta

Fall 2000

Canada

University of Alberta

Library Release Form

Name of Author: Pascal Poudenx
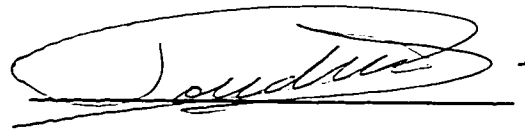
Title of Thesis: Plume Sampling of a Flare in Crosswind: Structure and
                          Combustion Efficiency

Degree: Master of Science

Year this Degree Granted: 2000

Permission is hereby granted to the University of Alberta Library to reproduce single copies
of this thesis and to lend or sell such copies for private, scholarly or scientific purpose only.

The author reserves all other publication and other rights in association with the copyright in
the thesis, and except as herein before provided, neither the thesis nor any substantial portion
thereof may be printed or otherwise reproduced in any material form whatever without the
author's prior written permission.

38 rue d'Occitanie,
31120 Roquettes,
France

University of Alberta

Faculty of Graduate Studies and Research

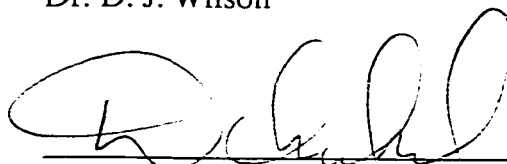The undersigned certify that they have read, and recommend to the Faculty of Graduate Studies and Research for acceptance, a thesis entitled <u>Plume Sampling of Flare in Crosswind: Structure and Combustion Efficiency</u> submitted by Pascal Poudenx in partial fulfillment of the requirements for the degree of Master of Science.

_____
Dr. L. Kostiuk

_____
Dr. D. J. Wilson

_____
Dr. M. D. Checkel

_____
Dr. W. Kindzierski

ABSTRACT

The plume of products from a burning gas jet in crosswind was investigated in a wind tunnel. Its temperature was used to track its shape and size up to three flame lengths downstream. The plume was shown to behave similarly to a non-reactant buoyant jet. The concentrations of CO_2, CO and CH_4 over a cross-section of the plume were measured by a multipoint sampling technique. The CO_2 stays in the core of the plume while CO and CH_4 go more on the sides. The mechanism lowering the combustion efficiency of the flare occurs very close to the exit of the jet. At the highest velocity ratio, ejection of unburned fuel near the exit of the stack is probably the cause of the reduction in the overall efficiency for increased wind speed. Probes of different sizes and shapes were simulated to test sampling strategies in the field.

ACKNOWLEDGEMENTS

TABLE OF CONTENTS

LIST OF TABLES

LIST OF FIGURES

NOMENCLATURE

Cp_∞ Heat capacity of air (J/(kg.K))

d Diameter (cm)

       s Inside stack diameter

       o Outside stack diameter

d_p^* Characteristic dimension of the plume (m)

F_b Buoyancy flux (m^4/s^3)

g Gravitational constant, $g = 9.81$ m/s^2

H_j Heat release rate (J/s)

h_o Initial height of the plume (m)

k Numbers of carbon atoms in hydrocarbon molecule

L Characteristic length scale (m)

l Numbers of hydrogen atoms in hydrocarbon molecule

M_A Molar weight of species A (kg/mol)

n Number of samples

P_L Local pressure (Pa)

p, s, t, u, w	Coefficients
q	Flow rate through a cross section of the plume (kg/s)
q_o	Flow rate of the jet (kg/s)
Q_{hv}	Heating value of the gas (J/kg)
R	Momentum ratio, $\quad R = \dfrac{\rho_j V_j^2}{\rho_\infty U_\infty^2}$
Ri	Richardson Number
R_j	Radius of the jet (m)
R_o	Effective radius of the source (m)
R_p	Radius of the plume (m)
$\overline{R}$	Ideal gas constant (J/(kg.K))
	L Local value
	∞ Crosswind value
r_{mb}	Derived ratio of momentum flux over Buoyancy flux ((m/s)$^{2/3}$)
	$r_{mb} = \dfrac{U_\infty}{V_j^{1/3}}$
T	Temperature (deg. C)
	background Minimal value on a map of temperature
	j Temperature of the jet

max   Maximal value on a map of temperature

plume   Threshold temperature used to define the plume

$$T_{plume} \geq \frac{T_{background} + T_{max}}{2}$$

L   Local measurement

sp   Temperature of stoichiometric products

U_∞ Velocity of the crosswind (m/s)

V_j Velocity of the gas jet (m/s)

X,Y,Z   Name of coordinate axis

Xo   Downstream distance from the stack (m)

α Fraction of product of combustion of a sample

av   Averaged value over a chosen area

β Entrainment coefficient

Δh Height of the plume (m)

b   Purely buoyant plume

m   Pure momentum plume

o   Plume with $R_o \neq 0$

$\Delta\rho_P$ Density difference (Pa)

P Between the plume and the crosswind

o Between the exit of the jet and the crosswind

η Carbon conversion efficiency (%)

av Averaged value over a chosen area

φ Heating Value (J/kg)

ρ Density (kg/m^3)

j Density of gas jet

∞ Density of cross-flow

L Local density

sp Density of stoichiometric products

θ Angle between the direction of the wind and the axis of the sampling probe (deg.)

$[A]$ Concentration of a species A (ppm or %)

P Species is coming from Products of combustion

G Species is coming from Gas

R Species is coming from Reaction of combustion

E Species is coming from Entrainment air

S Species is coming from the Sample

AV Averaged value

Chapter 1

INTRODUCTION

1.1 Solution Gas Flaring in Alberta

Solution Gas: Natural gas dissolved in crude oil as a result of reservoir pressures (Acad. Press Dict. of Sc. & Tech.).

To Flare: to burn with an unsteady flame, to stream in the wind (Merriam-Webster's dictionary).

Flare: a burner, usually installed outdoors in an elevated position, used to dispose of combustible waste gases from chemical or refining processes by igniting them (Acad. Press Dict. of Sc. & Tech.).

Flaring is an industrial process used by the production sector of the oil industry. The extraction of crude oil from the ground involves bringing to the surface a mixture of hydrocarbons that have been trapped for millions of years in underground pools. Once at the surface, the mixture consists of two components, a liquid, which is a mixture of water and crude oil, and a gas called natural gas. The fields of extraction are usually large areas with numerous batteries (groups of equipment for processing and storing the crude oil from wells). The battery site is where the water and the natural gas are separated from

the crude oil. Production of either oil or gas from each battery is then transported to a refinery where it will be modified to meet commercial needs.

If the costs of transporting the solution gas are too high, it can be disposed of by flaring directly at a battery site. To do so, the gas is separated from the liquid phase in a knockout drum and sent through a vertical pipe, the flare stack, where it is ignited.

The Alberta landscape displays numerous sites of this kind, marked by their visible flames. According to the Energy Utility Board (EUB), there were 4400 flares in the province in 1999. From the 22.919 billion cubic meters of solution gas produced in 1998, 1.287 billions cubic meters (5.6%) were flared (EUB Series 57, 1999). A typical flare installed on a battery site in Alberta is designed as follows. The vertical pipe is about ten centimetres in diameter. At the top of the pipe, a pilot light ensures that the gas will remain lit and burn upon contact with the oxygen of the atmosphere. Most flares have a crude wind screen device made of a larger tube (twenty centimetres in diameter), covering the last thirty centimetres or so of the pipe and extending slightly above the exit. The gas exits the stack with a velocity of about one to four meters per second.

Flaring is also used on other occasions, such as gas well testing. After a new well is drilled, its capabilities (production rate, quality) have to be assessed and the gas is flared during this period. Finally, flaring is used to dispose rapidly of a large volume of gas in case of emergency, or to purge a facility before maintenance. For this reason flaring is also visible on most petrochemical facilities.

1.2 Flare Efficiency

Flares release their emissions in the atmosphere. The quality of those emissions can be described by using the concept of overall combustion efficiency of a flare.

A review of the basic combustion processes is necessary to understand the concept of flare efficiency.

1.2.1 Basic Combustion Chemistry

The fuel in the natural gas being flared is mainly composed of hydrocarbons with the most predominant compound being methane (CH_4). The remainder is composed of higher hydrocarbons such as ethane (C_2H_6), propane (C_3H_8), etc., and some non-combustible gases such as carbon dioxide (CO_2) and nitrogen (N_2). Hydrogen sulphide (H_2S) can also be present in the natural gas. If the concentration of H_2S is greater than 1% the gas is defined as "sour". The research presented here does not deal with sour gas because of the high toxicity of H_2S.

The basic combustion process that occurs in the flame is an oxido-reduction process between the hydrocarbon fuel (C_kH_l) and oxygen (O_2) from the atmosphere. The ideal process where all of the fuel is fully oxidised, is given by:

$$C_kH_l + \left(k + \frac{l}{4}\right)O_2 \rightarrow k\,CO_2 + \frac{l}{2}H_2O \qquad (1.1)$$
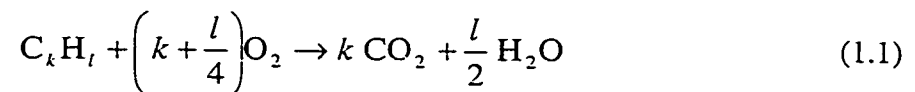
where k = number of carbon atoms in the molecule of hydrocarbon

l = number of hydrogen atoms in the molecule of hydrocarbon.

3

For simplicity, the nitrogen in the atmosphere has been left out of this global reaction. In this ideal situation, enough oxygen is provided and adequate conditions are met for the fuel gas to be entirely converted into carbon dioxide (CO_2) and water vapour (H_2O). This is the goal of flaring, turning the hydrocarbons of the solution gas into compounds that are naturally present in the atmosphere (CO_2 and H_2O) and therefore less harmful than the gas itself. Moreover, on a mass basis, the carbon dioxide from the combustion of methane has about twenty-one times less green house effect than the methane itself (Houghton et al., 1996).

However, reality is not an ideal process. A local deficiency in oxygen caused by some mixing difficulties between gas and air and/or the presence of other chemical compounds will affect the quality of the reaction. Consequently, new products are formed and emitted in the atmosphere. The actual overall reaction is more accurately described by:

$$C_k H_l + p\,O_2 \rightarrow s\,CO_2 + t\,CO + u\,H_2O + w\,HC \qquad (1.2)$$
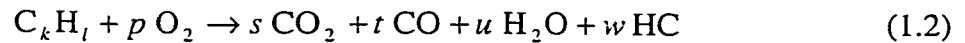
where HC = unburned hydrocarbons

p, s, t, u, w = coefficients

Again, the focus is only on the carbon-based compounds (i.e. ignoring oxides of nitrogen). The formation of carbon monoxide (CO) is one of the steps in the oxidation of the hydrocarbons. A second step of the chemical reaction is required to transform the CO into CO_2 before it leaves the flame. If there is a lack of oxygen, the residence time in the flame is too short, or the temperature is not high enough, this second process does not

occur and the final product contains some carbon monoxide, CO. Since CO is toxic at concentration as low as 50 ppm (Borghi and Destriau, 1995) its presence is undesirable.

The same conditions that produced CO also lead to the formation of unburned hydrocarbons (HC). The final products of the combustion may contain a very wide variety of hydrocarbon compounds, ranging from unaffected fuel molecules to numerous toxic and often carcinogenic compounds (e.g. volatile organic compounds, polynuclear aromatic hydrocarbons, aldehydes, etc). Hence, HC is the real problem for the local environment.

To summarise, a flare is supposed to convert the hydrocarbon fuels into carbon dioxide and water vapour but, if the combustion occurs in non-ideal conditions, other products are created as well. To quantify the fraction of gas turned into carbon dioxide by a flare, the concept of overall efficiency is used.

1.2.2 Definition of the Combustion Efficiency

A precise term to describe flare combustion efficiency is the Carbon Conversion Efficiency (η), since it quantifies the amount of carbon of the gas turned into carbon dioxide. It is defined as:

$$\eta = \frac{\text{mass of carbon in } CO_2 \text{ produced by flare}}{\text{mass of carbon contained in fuel}} \qquad (1.3)$$

Note that conversion efficiency is different than the concept of "destruction efficiency", which is defined as the mass fraction of hydrocarbons in the fuel that is

5

destroyed in its original form by being changed to other compounds, including CO2, plus other partially oxidised products.

Unless otherwise stated, the terms "efficiency" and "combustion efficiency" refer in this thesis to the Carbon Conversion Efficiency and not to the Destruction Efficiency.

By conservation of species, all of the carbon in the fuel ends up in the products either in the form of CO_2, CO, HC, or soot. Concerning the soot, it is a very difficult set of compounds to measure accurately, and hence there is a definite advantage in using natural gas as the fuel in the present research. The E.P.A. research showed that the amount of soot could be neglected if natural gas was burnt (Pohl and Soelberg, 1985). The present research will use only natural gas is order to assume the absence of soot in the carbon mass balance. Moreover, a gas chromatograph analysis of the products of combustion showed that the dominant hydrocarbon (HC) emitted from natural gas flares was in fact CH_4. For this reason, the unburned hydrocarbons (HC) will be labelled CH_4 in the rest of this thesis. Caution should applied by the reader because this assumption regarding the amount of soot emitted when burning other fuels (e.g., real solution gas) may not apply.Equation 1.3 becomes:

$$\eta = \frac{[CO_2] \cdot M_{CO_2} \cdot \dfrac{M_C}{M_{CO_2}}}{[CO_2] \cdot M_{CO_2} \cdot \dfrac{M_C}{M_{CO_2}} + [CO] \cdot M_{CO} \cdot \dfrac{M_C}{M_{CO}} + [CH_4] \cdot M_{CH_4} \cdot \dfrac{M_C}{M_{CH_4}}} \qquad (1.4)$$

where [a] = concentration of the species a (ppm)

M_a = molar weight of the species a (kg/mol).

Equation 1.4 simplifies to:

$$\eta = \frac{[CO_2]}{[CO_2]+[CO]+[CH_4]}$$

(1.5)

Equation 1.5 expresses combustion efficiency, η, as the ratio of the concentration of carbon dioxide over the concentrations of all the carbon-based compounds found in the products of the combustion. This is important because the concentrations are accessible by measurement.

1.2.3 Overall vs. Local Efficiency

Two types of efficiency, overall and local, will be mentioned throughout this dissertation. When concentrations are averaged over the entire plume of product coming from a combustion reaction then the calculation leads to the overall efficiency. However, if the measurement is performed over a small region of the flow compared to the total volume of products, then the local efficiency at the sample location is evaluated. From one measurement of local efficiency, the overall performance of the combustion process cannot directly be known since the plume of product might not be spatially homogeneous.

1.3 Potential Research Direction

In Alberta, the Energy Utilities Board, regulator of the energy industry, has set several guidelines for reducing the volume of solution gas flared. Based on 1996 annual volume, there should be a 15% decrease in volume of gas flared by the end of the year 2000 and a 25% decrease by the end of the year 2001 (EUB, Guide 60, 1999). Then, new

objectives would be set by the second half of 2001. Another goal of the EUB is the definition of minimal performance requirements for flares and the enforcement of those performances.

These regulatory requirements lead naturally to two parallel research directions. One is associated with reducing gas volumes flared and the other is associated with measuring the performance of flares. The research presented here focuses on measuring flare performance, but it is worth mentioning its relevance when other researchers are attempting to eliminate flares.

The second law of thermodynamics describes how the energy of a system always goes toward a "lower quality" state, but part of the energy can be converted into useful work during the transformation. Exergy, defined as the maximum work potential in a system, is used to quantify this process. With flaring, the chemical energy (high quality energy) is transformed into heat and dispersed into the atmosphere (low quality energy). No work is produced and therefore it is a pure waste of exergy.

As a result, one line of research would be to consider technologies that could produce a more useful outcome than flaring. For example, "mini" gas turbines have been suggested to generate electricity from the gas that was to be flared. Note that these devices also emit products of combustion to the atmosphere. A more complete presentation of alternatives for these gases is given in the report of Alberta Clean Air Strategic Alliance (CASA) (Holford & Hettiaratchi, 1998). Unfortunately, none of these alternative techniques can be rapidly implemented because of technical problems and

economic barriers. Consequently, the flares currently in use must still be dealt with for many years to come.

In fact, if flaring were shown to be an effective, low polluting means of disposing of theses gases, some facilities could be best served by continuing to flare. This proves flare performance becomes an important issue and there is currently no technology available to make these measurements. As a result, there is a need to measure the actual performance of a flare.

1.4 The University of Alberta Flare Research Facility

One currently active research program working on the flare performance is at the University of Alberta Flare Research Facility. The goal of the Flare Research Project at the University of Alberta is to find a definitive explanation for the performance of flares, especially regarding the influences of the crosswind on the efficiency. Using a closed loop wind tunnel, the Flare Project studies the performance of model scale flares between 1.27 and 3.81 cm in diameter and is working on models which could reliably predict the overall efficiency of flares for any conditions of gas velocities, gas composition, crosswind and stack diameter. Johnson and Kostiuk (2000) have shown systematic variations in overall efficiency of a flare as function of the jet and the crosswind velocities. For a given gas velocity, V_j, the overall efficiency decreases as the crosswind, U_∞, increases, while higher velocity jets are less susceptible to the wind.

Other research topics include the influence of the energy density of the flare gas on efficiency. The shape of the flame is being studied to predict the size of the flame

built. A speciation, or detailed analysis of the numerous carbon compounds produced by a flare, is also undertaken. The research presented here has also been conducted at this facility.

1.5 Goals of Thesis Research

A technique to measure the overall efficiency by analysing the composition of the plume near the flame is studied for this thesis research. The major hypothesis motivating this work is that the differences between results of previous field measurements of efficiency based on single-point measurements in the plume come from the fact that the local efficiency within a plume is not homogeneous in the mean. If the distribution of the local efficiency can be understood then plume sampling could be used more reliably. This approach of local measurements in the plume will also be a way to investigate the mechanism by which the overall efficiency decreases as the ratio of crosswind over gas velocity gets larger.

The goal of this research is to establish if the overall efficiency of solution gas flares can be measured from the analysis of a sample of products extracted from the plume near the flame. Along the way toward this goal, the dispersion of the flare's products of combustion by the crosswind and the local efficiency are investigated. It is the purpose of this thesis to report the progress achieved in all these areas. This thesis is organised around five specific research objectives that are:

- mapping the cross-section of a thermal plume from a flare in the region close to the flame

- developing a model for air entrainment into the plume near the flame

- describing the compositional structure of the plume in order to understand the origin of the inefficiency of the flame

- assessing how a multi-point plume sampling technique can measure the overall efficiency of model scale flares in the wind tunnel

- recommending an effective sampling technique for measuring the overall efficiency of full-scale flares.

Chapter 2

REVIEW OF RELEVANT LITERATURE

2.1 Full Scale Measurement of Flare Efficiency

2.1.1 Plume Sampling Without a Crosswind

There has been a wide range of studies on open pipe flares and commercial flares, with and without air or steam injection to reduce the emission or smoke and improve the combustion.

In the 1980's an important study on flaring was performed by the Energy and Environment Corporation for the U.S. Environmental Protection Agency (EPA). Previous researches, discussed in the EPA report (Pohl and Soelberg, 1985), mention several studies on commercial flares. Despite efforts to acquire the reports on these studies they could not be accessed so only information from the EPA report is included here. Among the seven studies reported from 1972 to 1983, only two, performed by McDaniel (1983), and Keller & Noble (1983), report an overall efficiency of flares lower than 90% (55% and 66% respectively). The fuel burned was a mixture of propylene and nitrogen with a heating value from 3 to 81 MJ/m^3. The five other studies report efficiencies over 90% while burning natural gas, propane, hydrogen & light hydrocarbon mixture or ethylene. The size of the flare tips of those seven studies varied from 1.3 cm up to 68.6 cm. The techniques used to measure the efficiency or the exact ambient conditions were not reported in the EPA study.

A flare test facility was built for the U.S. EPA study in El Toro, California (Pohl et al., 1986) where flares up to 30.5 cm in diameter were studied. This study investigated open pipe flares and commercial flares burning a mixture of Propane/Nitrogen. A screen was erected to protect the flares from the crosswind and tests were not performed on rainy days. The overall combustion efficiency was measured after collecting the products with a hood and five probes installed above the flame. The collection of the products lasted 20 minutes. The efficiency was reported as being over 98% as long as the flame was stable. Instability (flickering flame) was induced by excessive steam injection or excessive fuel jet velocity, drastically reducing the efficiency to around 55%. It should be mentioned that only tests with the 30.5 cm diameter stack had velocities in the range from 6 cm/s to 3m/s, typical of continuous solution gas flaring. For the air and steam assisted stack tips (3.8 cm and 9.6 cm in diameter) the maximum fuel gas velocity was to 276 m/s and 48 m/s respectively. The conclusions drawn from this study are:

1 - The proportion of soot in the carbon mass balance used to calculate the efficiency did not exceed 0.5 %.

2 - A single point measurement of the local efficiency provided the overall inefficiency (100% - efficiency) with an accuracy of 50% (i.e., 2% ± 1% for a 98% efficient flame).

3 - The lowest combustion efficiency was on the edges of the flame, so that a single point measurement in the centreline (directly above the stack) would overestimate the efficiency.

4 - The diameter of the flare did not seem to have an impact on the efficiency.

For more details, refer to the full report describing the facility and methodology used (D. Joseph et al., 1983).

2.1.2 Plume Sampling With a Crosswind

Just by blowing on a candle the major influence of a crosswind on a flame is evident. Crosswind is clearly an important parameter in understanding flares in the field. Siegel (1980) performed a study in Germany on a 5 m high, 0.7 m diameter flare burning a mixture of hydrogen/nitrogen/hydrocarbons (C1-C4). The flare was equipped with steam assistance. A single point-aspirating probe was used to sample gases around the flame. The effect of the wind was studied with a fan placed above the top of the stack and blowing horizontally. This means the stack was not in the cross-flow and there was no creation of a wake downwind of the stack, as would occur when the wind blows on the whole height of the stack. Successive measurements with the probe were made on a horizontal plane above the stack and on a vertical plane downwind of the stack in order to cover the entire plume. The reported combustion efficiency was above 97% for all conditions. Tests were performed with a gas velocity of 0.5 and 2 m/s. The crosswind fan was blowing at 6.7m/s or was turned off, but the natural crosswind ranged from 1.2 to 6 m/s during tests, which limits the accuracy of the value of the actual crosswind over the flare. Siegel (1980) also investigated a steam assisted pilot-size flare (4.6 m high, 20.3 cm in diameter) with an array of 40 to 60 probes. Results reported that the efficiency remained above 97% for gas with heating value of 56 MJ/m^3.

In a report for Environment Canada (SKM Consulting Ltd., 1988), reference is made to two other research projects (Colley, 1982, and Leahey, 1985), on the efficiency

of flares with hydrogen sulphide (H_2S). These report were unavailable and only a summary of the result from the report for Environment Canada is possible. The same idea lies behind the notion of sulphur efficiency and carbon efficiency. It quantifies the amount of harmful compound (H_2S) turned into a relatively safer compound. In 1982, Colley et al. studied two sites of solution gas flares in Alberta. The flares were of the open pipe (7.6 cm in diameter) type with a 3.8 cm opening and a windshield 15.2 cm in diameter and 30.5 cm long. H_2S efficiency was reported to be 38% and 100% on one site and 87%, 86% and 96% on the second site. No other details were found.

In 1985, Leahy et al. studied the H_2S efficiency of an Alberta acid gas flare (24 m high, 10.2 cm in diameter). The crosswind was recorded from 1.1 m/s to 6.1 m/s and the measured efficiency was 22%, 89%, 96% and 100 %. Again, the details of the technique used were not reported and reason for the variation in efficiency was not well described.

Romano (1983) also performed flare tests on a 4 m high stack with air and steam assistance. The overall efficiency was reported as being over 98% and tended to decrease when the air assistance jet was excessive. This was measured from a single point sampling of the plume downwind of the flame. The crosswind was not reported.

In 1996, Strosher reported the results of a study conducted in Alberta. The investigation covered laboratory scale and field studies of efficiency measurements. The different sampling techniques (single point in plume measurements, multipoint measurement and collection of the product with a hood) were assessed during lab tests. The field studies were conducted on two sites using only the single point plume measurement technique. The first site was equipped with a 12 m high, 0.2 m diameter

flare burning sweet solution gas (less than 1% of hydrogen sulphide). The combustion efficiency was measured as low as 62% and 71%. It appears the amount of liquid in the knockout system was correlated with the changing efficiency. The presence of droplets was responsible for the difference, the more droplets, the less efficient the flare. Moreover, most of the incompletely oxidised products were toxic compounds (e.g. volatile organic compounds, polynuclear aromatic hydrocarbons, aldehydes, etc). For similar flaring conditions, the sampling of product was performed at different distances from the flame. The calculated efficiency remained very stable (1% difference).

The second site in Strosher's study had a 15 m high, 7.6 cm diameter flare burning sour gas (20-25 % of hydrogen sulphide). The sampling lasted 80 minutes (60 minutes within the plume) and the measured efficiency was 82%. Similar to the sweet gas case, numerous toxic compounds were found in the products of combustion.

In both cases, the distance between the probe and the stack was not more than twice the length of the flame. The crosswind was found to decrease the efficiency. Also, numerous volatile and non-volatile hydrocarbon compounds were found in the plume.

2.1.3 Other Techniques for Measuring Efficiency

So far, the only technique described in the reports to measure the efficiency was the sampling of the entire or part of the plume of flares and the analysis of its composition.

Other techniques have also been used to estimate the efficiency of flares. Differential Absorption Light (DIAL) detection and a passive Fourier Transform Infrared

(FTIR) set-up were used by a British group (Kuipers et al.) to study open pipe flares (10 m high, 0.6 m in diameter) burning natural gas (93% methane, 6% ethane). Using these techniques, the efficiency was calculated along a line-of-sight through exhaust gas of the flare. Consequently there is line-of-sight spatial averaging, which is not the case with the technique of point sampling. During the tests, the crosswind ranged from 6 m/s to 11 m/s and the flame was 10 m to 40 m in length. The influence of the pilot light was also investigated. The overall efficiency remained in the 99.6-99.9% range for all tests.

2.2 Jets in a Crosswind

On a fundamental level, the present problem of bent-over plumes from flares can be compared to a buoyant jet in cross-flow. Due to the wide applications of a jet in cross-flow, the number of references is mammoth and only a brief review is provided here. For a more complete review, a paper written by Margason (1993) provides over 300 references to studies performed over the last 50 years.

2.2.1 Preliminary Explanations

Buoyant jets in cross-flow are often described by either ratios of momentum or ratios of momentum to buoyancy.

2.2.1.1 A Momentum Flux Ratio

One option to describe a buoyant jet in cross-flow is to assume the dominance of the momentum flux of the jet and the momentum flux of the cross-flow in establishing the flow. The ratio of these two momenta, R, is written as:

17

$$R = \frac{\rho_j V_j^2}{\rho_\infty U_\infty^2}$$ (2.1)

where ρ_j = density of the gas; ρ_∞ = density of the surrounding air

This momentum ratio is actually a ratio of fluxes where the areas of two streams are set equal to each other. For equal density flows or flows where ρ_∞ and ρ_j never change, the velocity ratio V_j / U_∞ is sometimes used to describe the condition of an experiment instead of R.

2.2.1.2 A Ratio of Momentum over Buoyancy

One other possibility to describe a jet in cross-flow is to assume that the two dominant forces are:

- the momentum of the cross-flow

- the buoyancy of the jet

The Richardson number is then used to express this ratio

$$Ri = \frac{g(\Delta\rho_P / \rho_\infty)L}{U_\infty^2}$$ (2.2)

where g = gravitational constant; L = a characteristic length scale

$\Delta\rho_P$ = density difference between the plume and the surrounding air.

In order to be useful, Ri should be related to the velocity conditions (V_j and U_∞) and to the dimension of the jet R_j. This is done using a mass balance for the simplified case of a non-reacting jet. The two control surfaces are:

- the exit of the jet:

  - flow rate at the exit of the stack of radius R_j: $\qquad q_o = \pi.V_j.R_j^2$

  - density difference with the surrounding air: $\qquad \Delta\rho_o$

- a section of the plume fully bent-over and advected by the crosswind:

  - flow rate through the plume of radius R_p: $\qquad q = \pi.U_\infty R_p^2$

  - density difference between the plume and the surrounding air: $\quad \Delta\rho_P$

A conservation of mass between the two surfaces will lead to:

$$\pi V_j R_j^2 \Delta\rho_o = \pi U_\infty R_p^2 \Delta\rho_P \qquad (2.3)$$

The expression of $\Delta\rho_P$ from 2.3 can be introduced in 2.2 and Ri can be written as:

$$Ri = g\frac{V_j}{U_\infty^3}\frac{\Delta\rho_o}{\rho_\infty}\left(\frac{R_j}{R_p}\right)^2 L \qquad (2.4)$$

In this form, the dependency on V_j and U_∞ are explicit and the complexity is transferred to R_p, which varies in the downstream direction. L is the length scale that relates to the distance between the regions of different density and can be replaced. The density difference applies between the inside and the outside of the plume so R_p can be used as a local length scale to replace L. Also, the density difference, $\Delta\rho_o/\Delta\rho_\infty$, is related

19

to the temperature of the plume can be assumed to remain constant for a given gas, with a given flame temperature (main source of energy for the plume). Using these assumptions, Equation 2.4 becomes:

$$Ri \propto g \frac{V_j}{U_\infty^3} \frac{R_j^2}{R_p} \qquad (2.5)$$

2.2.1.3 Reasons For Introducing R and Ri

Ri, as presented in 2.5, is still difficult to use because of its variation in the downstream direction but it is not the purpose of this thesis to do so. Nevertheless, a ratio of the jet velocity over the crosswind velocity V_j/U_∞^3 is visible in Equation 2.5. Later in this dissertation, when classifying the shapes of the plume, this velocity ratio will be compared to R, the momentum ratio, to sort in a coherent manner the plumes corresponding to different velocity conditions. For the range of velocities used during this research, the ratio V_j/U_∞^3 leads to extremely small values (from 0.59 $(m/s)^{-2}$) down to 0.00098 $(m/s)^{-2}$). For convenience, a new velocity ratio, r_{mb}, is used throughout this thesis because it leads to value from 1.19 to 10.08 $(m/s)^{2/3}$.

$$r_{mb} = \frac{U_\infty}{V_j^{1/3}} \quad [(m/s)^{2/3}] \qquad (2.6)$$

Should the velocity ratio, r_{mb}, more closely depict the behaviour of the plume than the momentum flux per unit area ratio, R, it will demonstrate that the dominant force acting on the plume is the buoyancy of the jet, not the jet momentum flux.

20

2.2.2 Non Reacting Jets

As early as 1936, research was conducted on the dispersion of smoke from chimneys (Bosanquet and Pearson, 1936) in order to predict concentrations of jet material at ground level.

A distinction must be made between buoyant and non-buoyant plumes. As long as the buoyancy is dominant (the density of the jet is significantly smaller or larger than the density of the ambient air), a "2/3 power law" predicts the height reached by a plume as it is advected downwind. These plume heights have been experimentally verified several times (Slawson, 1967, Hewett, 1971, Schartz, 1972). The name comes from the fact that on a large downwind scale, the plume rise increases as the distance with the power 2/3. On the other hand, when the momentum is dominant (e.g. the jet has the same density as the surrounding air), a "1/3 power law" describes more accurately the path of the plume.

Later, more elaborate models appeared. These models took into account the actual wind profile (Djurfors, 1978).

Rodi (1982) wrote a comprehensive review of the modelling of buoyant jets and plumes. Temperature profiles of a jet in crosswind were measured by Toften et al. (1993). The velocity ratio V_j/U_∞ used in that work was from 4 to 10. The nozzle, 30 mm in diameter, produced a uniform velocity profile with a turbulence intensity of 1.5% at any velocity. The effects of counter-rotating vortices giving a kidney shape to the plume were evident. It was also found that an increase in the crosswind turbulence reduced the strength of those vortices. Smith et al. (1998) thoroughly analysed the mixing of a round

jet in cross-flow. Instead of a tube entering inside the test section, it was a nozzle inserted flush with the wall that was creating the jet (diameter from 2 to 10 mm). The velocity ratio V_j/U_∞ for these tests was from 5 to 25. It was shown that the self-similarity in plume structure does not appear until a certain distance defined by the jet to cross-flow velocity ratio and the diameter of the jet. Also, it was shown that the plume was developing a non-symmetric pattern as it was advected downwind.

Although these models apply only to non-reacting fluid they contain many of the same general features in term of the path and shape of the plume of combustion products advected by the crosswind. However, in the case of a flare, combustion takes place and it is expected to have an effect on the growth of the plume since the temperature and the density will change along the flame.

2.2.3 Reacting Jets

Gollahalli & Brzustowski (1975) performed a systematic study of reacting jets in cross-flow. The jet was exiting from a 2.54 cm stack, which is a similar to one of the stacks used in the present study. The trajectory and size of the flame were studied and compared to a non-reacting turbulent jet in cross-flow. The regime studied covered a momentum ratio R from 63 up to 1873 and a jet Reynolds number from 16,000 to 68,300. The centreline trajectories were found to be very similar, but the width of the flame was found to be significantly larger than the width of a non-reacting plume.

A field study was performed by Leahey (1984) to observe the plume rise from flares in Alberta. The two flares studied were 30 and 42 m high. It was demonstrated

22

that over a distance of 450 m downwind the plume behaved very similarly to a non-reacting buoyant jet, following the "2/3 power law" and having an entrainment coefficient β of 0.5.

Huang and Yang (1996) studied the temperature and concentration profiles inside the flame from a 6 mm diameter stack placed in a wind tunnel. The momentum ratio R covered the range from 0.26 to 5.48 with a jet velocity ranging from 1 to 14 m/s for a fixed wind speed. The turbulence intensity at the exit of the burner tube (5 mm I.D.) was lower than 0.2%. They showed the different modes of the flame shape for the different momentum ratios. For the lowest jet-to-wind ratio, the flame was downwashed. Then, for a higher ratio, the downwashed flame disappeared in favour of a stationary recirculation zone on the lee side of the stack. They also showed the different temperature profiles of the flame depending on the mode. Finally, they presented the distributions of CO_2 and CO inside the flame. No investigation was performed beyond the flame.

2.3 Summary

Two major pieces of information can be drawn from this literature review:

1 The measurement of overall flare efficiency by plume sampling has been a technique widely used over the last 30 years, but trends within the results are difficult to interpret, especially during the most recent work. Also, there are very few details of the precise locations of the probes, especially in conditions with a crosswind.

2 In the far field, hundreds of flare diameters downwind from the flame tip, the products of combustion of a flare are expected to disperse like the plume of a non-reacting jet in cross-flow. Inside the flame, concentration profiles were investigated and differences between the distribution of the different combustion products were shown. No work was reported on the concentration of those products in the near field, the first 100 diameters downwind from the flame tip. A knowledge of this behaviour is essential in planning the optimum distribution of sampling points for field measurement of carbon conversion efficiency. Therefore, the present research will contribute to this topic.

Chapter 3

METHODOLOGY FOR EXPERIMENTS
AND DATA PROCESSING

The details of the experimental techniques and methodology used to achieve the research goals of this project are described in this chapter. The experimental apparatus is only introduced to provide a sense of how the measurements were made; a full description of the apparatus is the subject of the following chapter.

3.1 Dispersion of the Plume

3.1.1 Introduction

The first goal of this research was to understand the dispersion of the plume near the flame since there was little information found on this topic in the literature.

A method was needed to visualise the plume of products near the flame. In the region extending from the tip of the flame to a couple of flame lengths downstream, one of the parameters that differentiate the plume of products from the ambient air is temperature. When the products leave the flame, they are significantly hotter than the surrounding atmosphere. Therefore, the mean plume could be located by its mean temperature and visualised by constructing mean temperature maps at various cross-sections perpendicular to the flow downwind from the flame as shown in Figure 3.1.
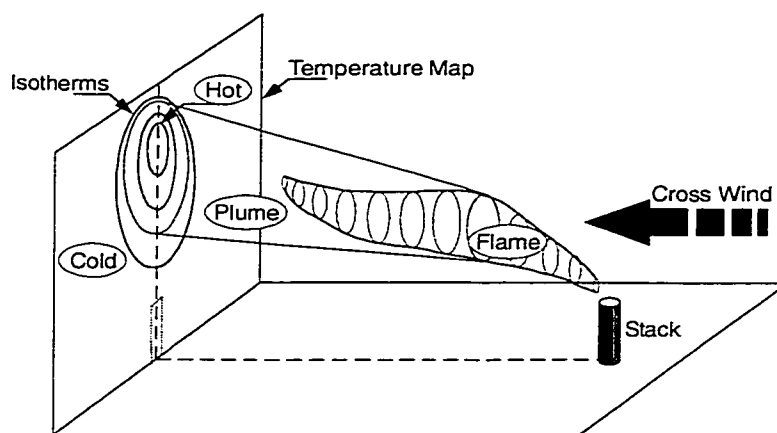
Figure 3.1: Model of Temperature Map of a Jet in Cross-Flow

An apparatus capable of measuring the mean temperature inside the plume without appreciably disturbing the flow was needed. For reasons of cost and ease of use, an array of thermocouples was chosen. A detailed description of the thermocouples, sampling and data processing is in Chapter 4.

Mean temperature maps were collected at various conditions of crosswind, gas velocity, stack diameter and distance from the stack. This data set was compared to an existing buoyant plume dispersion model known to work well on non-reactant plumes and on the far field of reacting jets as reported in the literature.

3.1.2 Plume Dispersion Model

The basis of this model is the balance between the momentum flux of the air and the buoyancy flux of the jet fluid. The main change in the present case from the usual use of a plume dispersion model is the fact that the jet is reacting and the area of interest is close to the reacting zone. From the exit of the stack to the tip of the flame, the

26

buoyancy properties of the jet are evolving along the flame because the combustion induces dramatic changes of temperature.
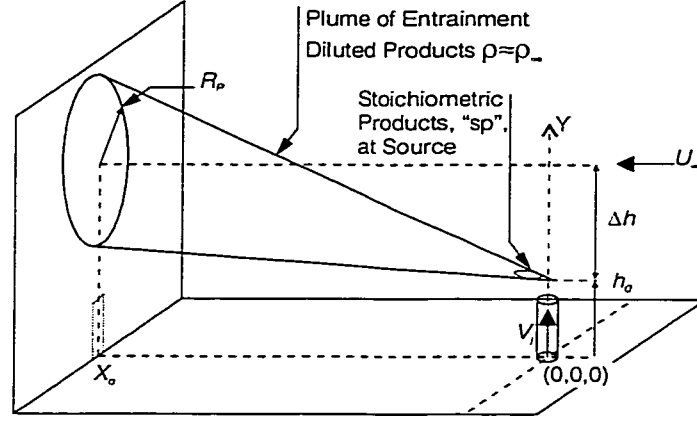
Figure 3.2: Plume of a Non Reacting Buoyant Jet in Cross-Flow

Figure 3.2 shows an ideal situation where there is a point reaction at the exit of the stack. Then, the products behave like a non-reacting buoyant jet (jet with a lower density than the surrounding fluid). This model gives the height of the plume centreline, Δh, reached in a given crosswind, U_∞, gas exit velocity, V_j, stack diameter, d_s, and distance from the stack, X_o.

$$\Delta h = \left(\frac{3}{2\beta^2}\right)^{1/3} \cdot \frac{g^{1/3} \cdot Q_{hv}^{1/3} \cdot R_j^{2/3} \cdot V_j^{1/3}}{T_{sp}^{1/3} \cdot C_{p\infty}^{1/3} \cdot U_\infty} \cdot X_o^{2/3} \qquad (3.1)$$

where Q_{hv} = heating value of the gas (J/kg).

T_{sp} = temperature of stoichiometric products.

Then, Briggs entrainment theory (Briggs, 1975) links the plume rise with a characteristic dimension of the plume, R_p:

27

$$R_p = \beta \cdot \Delta h \tag{3.2}$$

$$R_p = \left(\frac{3\beta \cdot Q_{hv}}{2 \cdot T_{sp} \cdot C_{p\infty}} \right)^{1/3} \cdot g^{1/3} \cdot R_j^{2/3} \cdot \frac{V_j^{1/3}}{U_\infty} \cdot X_o^{2/3} \tag{3.3}$$

The first term in brackets remains constant when:

- the same gas is used for all tests,

- the gas contains negligeable amount of non-combustible elements (CO_2),

- the combustion is almost complete ($\eta \approx 1$),

- The conditions of pressure does not vary too much.

Finally, the radius of the plume is:

$$R_p \propto g^{1/3} \cdot R_j^{2/3} \cdot \frac{V_j^{1/3}}{U_\infty} \cdot X_o^{2/3} \tag{3.4}$$

The details of Briggs' plume rise model are presented in Appendix A.

For the characteristic dimension of non-reacting plumes, the radius of the plume, R_p, is often chosen, but here a modification is introduced since the shapes of plumes are not circular and actually show dramatically different shapes over the range of test conditions. Therefore, to compare plumes of different shapes, the square root of the cross sectional area of the plume, d_p^*, will be used as a characteristic length scale.

As mentioned earlier, the temperature is used to detect the mean plume. A limit between what is considered as the mean plume (volume containing significant amount of the products of combustion) and what is not has to be defined. It was decided that a region that would be considered as part of the plume has a temperature more than half the temperature difference between the hottest point found in a section and the coldest point.

$$T_{plume} \geq \frac{T_{background} + T_{max}}{2} \qquad (3.5)$$

This definition is consistent with the notion of the half-width of a free jet. The shapes of plume and the correlation of their size with the buoyant jet model will be presented in Chapter 5.

3.2 Measurement of Local Efficiency

3.2.1 Local Composition in Plume

Once the plume is located, the next objective of this research was to measure the compositional structure of the plume. This means answering questions such as:

- Are the products of combustion evenly distributed in the plume?

- Is a single sample drawn from the plume representative of its overall combustion efficiency?

Pohl et al. (1985) showed the efficiency was lower on the sides of the plume even if there was no wind. So the local efficiency is not expected to be uniform in conditions of crosswind. To study the non-uniformity of the plume, the local gas composition must

be measured and, similar to the temperature maps, concentration maps (i.e. CO_2, CO, CH_4) must be created at various cross-sections of the plume. The apparatus to make these measurements needs to be mobile relative to the flow and have the capability to collect multiple simultaneous samples. This multiple sampling would accelerate the process to examine the whole plume at stable concentrations and help maximise the precision of the measurement. A linear array of 20 sample probes was used. This apparatus and the procedure of the tests are described in Chapter 4.

From the maps of composition of CO_2, CO, CH_4, which are the major carbon containing species of natural gas combustion, the local combustion efficiency was calculated. The precise distribution of local efficiency for various wind conditions could provide evidence on the mechanism by which the wind affects the overall efficiency.

3.2.2 Calculation of Local Efficiency

The efficiency for natural gas flares (non-sooting flames), as defined earlier, can be calculated as a ratio of concentrations.

$$\eta = \frac{[CO_2]_P}{[CO_2]_P + [CO]_P + [CH_4]_P} \qquad (3.6)$$

where $[A]_P$ = concentration of the species A in the PRODUCTS of combustion.

This only works properly if the analysis is done over "pure" products, in a closed environment such as a reactor. In the case of a flare, three parameters complicate the problem:

30

- It is an open system. The flame is surrounded by a flow of moving air and as the products leave the flame they mix with this surrounding air and dilute as illustrated in Figure 3.3.
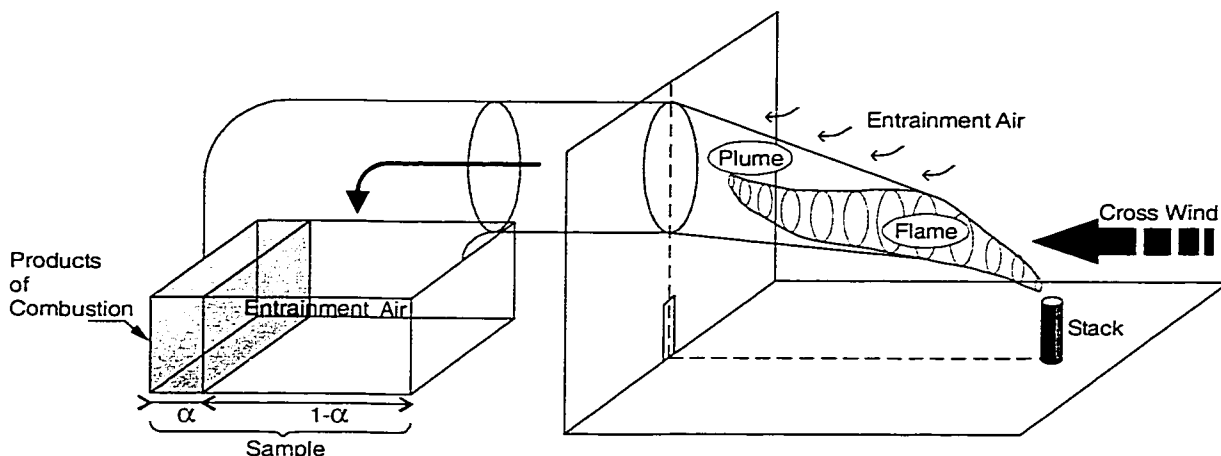
Figure 3.3: Sketch of a Flare in Cross-Flow Showing the Mixing of the Products of Combustion with the Entrainment Air

- The mixing air naturally contains compounds also found in the products like carbon dioxide, carbon monoxide and unburned hydrocarbons. Therefore, if the concentrations in the sampled gases are directly used in the calculations without noticing that part of each compound is coming from the air and not from the flame, a systematic error will result.

- The flared gases may also contain CO_2. Therefore, even pure products contain a certain amount of CO_2 that is not resulting from the combustion and should not be included in the calculation of the efficiency. The following figure illustrates these three foregoing points.
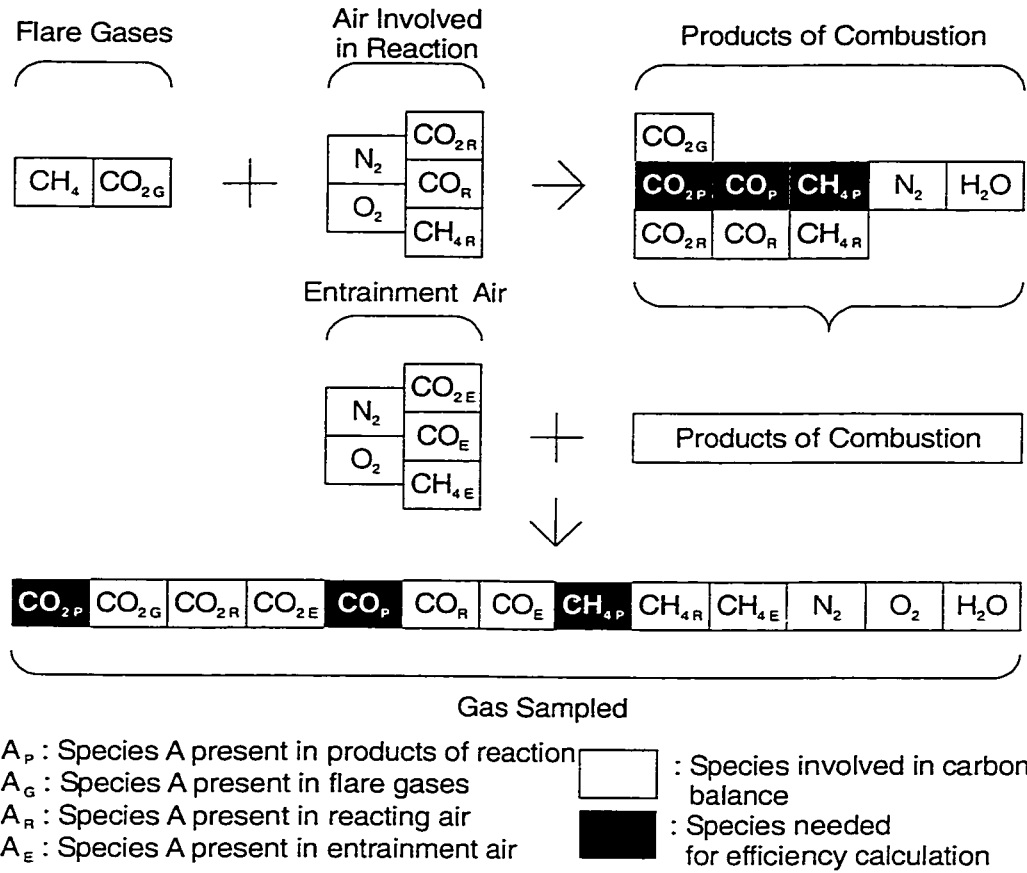
Figure 3.4: Schematic of Origins of Various Major Species in Gas Sampled from Plume of Flare

A raw calculation of the efficiency solely based on the analysis of the sample

would be:

$$\eta_{raw} = \frac{[CO_2]_P + [CO_2]_G + [CO_2]_R + [CO_2]_E}{\begin{array}{c}[CO_2]_P + [CO_2]_G + [CO_2]_R + [CO_2]_E + [CO]_P + [CO]_R + [CO]_E \cdots \\ \overline{\cdots + [CH_4]_P + [CH_4]_R + [CH_4]_E}\end{array}} \cdots$$

(3.7)

when the real efficiency is the result of:

$$\eta = \frac{[CO_2]_P}{[CO_2]_P + [CO]_P + [CH_4]_P}$$

(3.8)

Hence, something needs to be done to work from Equation 3.7 to 3.8.

First, an order of magnitude analysis will highlight if the relative importance of the elements of 3.7.
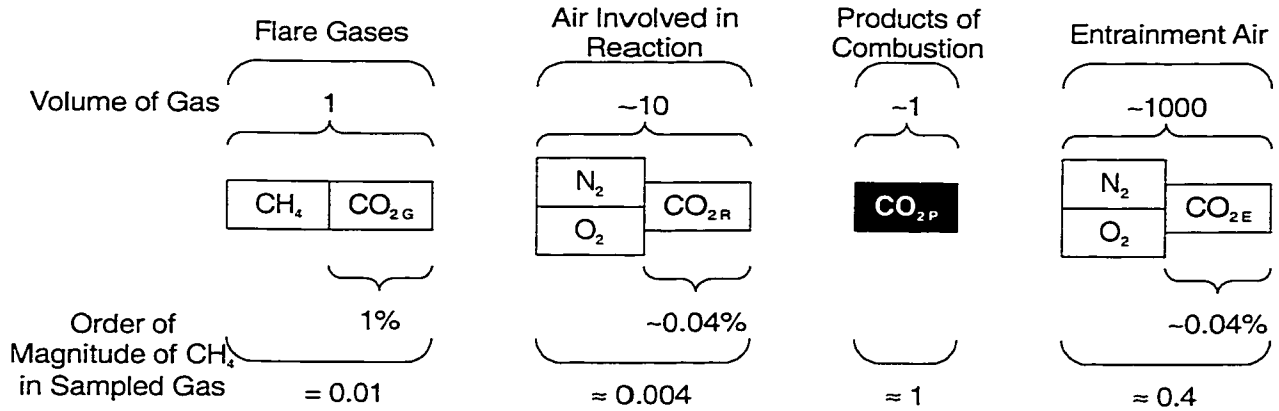
Figure 3.5: Order of Magnitude Comparison Between the Different Sources of CO₂

Figure 3.5 shows 1 mole of gas being burned. A gas analysis of natural gas showed the fraction of carbon dioxide in natural gas ($CO_{2\,G}$) was slightly under 1%. A stoichiometric reaction of methane will use almost 10 moles of air for 1 mole of natural gas and will produce 1 mole of carbon dioxide ($CO_{2\,P}$). Then, it seems reasonable to assume a dilution of the product with the entrainment air of 100:1, therefore 1000 moles of entrainment air for 10 moles of products. Both reacting air and entrainment air contains about 400 ppm of carbon dioxide ($CO_{2\,R}$ and $CO_{2\,E}$). Under these circumstances, the carbon dioxide coming from the gas ($CO_{2\,G}$) and the reacting air ($CO_{2\,R}$) can be neglected because they represent less than 1% of the amount of carbon dioxide produced by the reaction ($CO_{2\,P}$).

$$[CO_2]_P + [CO_2]_G + [CO_2]_R \approx [CO_2]_P \qquad (3.9)$$

In contrast, $CO_{2\ E}$ coming from the entrainment air is as high as half of the amount coming from the reaction and therefore cannot be neglected.

Similar arguments are made for carbon monoxide and the unburned hydrocarbon in Figure 3.6 and 3.7:
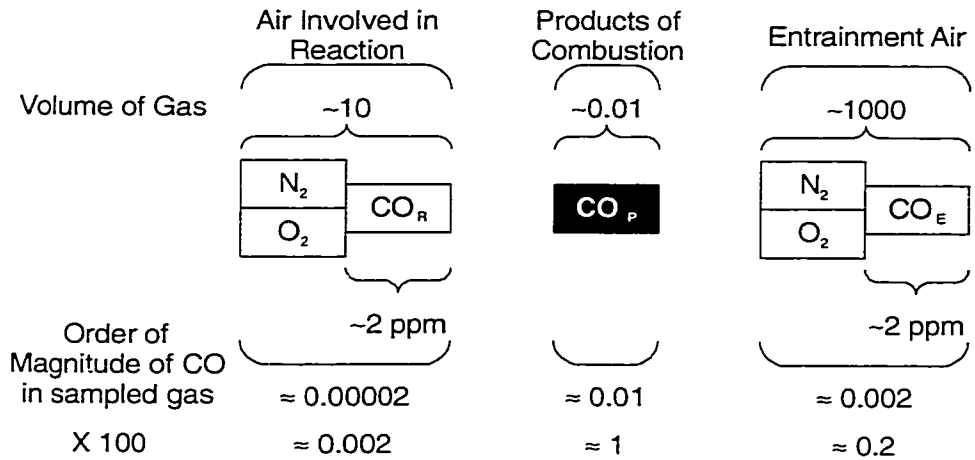

Figure 3.6: Order of Magnitude Comparison Between the Different Sources of CO
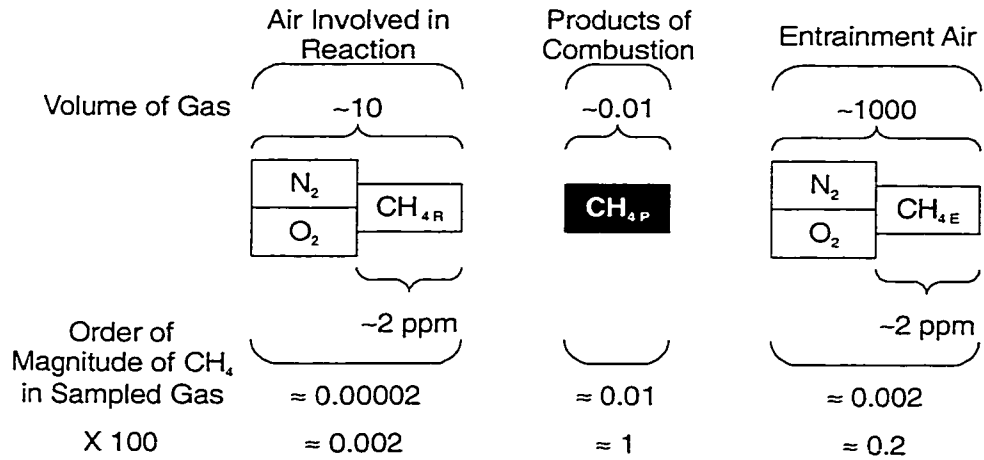

Figure 3.7: Order of Magnitude Comparison Between the Different Sources of CH₄

For both carbon monoxide and unburned hydrocarbon, the natural background can be estimated at 2 ppm. So, relative to the carbon monoxide produced and estimated

34

at 1% of the gas burned, the carbon monoxide and hydrocarbon coming from the reacting air can be neglected, but this is not the case for the ones coming from the entrainment air.

$$[CO]_P + [CO]_R \approx [CO]_P \tag{3.10}$$

$$[CH_4]_P + [CH_4]_R \approx [CH_4]_P \tag{3.11}$$

So, Equation 3.7 can be rewritten as:

$$\eta_{raw} = \frac{[CO_2]_P + [CO_2]_E}{[CO_2]_P + [CO_2]_E + [CO]_P + [CO]_E + [CH_4]_P + [CH_4]_E} \tag{3.12}$$

In order to access the real efficiency, CO_2 E, CO E and CH_4 E should be evaluated. A way to solve this problem is to measure the volume fraction of products, α, in the sample (see Figure 3.3). Combustion uses the oxygen from the air. If the amount of air coming to the flare was just the right amount to provide enough oxygen to react with the gas, there would not be any oxygen left downstream of the flame. From this observation one can build a scale of dilution based on the oxygen concentration in a sample as shown in Figure 3.8 and Equations 3.13, 3.14 where a high level of oxygen would correspond to a small amount of product and a low level of oxygen to a high proportion of product in the sample. The gases sampled from the plume have an O_2 concentration of $[O_2]$ s (S for sample) (Figure 3.8 (a)). These blended gases can be separated into "pure" entrainment air and products of combustion (Figure 3.8 (b)). The O_2 concentration of the entrainment air, $[O_2]$ E, is that measured in the tunnel at the time of the experiment (approx. 21%). The balance of the sample gases is just the products of combustion with an O_2

concentration $[O_2]_P$ equal to zero. Hence, the only remaining unknown is α which can be calculated.

(a)   (b)
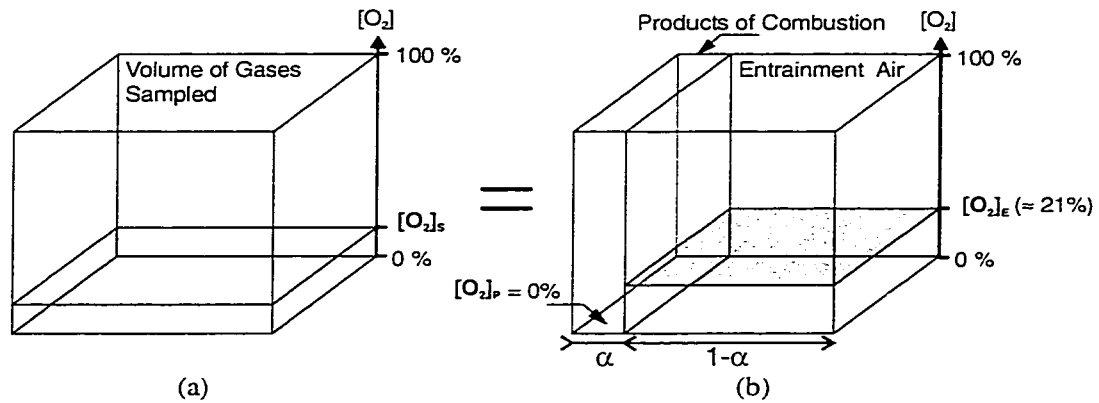
Figure 3.8: Schematic to Show the Separation of the Volume of Sampled Gases Between Entrainment Air and Products of Combustion Using O_2 Concentrations

$$[O_2]_S = [O_2]_E \cdot (1-\alpha) \qquad\qquad (3.13)$$

$$\Rightarrow \qquad \alpha = 1 - \frac{[O_2]_S}{[O_2]_E} \qquad\qquad (3.14)$$

Figure 3.9 shows a similar separation between the CO_2 E coming from the entrainment air and the CO_2 P coming from the reaction.
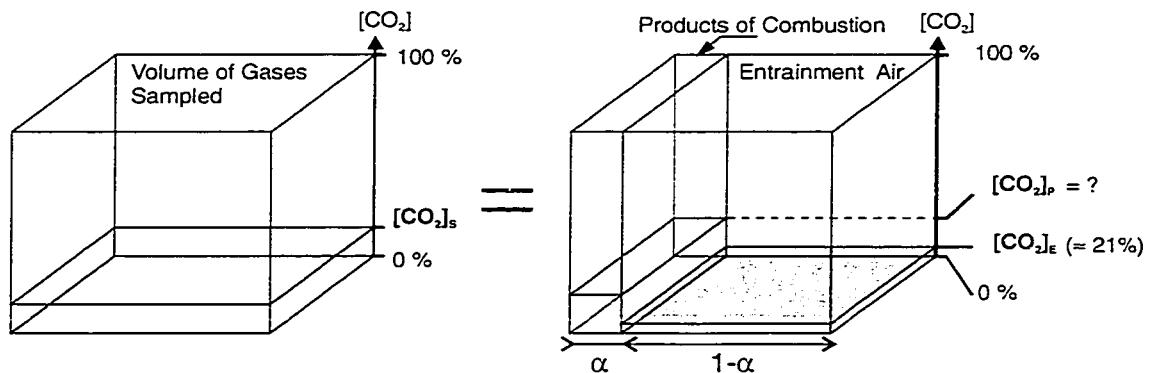
Figure 3.9: Schematic to Show the Use of the Volume Fraction of Products in the Sample to Calculate the CO_2 Concentration in the Products of Combustion

36

$$\alpha \cdot [CO_2]_P + (1-\alpha) \cdot [CO_2]_E = [CO_2]_S \qquad (3.15)$$

$$[CO_2]_P = \frac{[CO_2]_S - (1-\alpha) \cdot [CO_2]_E}{\alpha} \qquad (3.16)$$

Since the fraction α was evaluated with the level of oxygen in the sample, the concentration of CO_2 in the products can be calculated.

The same process can be applied for CO and CH_4:

$$[CO]_P = \frac{[CO]_S - (1-\alpha) \cdot [CO]_E}{\alpha} \qquad (3.17)$$

$$[CH_4]_P = \frac{[CH_4]_S - (1-\alpha) \cdot [CH_4]_E}{\alpha} \qquad (3.18)$$

and then the calculation of the real efficiency is performed.

$$\eta = \frac{[CO_2]_P}{[CO_2]_P + [CO]_P + [CH_4]_P}$$

The sensitivity to the measurements and uncertainty of these calculations are presented in Appendix B.

3.3 From Local to Overall Efficiency

The spatial distribution of local efficiency will be used to look for the reasons why the overall efficiency changes with varying wind speed, jet exit velocity or flare stack diameter.

37

Consequently, the last goals of this research will link the local efficiency measured by point sampling (Section 3.2) and the overall efficiency measured in the facility using the accumulation of all the products of combustion in the closed-loop wind tunnel. This latter technique has been refined over the past three years and now provides accurate results of overall efficiency. See Appendix C for details.
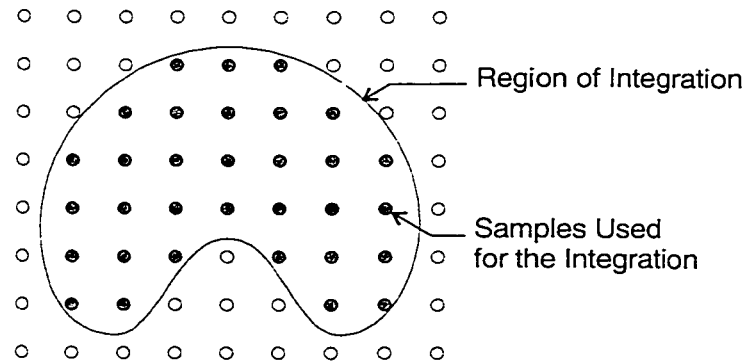
Figure 3.10: Schematic of the Integration of the Local Efficiency over a Region

An estimated overall efficiency is calculated by integrating the local efficiency calculated at many points (approx. 300) over the entire section of the plume as shown in Figure 3.10.

The integration is performed as follows:

1. Definition of the region where the efficiency will be included in the integration. This is based on setting an upper bound on the amount of entrainment air in the sample and hence it is limited by the accuracy of the gas analysers.

2. Calculation of the local density. If the entire plume had a uniform density, a simple average over all the sampling points would provide a mean value of CO_2, CO and CH_4. The temperature over the sampling area is uneven, regions of high temperature in the plume have a low density and contain a smaller mass of products but have the highest concentrations of products. The local density is calculated as:

$$\rho_L (kg/m^3) = \frac{P_L (Pa)}{\overline{R}_L \cdot T_L (K)}$$ (3.19)

where $\overline{R}_L$ = Specific gas constant. Because the dilution with the entrainment air is large: $\overline{R}_L = 287$ J/kg.K. P_L = Local pressure T_L = Local temperature.

3. Calculation of weighted (average) species concentrations, $[A]_{AV}$, over the plume is done by multiplying the concentration at each point by the density and dividing the sum by the sum of the density. This is done separately for both sample and entrainment air.

$$[CO_2]_{S/E\,AV} = \frac{\sum_n (\rho_L \cdot [CO_2]_{S/E})}{\sum_n \rho_L}$$ (3.20)

4. Calculation of an average fraction of products, α_{AV}, assuming that the products are going to homogenise before arriving in analysers. The same region as above is chosen.

$$\alpha_{AV} = \frac{\sum_{n} \alpha_L}{n} \qquad (3.21)$$

where n = number of samples in the average

5. Correction of the concentrations of CO_2, CO and CH_4 with the average dilution in a similar manner to local dilution.

$$[CO_2]_{PAV} = \frac{[CO_2]_{SAV} - (1 - \alpha_{AV}) \cdot [CO_2]_{EAV}}{\alpha_{AV}} \qquad (3.22)$$

$$[CO]_{PAV} = \frac{[CO]_{SAV} - (1 - \alpha_{AV}) \cdot [CO]_{EAV}}{\alpha_{AV}} \qquad (3.23)$$

$$[CH_4]_{PAV} = \frac{[CH_4]_{SAV} - (1 - \alpha_{AV}) \cdot [CH_4]_{EAV}}{\alpha_{AV}} \qquad (3.24)$$

6. Calculation of the overall efficiency with corrected concentration becomes:

$$\eta_{AV} = \frac{[CO_2]_{PAV}}{[CO_2]_{PAV} + [CO]_{PAV} + [CH_4]_{PAV}} \qquad (3.25)$$

and is representative of the measurement from a hood placed over the entire area of integration.

3.4 Application to Full Scale Testing

Integrated local efficiency has also been used to simulate the results that would exist if a specific shape of hood were used to sample a large portion of the plume. Several shapes were simulated:

1. a thin vertical slot which combines the advantages of a small flow sampled with a large spatial averaging

2. either a circular or elliptic hood fitting the shape of the plume

3. a rectangular hood.

The reason for integrating over these shapes is to explore the quality of the efficiency results for field studies where collecting the whole plume is not practical.

Chapter 4

FACILITY AND EQUIPMENT

The facility and equipment used to reach the objectives set in the previous chapter are described in this chapter.

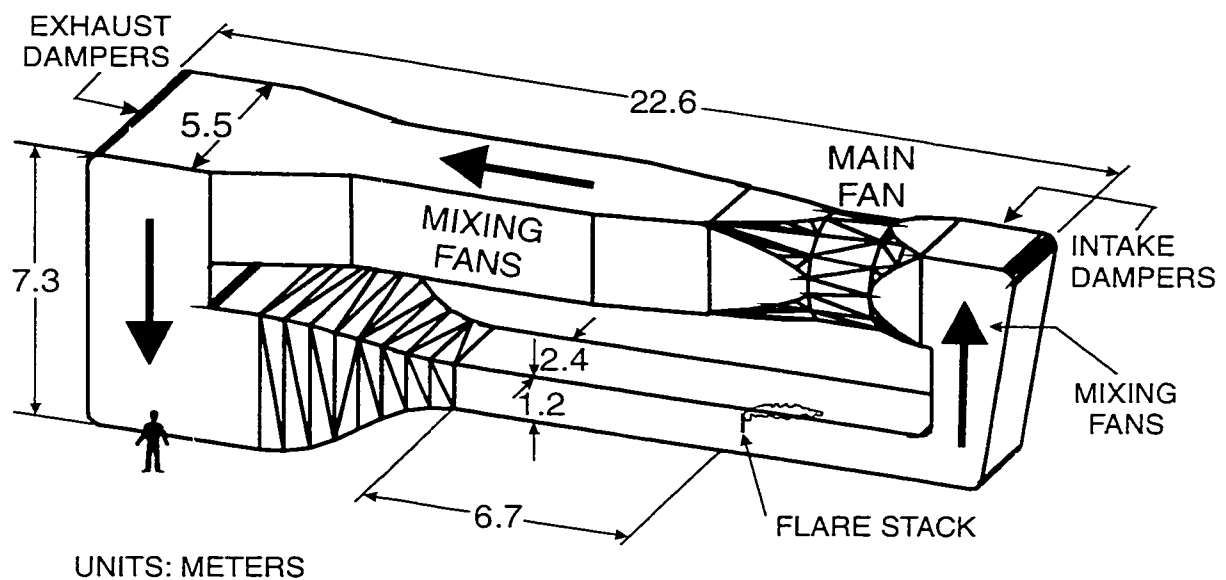## 4.1 Wind Tunnel

Figure 4.1: Schematic of Wind Tunnel

All the tests were performed in a closed-loop wind tunnel shown schematically in Figure 4.1. The internal total volume is approximately 350 m³. A 150 kW DC motor drives a 3m diameter fan that is capable of producing a stable crosswind from 1.0 to 35m/s. The wind speed is measured with a Pitot tube and a propeller. Arrays of turning

vanes are employed at each of the four ninety degree bends in the tunnel to maintain the integrity of the flow. A series of fine mesh screens and a 6.3:1 area ratio convergent nozzle produce a near uniform plug flow in the 1.2 m high by 2.4 m wide test section that follows. A hot wire probe (0.004 mm diameter) was used to characterise the velocity field in the test section. Representative mean velocity profiles along the axes of symmetry of the test section at the stack location can be found in Appendix D. The boundary layer is approximately 12 cm thick at the stack location and the r.m.s. turbulent velocity fluctuation in the core flow is constantly less than 0.4% except at low wind speeds (<2 m/s) where this intensity rises to about 1.8%. Filtering has shown that the increase in turbulence is a result of small, low frequency (<0.2 Hz) oscillations of the mean wind speed, which are associated with the control circuitry of the wind tunnel fan and not turbulence.

Fresh air can be continuously introduced into the wind tunnel by two sets of dampers during a test to maintain a stable level of concentrations or the dampers can be closed and the products then accumulate in the wind tunnel. The total volume is such that the concentration of oxygen does not significantly vary during a test with dampers closed.

Gas detectors to monitor the concentration of hydrocarbons are installed inside and outside of the wind tunnel and ensure safety in the facility.

4.2 Flare Stacks

Typical full-scale flares are 10.2 cm in diameter (4 inches Schedule 40 pipe). The three flares used in this research are scale model pipe flares made of steel tubing with an

inner diameter of 16.7, 22.1 and 33.3 mm. This corresponds to nominally 0.75, 1 and 1.5 inch tube. The ratio of inner diameter over outer diameter was held constant at 0.9 for all stacks used.

The internal flow in the full-scale flare is turbulent. To maintain the same flow regime inside the scaled-down flare, a turbulence generator was inserted in the tube and its effect on the flow was checked by LDV. The turbulence generator used was a perforated plug, which had holes 13.5% of the inner diameter in a staggered pattern that created 65% blockage as shown in Figure 4.2.
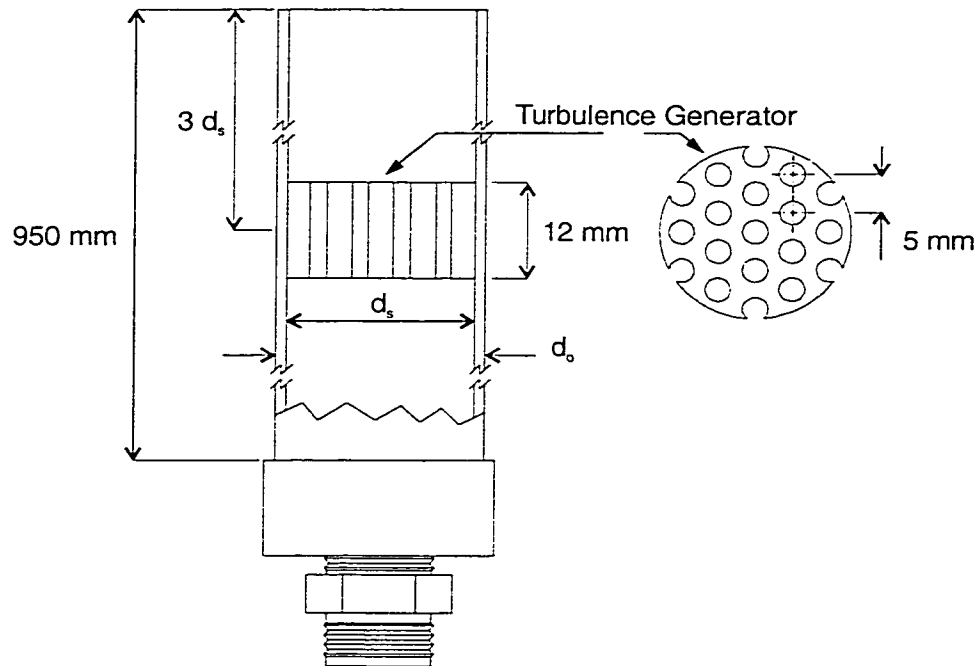

Figure 4.2: Schematic of Model Flare Stack

The full-scale flares with an outside diameter of 114.3 mm have a regime of laminar boundary layer. The small-scale flares should be in the same regime. By looking at the deposit of soot on the pipe, it is confirmed that the regime is laminar. The

soot was deposited in the wake region up to +/- 90 deg. from the leading stagnation point of the stack.
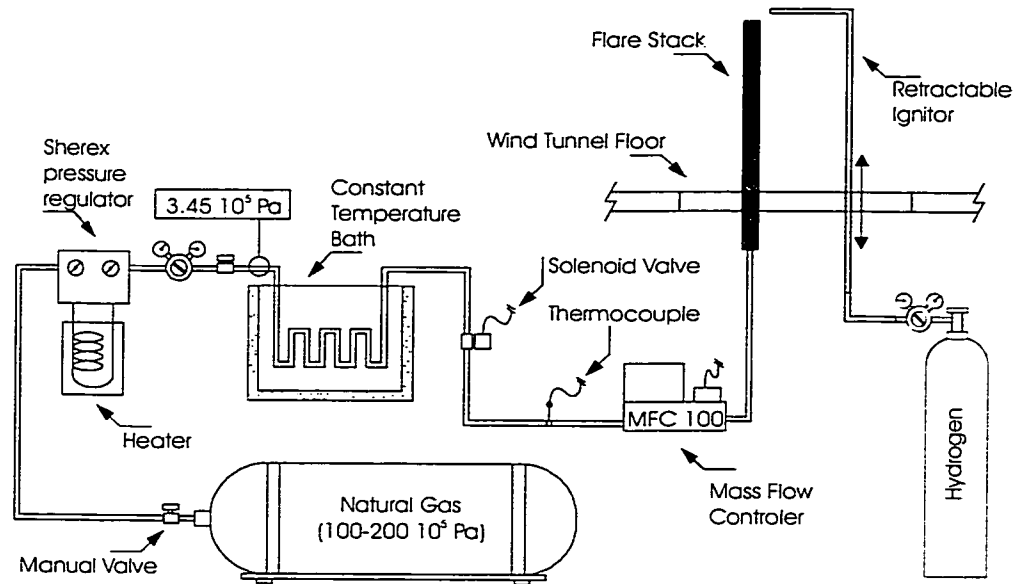
4.3 Gas Supply System

Figure 4.3: Schematic of Gas Supply System

The flare can burn natural gas, propane or a mixture of fuel that could include the addition of carbon dioxide and/or nitrogen. All of the tests presented in this thesis are done with natural gas, so Figure 4.3 only presents the corresponding piping schematic for this gas. Natural gas is depressurised from its storage pressure down to 3.45 Bar. It is then drawn through metal coils into a temperature-controlled bath in order to bring its temperature back to a known and constant value after depressurisation. A computer-controlled mass-flow meter sets the amount of gas sent for burning at the stack. Also shown in Figure 4.3 is the ignition system for the flare. A retractable hydrogen jet flare that is ignited by a manual spark system provides a robust means of igniting the flare.

4.4 Mobile Traverse

Figure 4.4 shows the mobile traverse installed in the test section downwind of the flare stack. Vertical and cross-stream horizontal axes are motorised and computer-controlled. Rollers mounted on rails allow manual motion along the third axis (streamwise) from the location of the stack to 4 m downstream in 10 cm increments. Probes used to map the temperature field downwind of the flame and the ones to collect samples of the plume are mounted on this traverse.
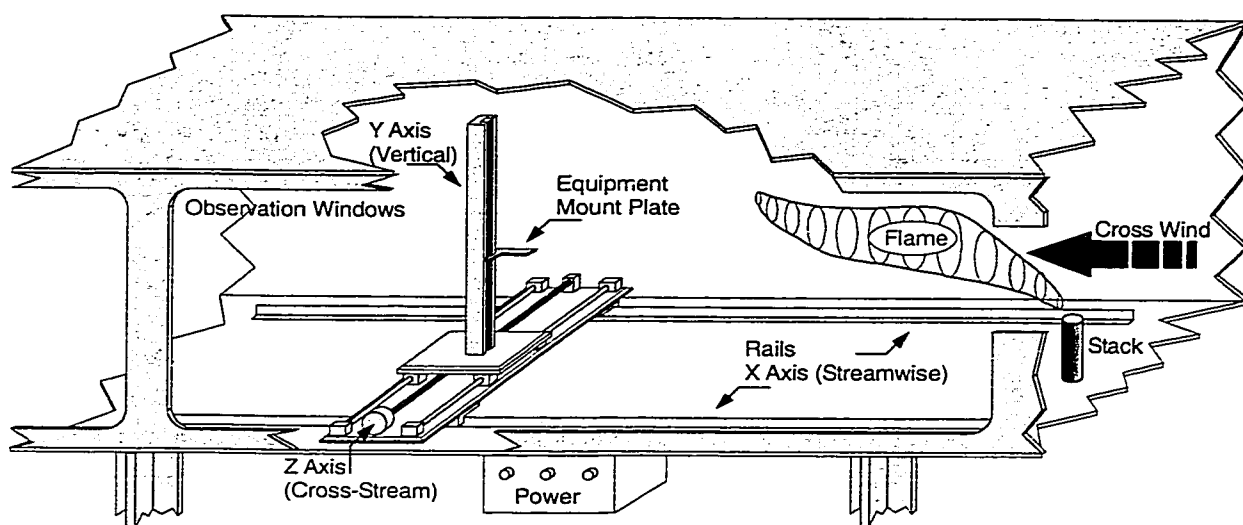

Figure 4.4: Sketch of Mobile Traverse

4.5 Temperature Detectors

To rapidly create maps of temperature, an array of twenty-seven type T (copper-constantan) thermocouples was built and installed on the traverse as shown in Figure 4.5. Thermocouples were inserted in stainless steel tubing and only the junctions (approx. 1 mm in diameter) were exposed 5 mm in front of the holder. The spacing between each junction was 2 cm. A data acquisition system with integrated cold junction compensation

was used to measure the thermocouple outputs. The conversion of voltage to temperature is done by a built-in routine of LabVIEW®. The temperatures were sampled at 50 Hz over a 10 second period to take into account the fluctuation of the flow. The duration of 10 seconds was chosen after specific preliminary experiments. Complete 2D maps of sections of the plume are performed within 7 minutes.
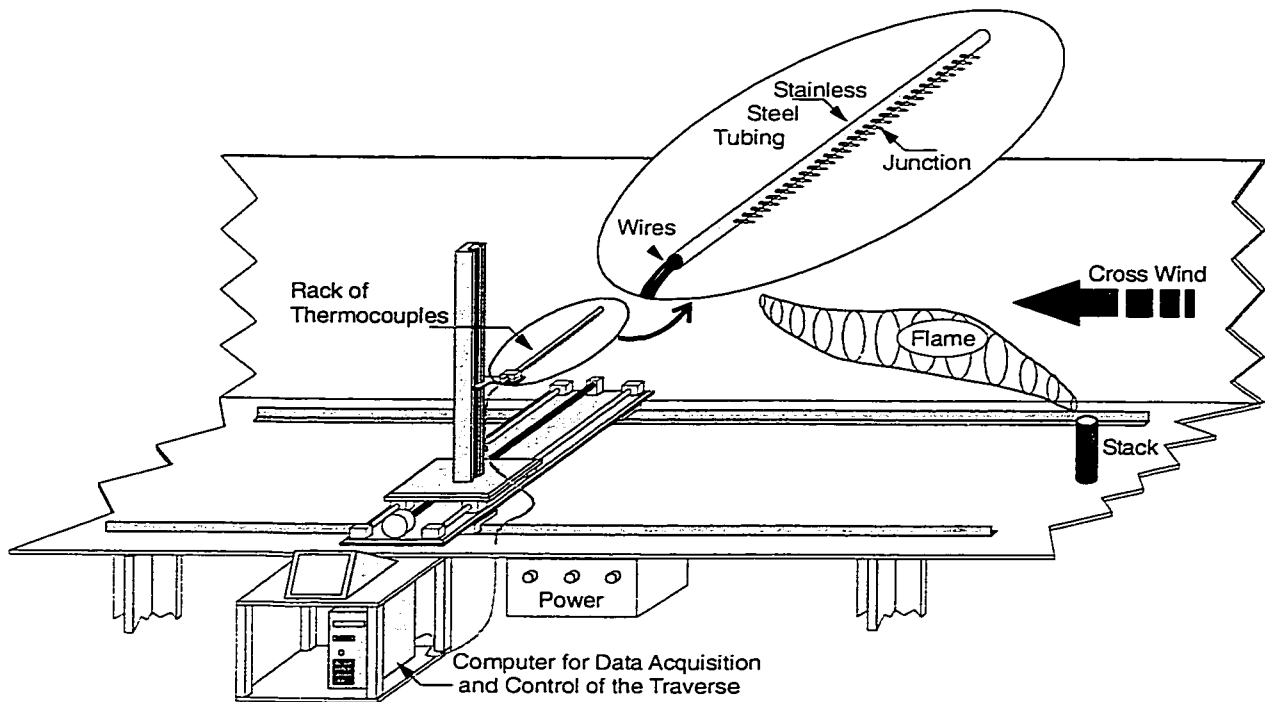
Figure 4.5: Sketch of Temperature Detectors

4.6 Plume Sampling Apparatus

Multiple single point sampling was used to create 2D maps of selected mean species concentrations (i.e. CO_2, CO, CH_4). Since a flame in the wind is not stable, the mean composition cannot be measured by a direct on-line analysis. The gases were first sampled at a point over a suitably long period and these gases were blended to create a

homogeneous mixture before being analysed. This blending was achieved by sampling the tunnel flow isokinetically for a period to fill 25 litres Teflon® sampling bags. The gases mixed in the bags and then were resampled and transferred to the gas analysers. Figure 4.6 shows a schematic of the device.
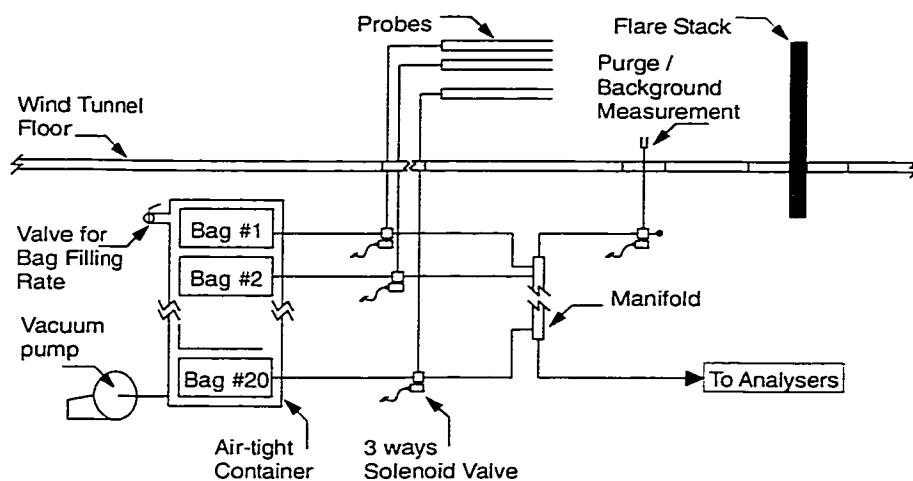

Figure 4.6: Schematic of Plume Sampling Apparatus

The probes (stainless steel tubing) with a nominal diameter of 4.5 mm I.D. (1/4 in. nominal) were installed on the mobile traverse. They could be installed in a linear pattern or in a grid pattern. A grid pattern was used during the first tests on a new plume to discover its overall size and shape. After, for the detailed analysis of the plume, probes were set in a vertical linear pattern and moved laterally in 2 cm steps to cover the entire plume. Each probe was connected to an independent 3-way solenoid-valve. One exit of the valve was connected to the sampling bags. The other exit was installed on a stainless steel manifold that groups all the lines before passing through an auxiliary sample pump to the analysers. This set-up allowed 20 samples to be drawn simultaneously and then analysed separately. The solenoid valves were controlled manually. Connections

between the components were made with Teflon® tubing of 4.5 mm. I.D. (1/4 in. nominal).

The 20 bags were placed in an airtight container, connected to a vacuum pump/blower that can change container pressure. A pressure transducer provides the feedback on the pressure inside the container. The bags were filled by lowering the pressure inside the container to a given level. By changing the pressure, the rate of gas sampling could be controlled and consequently the isokineticity of the sampling. Once the bags were filled, the vacuum pump was shut off and the valve left open so the container returned to atmospheric pressure. Then, a switch of position in one of the 3 way valves and the start of the auxiliary sampling pump sends the gas contained in the chosen bag toward the analysers for 90 seconds. Appendix E shows typical readings of the analysers during these 90 second periods.

When one bag was analysed the others remained open to the probe, but the length of the tube (4.5 m) inhibited any significant exchange between the sample and the atmosphere after the bag was filled. The total volume of tubing in the system represents 1% of the volume of the bags.

The reliability of the whole sampling system was tested during preliminary tests. The wind tunnel was filled with known concentrations of CH_4 and CO_2 and sampling was performed with the bags. It appeared that, due to their design, the bags could not be perfectly emptied and a small pocket of gas always remained from the previous filling. Preliminary tests showed that if the bags were filled twice, there was no detectable cross-contamination between samples. This procedure, used for all tests, provided a reading

within one percent of the expected value. See Appendix F for exact dimensions of the apparatus and details of the procedure.

4.7 Gas Analysers

The samples arriving from the sampling bags through Teflon® tubing were drawn by vacuum pumps with Teflon® coated diaphragms. Independent lines with rotameters fed each analyser at their required flow rate (approximately 1100 ml/min.). The heart of the system was the measurement of gas concentrations performed by a series of four Rosemount gas analysers as shown in Figure 4.7.
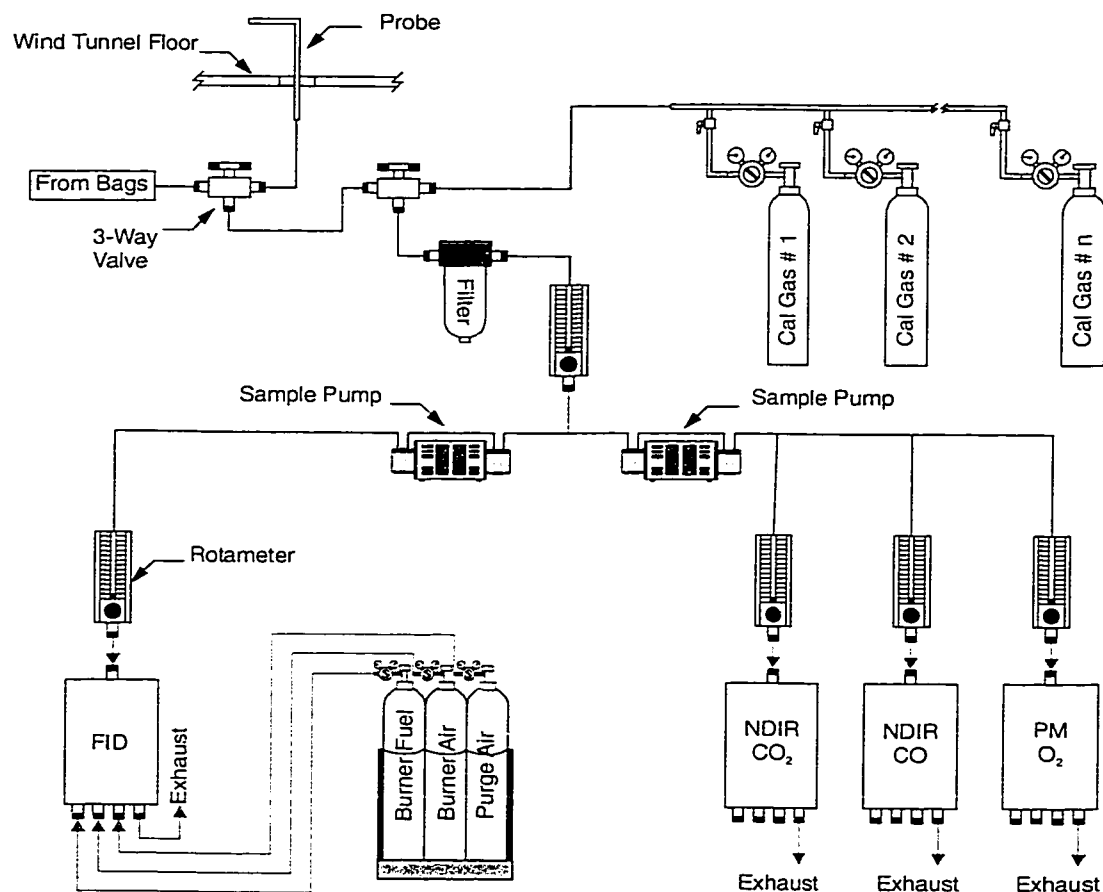

Figure 4.7: Schematic of Gas Analysers Network

After being calibrated, analysers installed in parallel provided the composition of samples coming from a fixed probe or from the bags.

One paramagnetic detector measured the oxygen (O_2) concentration. The principle of the detection is based on the magnetic properties of the O_2 molecule. Placed in a magnetic field the oxygen acts like a magnet and modifies the force balance on a test cell placed in the gas flow to be analysed. The concentration of O_2 is proportional to the force induced on the test cell. The stability of such detectors is excellent.

One flame ionisation detector measured the concentration in hydrocarbon compounds. The sample is burned in a hydrogen flame where the carbon atoms emit ions. The ionisation current caused by the ions on polarised electrodes is directly proportional to the concentration in carbon atoms of the sample being burnt. The analyser is calibrated with methane.

Two non-dispersive infrared detectors measure CO and CO_2. For each analyser, an infrared beam was sent through two separate cells. One contains a reference gas, the other the gas to be analysed. The difference of energy due to the absorption of the beam by the gas is detected by a "gas microphone" using the Luft principle. The concentration of the sample in CO or CO_2, proportional to the absorbed energy, was then calculated.

The outputs (0-5V range) of the four analysers were acquired through a data acquisition card to the computer controlling the facility. Table 4.1 shows the range and the uncertainty of each analyser used.

Type	Range	Unit	Uncertainty	Unit
O2	0-25	%	0.25	%
CH4	0-500	ppm	5	ppm
CO	0-100	ppm	1	ppm
CO2	0-10 000	ppm	100	ppm

Table 4.1: Range and Uncertainty of Gas Analysers

4.8 Computers and Software

The Flare Research Facility at the University of Alberta is computer-controlled. One computer is devoted to the control of the wind tunnel (wind speed, opening of dampers), the gas supply (flow-control solenoids) and the acquisition of the gas analysers outputs. A second computer controls the traverse and the temperature probes when necessary. Data values are stored and post-processed on a remote third computer. All computers are Pentium II based (450Mhz min.) network connected with Windows NT® and the main computer has a RAM of 382 MB.

Data acquisition and control software was developed under LabVIEW® (National Instruments™), a powerful graphical developer with numerous built-in routines. During a test, the main program, running on the computer controlling the wind tunnel, saved a master file with all the parameters of the test such as air temperature, pressure, wind speed, gas flow rate and the reading of the gas analysers. Grapher™ and Surfer® (Golden Software Inc.) were used for the creation of graphs (2D and 3D respectively).

Chapter 5

RESULTS AND ANALYSIS

The experimental work is divided into three topics. First, there is the measurement of the plume size with respect to its location as determined by spatial distribution maps of temperature. These data are compared to a standard plume rise model. Secondly, data of the plume's composition and the calculation of the efficiencies (local and overall) are presented. Finally, maps of efficiency are used to determine what would be the most suited shape of hood to properly collect the plume for an overall efficiency measurement.

5.1 Mean Thermal Structure of the Plume

Except for the study by Huang and Yang (1996), most of the experiments on jet diffusion flame in crosswind were performed in a regime where the velocity of the jet was larger or much larger than the velocity of the cross-flow (i.e. $4 < V_j/U_\infty < 50$). However, in the case of continuous solution gas flaring, the velocity of the jet is of the order of magnitude of 1 m/s and therefore is often lower than the velocity of the wind. In the wind tunnel, experiments were performed with the following conditions:

- Fuel: natural gas (see Table 5.1 for composition)

- Gas Jet Velocity, V_j, (m/s): 0.5, 1, 2

- Crosswind Velocity, U_∞, (m/s): 1.5, 2, 3, 4, 6, 8.

Component	CH4	C2H6	CO2	N2
Mean %	94.96	2.4	0.81	1.74
Max. Deviation %	1.3	1.25	0.04	0.07

Table 5.1: Natural Gas Composition

The mean temperature was the scalar used to track the plume. Figure 5.1 (at the end of the chapter) shows the type of map that was used to define the location of the plume. The mean temperature data are presented here in two ways. First, as a contour plot with selected isotherms drawn and second as a surface where the height above the base plan represents the temperature. Shading is also used to represent the temperature. The locus (0,0) defines the exit of the stack. The thicker contour shows the iso-temperature corresponding to the half value between the highest and lowest temperature recorded. This will be used as the threshold to define the limit of the plume.

5.1.1 Shapes of Plumes Cross-Sections

In total, 149 cross-sections shapes and sizes of plumes were recorded. These plumes needed to be classify by shape in order to provide useful information. The first attempt of classification was by increasing momentum ratio, as defined in the section 2.2.1. A certain evolution of the shapes was visible, but there was something "wrong" when the experimental results were ordered this way. Plume shapes did not evolve progressively shifted back and forth as the momentum ratio was increased. This suggested a different way to organise the data. Rather than momentum ratio, the ratio r_{mb}, which combines the ratio of momentum to buoyancy as defined in section 2.2.1.3, was used to classify experimental results. With the new classification, all shapes seemed

to line-up in an elegant evolutionary pattern, which will be described in the following sections.

5.1.1.1 The Kidney Shape

At low crosswinds ($U_\infty \approx V_j$), the flame is fully bent downstream. The products, instead of rising vertically are advected by the crosswind. When U_∞ and V_j are of the same value, the plume appears in the shape of a kidney as shown in Figure 5.2 (a).

Flames in this situation were bent over but were still located predominately above the top of the stack. The dominant flow structure for these flames is a pair of counter-rotating vortices that are associated with bending the jet flow over to the direction of the cross-flow (Smith and Mungal, 1998). There is a pair of maximum temperature peaks horizontally spaced at the core of the vortices. Since the flame is above the stack, it is not significantly affected by any of the wake flow structures created by the stack. As the flow progresses downstream, the counter-rotating vortices continue to draw cold ambient fluid into the bottom of the plume structure as it mixes with the surrounding air. The kidney shaped plume is observed at velocity ratio, r_{mb}, from 1.19 $(m/s)^{2/3}$ to 5.04 $(m/s)^{2/3}$, when burning natural gas in air. The size of the plume tends to shrink as the velocity ratio increases as shown by Figure 5.2 (b).

5.1.1.2 The Circular Shape

As $U_\infty/V_j^{1/3}$ is increased, the trajectory of the flame becomes more horizontal and the kidney shrinks and moves downward. The product gases are located closer to the region of the flow under the influence of the wake structures created by the stack. First, a

little part of the products gets trapped in this region and a tongue appears underneath the kidney.

Figure 5.2 (c) shows how the plume is distorted by the wake vortices, which draw jet fluid (at this point being products of combustion) downward (Smith and Mungal, 1998). Initially, the impact of the hot fluid being transported down by the wake vortices is only seen as an intermittent finger of product gases being extracted from the main plume. As the crosswind is increased further, more gases are drawn into the wake vortices (Figure 5.2 (d)). Based on Figure 5.2, these more circular shaped plumes occur when 5.04 $(m/s)^{2/3} < r_{mb} < 7.56$ $(m/s)^{2/3}$ for natural gas in air flow.

5.1.1.3 The Downwashed Shape

At yet higher values of r_{mb} a second temperature peak (below the stack tip height) appears. The relative magnitude of that second peak grows with increasing cross-flow velocity as illustrated by Figure 5.2 (e). This starts appearing at velocity ratio, r_{mb}, of 7.56 $(m/s)^{2/3}$ until 10.08$(m/s)^{2/3}$, for burning natural gas in air. These plumes are called downwashed plume.

Figure 5.2 (f) shows the situation with the highest ratio, r_{mb}, $(8/0.5^{1/3}=10.08$ $(m/s)^{2/3})$. Under these conditions the bulk of the flame is trapped in the recirculation zone behind the stack and the entire plume is now affected by the wake flow. The upper peak has almost completely disappeared and most of the products are in the lower peak. Its shape is nearly circular and its maximum mean temperature is located beneath the stack tip height. For velocity ratios, r_{mb}, larger than 10.08 $(m/s)^{2/3}$, the upper peak simply

disappears and only the lower one remains. In these conditions the flame looks like a blue vertical disk attached to the lee side of the stack.

5.1.1.4 Remarks

From observations during tests, kidney plume and downwashed plume seem to be "stable" compared to the circular plume, which appears to be a transition between the two states. As the plume shrinks under the effect of increasing velocity ratio, it keeps its kidney shape until a threshold is reached. Then, the transformation into a downwashed plume seems to be triggered by a very small change in the velocity ratio r_{mb}. Therefore, it was very delicate to obtain temperature maps showing an evolution within the circular type of plume. For details, Appendix G contains all the temperature maps recorded.

5.1.2 Model of Plume Entrainment

5.1.2.1 Scaling

The self-similar shape of non-reacting plumes as they evolve in the downstream direction has been well characterised by Smith and Mungal (1998). The entrainment of ambient air into the jet fluid causes the jet to disperse and spread. Reviewing all the contour plots shows that the plume of model size flares seems to spread in the downstream direction in a manner very similar to non-reacting plumes, as shown in Figure 5.3.

Also, the effects of the stack diameter and gas velocity are clearly visible in Figure 5.4 and 5.5 and seem to evolve in a manner proper for scaling (smaller r_{mb} are more kidney like and larger r_{mb} are more circular). To correlate the size of plumes from

flares of varying exit velocity, stack diameters and crosswind speeds, a buoyant jet model described in section 3.1.2 was chosen. For this model, the plume radius was predicted to be scalable with experimental adjustable variables (i.e. X_o, d_s, V_j and U_∞). In this section, the correlation between the measured characteristic dimension of the plume and that predicted by the model is tested. The characteristic dimension of the plume, d_p^*, is defined as the square root of the area contained within the 50% contour of each plume. Figure 5.6 shows the measured characteristic dimension, d_p^*, from 129 plumes plotted relative to the ratio characteristic of the radius of the plume that was to scale with $g^{1/3}.X_o^{2/3}.d_s^{2/3}.V_j^{1/3}/U_\infty$. The plumes used in Figure 5.6 cover a range of r_{mb} from 1.19 to 8 $(m/s)^{2/3}$. There are two reasons why not all of the 149 maps recorded were used. First some plumes were larger than the map and therefore, the area of the plume could not be measured. Also, the plumes corresponding to a velocities ratio of 10.08 $(m/s)^{2/3}$ $(U_\infty = 8$ m/s, $V_j = 0.5$ m/s) are not included in the fit because these plumes were characterised by a very low maximum temperature (below 60 deg. C). Consequently, the uncertainty on their characteristic dimension, d_p^*, based on the temperature difference between the hottest point and the background temperature was too large. However, the rest of the data align on a straight line shows that a semi-empirical relation can be evaluated giving the characteristic length, d_p^*, when conditions of distances from the flare, flares diameter, exit velocities and crosswind speeds are chosen. For the group of plumes studied, this relation is:

$$d_p^* = 2.3830 * g^{1/3} \frac{V_j^{1/3}}{U_\infty} X_o^{2/3} d_s^{2/3} - 0.0139 \tag{5.1}$$

with the following units: d_p^*,(m), g (m/s^2), V_j (m/s), U_∞ (m/s), X_o (m/s) and d_s (m).

58

Since this relation was a result of a model based on momentum and buoyancy, and the data collapsed, this is further evidence that the flow is dominated by buoyancy forces.

5.1.2.2 Limitations

The scaling model described above provides a characteristic length, which was derived from the area of the plume. Relating this characteristic length back to a physical dimension of the plume without information on the shape of the plume is not possible. This characteristic length would match the width and the vertical thickness of a plume only if the plume was square. Figure 5.7 shows the actual width of the plume compared to the calculated characteristic length. For 95% of the plume tested, the actual width is larger than the characteristic length and the median value of this underestimation is about 25%.

If the width of the plume is on average 25% larger and if the area is correct, the vertical thickness would have to be smaller than d_p^*. Figure 5.8 shows the ratio of width over vertical thickness measured for most of the plumes. Up to 6 m/s per second of crosswind, the ratio is visibly above 1 confirming that the plumes are more wide than high. This corresponds mostly to the kidney shapes plume. Only for the highest crosswinds, when the plume is downwashed, has the vertical thickness of the plume became larger than the width.

5.1.2.3 Comments

The purpose of the Equation 5.1 was to relate a characteristic length, not a physical dimension of the plume, to the conditions that create the plume. However, it

shows there is self-consistency within the different plumes and their general behaviour can be compared to one of a non-reactant buoyant jet. In parallel, the difference between this characteristic length and the width of the plume showed that, on average for the range of kidney shaped plumes observed, its width is about 20-25% larger than vertical thickness.

5.2 Compositional Structure of the Plume and Local Efficiency

5.2.1 Concern over Sampling Near a Flame

Initially, a heated sampling line and an airflow dryer was installed between the manifold near the sampling bags and the analysers (see Figure 4.7) because a significant amount of water vapour produced by the flame was expected. The major risk with water is the condensation along the sampling line as the temperature of the sample decreases. Then, the composition of CO_2 and CO in the sampled can be altered by being absorbed into the liquid water. After experimenting, the actual dilution of the product with the normally dry ambient air was such that it appeared there would not be any risk of condensation inside the sampling line.

The other advantage of sampling after a large amount of dilution of the products in air was the low temperature of the product. Within half a meter after the tip of the flame, the mean temperature is under 200 deg. C so the reactions of combustion have already stopped.

5.2.2 Maps of Local Composition and Efficiency

Four detailed compositional maps showing the spatial distribution of CO_2, CO, CH_4 and O_2 corresponding to a kidney-shaped plume, a circular plume and a downwashed plume, are going to be described hereafter. The three tests involve a flare gas exit velocity, V_j, of 1 m/s and crosswind speeds, U_∞, of 2, 4 and 8 m/s. From these compositional data two-dimensional local efficiency maps have been calculated.

5.2.2.1 Composition and Efficiency of a Kidney Shaped Plume

For the case $U_\infty = 2$ m/s, $V_j = 1$ m/s, the probes are placed at a distance, downstream of the stack, X_o of 110 cm, and the flame is approximately 80 cm long.

Figures 5.9 (a, b, c and d) show normalised concentrations of CO_2, CO, CH_4 and O_2. For this normalisation scales the background is set to 0 and the highest concentration is set to 1. Dimensions are indicated in centimetres relatively to the tip of the stack. The O_2, is used to determine the amount of air entrained in the plume (section 3.2.2). The most concentrated part of the plume contains 6.3 % of products of combustion.

At first sight, the concentrations of CO_2, CO and CH_4 have definitive similarities with the temperature profiles. The 50% temperature contour matches quite closely with the 50% concentration contour (shown on theses figures as thicker line) since the difference between the respective areas is 2.3%. The CO_2 concentration distribution differs from those for CO and CH_4. While the 90% contour of the CO_2 is mostly visible on the centre line and a little bit in the tips of the kidney, the same contour appears only on the tips of the kidney for both CO and CH_4. Those latter species only reach 60-70 % of their own maximal concentrations in the centre line. Now, it should be noticed that in

absolute value, the concentration of CO and CH_4 are extremely low (below 10 ppm) compared to the concentration of CO_2 (7872 ppm max.). Consequently the efficiency remains very high all over the plume as shown in Figure 5.10.

The pattern of the efficiency maps differs from the ones on CO_2, CO and CH_4 maps. A vertical distribution is visible. The lower half of the plume shows signs of having the lower efficiency relatively to the upper half. Better burning conditions in the upper half of the flame (direct contact with the entrainment air) that for the bottom half (already presence of products advected from upstream) could explain this difference. However, the efficiency is essentially close to 100% everywhere.

5.2.2.2 Composition and Efficiency of a Circular Plume

For the case $U_\infty = 4$ m/s, $V_j = 1$ m/s, the probes are placed at a distance, X_o, downstream of the stack of 140 cm, and the flame is approximately 120 cm long. The most concentrated part of the plume contains 6.8 % of products.

Again, the mean concentration contours shown in Figure 5.11 have a distinct similarity with the temperature profiles. The downward finger of products visible under the kidney highlights the effect of the wake of the stack and its ability to extract products from the main plume.

Figures 5.11 (a,b,c) show the differences between concentration contours of CO_2 from CO and CH_4. The same kind of distribution as in the previous example is visible over the plume with the maximum of CO_2 (8275 ppm) mostly in the centre while CO and CH_4 appears in the tips of the kidney. Again, those latter species only reach 60-70 % of

their own maximal concentrations in the centre line. This time though, the level of CO and CH_4 are more significant with respective maximums of 43 and 65 ppm.

Figure 5.12 shows the local efficiency calculated in the region containing more than 10 % of the highest concentration. The local efficiency ranges from 98.5 to 99.4 %. Again the lowest efficiency appears in the lower half of the kidney.

5.2.2.3 Composition and Efficiency of a Downwashed Plume

In the case $U_\infty = 8$ m/s, $V_j = 1$ m/s, the flame is approximately 90 cm long and the probes placed 110 cm from the stack. The most concentrated part of the plume contains 3.8 % of products.

Figures 5.13 (a,b,c) show the stronger influence of the stack and its wake on the products. The displacement of products is now so strong that products are dispatched over two regions. One region is above the stack tip height and the second is below.

There is a distinctly different mapping between the concentrations of CO_2 and CO relative to CH_4. The maximum concentration of CO_2 (4864 ppm) and CO (107 ppm) occur in a region above the stack tip, which was directly downstream of the tip the flame. These gases also appear in a region under the stack tip with concentrations between 40 and 50 % of their maximums. The CH_4 had its maximum concentration (357 ppm) region spread between the near flame tip region and the region directly downwind of the tip of the stack. Figure 5.13 shows that the peak of CH_4 near the point (0,0) was also the location of the lowest local efficiency (~67 %). This was the lowest local efficiency observed.

5.2.3 Observation Based on Species Concentration Maps

The crosswind is one of the main factor influencing the efficiency of the model flares in the wind tunnel. Detailed maps of local efficiency show that the reduction of efficiency is not a general trend over the entire plume. If this was so, the efficiency would be uniform throughout the plume. The fact that different products end up in different places of the plume suggests that the phenomena responsible for the creation of CO and CH_4 occurs early in the formation of the reacting jet flow. At higher crosswind a fraction of the gas seems to be ejected from the main stream below the flame and does not burn with the flame. This appears to be the main source of lower efficiencies.

5.3 Technique of Plume Sampling

5.3.1 Integrated Efficiency

The overall performance of a flare defined by its overall efficiency will be presented in this section.

If it is assumed that the area sampled by the probes is large enough that the entire products are advected through it, the overall efficiency can be calculated by a weighted integration of the local efficiency as detailed in Chapter Section 3.4. The three cases considered in the previous section will be used to illustrate this process.

First, the case $U_\infty = 2$ m/s, $V_j = 1$ m/s (Figure 5.10). The integrated efficiency over the area with a concentration of products higher than 10% of the most concentrated part of the plume results in an estimated overall efficiency of 99.8%. Johnson and Kostiuk (2000), using the technique of accumulating species in the wind tunnel also

measured and efficiency above 99.5 % for the same conditions. Since the efficiency is so high and its variance is small, this example may not be the most illustrative.

For the case $U_\infty = 4$ m/s, $V_j = 1$ m/s, the variation of efficiency inside the plume is broader (Figure 5.12). The integrated efficiency over the entire plume gives a result of 98.9% while the local efficiency varies from 98.5 to 99.5 %. For the same conditions, Johnson and Kostiuk (2000) measures an efficiency of 99.1 %.

For the case $U_\infty = 8$ m/s, $V_j = 1$ m/s (Figure 5.14), the local efficiency goes down to 67%. But since this happens in a region with a low density of products of combustion (only 20-30 % of the maximum product concentrations), the weighted combustion efficiency over the entire plume remains at 93.6 %. In this case, Johnson and Kostiuk (2000) measures an efficiency of 96.9%. The wind has to reach 9.5 m/s in order to measure an overall efficiency of about 93.6%. This case, in particular, highlights the problems of single point sampling techniques.

5.3.2 Simulated Alternate Sampling Techniques

The major problem with the multi-points sampling technique used in this thesis for field-testing is on a practical engineering level. This method is a long process if done with few probes or can become costly if done with numerous probes (approximately 300 for a complete map). Also, it requires stable conditions (crosswind and gas velocity) during the test. Therefore, it would be interesting to compare the accuracy of the results obtained by a detailed mapping of the local efficiency with the results obtained by various faster sampling techniques.

5.3.2.1 Single Point Sampling

This technique has the major advantage of being easy to use. A single probe aspiring a small amount of gas is easier to handle than either multiple probes or a large hood sampling cubic meters of air. Unfortunately, the non-uniformity of efficiency in the plume in conditions of strong crosswind makes this approach unlikely to result in an efficiency close to the value of the overall efficiency of a plume because of the spatial variation in local efficiency. Analysing the efficiency distribution produces an interesting result. Increasing the threshold used to separate ambient air from product can artificially reduce the area included in the integrated overall efficiency. It was discovered that as the minimal level included is raised from 10%, to 50%, or even more, of the maximum concentration, the result remains remarkably stable as shown in Figures 5.15, 5.16 and 5.17. Ultimately if the sample is performed at the location of the highest concentration of products, the result is very close to the overall efficiency obtained by integrating over the entire plume or by measuring the rise of concentrations in the wind tunnel.

This can be explained by the fact that most of the product actually concentrates in a small area which dominates the integration of the weighted efficiency.

A problem arises when the flame and therefore the plume will be moved around by unstable wind conditions. Maintaining the probe inside the region the most concentrated in products of combustion will become extremely challenging.

5.3.2.2 Round Hood Sampling

Another possibility to solve the problem due to the instability of the flame while keeping the advantage of single point sampling is to use a relatively large hood that

would extract the core of the plume. The simplest shape is a circular hood. The study of the shapes of the plume showed that a plume has, in general, a width 25% larger than its vertical thickness. In order for the hood to fit the plume better, the same ratio could be applied to its shape, leading to an elliptic hood. Figures 5.18, 5.19 and 5.20 show the overall efficiency against the size of the hood for the three sets of conditions.

Figure 5.18 shows that as long as the hood remains entirely inside the plume, there is no real change in the efficiency. Only the concentrations go down as the diameter is increased since there are fewer products on the edges of the plume than in the centre. This shows that it is not necessarily the biggest hood that will provide the most accurate results. Using an elliptic hood instead of a circular one does not improve the results either since the concentrations are lower.

Figure 5.19, and especially Figure 5.20, display a broader dispersion in the estimated overall efficiency. Two points can explain this. First, the plume does not have a shape that fit the shape of a large circular hood. So a large amount of the sample does not belong to the plume and the results are affected. On the other hand, the plume has a strong vertical variation in the local efficiency. A smaller hood would then only sample one region of the plume and the results would be different for each region. For these reasons different shapes of hood have to be tested.

5.3.2.3 Vertical Slot Sampling

The symmetry across the centreline of the plume is noticeable for every type of plume. Therefore a sampling just along the centreline could potentially be enough to properly evaluate the overall efficiency of the map. A thin vertical probe is simulated in

Figures 5.21, 5.22 and 5.23. Results are compared as an error is introduced in its lateral positioning (relative to the centre line). This will simulate a change in the wind direction during a sampling period.

Figure 5.23 shows that the highest concentrations are measured in the centreline and the dilution remains under 1/100 as long as the probe remains inside the half-plume contour. However, off the centreline, the concentration drops below this level of 1/100 often considered as a lower limit for reliable sampling and the efficiency rises slowly up to 100% when only ambient air is left in the sample.

In outdoor conditions, this means the wind direction should not vary by more than a certain angle, θ, in one direction or the other in order for the probe to remains inside the plume (see Figure 5.24). The results for the 3 conditions tested are:

- $r_{mb} = 2 \ (m/s)^{2/3}$, $\theta = 5°$ see Figure 5.21

- $r_{mb} = 4 \ (m/s)^{2/3}$, $\theta = 3.3°$ see Figure 5.22

- $r_{mb} = 8 \ (m/s)^{2/3}$, $\theta = 1°$ see Figure 5.23

This shows that the wind condition will have a major effect on the accuracy of the measurement of the efficiency. Also, this could explain why very high efficiency has most of the time been measured in the field. When the crosswind is relatively small, the efficiency remains high. As the crosswind increases and induces a lower efficiency, the condition of the measurement becomes more delicate and the chance of measuring just ambient air (with an "efficiency" close to 100% due to natural concentrations in CO_2, CO and CH_4) instead of actual product of combustion increases.

5.3.2.4 Rectangular Hood Sampling

This type of hood was tested only for the condition r_{mb} = 8 (m/s)$^{2/3}$ because of the elongated shape of the plume. A lower dilution ratio than with a vertical slot probe are obtained as illustrated in Figure 5.25. The dilution is equivalent to the one obtained with a circular probe of the same diameter but the result is more stable since most of the plume is sampled. For a width of 8 cm, the circular probe measures efficiency varying from 87.38 to 91.03 % when the rectangular hood gives 90.05 %. But these values are still different than what is believed to be the real efficiency measured by integrating the entire plume (93.6%).

5.3.2.5 Limitations

The results obtained for the different shapes of hood are only simulations from tests performed in very controlled conditions. Therefore this chapter does not indicate which hood is guaranteed to work in a larger scale but it compares different possibilities and indicates which ones are more likely to give reliable results. Moreover, as the scale changes, new phenomena can appear and the effects of turbulence have not been investigated. This section also warned that the direction of crosswind would have the strongest effect on the results.

5.4 Summary

From the previous discussion, three important points were made and should be restated.

1. The mean cross-sectional structure of the thermal plume just downwind of the flame was extensively analysed for a range of velocity ratios ($1.19 < r_{mb} < 10.08$ (m/s)$^{2/3}$). As the velocity ratio increases, the plume of products evolves from a kidney to a fully downwashed shape. During the transition between the two shapes, the plume first moves downward to the height of the stack exit and then splits into two plumes, one above the stack exit height, the other below. This transition seems to be triggered by a very small change in the velocity ratio r_{mb}. A buoyant plume rise model was used to scale a characteristic dimension of the plumes, d^*_p, against the important variables such as crosswind, U_∞, jet velocity V_j, stack diameter, d_s, and distance from the stack, X_o. The data correlated with:

$$d^*_p = 2.3830 * g^{1/3} \frac{V_j^{1/3}}{U_\infty} X_o^{2/3} d_s^{2/3} - 0.0139$$

The characteristic dimension of the plume was calculated by the square root of the plume cross-sectional area defined by the half mean temperature contour. Except for the fully downwashed plume, which have a vertical silhouette, the width of the cross-section of the thermal plume is approximately 25% larger than its vertical thickness.

2. The composition of the plume products of combustion in the cross-sections were analysed in terms of mean CO_2, CO and CH_4 concentrations by a multi-point sampling device for three velocities ratio: $r_{mb} = 2$, 4 and 8 (m/s)$^{2/3}$. At the two lower velocity ratios, the CO_2 tended to accumulate near the centreline of the plume while the CO and HC accumulated more on the bottom of the plume. Consequently, the local combustion efficiency is lower in the bottom half of the plume. This suggests that the top and front of the flame have a higher efficiency than the bottom and back

(leeward side) of the flame. The case with the higher velocity ratio showed an important region of unburned hydrocarbons near the stack exit height. These results suggested that part of the fuel might have been stripped from the main stream just at the exit of the stack. This could be a mechanism for the lower overall performance observed at high crosswind.

3. An estimation of the overall efficiency from a single point sampling of the plume is very sensitive to probe position because of the non-uniformity in the local composition inside the plume. However, in controlled conditions such as in the wind tunnel, a sample in the most concentrated part of the plume can provide a good first estimate of the overall performance. Simulations from the data provided by the multi-point sampling device shows two other results. For a lower velocity ratio r_{mb}, a large circular hood centred on the plume could provide a good measurement of the overall performance. For a higher velocity ratio, a sample collected from along the full centreline of the plume provided a more accurate result because of the vertical symmetry of the plume and the large vertical difference in local efficiency.

: 50% Temperature Contour.

: Stack Projection.

Temperature Scale (deg. C)

20   60   90   160   220
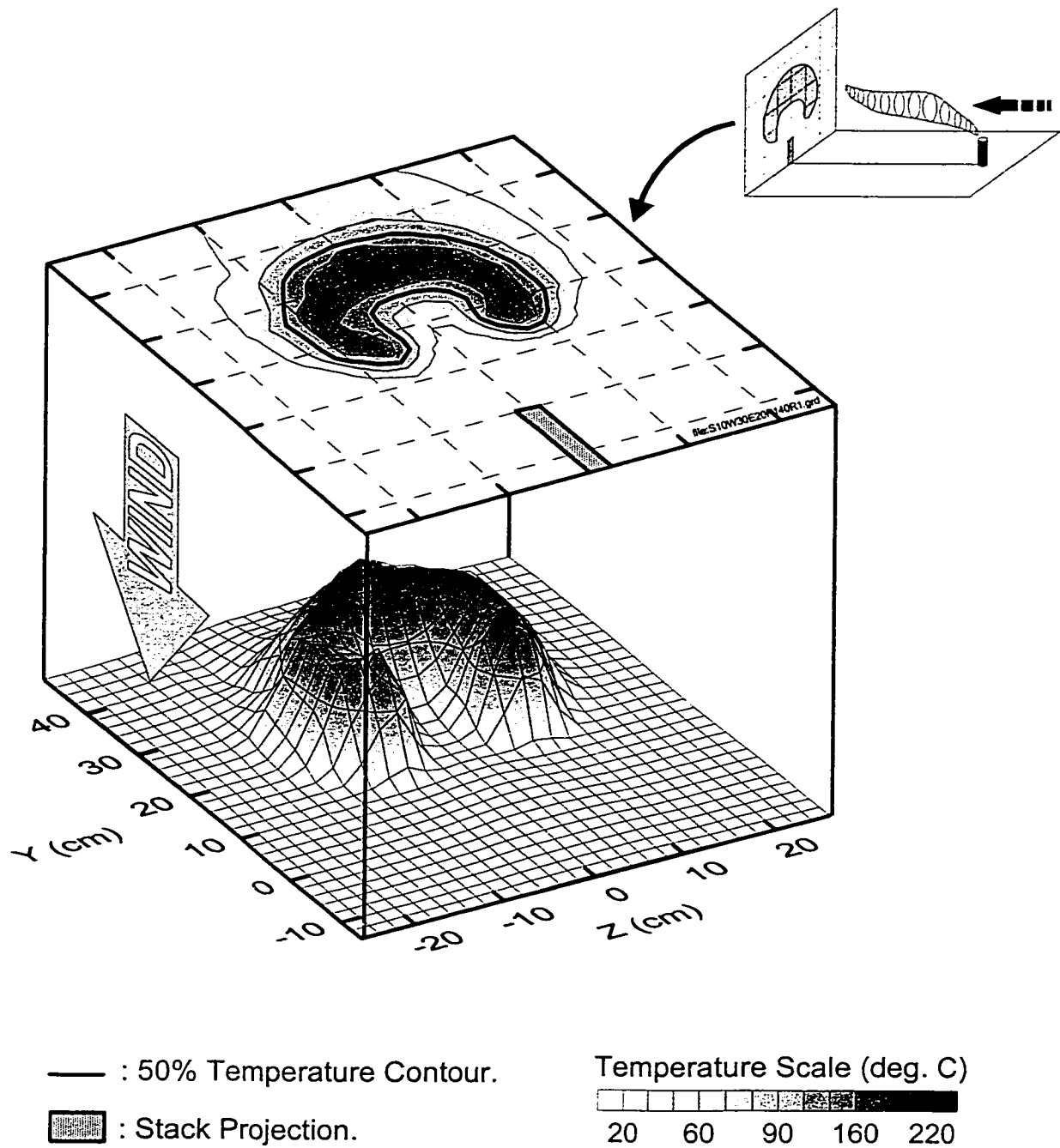
Conditions: $V_j = 2$ m/s ; $U_\infty = 3$ m/s (r_{mb} = 2.38 $(m/s)^{2/3}$; $R = 0.33$)
$d_s = 2.21$ cm ; $X_o = 1.4$ m

**Figure 5.1: Temperature Profile of a Section of a Plume
Behind a Flame of Natural Gas in Crosswind**
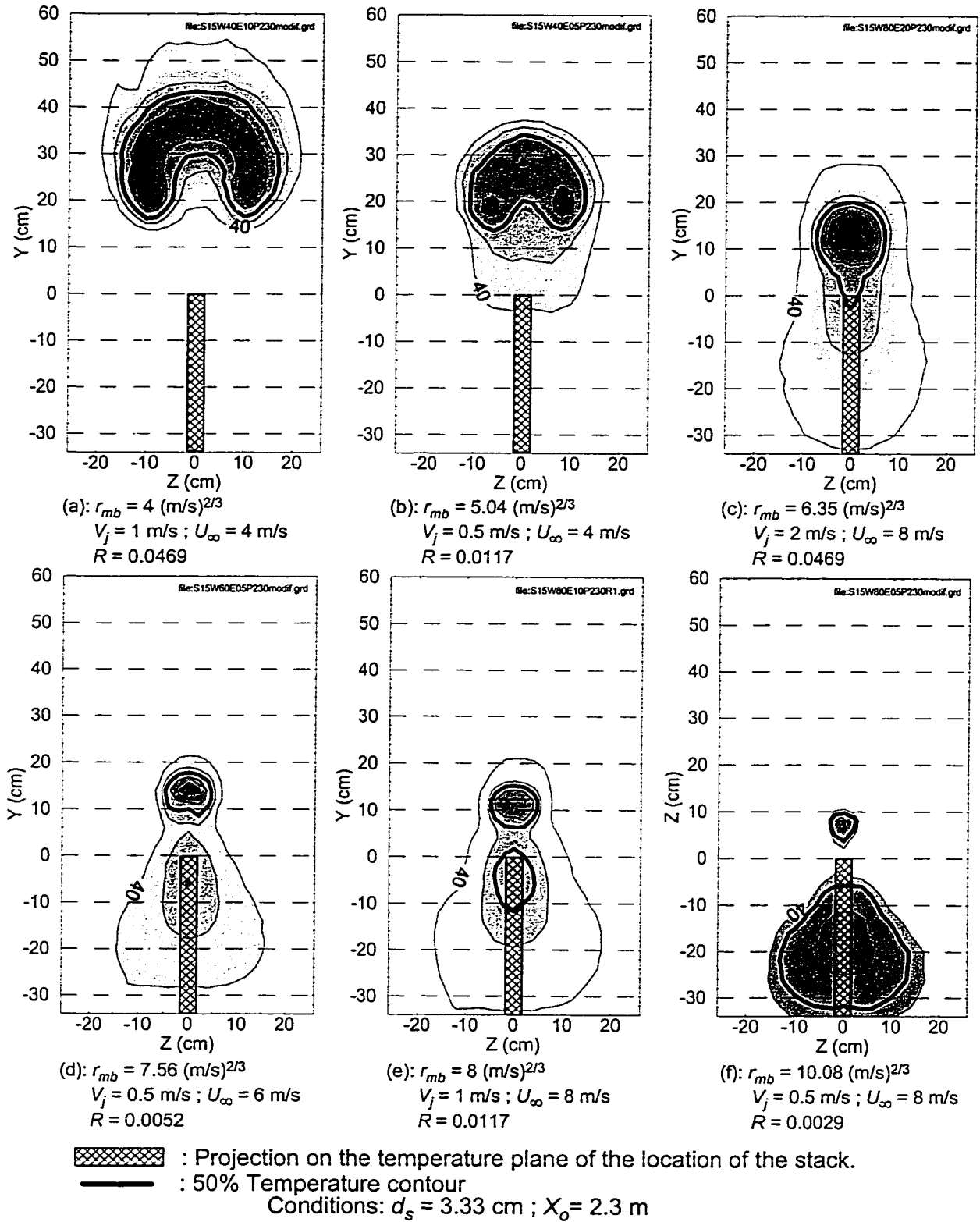
Figure 5.2: Effect of Varying Velocity Ratio, r_{mb}, on Temperature Profile of a Section of a Plume Behind a Flame of Natural Gas for Constant Stack Diameter

(a): r_{mb} = 4 (m/s)$^{2/3}$
V_j = 1 m/s ; U_∞ = 4 m/s
R = 0.0469

(b): r_{mb} = 5.04 (m/s)$^{2/3}$
V_j = 0.5 m/s ; U_∞ = 4 m/s
R = 0.0117

(c): r_{mb} = 6.35 (m/s)$^{2/3}$
V_j = 2 m/s ; U_∞ = 8 m/s
R = 0.0469

(d): r_{mb} = 7.56 (m/s)$^{2/3}$
V_j = 0.5 m/s ; U_∞ = 6 m/s
R = 0.0052

(e): r_{mb} = 8 (m/s)$^{2/3}$
V_j = 1 m/s ; U_∞ = 8 m/s
R = 0.0117

(f): r_{mb} = 10.08 (m/s)$^{2/3}$
V_j = 0.5 m/s ; U_∞ = 8 m/s
R = 0.0029

▨▨▨▨▨ : Projection on the temperature plane of the location of the stack.
───── : 50% Temperature contour
Conditions: d_s = 3.33 cm ; X_o = 2.3 m
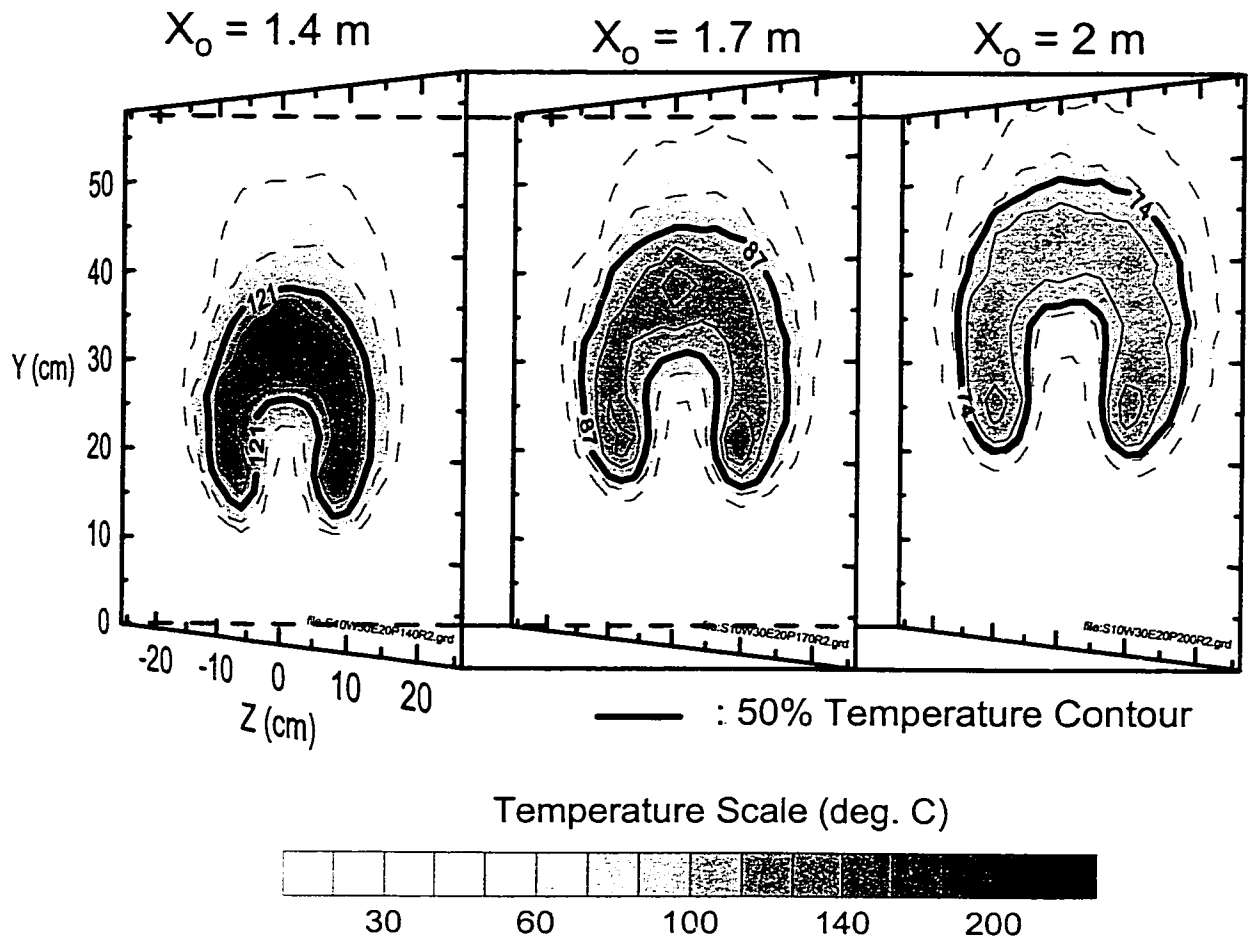
73

Figure 5.3: Spread of the Plume of a Flame of Natural Gas with Increasing Distance from the Stack for Constant Velocity Ratio, r_{mb}, and Stack Diameter

d_s = 1.67 cm d_s = 2.21 cm d_s = 3.33 cm

Conditions: X_0 = 1.7 m ; V_j= 2 m/s ; U_∞ = 3 m/s (r_{mb} = 2.38 $(m/s)^{2/3}$; R = 0.333)
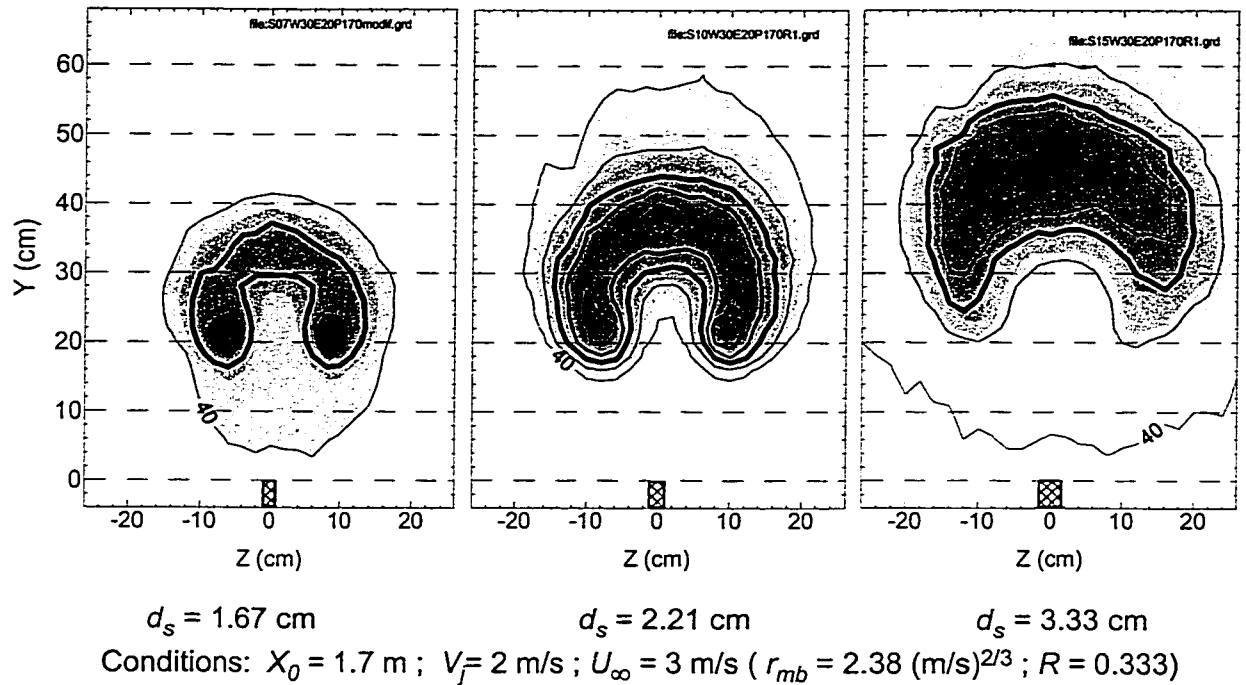
Figure 5.4: Effect of Varying Stack Diameter for Constant Distance from the Stack and Crosswind

V_j = 0.5 m/s V_j = 1 m/s V_j= 2 m/s

r_{mb} = 7.56 $(m/s)^{2/3}$ r_{mb} = 6 $(m/s)^{2/3}$ r_{mb} = 4.76 $(m/s)^{2/3}$

R = 0.0052 R = 0.0208 R = 0.0833

Conditions: d_s= 2.21 cm ; X_0 = 1.4 m ; U_∞ = 6 m/s
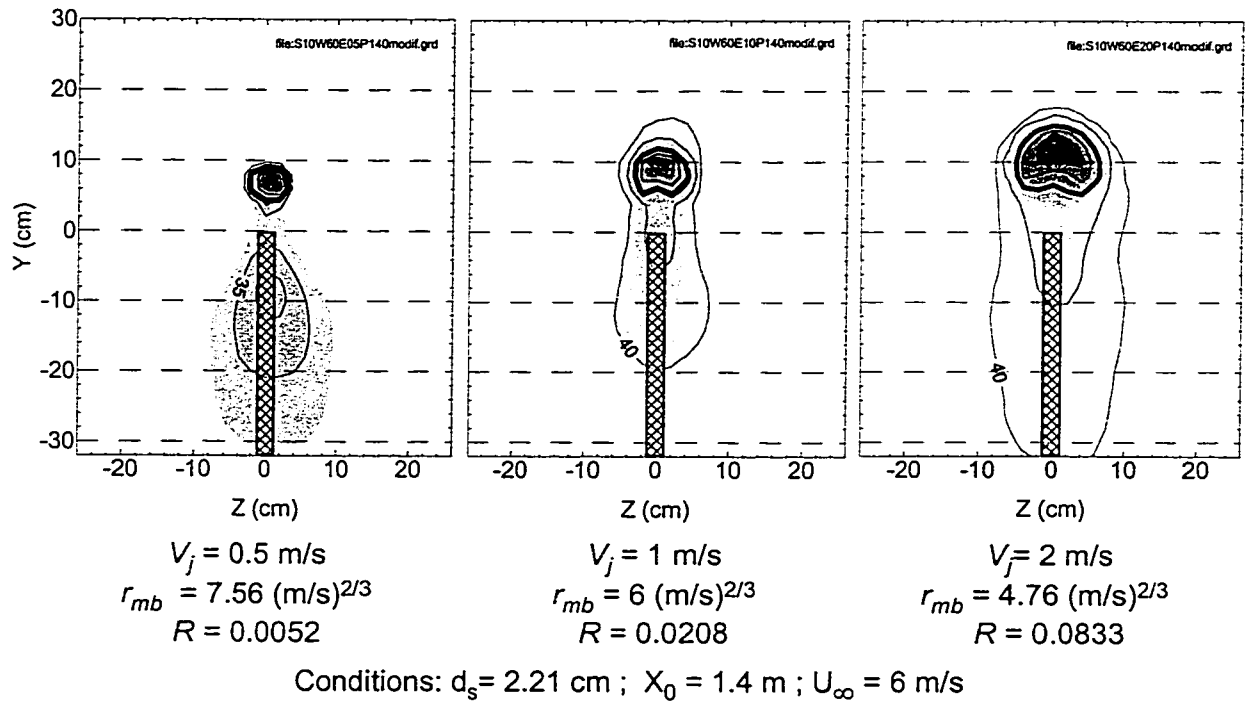
Figure 5.5: Effect of the Varying Jet Velocity for Constant Stack Diameter and Crosswind

75

Figure 5.6: Characteristic Dimension of the Plume for the Different Shapes

Figure 5.7: Histogram Comparing the Characteristic Dimension
with the Width of the Plume

Figure 5.8: Ratio Width/Vertical Thickness of the Plume Versus Crosswind
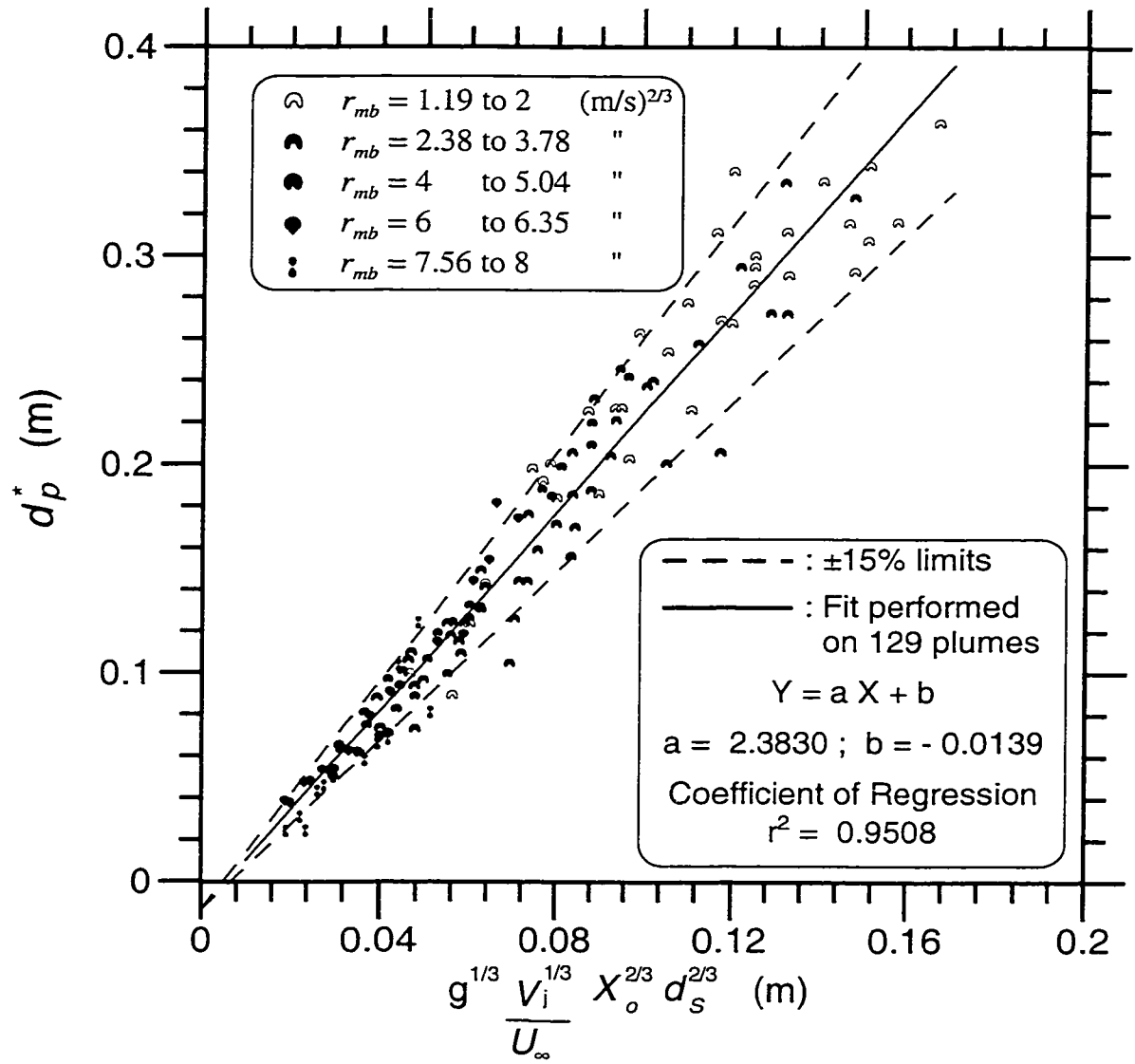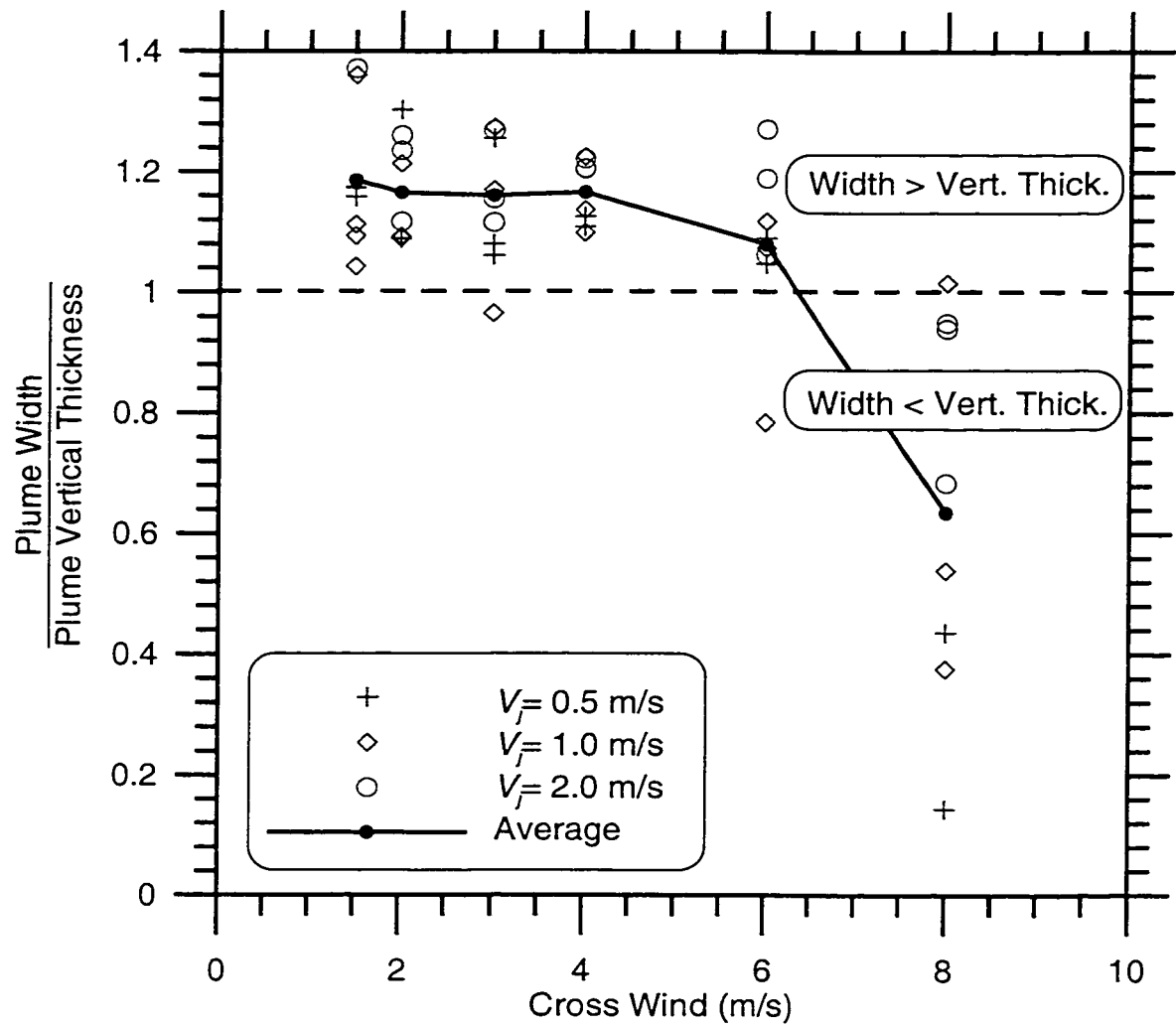
Conditions:

d_s = 1.9, 2.54, 3.8 cm ; V_j : 0.5,1 & 2 m/s

U_∞ : 1.5 - 8 m/s ; X_o : 0.5 - 2.9 m
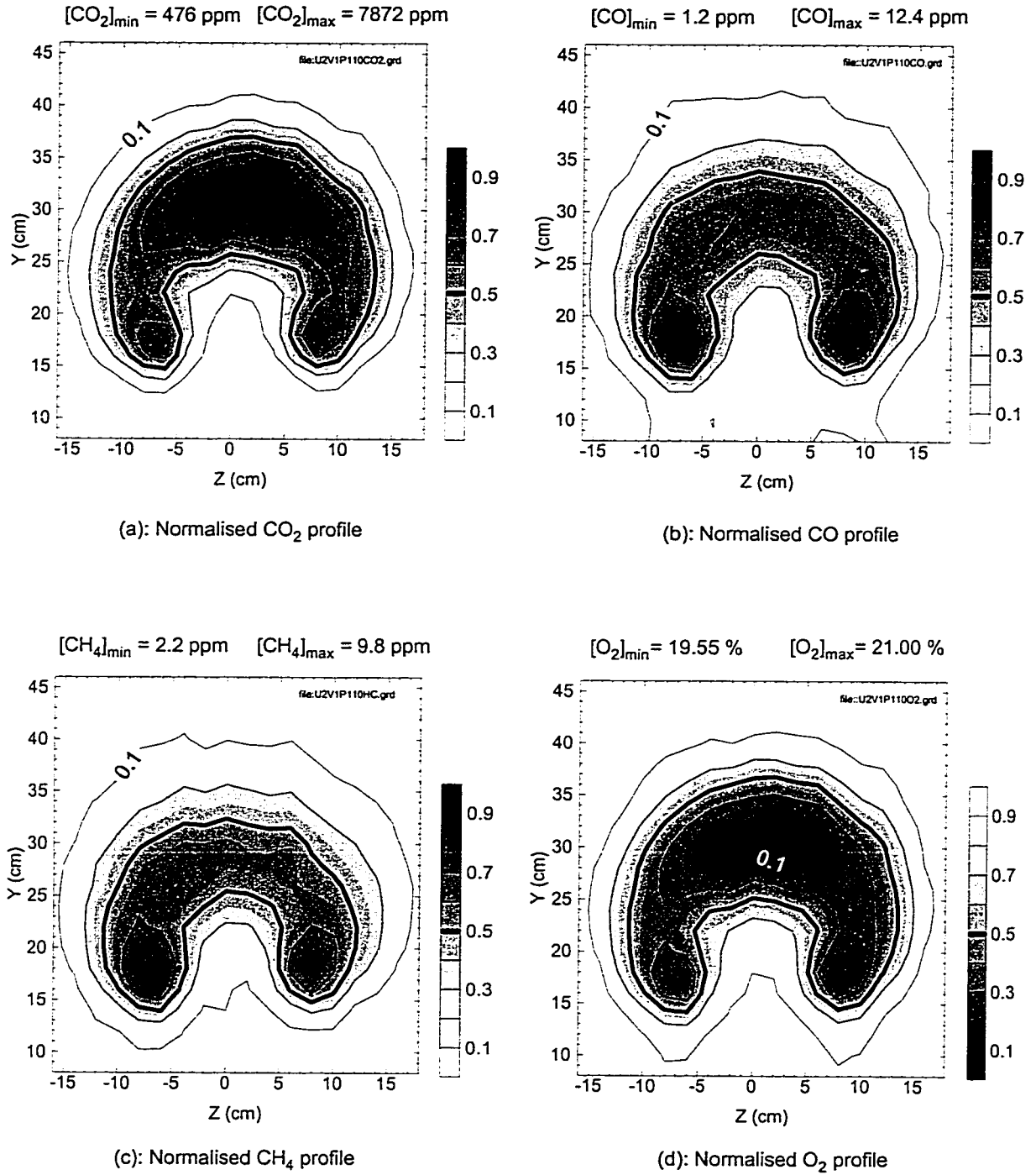
Figure 5.9: CO_2, CO, CH_4 and O_2 Normalised Concentration Profiles for $r_{mb}=2(m/s)^{2/3}$
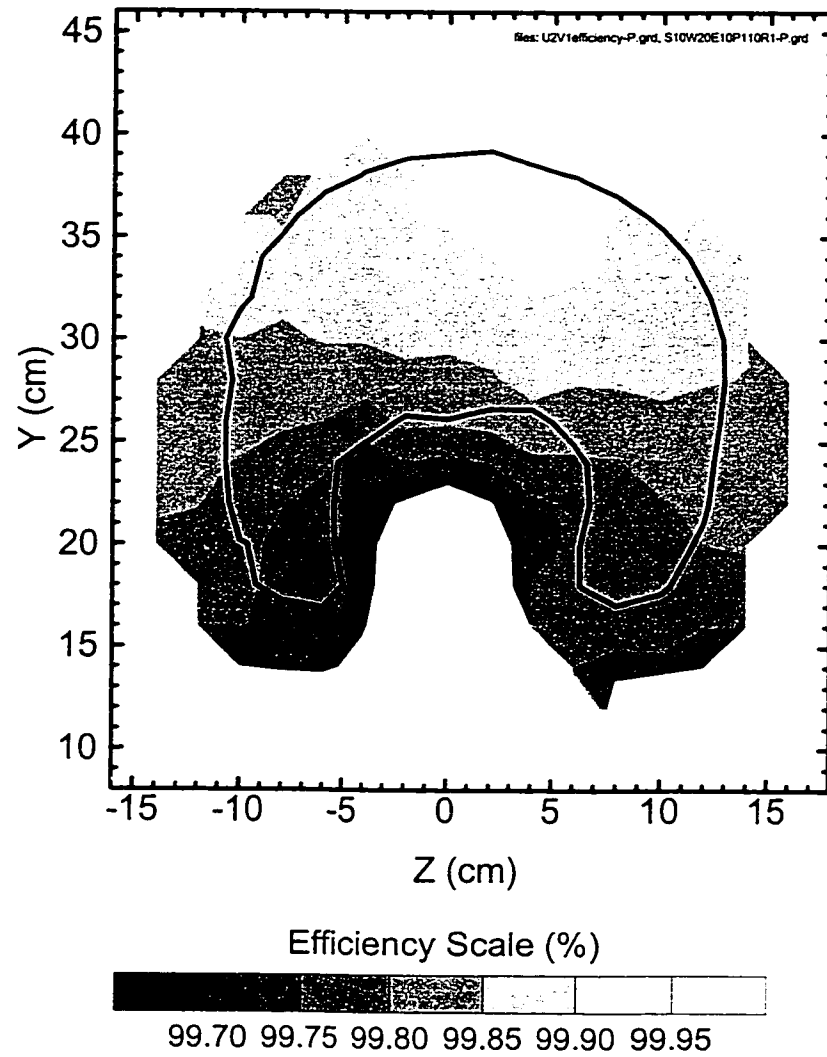
Efficiency Scale (%)

99.70 99.75 99.80 99.85 99.90 99.95

——— : 50% Temperature Contour

Note: Efficiency is only displayed where the concentration of products
is at least 10% above the minimum level (background concentration)

Conditions:
$d_s = 2.21$ cm ; $X_o = 1.1$ m ; $r_{mb} = 2$ (m/s)$^{2/3}$
$V_j = 1$ m/s ; $U_\infty = 2$ m/s ; $R = 0.1875$
Overall Efficiency >99.5 %

Figure 5.10: Local Efficiency Map with Temperature Contour for $r_{mb} = 2$ (m/s)$^{2/3}$

$[CO_2]_{min}$ = 550 ppm $[CO_2]_{max}$ = 8275 ppm

(a): Normalised CO_2 profile

$[CO]_{min}$ = 4.0 ppm $[CO]_{max}$ = 43.3 ppm

(b): Normalised CO profile

$[CH_4]_{min}$ = 3.4 ppm $[CH_4]_{max}$ = 64.5 ppm

(c): Normalised CH_4 profile

$[O_2]_{min}$ = 19.62 % $[O_2]_{max}$ = 21.12 %

(d):Normalised O_2 profile

▨ : Projection on the temperature plane of the location of the stack.
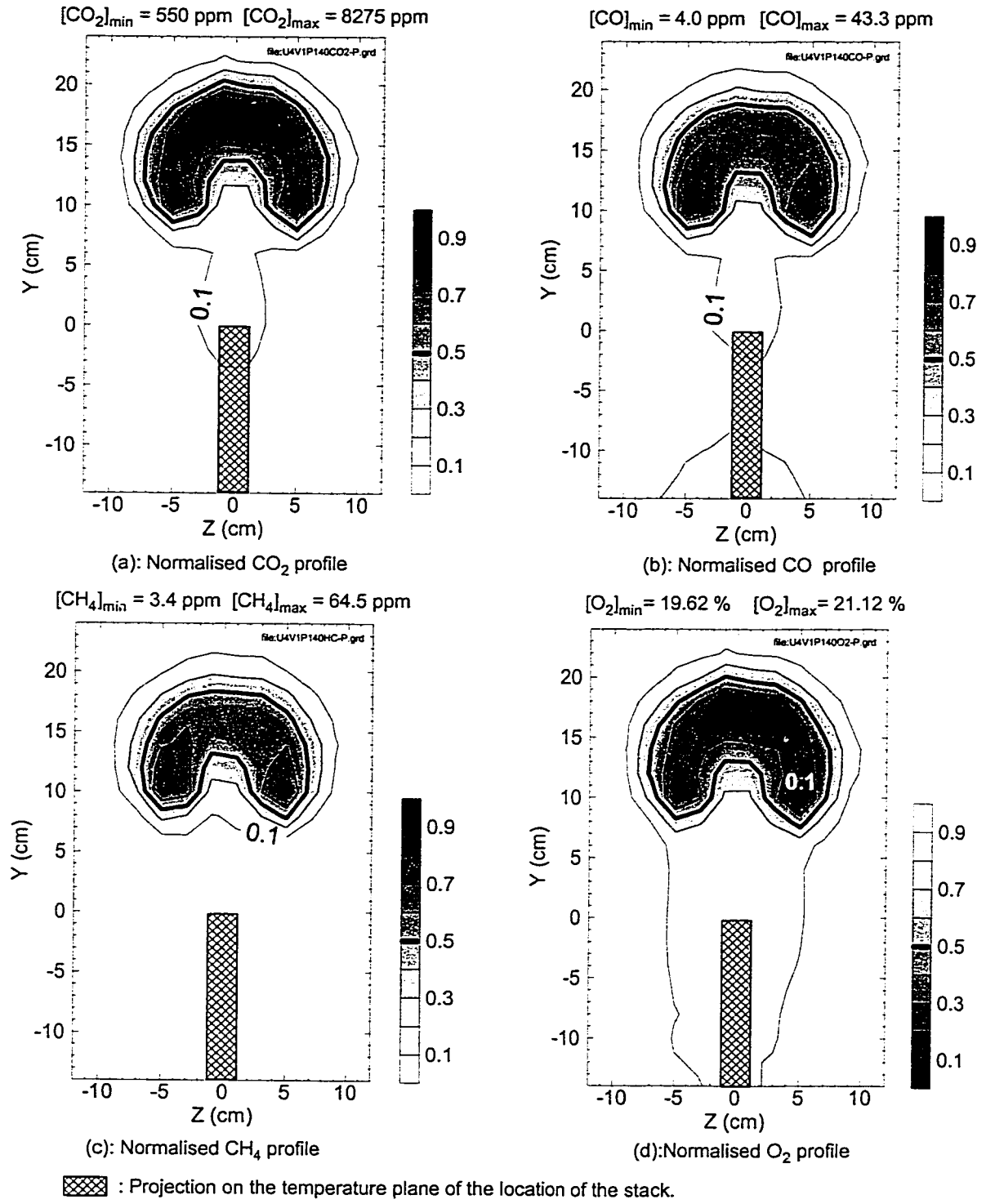
Conditions:

d_s = 2.21 cm ; X_0 = 1.4 m ; r_{mb} = 4 $(m/s)^{2/3}$

V_j = 1 m/s ; U_∞ = 4 m/s ; R = 0.0469

Figure 5.11: CO_2, CO, CH_4 and O_2 Normalised Concentration Profiles for r_{mb}=4(m/s)$^{2/3}$
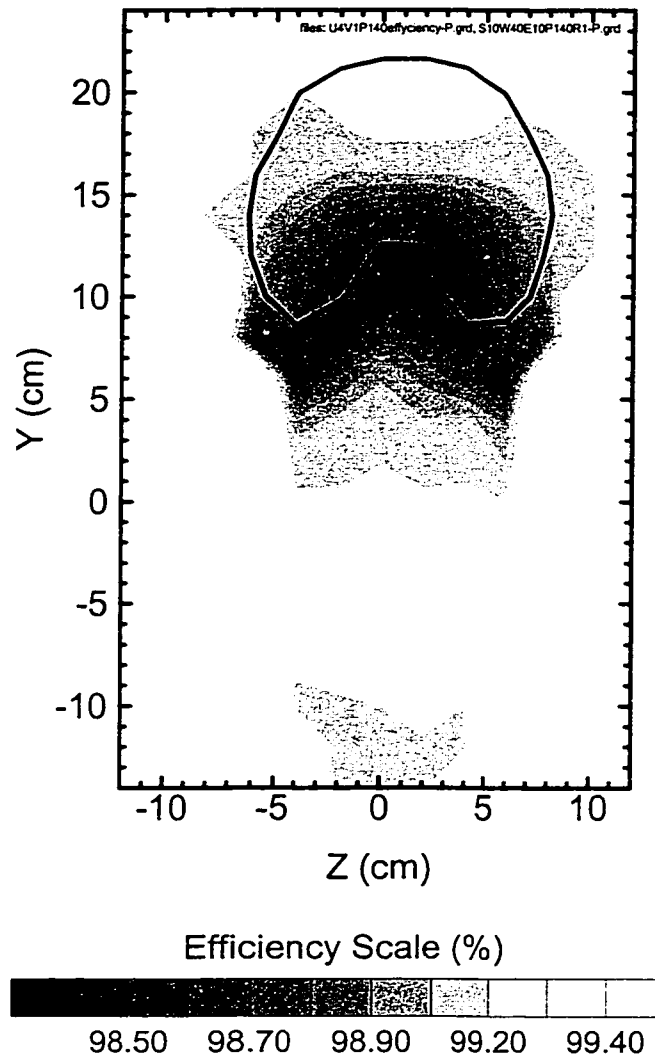
Efficiency Scale (%)

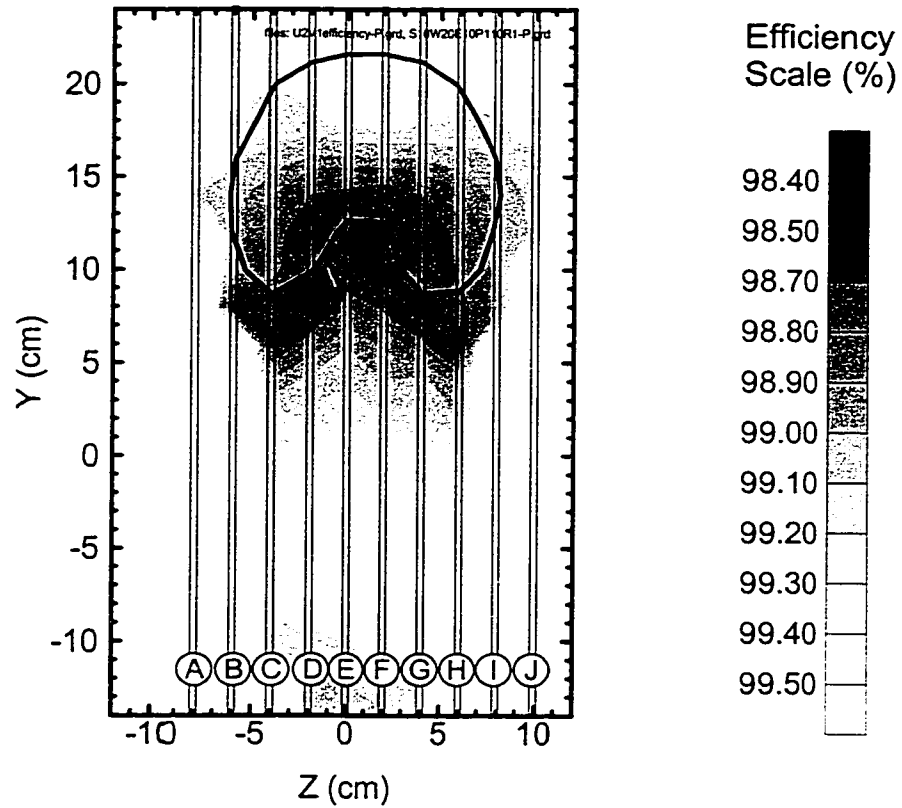98.50   98.70   98.90   99.20   99.40

——— : 50% Temperature Contour

Note: Efficiency is only displayed where the concentration of products
is at least 10% above the minimum level (backgournd concentration).

Conditions:
$d_s = 2.21$ cm ; $X_o = 1.4$ m ; $r_{mb} = 4$ (m/s)$^{2/3}$
$V_j = 1$ m/s ; $U_\infty = 4$ m/s ; $R = 0.00469$
Overall Efficiency = 99.1 %

Figure 5.12: Local Efficiency Map with Temperature Contour for $r_{mb} = 4$ (m/s)$^{2/3}$

$[CO_2]_{min} = 501$ ppm $[CO_2]_{max} = 4864$ ppm

$[CO]_{min} = 3.3$ ppm $[CO]_{max} = 106.5$ ppm

(a): Normalised CO_2 profile

(b): Normalised CO profile

$[CH_4]_{min} = 6.0$ ppm $[CH_4]_{max} = 357.3$ ppm

$[O_2]_{min} = 20.20$ % $[O_2]_{max} = 21.11$ %

(c): Normalised HC profile

(d): Normalised O_2 profile

▨ : Projection on the temperature plane of the location of the stack.
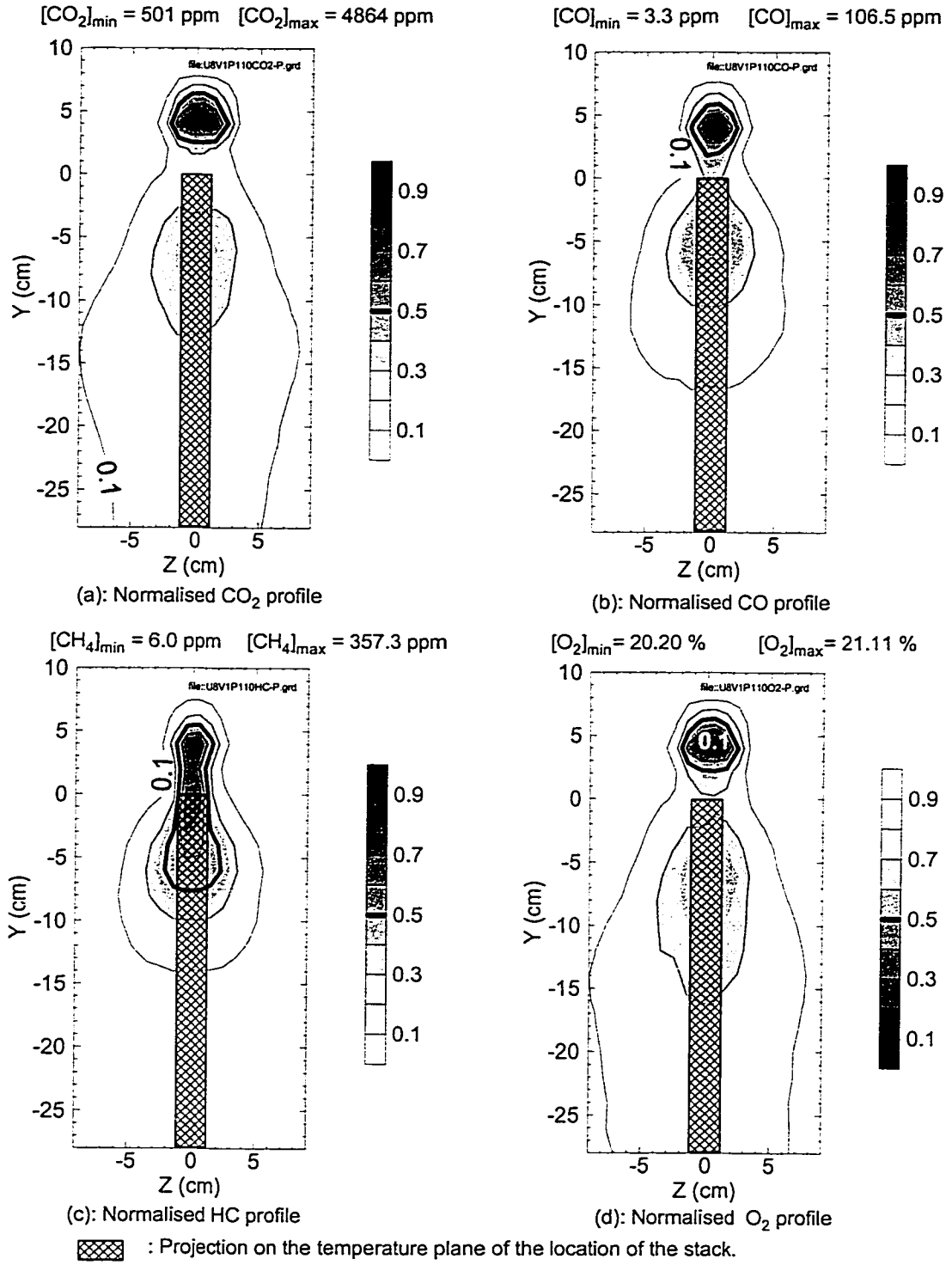
Conditions:

$d_s = 2.21$ cm ; $X_o = 1.1$ m ; $r_{mb} = 8$ (m/s)$^{2/3}$

$V_j = 1$ m/s ; $U_\infty = 8$ m/s ; $R = 0.0117$

Figure 5.13: CO_2, CO, CH_4 and O_2 Normalised Concentration Profiles for $r_{mb}=8(m/s)^{2/3}$
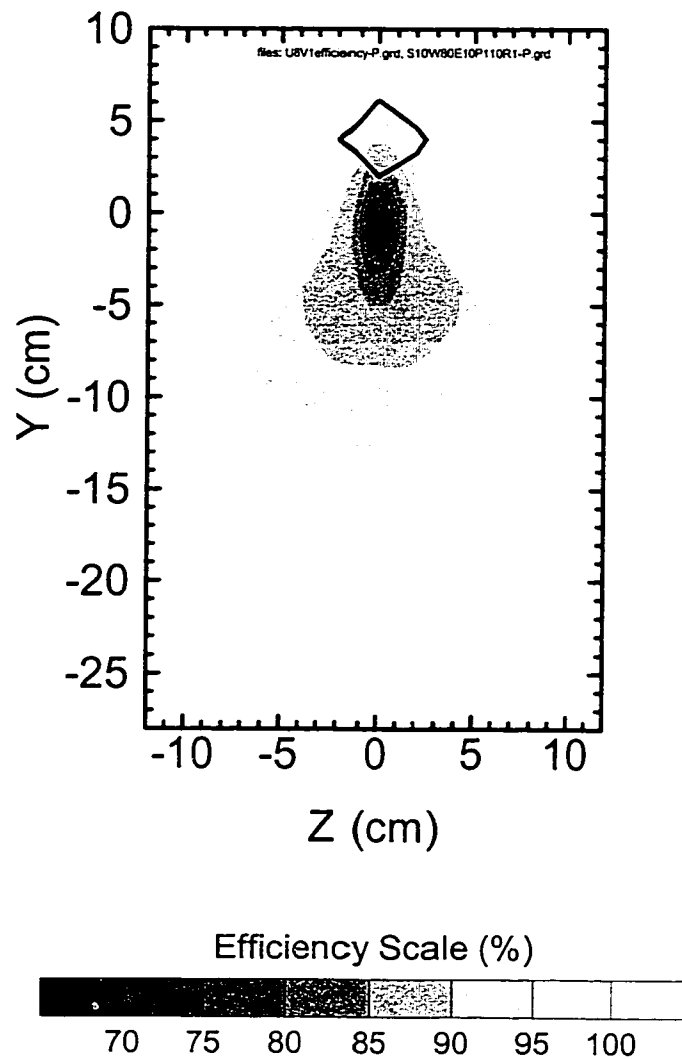
Figure 5.14: Local Efficiency Map with Temperature Contour for $r_{mb} = 8$ (m/s)$^{2/3}$

Efficiency Scale (%)

70   75   80   85   90   95   100

——— : 50% Temperature Contour

Note: Efficiency is only displayed where the concentration of products is 10% above the minimum level (background concentration).

Conditions:
d_s = 2.21 cm ; X_o= 1.1 m ; r_{mb} = 8 (m/s)$^{2/3}$
V_j = 1 m/s ; U_∞ = 8 m/s ; R = 0.0117
Overall Efficiency = 96.9 %
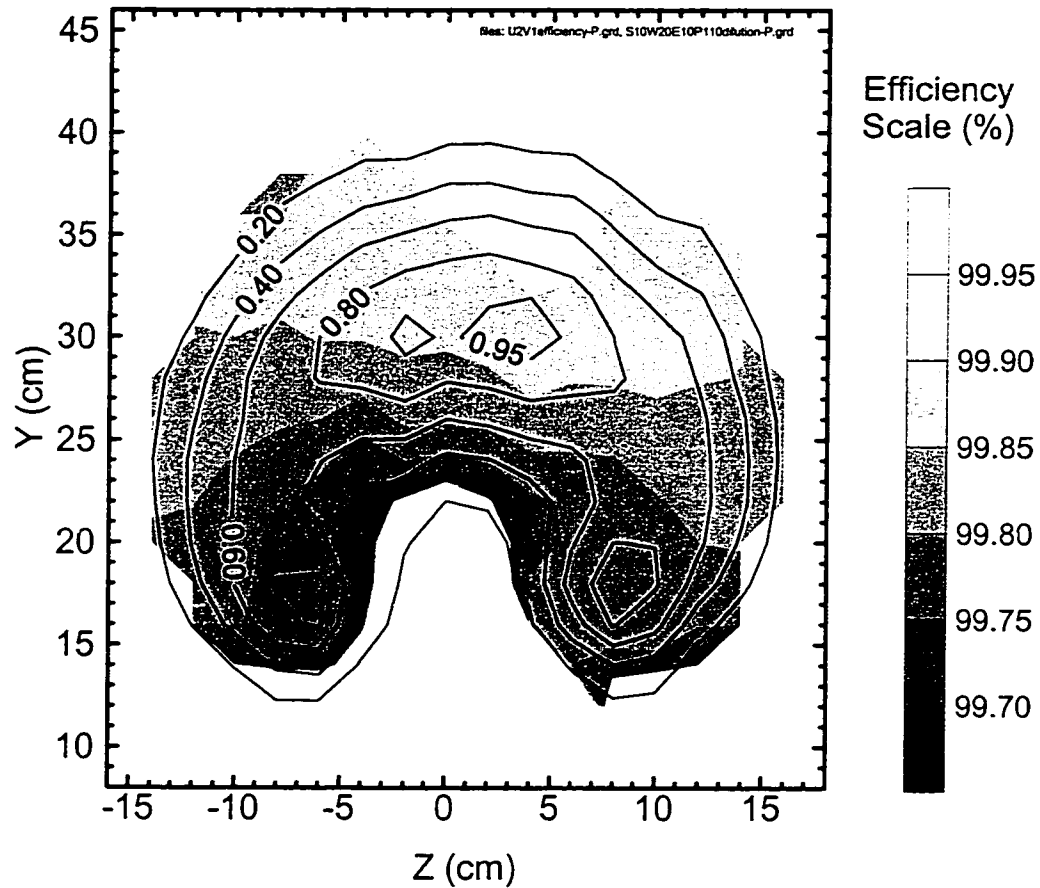
— 0.20 —— : Density of products based on normalised O_2
Concentration (see Figure 5.9-d)

Threshold	Efficiency (%)	Dilution Ratio	CO2 Conc. (ppm)	CO Conc. (ppm)	HC (ppm)
0.2	99.82	1/27	4494	7.03	5.89
0.4	99.83	1/24	5249	7.72	6.44
0.6	99.83	1/20	6011	8.42	6.95
0.8	99.84	1/18	6864	8.98	7.25
0.95	99.81	1/16	7840	9.03	6.87

Note: Efficiency is only displayed where the concentration of products
is at least 10% above the minimum level (background concentration)

Conditions:
d_s = 2.21 cm ; X_o = 1.1 m ; r_{mb} = 2 $(m/s)^{2/3}$
V_j = 1 m/s ; U_∞ = 2 m/s ; R = 0.1875

Figure 5.15: Overall Efficiency Calculated from the Local Efficiency
for Varying Area for r_{mb} = 2 $(m/s)^{2/3}$
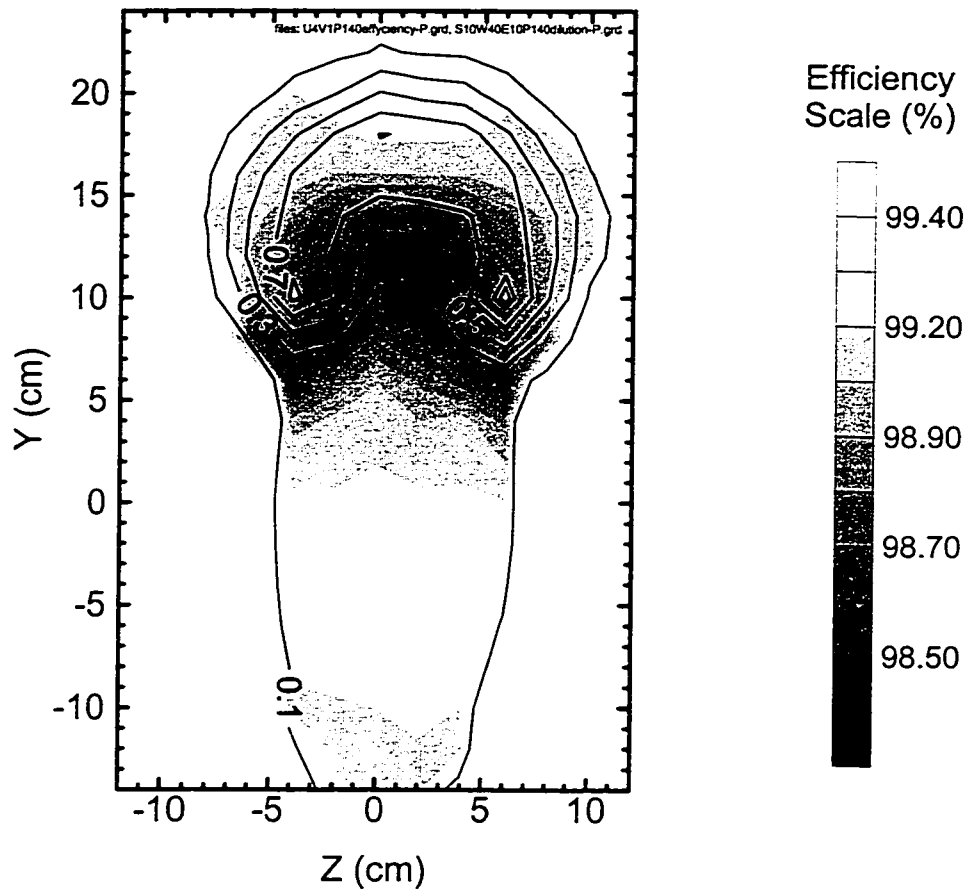
—— 0.1 —— : Density of products based on normalised O_2 Concentration (see Figure 5.11-d)

Threshold	Efficiency (%)	Dilution Ratio	CO2 Conc. (ppm)	CO Conc. (ppm)	HC (ppm)
0.1	98.96	1/46	2628	14.2	15.7
0.3	98.91	1/23	5354	25.7	35.2
0.5	98.91	1/20	6149	29.1	40.6
0.7	98.95	1/18	7123	32.3	45.4
0.9	98.90	1/15	8108	37.9	54.0
0.95	98.72	1/15	8275	43.3	64.5

Note: Efficiency is only displayed where the concentration of products is at least 10% above the minimum level (backgournd concentration).

Conditions:
d_s= 2.21 cm ; X_o = 1.4 m ; r_{mb} = 4 (m/s)$^{2/3}$
V_j = 1 m/s ; U_∞ = 4 m/s ; R = 0.00469

Figure 5.16: Overall Efficiency Calculated from the Local Efficiency for Varying Area for r_{mb} = 4 (m/s)$^{2/3}$
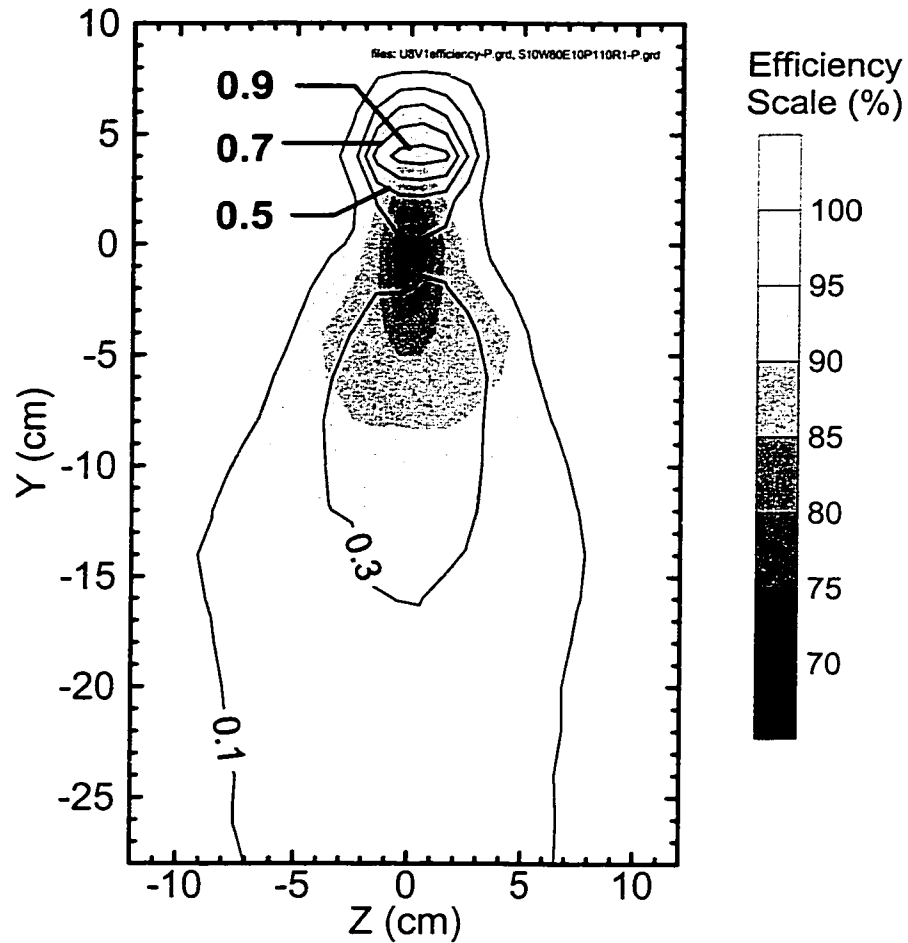
— 0.1 —— : Density of products based on normalised O_2
Concentration (see Figure 5.13-d)

Threshold	Efficiency (%)	Dilution Ratio	CO2 Conc. (ppm)	CO Conc. (ppm)	HC (ppm)
0.1	93.42	1/109	1402	19.8	54.9
0.3	90.83	1/61	2153	40.8	138
0.5	93.11	1/32	4106	74.2	205
0.7	92.66	1/28	4626	86.9	252
0.9	92.05	1/27	4807	95.7	289

Note: Efficiency is only displayed where the concentration of products
is 10% above the minimum level (background concentration).

Conditions:
d_s = 2.21 cm ; X_o= 1.1 m ; r_{mb} = 8 $(m/s)^{2/3}$
V_j = 1 m/s ; U_∞ = 8 m/s ; R = 0.0117

**Figure 5.17: Overall Efficiency Calculated from the Local Efficiency
for Varying Area for r_{mb} = 8 $(m/s)^{2/3}$**
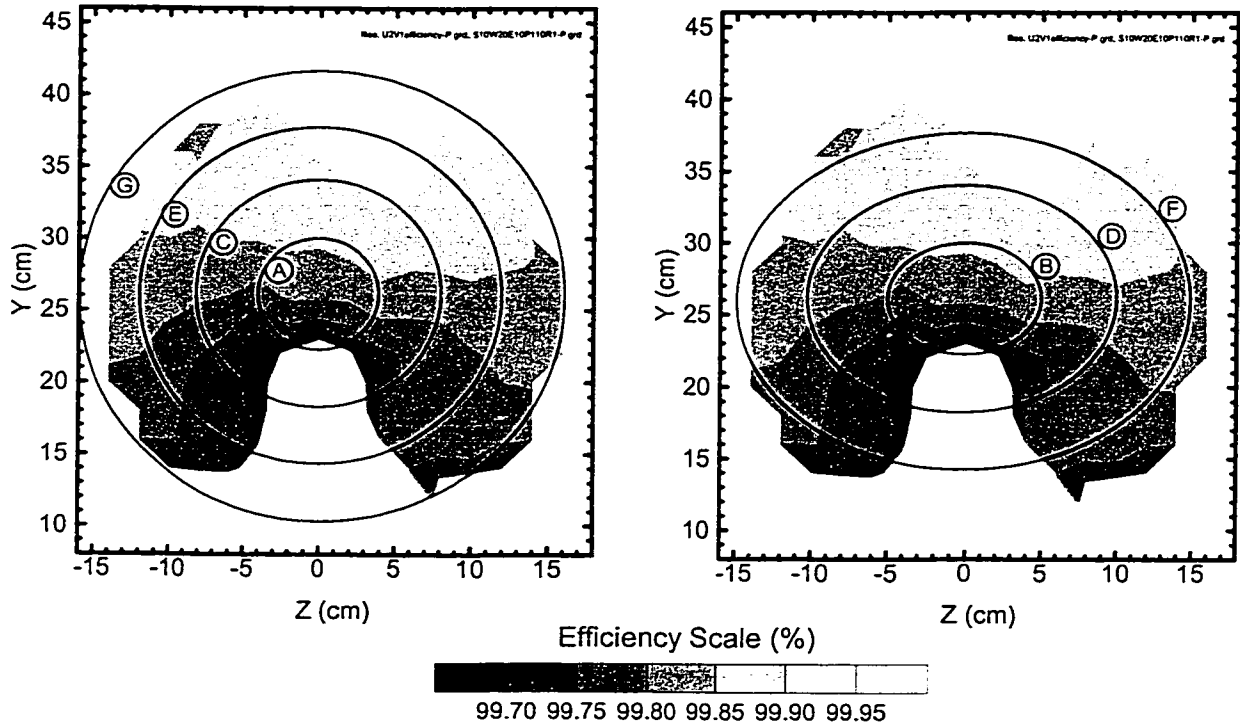
Efficiency Scale (%)

99.70 99.75 99.80 99.85 99.90 99.95

Location	Type	Diameter (cm)	Efficiency (%)	Dilution Ratio	CO2 Conc. (ppm)	CO Conc. (ppm)	HC (ppm)
A	Circular	8	99.81	1/25	4695	7.5	6.4
B	Elliptic	8-10	99.81	1/24	4761	7.5	6.5
C	Circular	16	99.82	1/25	4727	7.2	6.2
D	Elliptic	16-20	99.82	1/25	4819	7.3	6.2
E	Circular	24	99.82	1/28	4307	6.8	5.8
F	Elliptic	24-30	99.82	1/32	3844	6.4	5.4
G	Circular	32	99.82	1/39	3141	5.7	4.9

Notes : 1 - Efficiency is only displayed where the concentration of products
is at least 10% above the minimum level (background concentration).
2 - Hood centered at + 26 cm.

Conditions:
d_s = 2.21 cm ; X_o= 1.1 m ; r_{mb} = 2 (m/s)$^{2/3}$
V_j = 1 m/s ; U_∞ = 2 m/s ; R = 0.1875
Overall Efficiency >99.5 %

Figure 5.18: Simulation of the Overall Efficiency Measured by a Probe
with Circular and Elliptic Shaped Hood for r_{mb} = 2 (m/s)$^{2/3}$
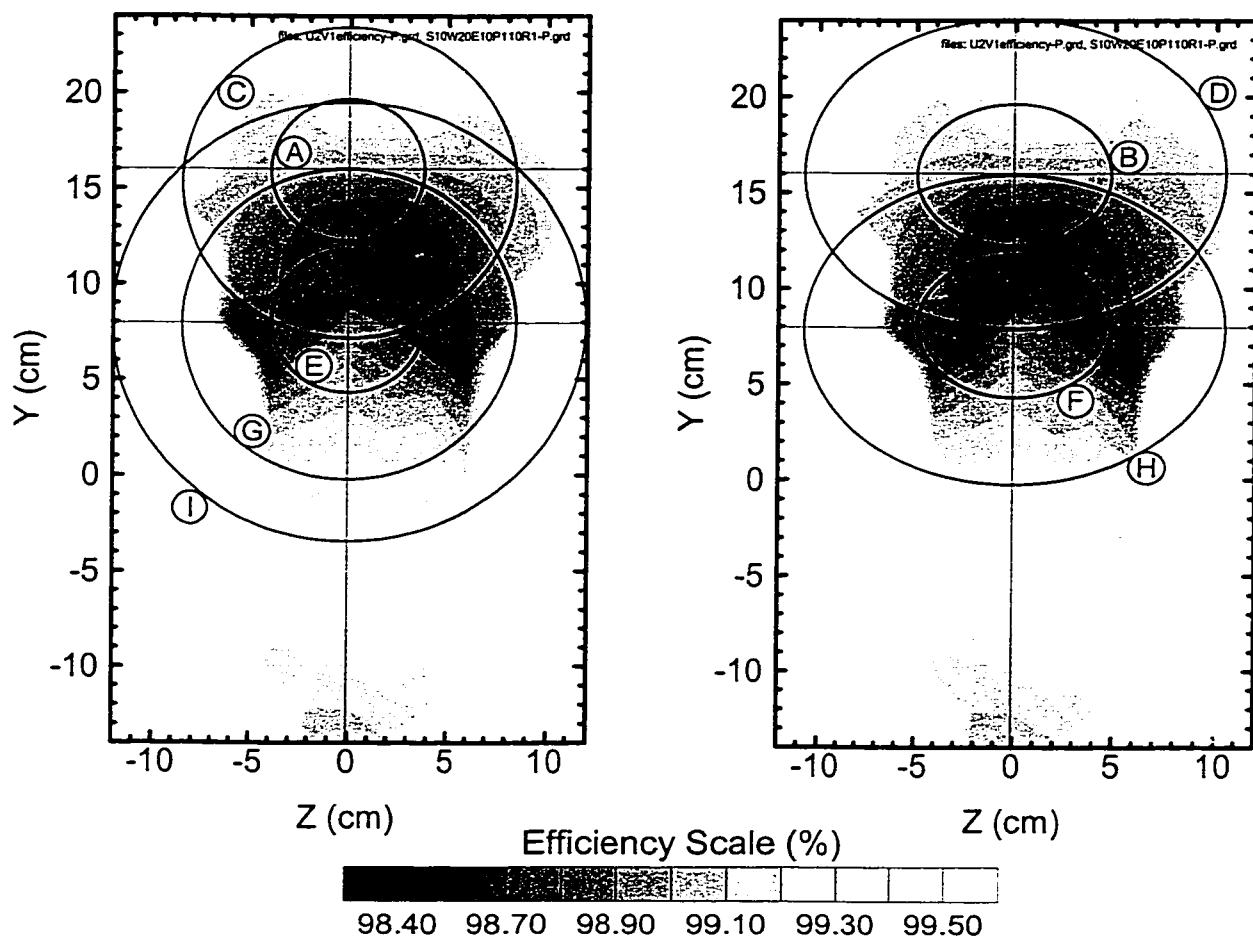
88

Efficiency Scale (%)

| 98.40 | 98.70 | 98.90 | 99.10 | 99.30 | 99.50 |

Location	Type	Diameter (cm)	Efficiency (%)	Dilution Ratio	CO2 Conc. (ppm)	CO Conc. (ppm)	HC (ppm)
A	Circular	8	98.98	1/22	5579	26.2	35.8
B	Elliptic	8-10	98.99	1/22	5739	25.9	35.2
C	Circular	16	98.92	1/35	3586	17.8	23.1
D	Elliptic	16-20	98.93	1/40	3108	15.7	19.9
E	Circular	8	98.61	1/44	2491	15.8	19.7
F	Elliptic	8-10	98.61	1/44	2502	15.8	19.8
G	Circular	16	98.80	1/41	2753	15.5	19.1
H	Elliptic	16-20	98.82	1/46	2438	13.8	16.73
I	Circular	24	98.94	1/54	2199	11.95	13.61

Note : Efficiency is only displayed where the concentration of products
is at least 10% above of the minimum level (background concentration).
Conditions:
d_s = 2.21 cm ; X_o= 1.4 m ; r_{mb} = 4 $(m/s)^{2/3}$
V_j = 1 m/s ; U_∞ = 4 m/s ; R = 0.0469
Overall Efficiency = 99.1 %

Figure 5.19: Simulation of the Overall Efficiency Measured by a Probe
with Circular and Elliptic Shaped Hood for r_{mb} = 4 $(m/s)^{2/3}$
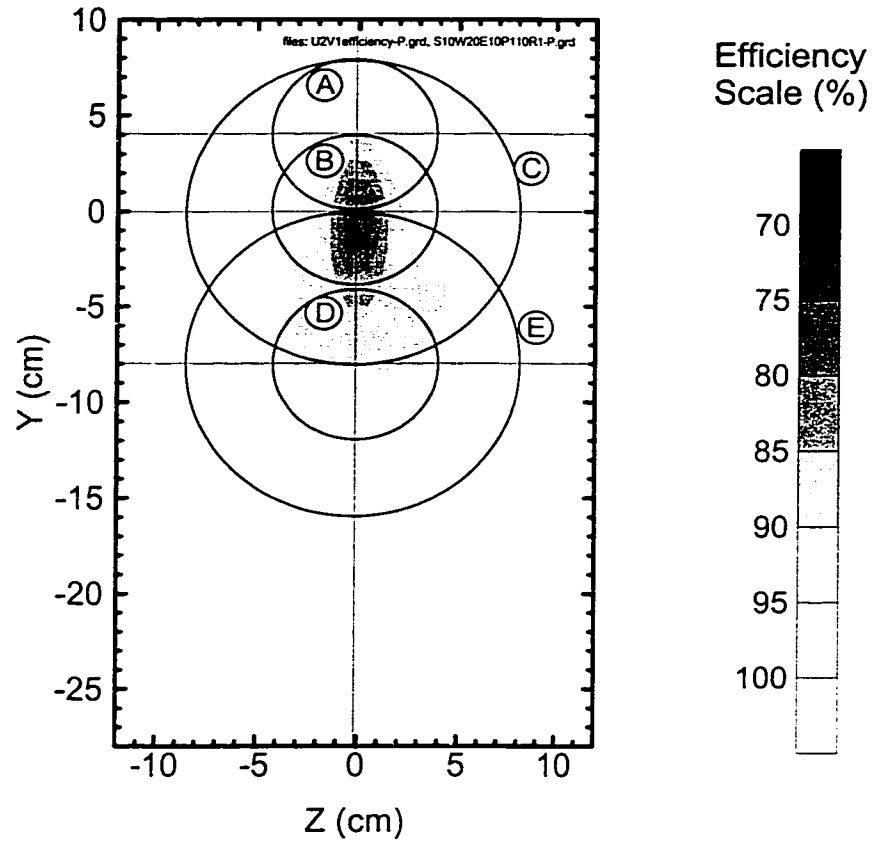
Location	Diameter (cm)	Y (cm)	Efficiency (%)	Dilution Ratio	CO2 Conc. (ppm)	CO Conc. (ppm)	HC (ppm)
A	8	4	91.03	1/95	1493	25.5	83.5
B	8	0	87.38	1/87	1608	33.2	138.0
C	16	0	89.22	1/134	1202	21.5	73.6
D	8	-8	89.93	1/71	1926	37.8	133.0
E	16	-8	91.01	1/111	1410	23.4	77.1

Note : Efficiency is only displayed where the concentration of products
is at least 10 % above the minimum level (background concentration).

Conditions:
d_s = 2.21 cm ; X_o= 1.1 m ; r_{mb}= 8 $(m/s)^{2/3}$
V_j = 1 m/s ; U_∞ = 8 m/s ; R = 0.0117
Overall Efficiency = 96.9 %

Figure 5.20: Simulation of the Overall Efficiency Measured by a Probe
with Circular Shaped Hood for r_{mb} = 8 $(m/s)^{2/3}$

90
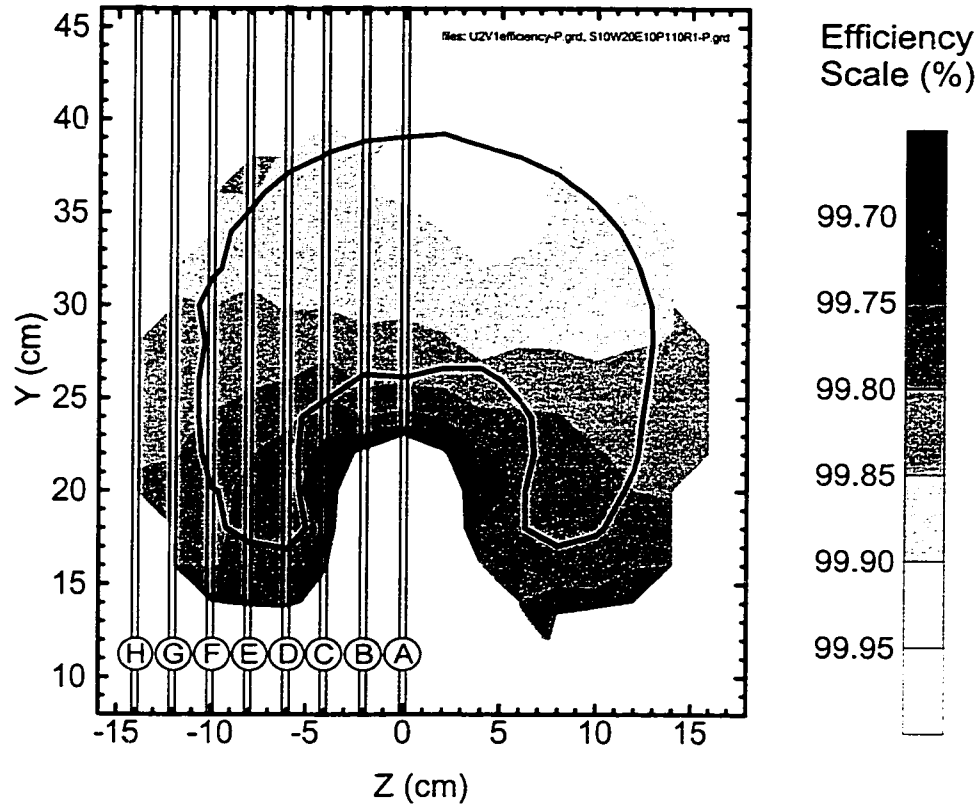
— : 50% Temperature Contour.

Location	Efficiency (%)	Dilution Ratio	CO2 Conc. (ppm)	CO Conc. (ppm)	HC (ppm)
A	99.83	1/50	2352	5.0	4.2
B	99.83	1/47	2530	5.3	4.4
C	99.79	1/44	2715	4.4	4.8
D	99.79	1/37	3150	5.0	5.2
E	99.78	1/40	2946	4.6	5.1
F	99.80	1/56	2258	3.2	4.4
G	99.82	1/99	1573	2.7	3.4
H	99.80	1/308	844	2.6	3.3

Note : Efficiency is only displayed where the concentration of products
is at least 10% above the minimum level (background concentration).

Conditions:
d_s = 2.21 cm ; X_o= 1.1 m ; r_{mb} = 2 (m/s)$^{2/3}$
V_j = 1 m/s ; U_∞ = 2 m/s ; R = 0.1875

**Figure 5.21: Simulation of the Overall Efficiency Measured by a Thin Vertical Probe
for Varying Lateral Position for r_{mb} = 2 (m/s)$^{2/3}$**

91

Efficiency
Scale (%)

98.40
98.50
98.70
98.80
98.90
99.00
99.10
99.20
99.30
99.40
99.50

Location	Efficiency (%)	Dilution Ratio	CO2 Conc. (ppm)	CO Conc. (ppm)	HC (ppm)
A	99.06	1/538	761.7	5.4	4.2
B	99.04	1/101	1484	8.8	8.0
C	98.93	1/52	2244	12.8	13.5
D	98.89	1/50	2372	13.7	14.9
E	99.05	1/55	2218	12.4	11.8
F	99.00	1/56	2184	12.2	12.3
G	98.94	1/51	2352	13.2	14.0
H	98.92	1/50	2351	13.0	14.6
I	99.04	1/92	1580	8.9	8.9
J	99.13	1/368	823.2	5.9	4.6

—— : 50% Temperature Contour.

Note : Efficiency is only displayed where the concentration of products is at least 10% above the minimum level (background concentration).

Conditions:
$d_s = 2.21$ cm ; $X_o = 1.4$ m ; r $r_{mb} = 4$ $(m/s)^{2/3}$
$V_j = 1$ m/s ; $U_\infty = 4$ m/s ; $R = 0.0469$

Figure 5.22: Simulation of the Overall Efficiency Measured by a Thin Vertical Probe for Varying Lateral Location for $r_{mb} = 4$ $(m/s)^{2/3}$
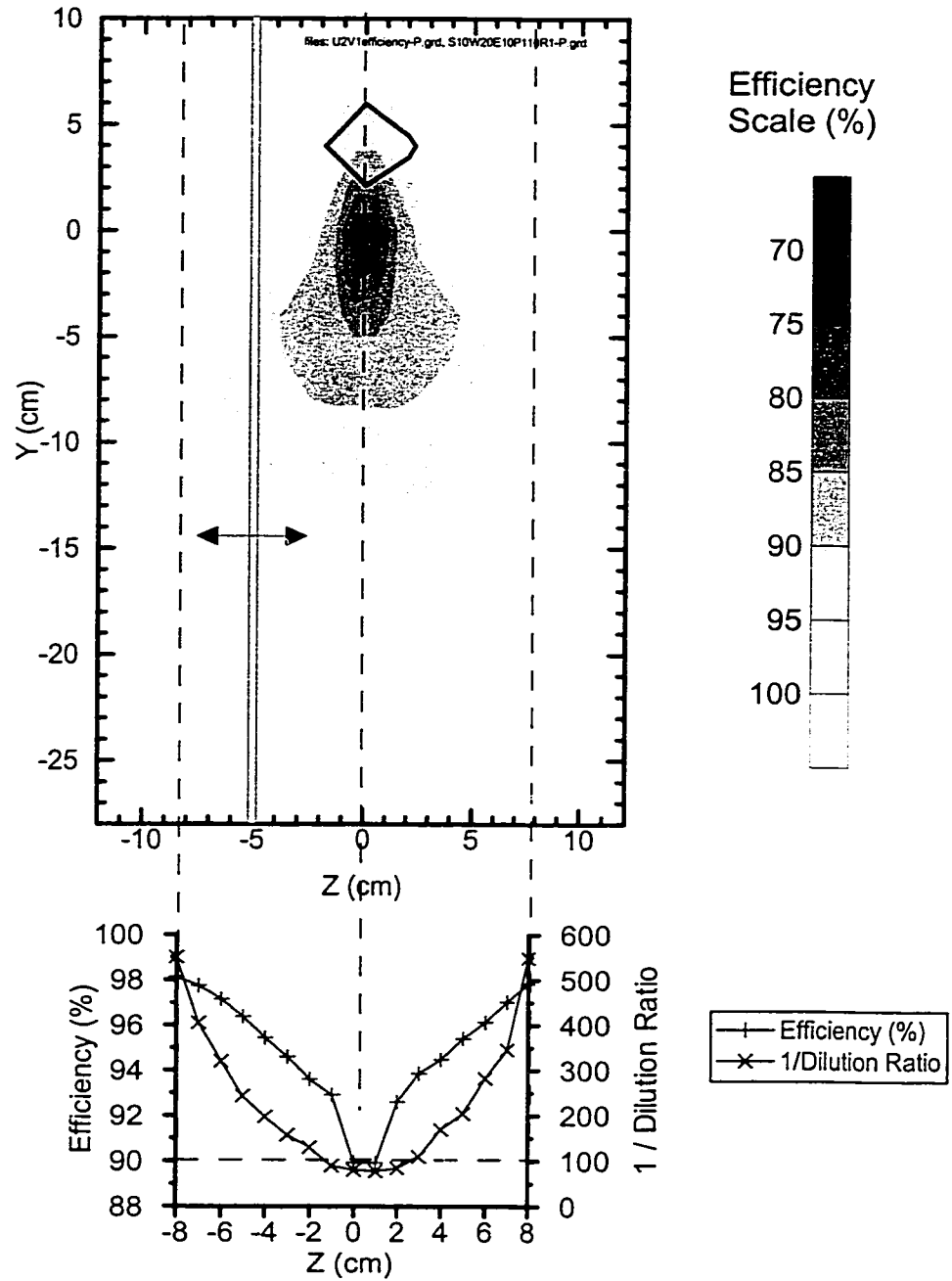
Figure 5.23: Simulation of the Overall Efficiency Measured by a Thin Vertical Probe for Varying Lateral Location for $r_{mb} = 8$ (m/s)$^{2/3}$

The figure includes:

Efficiency Scale (%) colorbar with values: 70, 75, 80, 85, 90, 95, 100

Conditions:
$d_s = 2.21$ cm ; $X_o = 1.1$ m ; $r_{mb} = 8$ (m/s)$^{2/3}$
$V_j = 1$ m/s ; $U_\infty = 8$ m/s ; $R = 0.0117$

—— : 50% Temperature Contour.

Note : Efficiency is only displayed where the concentration of products is above 10% of the maximum level.

Legend:
+— Efficiency (%)
×— 1/Dilution Ratio
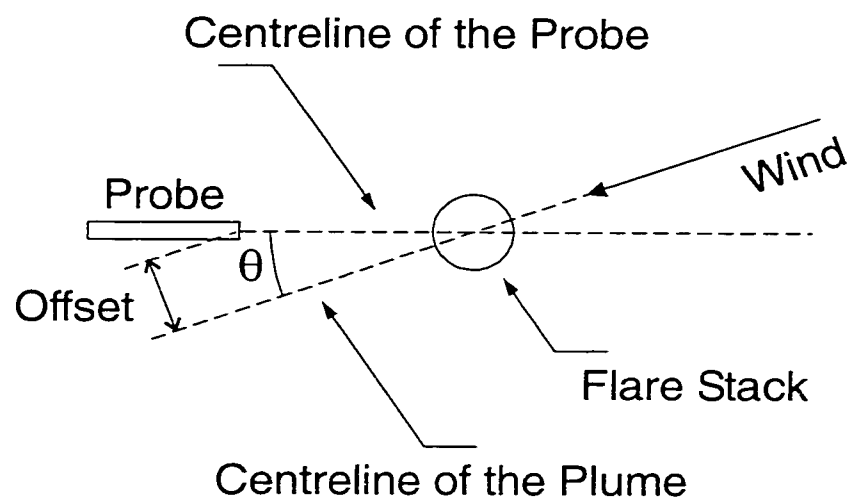
Figure 5.24: Sketch to Show how the Wind Direction Creates Error in Probe
Position Relative to Centreline
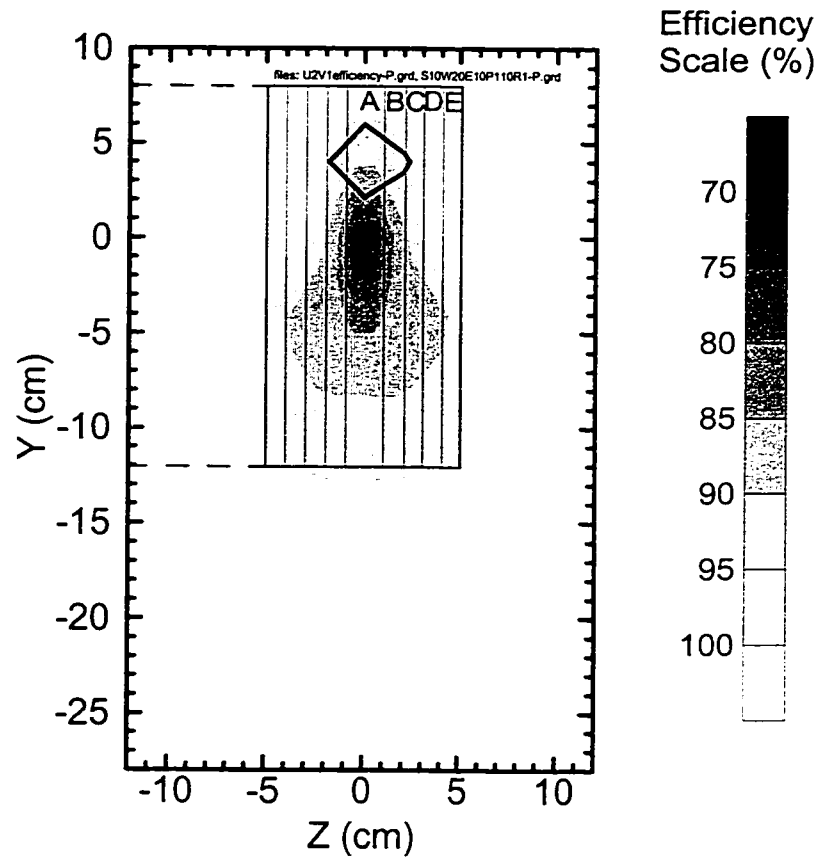
— : 50% Temperature Contour.

Location	Width (cm)	Efficiency (%)	Dilution Ratio	CO2 Conc. (ppm)	CO Conc. (ppm)	HC (ppm)
A	2	88.38	1/64	2034	41.9	179.0
B	4	89.28	1/70	1904	37.5	142.0
C	6	89.80	1/79	1740	33.1	119.0
D	8	90.05	1/91	1574	29.0	101.0
E	10	90.26	1/104	1441	25.7	86.5

Note : Efficiency is only displayed where the concentration of products is at least 10 % above minimum level (background concentration).

Conditions:

d_s = 2.21 cm ; X_o= 1.1 m ; r_{mb} = 8 (m/s)$^{2/3}$

V_j = 1 m/s ; U_∞ = 8 m/s ; R = 0.0117

Figure 5.25: Simulation of the Overall Efficiency Measured by a Probe with a Rectangular Hood of Varying Width for r_{mb} = 8 (m/s)$^{2/3}$

Chapter 6

CONCLUSIONS

6.1 Plume Shape and Modelling

The dispersion of the plume of a model scale natural gas flare in the region close to the flame was investigated. The temperature was chosen as the relevant parameter to track its evolution. It was shown that the plume behaved similarly to a non-reacting buoyant jet in cross-flow and a characteristic length, d_p^*, could be determined using the ratio $g^{1/3}.X_o^{2/3}.d_s^{2/3}.V_j^{1/3}/U_\infty$. The data correlated with $d_p^*=2.3830*g^{1/3}.X_o^{2/3}.d_s^{2/3}.V_j^{1/3}/U_\infty - 0.0139$. This scaling parameter originates from a model that considers the crosswind momentum and the buoyancy of the jet as the important forces in the flow. It was also shown that the plume has a width 20-25% larger than its vertical thickness when the crosswind is below 6 m/s. Then, for higher velocity, the plume collapses, due to the wake of the stack, in a shape that is narrow and tall. Over the range of velocity ratios, r_{mb}, observed (1.19 to 10.08 $(m/s)^{2/3}$), the plume can take three distinct shapes. For the lower r_{mb}, it takes the shape of a kidney, where the dominant flow structure is a pair of counter-rotating vortices. For the higher r_{mb} the plume is downwashed and trapped in the wake of the stack because the momentum of the cross-flow is dominant. The transition between those two shapes displays an unstable circular plume (remains of the shrunk kidney) with underneath, a growing second plume in the wake of the stack.

6.2 Plume Sampling and Efficiency

The composition of the plume were analysed in terms of mean CO_2, CO and CH_4 concentrations by a multi-point sampling device for 3 different velocity ratio: $r_{mb} = 2, 4$ and 8 $(m/s)^{2/3}$. The distribution of the products is not uniform over a section of the plume. CO_2 maximum, similarly to the temperature field, preferentially appears in the centre of the plume while CO and CH_4 accumulate on the bottom sides of the plume. This suggests the top and front of the flame have a higher efficiency than the bottom and back (in the leeside) of the flame. The decrease in efficiency is not a general trend over the whole flame but more a local phenomenon. Moreover, as the velocity ratio, r_{mb}, reaches 8 $(m/s)^{2/3}$, a source of CH_4 is clearly visible in the wake flow of the stack indicating ejection of flare gas by interactions with the wake flow structure. This has the effect of decreasing the overall efficiency extremely rapidly. Finding a way to stop this ejection would certainly improve the efficiency of flares in conditions with a strong crosswind.

It was also shown that the overall efficiency could be evaluated in the controlled environment of a wind tunnel by measuring and integrating the local efficiency across the entire section of the plume.

6.3 Simulation For Flares Testing

The detailed local composition data allowed simulations of sampling various parts of the plume under three conditions. The three conditions correspond to the two extreme shapes (kidney and downwashed) and the transitional shape described in the foregoing section. An estimation of the overall efficiency from a single point sampling of the

plume is very sensitive to probe position because of the non-uniformity in the local composition inside the plume. However, in controlled conditions such as in the windtunnel a sample in the most concentrated region of the plume can provide a good estimate of overall efficiency. In case of a more turbulent wind, a larger circular hood would work better. As the velocity ratio increases in favour of the crosswind, a sample collected from along the full centreline of the plume should be preferred to account for the vertical spatial variation in the local efficiency of the plume. Finally, for the strongest wind, the vertical probe could be broader to avoid the risk of sampling outside of the plume as the wind direction might not be constant.

6.4 Further Work

The future of this project would consist of scaling up the technique of plume sampling following the directions set by this work. The influence of the unstable wind conditions should be thoroughly investigated. The effect of the turbulence with a fixed direction of the wind should be studied along with the influence of a change in the wind direction for non-turbulent conditions. The controlled environment of a larger wind tunnel would allow larger flares to be tested. This full-scale work could bring a definitive answer on the reliability of techniques of plume sampling to measure the efficiency of solution gas flares in the field.

REFERENCES

1   Academic Press Dictionary of Science and Technology: Petroleum Eng. Section, On-line.

2   Academic Press Dictionary of Science and Technology: Chemical Eng. Section, On-line.

3   R.Borghi and M.Destriau (1995), La combustion et les Flammes, Editions Technip, Paris, pp. 351-354.

4   C.H. Bosanquet and J.L. Pearson (1936) "The Spread of Smoke and Gases from Chimneys", Trans. of the Faraday Soc. Vol. 32, pp 1249-1264.

5   G.A. Briggs (1975), "Plume Rise Predictions", Chapter 3 Lecture on Air Pollution and Environmental Impact Analyses, American Meteorological Society, pp 59-111.

6   S.Djurfors and D. Netterville (1978), "Buoyant Plume Rise in Non-Uniform Wind Conditions", Syncrude Canada Ltd. Professional Paper 1977-3, Air Pollution Control Association, Journal, Vol. 28, No. 8, pp. 780-784.

7   Energy Utilities Board (1999), Guide 60, Updates and Clarifications, Energy Utilities Board.

8   Energy Utility Board (1999), News Release of July 29 1999.

9   Energy Utility Board (1999), EUB Statistical Series 57: Field surveillance 1998/1999 Provincial Summaries.

10 Flare Research Project (2000), "Interim Report", University of Alberta Flare Research Project.

11 S.R. Gollahalli, T.A. Brzustowski and H.F. Sullivan (1975), "Characteristic of a Turbulent Propane diffusion flame on Crosswind", Trans. of the Canadian Soc. of Mech. Eng., Vol. 3, No. 4, pp 205-214.

12 T.A. Hewett, J.A. Fay and D.P. Hoult (1971), "Laboratory Experiments of Smokestack Plumes in a Stable Atmosphere", Atmospheric Environment, Vol. 5, pp 767-789.

13 M. R. Holford and J. Patrick Hettiaratchi (1998), "An Evaluation of Potential Technologies for Reducing Solution Gas Flaring in Alberta", report prepared for the Clean Air Strategic Alliance (CASA) Flaring Project Team.

14 J.T. Houghton, L.G. Meira Fihlo, B.A. Callander, N. Harris, A. Kateenger and K. Marshell (1996), "Climate Change 1995: The Science of Climate Change", Intergovernmental Panel on Climate Change (IPCC), Cambridge University Press, Cambridge, U.K., 572 Pages.

15 R. F. Huang and M. J. Yang (1996), "Thermal and Concentration Fields of Burner Attached Jet Flames in Cross-Flow", Combustion and Flames, Vol. 105, pp 211-224.

16 M.R. Johnson and L.W. Kostiuk (2000) "Efficiency of Low Momentum Jet Diffusion Flames in Crosswinds", accepted for publication in Combustion and Flame, April, 9.

17 D. Joseph, J. Lee, C. McKinnon and R. Payen (1983) "Evaluation of Efficiency of Industrial Flares: Background-Experimental Design-Facility". Environmental Protection Agency Report EPA-600/2-83-070.

18 N. Keller and R. Noble (1983) "RACT For VOC- A Burning Issue", Pollution Engineering, July.

19 E.W. Kuipers, B.Jarvis, S.J. Bullman, D.K. Cook and D.R. McHugh (1996) "Combustion Efficiency of Natural Gas Flares, Effect of Wind Speed, Flow Rates and Pilots". Internal Report, Shell Research and Technology Thorton and British Gas Research Centre.

20 D.M. Leahey and M.J.E. Davies (1984), "Observations of Plume Rise from Sour Gas Flares", Atmospheric Environment, Vol. 18, No. 5, pp. 917-922.

21 M. McDaniel (1983), "Flare Efficiency Study", EPA report No. 600/2-83-052, July.

22 R. J. Margason (1993) "Fifty years of Jet in Cross-Flow Research", AGARD Conference Proceedings, pp. 1-48.

23 Merriam-Webster's dictionary. On-line

24 J. H. Pohl and N.R. Soelberg (1985), "Evaluation of Efficiency of Industrial Flares: Flare Head Design and Gas Composition. Environmental Protection Agency Report EPA-600/2-85-106.

25 J. H. Pohl, J. Lee and R. Payne (1986) "Combustion Efficiency of Flares", Combust. Sci. and Tech., Vol. 50, pp. 217-231.

26 W.Rodi (1982), Turbulent Buoyant Jets and Plumes, The Science and Applications of Heat and Mass Transfer, Pergamon Press.

27 R.R. Romano (1983), "Control Emissions with Flare Efficiency", Hydrocarbon Processing, pp. 78-80.

28 J. Shwartz and M. P.Tulin (1972), "Chimney Plumes in Neutral and Stable Surroundings", Atmospheric Environment Vol. 6, pp. 19-35.

29 K.D. Siegel (1980), "Uber den Umsatzgrad von Fackelgas in Raffineriehochfackeln". Report on BMI-BMFT-DGMK-Gemeinschaftsprojekt 135-02,PhD. Dissertation, University of Karlsruhe.

30 SKM Consulting Ltd (1988), "Review and Assessment of Current Flaring Technology", Environment Canada, Report CP(EP) WNR-87/85-5, pp.8.6.

31 P.R. Slawson and G.T. Csanady (1967), "On the Mean Path of Buoyant, Bent-Over Chimney Plumes", J. Fluid Mech, Vol. 28 part 2, pp.311-322.

32 S.H. Smith and M.G. Mungal (1998), "Mixing, Structure and Scaling of the Jet in Cross-Flow", J. Fluid Mech., Vol. 357, pp.83-122.

33 M.Strosher (1996), "Investigations of Flares Gas Emissions in Alberta", Alberta Research Council Environmental Technologies.

34 T.H. Toften, A.E. Holdo and D.Kapfer (1993), "Effects of Free-Stream Turbulence on Jet in Cross-Flow", AGARD Conference proceedings, pp35-1 35-10.

APPENDIX A: Air Entrainment
and Plume Rise

The radius of the plume, R_p, is going to be expressed as a function of the radius of

the stack, R_j, the jet velocity, V_j, the crosswind, U_∞, and the distance from the stack, X_o.
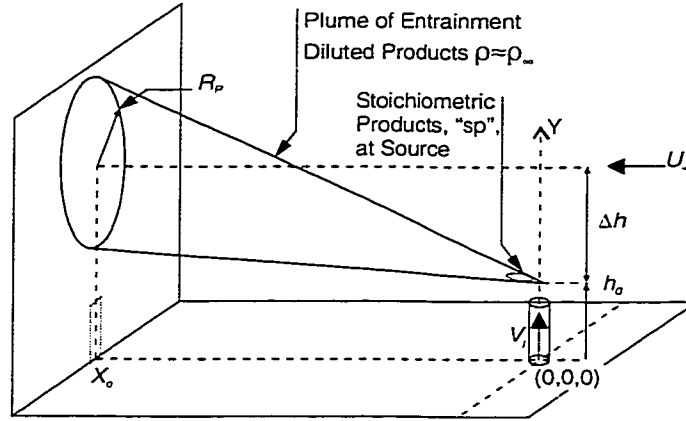
Figure A.1: Plume of a Non Reacting Buoyant Jet in Cross-Flow

At the start is the conventional definition of buoyancy flux $(m^4.s^{-3})$:

$$F_b = g \cdot \left(\frac{\rho_\infty - \rho_{sp}}{\rho_\infty} \right) \cdot V_j \cdot R_j^2 \qquad (A.1)$$

where ρ_{sp} = density of idealised stoichiometric products.

With ideal gas law $P = \rho \overline{R} T$, A.1 becomes:

$$F_b = g \cdot \left(\frac{T_{sp} - T_\infty}{T_{sp}} \right) \cdot V_j \cdot R_j^2 \qquad (A.2)$$

where T_{sp} = temperature of idealised stoichiometric products.

For a hot source, the expression of the heat release rate (J.s^{-1}) can be used:

$$H = \pi \cdot R_j^2 \cdot V_j \cdot \rho_j \cdot C_{p\infty} \cdot \left(T_{sp} - T_\infty\right)$$

(A.3)

Or the expression of the heating value Q_{hv} (J.kg^{-1}) can also be used

$$Q_{hv} = \frac{H}{\pi \cdot R_j^2 \cdot V_j \cdot \rho_j} = C_{p\infty} \cdot \left(T_{sp} - T_\infty\right)$$

(A.4)

Combining A.2 and A.4:

$$F_b = g \cdot \frac{Q_{hv}}{T_{sp} \cdot C_{p\infty}} \cdot V_j \cdot R_j^2$$

(A.5)

Assuming that U_∞ is constant with height, the jet is fully bent-over and the Boussinesq approximation (density difference negligible except at the source) is applicable. For a purely buoyant plume with no momentum and an effective source diameter, $R_o = 0$, the buoyant rise is:

$$\Delta h_b = \left(\frac{3}{2\beta^2}\right)^{1/3} \cdot \frac{F_b^{1/3}}{U_\infty} \cdot X_o^{2/3}$$

(A.6)

Note that:

- For a pure momentum jet with effective source diameter, $R_o = 0$.

$$\Delta h_m = \left(\frac{3}{\beta^2}\right)^{1/3} \cdot \frac{F_m^{1/3}}{U_\infty} \cdot X_o^{1/3}$$

(A.7)

where F_m = the momentum flux (m^4.s^{-2})

- For a jet with $R_o \neq 0$.

$$\Delta h_o = \frac{R_o}{\beta} \qquad \text{with} \qquad R_o = \left(\frac{\rho_j}{\rho_\infty} \cdot \frac{V_j}{U_\infty} \right)^{1/2} \cdot R_j \qquad (A.8)$$

- For a combination of the foregoing cases.

$$\Delta h = \left(\Delta h_m^{\ 3} + \Delta h_b^{\ 3} + \Delta h_o^{\ 3} \right)^{1/3} - \Delta h_o \qquad (A.9)$$

Combining A.5 and A.6:

$$\Delta h_b = \left(\frac{3}{2\beta^2} \right)^{1/3} \cdot \frac{g^{1/3} \cdot Q_{hv}^{1/3} \cdot R_j^{2/3} \cdot V_j^{1/3}}{T_{sp}^{1/3} \cdot C_{p\infty}^{1/3} \cdot U_\infty} \cdot X_o^{2/3} \qquad (A.10)$$

The radius of the plume, R_p, can then be expressed as:

$$R_p = R_o + \beta \cdot \Delta h \qquad (A.11)$$

Assuming $R_o = 0$, $\Delta h_m = 0$ and $\Delta h_o = 0$,

$$\Delta h = \Delta h_b \qquad (A.12)$$

A.11 then becomes:

$$R_p = \beta \cdot \Delta h_b \qquad (A.13)$$

Finally, combining A.10 and A.13:

$$R_p = \beta \cdot \left(\frac{3}{2\beta^2} \right)^{1/3} \cdot \frac{g^{1/3} \cdot Q_{hv}^{1/3} \cdot R_j^{2/3} \cdot V_j^{1/3}}{T_{sp}^{1/3} \cdot C_{p\infty}^{1/3} \cdot U_\infty} \cdot X_0^{2/3} \qquad (A.14)$$

104

or,

$$R_p = \left(\frac{3\beta \cdot Q_{hv}}{2 \cdot T_{sp} \cdot C_{p\infty}} \right)^{1/3} \cdot g^{1/3} \cdot R_j^{2/3} \cdot \frac{V_j^{1/3}}{U_\infty} \cdot X_o^{2/3} \qquad (A.15)$$

The first term in brackets remains constant when the same gas is used, the combustion is almost complete ($\eta \approx 1$) and the conditions of pressure does not vary too much. Finally, the radius of the plume is:

$$R_p \propto g^{1/3} \cdot R_j^{2/3} \cdot \frac{V_j^{1/3}}{U_\infty} \cdot X_o^{2/3} \qquad (A.16)$$

105

APPENDIX B: Sensitivity and Uncertainty of Efficiency Calculation

The calculation of the efficiency is based on the measurement of 8 different concentrations:

$$\eta = \frac{[CO_2]_S - \left(\frac{[O_2]_S}{[O_2]_E}\right)[CO_2]_E}{[CO_2]_S + [CO]_S + [CH_4]_S - \left(\frac{[O_2]_S}{[O_2]_E}\right)\left([CO_2]_E + [CO]_E + [CH_4]_E\right)} \qquad (B.1)$$

where the subscript S indicates concentrations of the sample and the subscript E indicates the concentrations of entrained air measured before a test.

The sensitivity analysis consists in examining the change in the calculated efficiency when a change occurs in one of the variables. By repeating the process for each variable, the variables which will have the most effect on the results can be determined.

Two cases are presented. The first one with "typical" values of concentrations for a very highly efficient flame and the second for a low efficiency flame.

Efficiency	99.65	%
CO2s	8000	ppm
CO2b	500	ppm
COs	10	ppm
COb	2	ppm
HCs	20	ppm
HCb	2	ppm
O2s	20	%
O2b	21	%
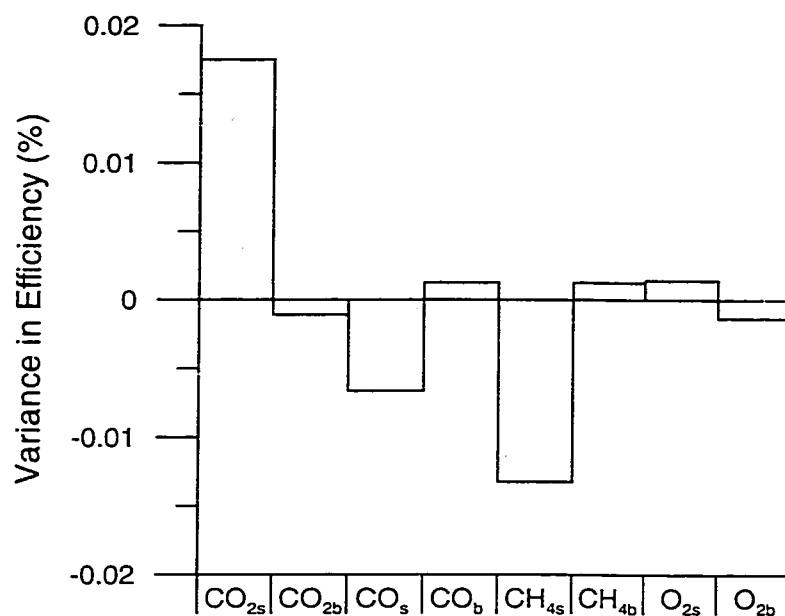
Figure B.1: Sensitivity to a 5% Change in Variables, Case 1

Efficiency	89.66	%
CO2s	4000	ppm
CO2b	500	ppm
COs	60	ppm
COb	2	ppm
HCs	350	ppm
HCb	2	ppm
O2s	20	%
O2b	21	%
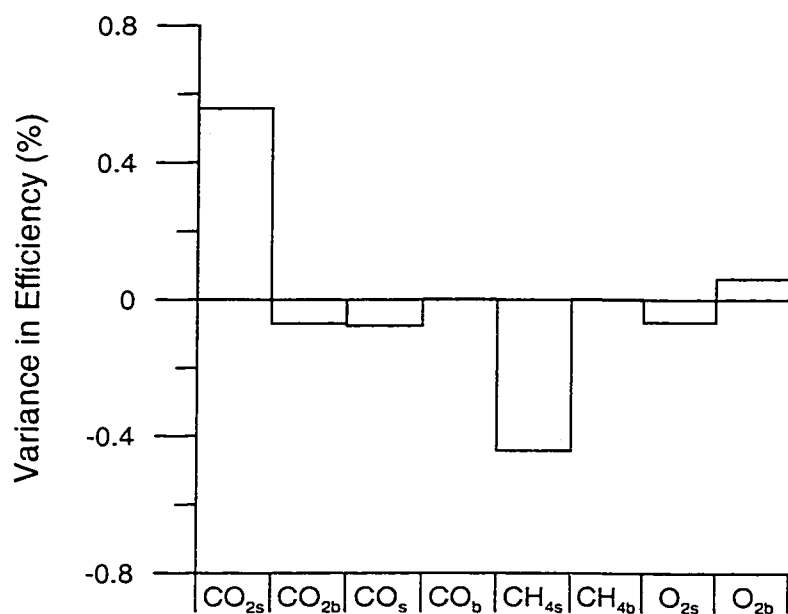
Figure B.2: Sensitivity to a 5% Change in Variables, Case 2.

107

From Figure B.1 and B.2, the two most important measurements are the concentration of carbon dioxide and unburned hydrocarbons in the sample. It is also important to notice that the change remains very small, under one percent and that the reading of the background concentrations do not have a major effect on the calculation. This is an interesting point considering how delicate the measurement of a few ppm of a compound can be.

Note: instead of efficiency, one can measure the performance of a flare in inefficiency, which is the complement of the efficiency on a 100% scale. Since the inefficiency has an absolute value much smaller than the efficiency (1% for 99%, 10% for 90%) its sensitivity is proportionally amplified. A change of 5% in the measurement of the carbon dioxide in the sample will have an effect of 5.03% in case 1 and 4.84% in case 2. The others variables keep the same relative effect compared to the CO_{2s} measurements.

The uncertainty analysis provides information on reliability of results. Each of the variables used in the calculation had an uncertainty due to, for example, the accuracy of the analysers.

The uncertainty, ε_η, of the efficiency, η, can be calculated as:

$$\varepsilon_\eta^{\ 2} = \sum_{i=1}^{n} \left(\frac{\partial \eta}{\partial x_i} \right)^2 \varepsilon_{x_i}^{\ 2} \tag{B.2}$$

where x_i = variable in efficiency equation

                                         ε_{xi} = uncertainty of variable x_j.

                                         n = total number of variable.

In order to calculate the uncertainty, ε_η, the partial derivation of the expression

B.1 must be expressed against each one of the eight variables. Then, the uncertainty, ε_{xi},

of each one of the variables must be evaluated. It is, in the present case, 1% of the full

scale of the range used during the measurement of the concentration for each compound.

A typical value for each variable is chosen and inserted in the expression B.2.

Table B.1 presents the uncertainty and typical value for the 8 variables.

Variable	Range	Unit	Uncertainty	Unit	Typical Value	Unit
CO2s	0-10 000	ppm	100	ppm	5000	ppm
CO2b	0-10 000	ppm	100	ppm	500	ppm
COs	0-100	ppm	1	ppm	50	ppm
COb	0-100	ppm	1	ppm	2	ppm
HCs	0-500	ppm	5	ppm	100	ppm
HCb	0-500	ppm	5	ppm	2	ppm
O2s	0-25	%	0.25	%	20	%
O2b	0-25	%	0.25	%	21	%

Table B.1: Uncertainty of Variables for Uncertainty Calculation

The computation of each derivative with the foregoing values gives:

$$\frac{\partial \eta}{\partial CO_{2s}} = 6.703248 \; ; \; \frac{\partial \eta}{\partial CO_{2b}} = -6.384046 \; ; \; \frac{\partial \eta}{\partial CO_s} = -207.459514 \; ; \; \frac{\partial \eta}{\partial CO_{2s}} = 197.551918$$

$$\frac{\partial \eta}{\partial CH_{4s}} = -207.459514 \; ; \; \frac{\partial \eta}{\partial CH_{4b}} = 197.551918 \; ; \; \frac{\partial \eta}{\partial O_{2s}} = -0.0120091 \; ; \; \frac{\partial \eta}{\partial O_{2b}} = 0.0114372$$

It leads to an uncertainty, ε_η,

$$\varepsilon_\eta = 0.00449216 \text{ for } \eta = 96.8696 \text{ \%}$$

which represents for a typical value of efficiency:

$$\frac{\varepsilon_\eta}{\eta} = 0.464 \text{ \%}$$

In other word, taking the example of this typical efficiency, the result will be indicated as:

$$\eta = 96.9 \pm 0.5 \text{ \%}$$

APPENDIX C: Measurement of Overall Efficiency in Closed-Loop Wind tunnel

This appendix describes the method used to calculate the overall efficiency by monitoring the rise in concentrations inside the closed-loop wind tunnel.

Concentrations of the major carbon-containing species, carbon dioxide (CO_2), carbon monoxide (CO), and unburned hydrocarbons (CH_4), are sampled and continually monitored during a test. The sampling occurs 40 m downstream of the stack (almost one complete loop inside the wind tunnel). Therefore the products of combustion are homogenised with the air stream before analysis with online gas analysers.

Figure C.1 shows typical time traces of the species concentrations of these species during an experiment. Outside air ([CO_2]~400 ppm, [CH_4]~2 ppm, and [CO]~2 ppm) is first used to purge the tunnel and fill it with fresh air. Then, the fuel flow is set and the stack lit (at t~30 s in Figure C.1). Gas is burned for several minutes (approximately 6 minutes for the tests shown in figure C.1). Finally, the fuel is shut off and the tunnel is purged again with fresh air to prepare for the next test. The rates of accumulation of these species during the steady burning period are used in the mass balance for the calculation of the overall efficiency (η) of the flame:

$$\eta = \frac{\text{Mass Flow Rate of C in form of } CO_2 \text{ produced by the flame}}{\text{Mass Flow Rate of C in form of hydrocarbon in the fuel}}$$

where, the denominator of this expression is calculated from the sum of the accumulation rates of CO_2, CO and unburned hydrocarbons. Leakage from the tunnel is

inherently accounted for in the mass balance because once mixed, all species leak proportionally to their concentration. As with the technique of measurement of the local efficiency, the mass of soot in the combustion products is neglected.
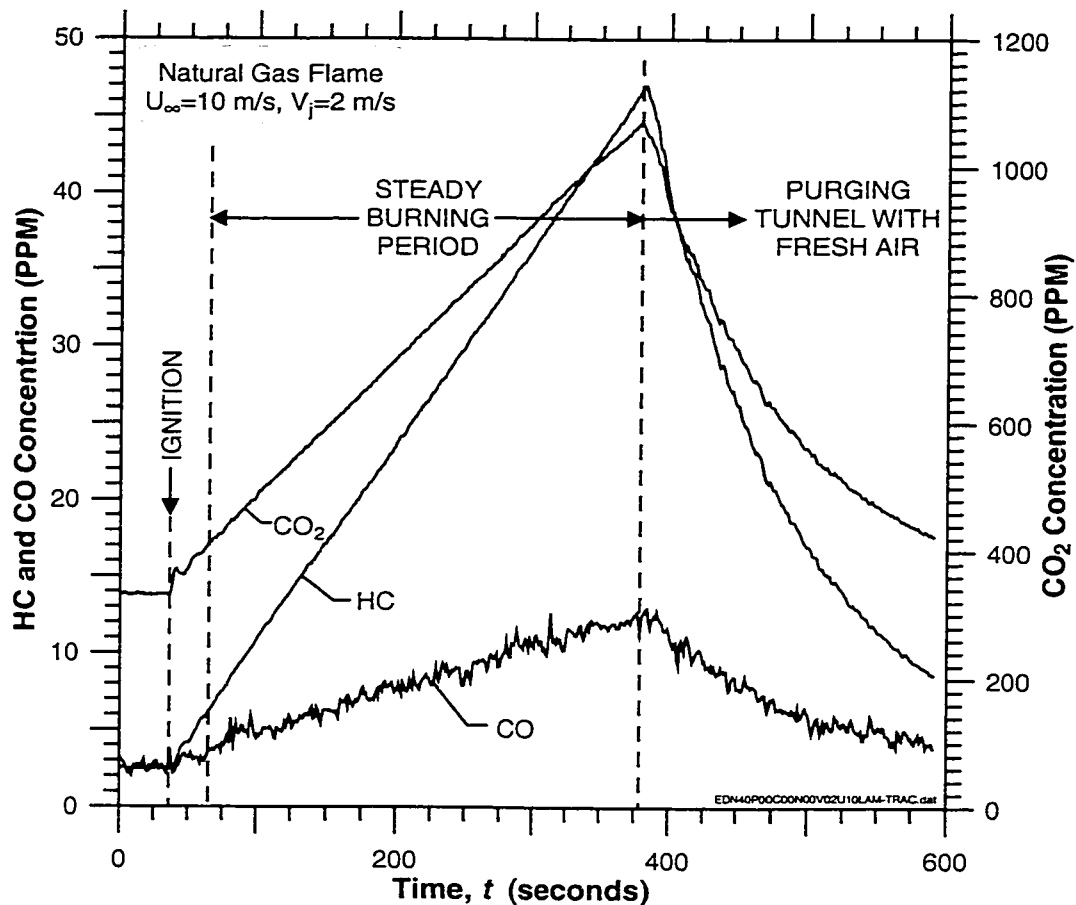
Figure C.1: Time Tracer of Concentration During a Test of Overall Efficiency Measurement by Accumulation of Products

The wind tunnel contains enough air that the maximum concentrations reached at the end of each tests remain small ($CH_4 < 250$ ppm) and the effects of reburning are negligible. The experimental error in the measured combustion efficiency with this technique of carbon mass balance based on accumulation rates of each species is less than 0.5% absolute.

APPENDIX D: Velocity Profiles of the Wind Tunnel

Figure D.1 presents the velocity profiles and turbulence intensity in the test

section of the wind tunnel along two axes displayed in Figure D.2.
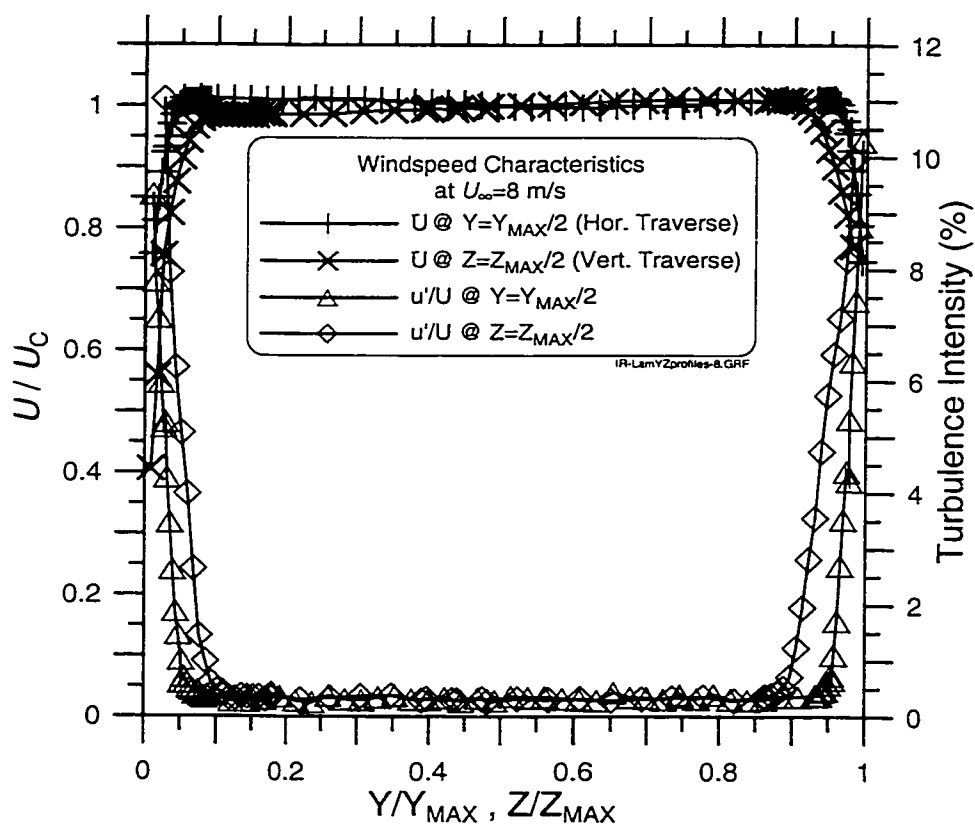
Figure D.1: Horizontal and Vertical Velocity and Turbulence Intensity Profiles across the Test Section of the Wind Tunnel at the Location of the Flare
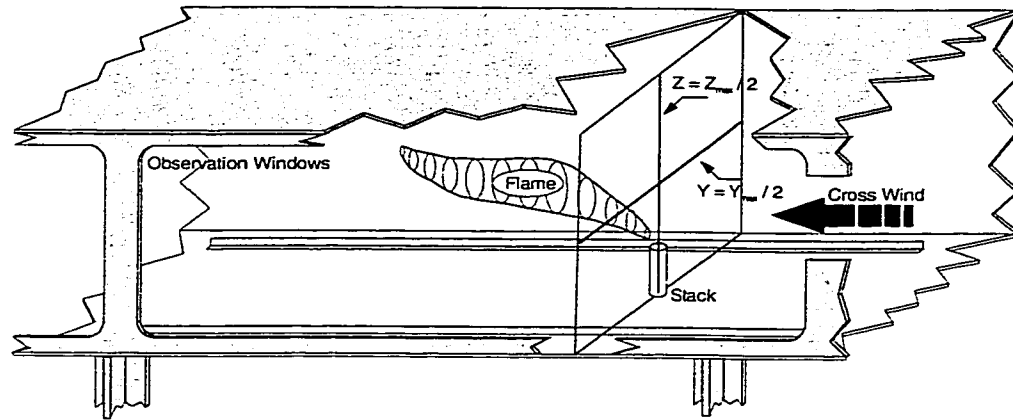
Figure D.2: Sketch Showing the Location of Measurements of Velocity Profiles and Turbulence Intensity of the Wind Tunnel

APPENDIX E: Analyser Output During Bag Analysis

Figure E.1 displays a typical output during the analysis of the sampling bags used during multi-point sampling test of the plume. It shows the analysers reading while 3 bags are being analysed. The transient period is visible for the first 15 second. Then, the outputs stabilise, proving that the mixture in the sampling is now homogenous.
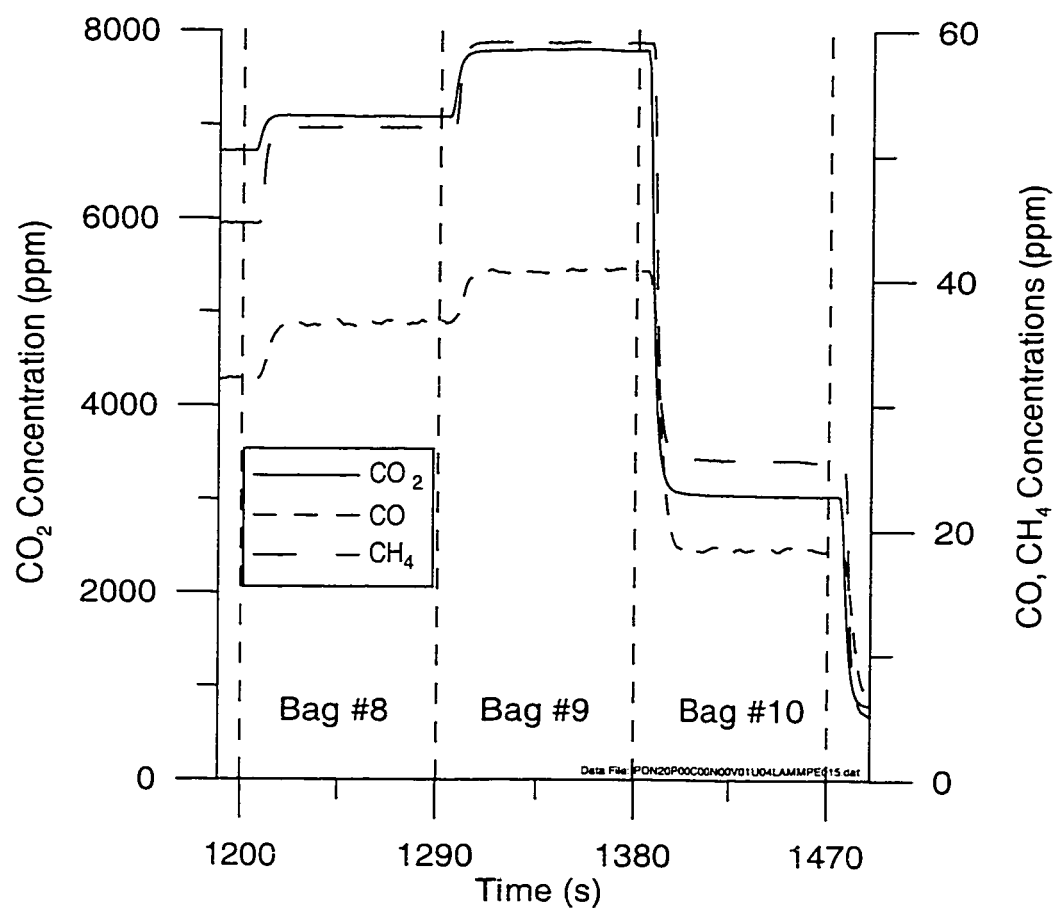
Figure E.1: Typical Analyser Output During the Analysis of Sample of the Plume

APPENDIX F: Plume Sampling Apparatus

Table F.1: Lists the materials needed for the plume sampling apparatus used in this research.

Figure F.1 and F.2: Engineering drawing for the sample probes and the airtight container.

Table F.2: Checklist used during the record of the local compositional structure of the plumes.

Designation	Quantity	Specification	Note
Probes	21	- Stainless Steel Tubing - Nominal diameter: 1/4" - I.D. = 4.55 mm - Length = 30 cm	- Inlet filed on the inside and outside to decrease flow disturbance. - See Figure F.1.
Connection Probe/Solenoid-valve	21	-Teflon® - Nominal diameter: 1/4" - I.D. = 4.55 mm - Length = 4.5 m	
Connection Bags/Solenoid-valve	20	- Teflon® - Nominal diameter: 1/4" - I.D. = 4.55 mm - Length = 3.5 m	
Sampling Bags	20	- Tedlar® - Nominal Capacity 25 l. - Size: 44.4 x 61 cm	
Airtight Box	1	- Ply Wood 3/4 - Length: 192.5 cm - Width: 77.3 cm - Height : 101.5 cm	- 2 reinforcement bar at the top, 1 at the bottom. - Manual valve for pressure relief. - See Figure F.2.
3 way solenoid-valve	21	- Brass Body - Pipe size : 1/4" N.P.T. - Orifice size: 11/64" - Operating pressure: 20 psi - Voltage 120V AC.	- Universal operation (pressure at any port).
Manifold	1	- Stainless Steel Tubing - Core diameter: 3/8" - Core Length: 40 cm. - Connections diameter: 1/4" - Connections Length: 2 cm.	- Connections every 2 cm lengthwise and rotated by 90 degree.
Connection Manifold/Analysers	1	- Teflon® - Nominal diameter: 1/4" - I.D. = 4.55 mm - Length = 6+1 m	- An auxiliary diaphragm pump is installed 1 m after the manifold.

Table F.1: Elements of the Plume Sampling Apparatus

117

Total volume of tubing from probe to analysers:

$$V_{tubing} = \pi \cdot \frac{ID^2}{4} \cdot L = 0.25 \text{ liter} \qquad \text{for } L = 15 \text{ m}$$

The bags have a capacity of 25l so the volume of tubing represents 1% of the volume of the bag.
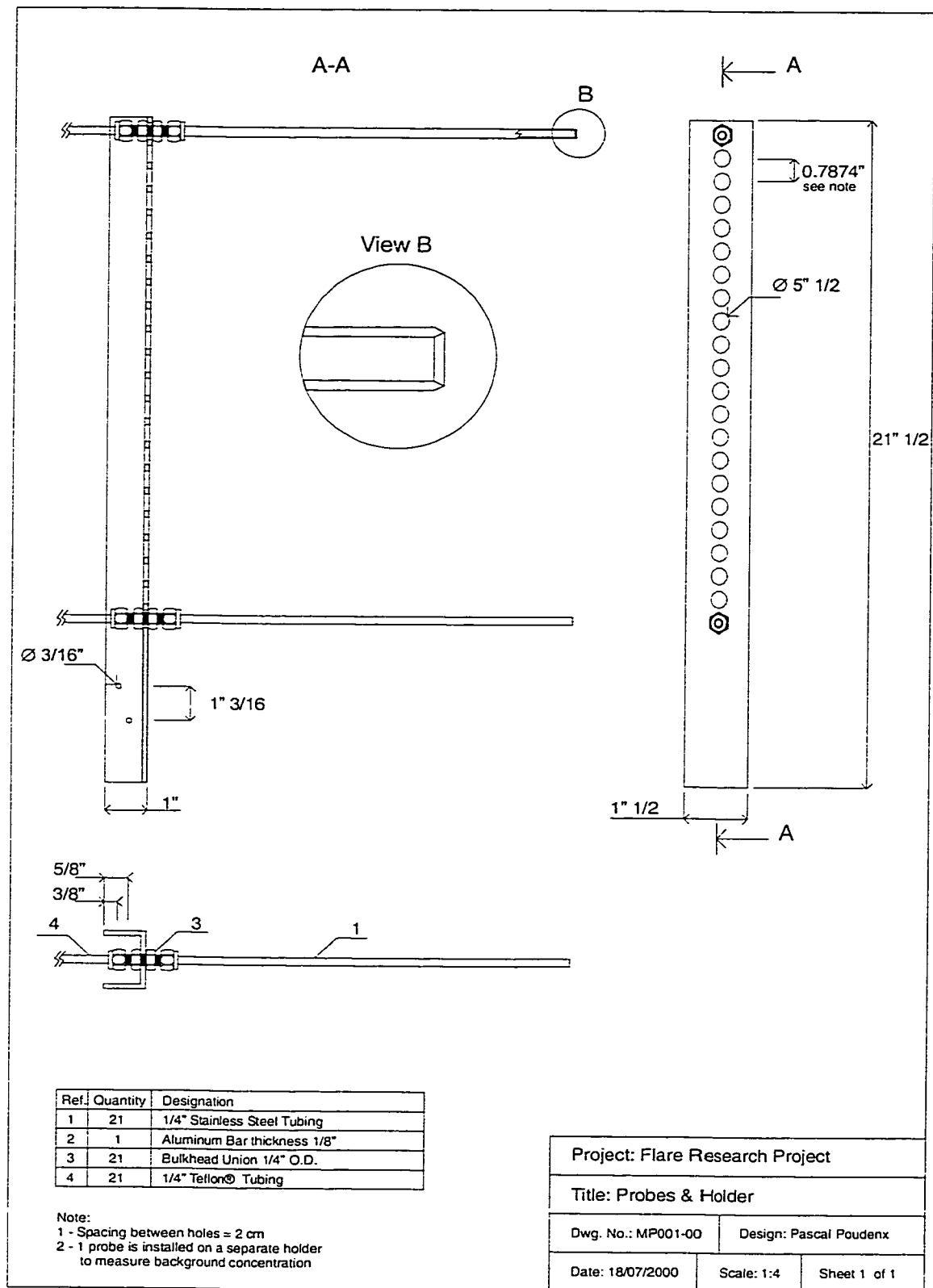
Figure F.1: Engineering Drawing of Probes and Holder

A-A

B

A

View B

Ø 5" 1/2

0.7874"
see note

21" 1/2

Ø 3/16"

1" 3/16

1"

1" 1/2

A

5/8"
3/8"

4   3   1

Ref.	Quantity	Designation
1	21	1/4" Stainless Steel Tubing
2	1	Aluminum Bar thickness 1/8"
3	21	Bulkhead Union 1/4" O.D.
4	21	1/4" Teflon® Tubing

Note:
1 - Spacing between holes = 2 cm
2 - 1 probe is installed on a separate holder
    to measure background concentration

Project: Flare Research Project

Title: Probes & Holder

Dwg. No.: MP001-00	Design: Pascal Poudenx	
Date: 18/07/2000	Scale: 1:4	Sheet 1 of 1

119

Ref.	Quantity	Designation
1	xx	Ply wood panel thickness 3/4"
2	2	15"x15" Plexiglass windows thickness 1/4"
3	20	25 l. Tedlar sampling bag
4	1	Connector for sampling line
5	1	2" manual valve
6	1	2" Inlet for Vacuum pump
7	1	1/4" Inlet for pressure transducer
8	14	lock

Project: Flare Research Project

Title: Box and Bags

Dwg. No.:MP003-00	Design: Pascal Poudenx	
Date: 19/07/2000	Scale 1:20	Sheet 1 of 1

Figure F.2: Engineering Drawing of Air-Tight Container with Bags

The following is the checklist used during tests.

CHECKLIST MPE TESTS

1	☐	Check Positions of the probes
2	☐	Vacuum Pump on position Vacuum
3	☐	set the wind tunnel (wind, gas)
4	☐	light the stack
5	☐	Fill in bags for 1 minute 30
6	☐	Stop Gas
7	☐	Vacuum Pump on position Pressurize
8	☐	empty bags for 2 minutes 30
9	☐	Purge Wind Tunnel
10	☐	Vacuum Pump on position Vacuum
11	☐	set the wind tunnel (wind, gas)
12	☐	light the stack
13	☐	Fill in bags for 2 minute 45
14	☐	Stop Gas
15	☐	Switch to Purge Probe
16	☐	Stop wind and mixing fans
17	☐	Start Analysis
18	☐	Vacuum Pump on position Pressurize
19	☐	Purge Wind Tunnel
20	☐	Empty bags for 2 minutes 30
22	☐	Vacuum Pump on position Vacuum
23	☐	Fill in bags for 2 minutes
24	☐	Vacuum Pump on position Pressurize
25	☐	Empty bags for 2 minutes 30
26	☐	Vacuum Pump on position Vacuum
27	☐	Fill in bags for 2 minutes
28	☐	Vacuum Pump on position Pressurize
29	☐	Empty bags for 2 minutes 30
30	☐	Move Probes

☑ : In progress
☒ : Done

Table F.2: Check List For Multipoint Sampling Test

First the wind tunnel is purged with fresh air. The conditions of the test (crosswind and gas velocity) are set and the flare lit. Then bags are filled once, the flame shut down, the bags emptied by pressurising the container while the windtunnel is purged. The flame is then lit a second time and the bags filled again. Then the flame is shut down, and the bags are analysed. Each bag is drawn for ninety seconds to be sure the line between the bag and the analysers is full of sampling gas and the analysers had time to adapt (see Appendix E).

In total a complete test takes forty-five minutes. Therefore, the time dependency of the concentrations of sample stored inside the bags was also tested. Over a period of one hour no difference appeared in concentrations.

APPENDIX G: Temperature Maps

This appendix contains the 149 plume mean temperature maps measured during this project.

The maps are organised by increasing stack diameter, d_s, jet velocity, V_j, and crosswind, U_∞:

- $d_s = 1.67$ cm $V_j = 0.5$ m/s $U_\infty = 1.5, 2, 3$ m/s

- $d_s = 1.67$ cm $V_j = 1.0$ m/s $U_\infty = 1.5, 2, 3, 4, 6, 8$ m/s

- $d_s = 1.67$ cm $V_j = 2.0$ m/s $U_\infty = 1.5, 2, 3, 4, 6, 8$ m/s

- $d_s = 2.21$ cm $V_j = 0.5$ m/s $U_\infty = 1.5, 2, 3, 4, 6, 8$ m/s

- $d_s = 2.21$ cm $V_j = 1.0$ m/s $U_\infty = 1.5, 2, 3, 4, 6, 8$ m/s

- $d_s = 2.21$ cm $V_j = 2.0$ m/s $U_\infty = 1.5, 2, 3, 4, 6, 8$ m/s

- $d_s = 3.33$ cm $V_j = 0.5$ m/s $U_\infty = 1.5, 2, 3, 4, 6, 8$ m/s

- $d_s = 3.33$ cm $V_j = 1.0$ m/s $U_\infty = 1.5, 2, 3, 4, 6, 8$ m/s

- $d_s = 3.33$ cm $V_j = 2.0$ m/s $U_\infty = 2, 3, 4, 6, 8$ m/s

data files : S07W15E05P050.grd, S07W15E05P080.grd, S07W15E05P110.grd
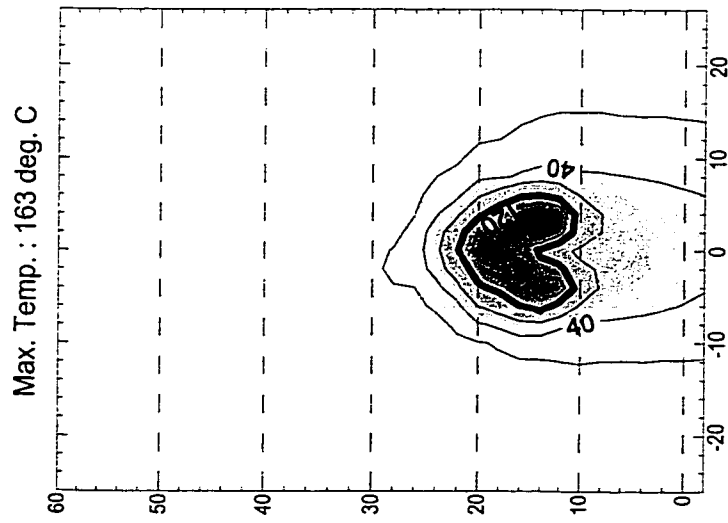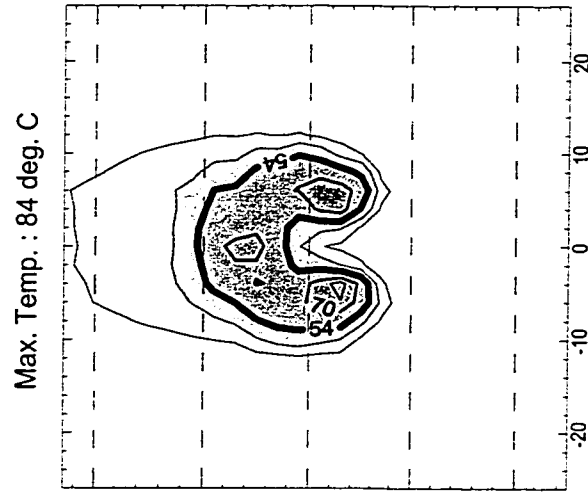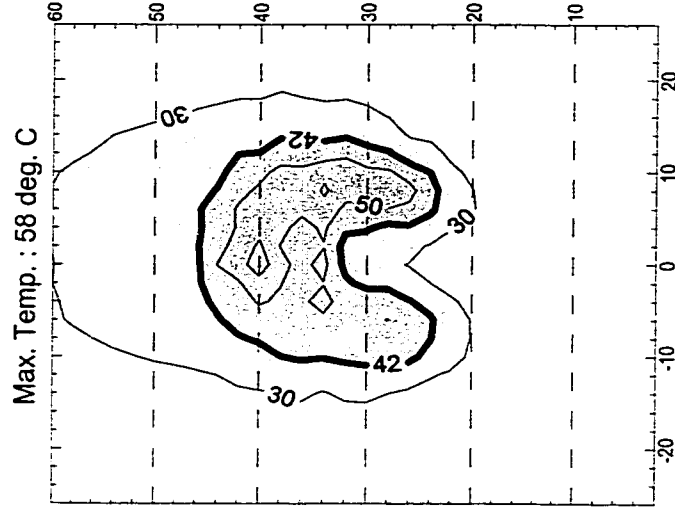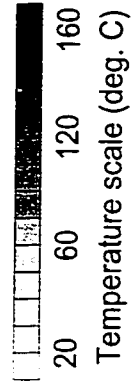
Max. Temp. : 163 deg. C

Max. Temp. : 84 deg. C

Max. Temp. : 58 deg. C

Distance : 50 cm

Distance : 80 cm
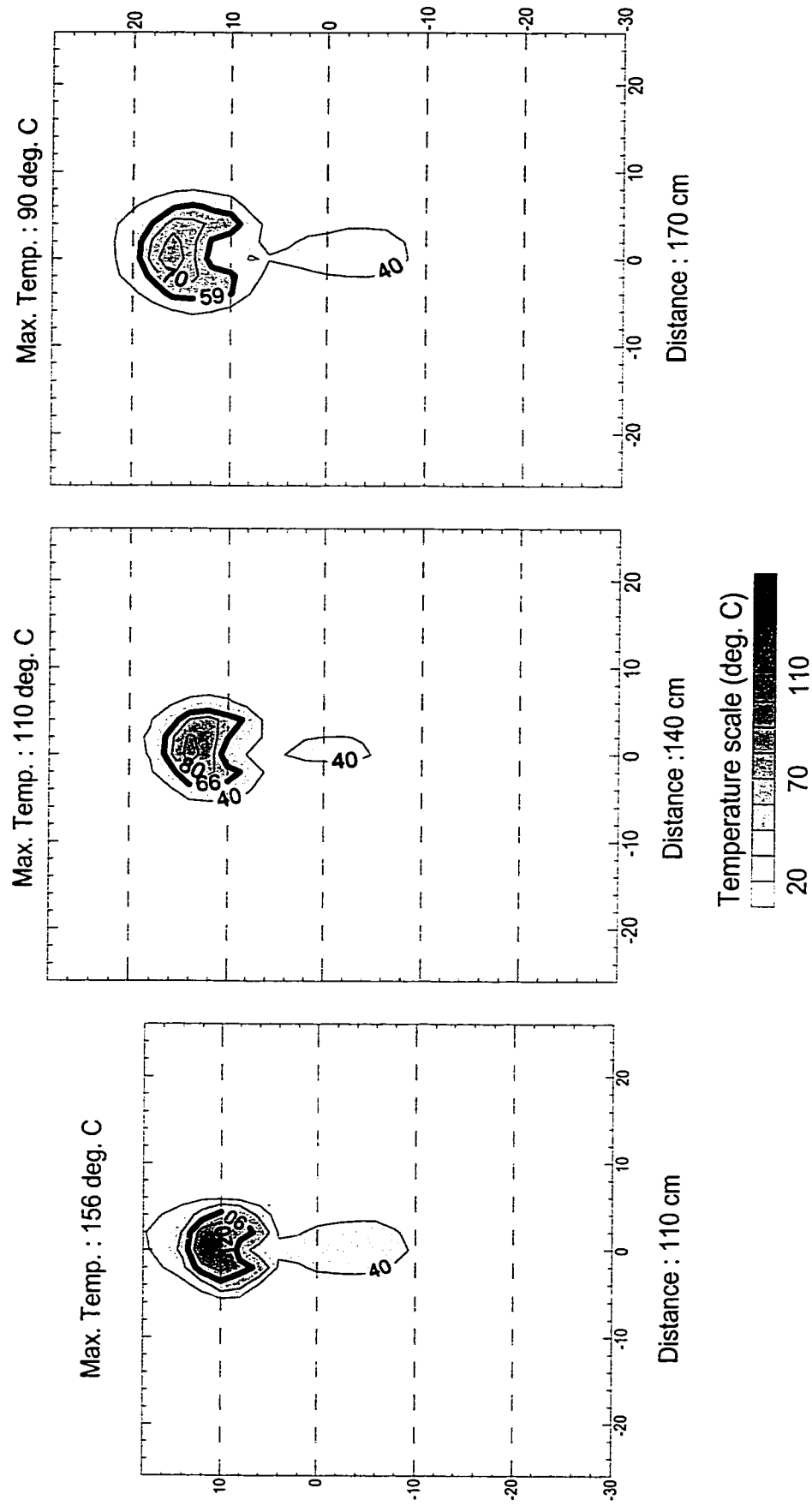
Distance : 110 cm

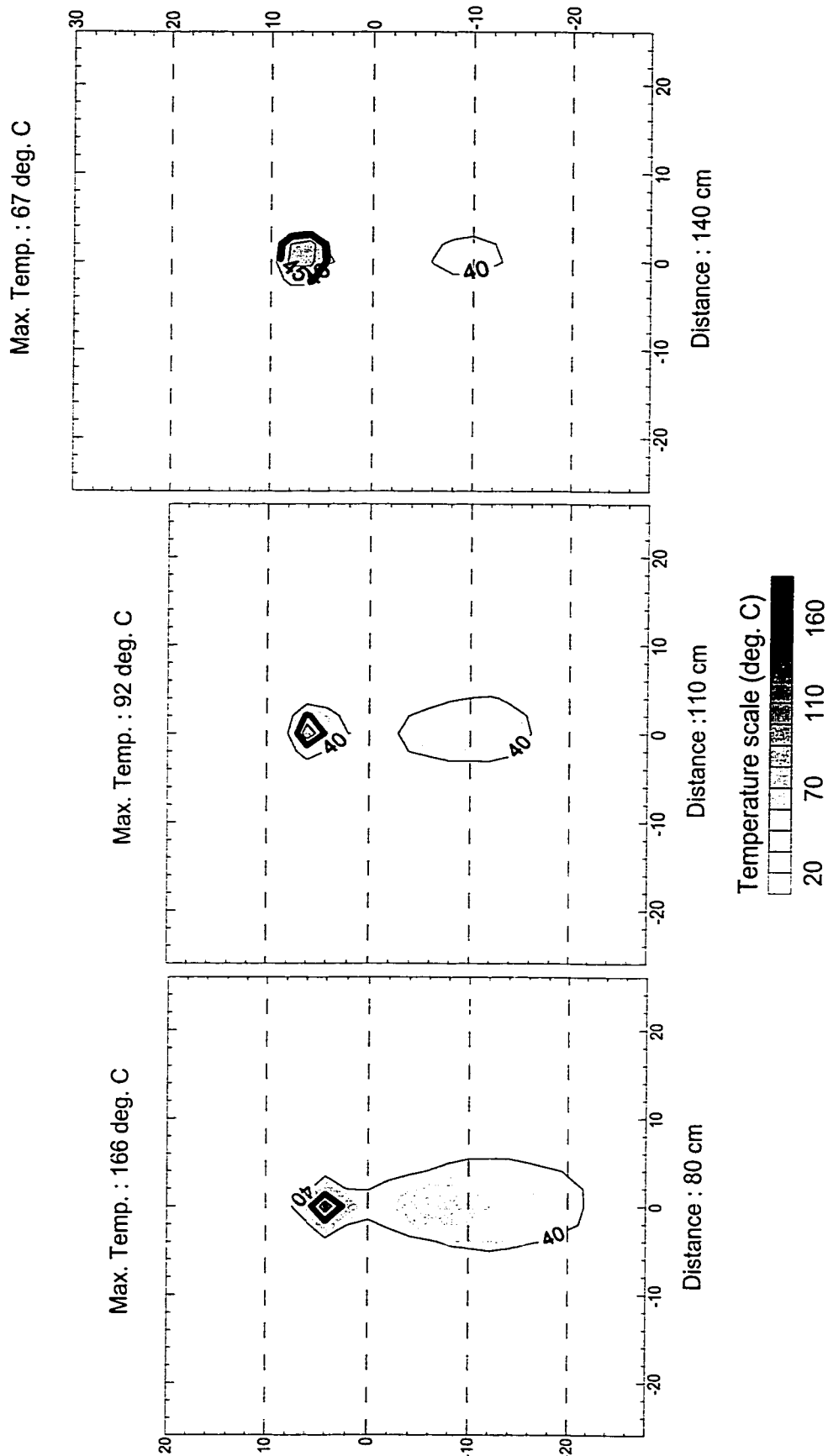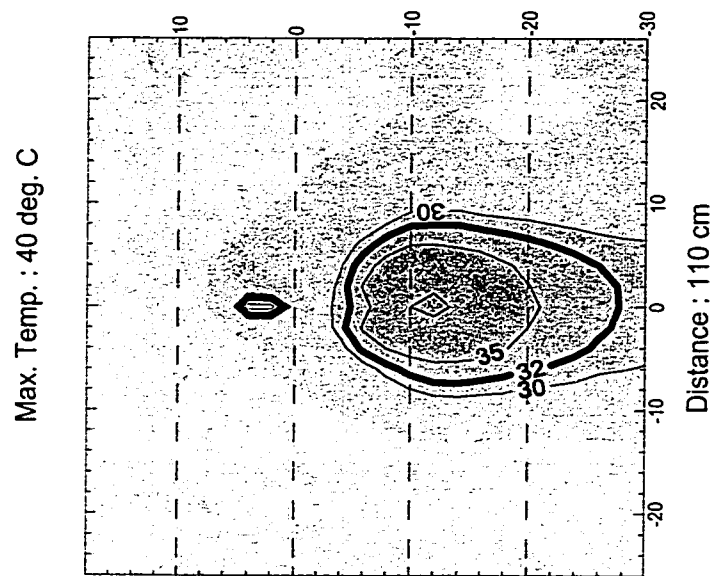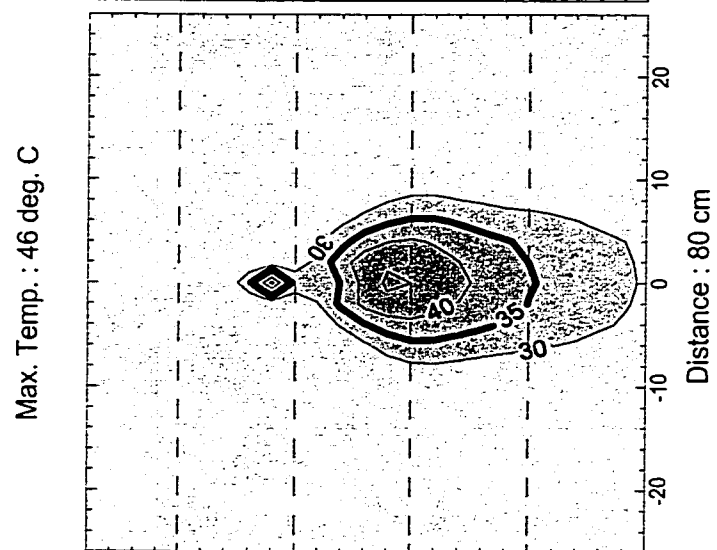Temperature scale (deg. C)

20   60   120   160

Notes:
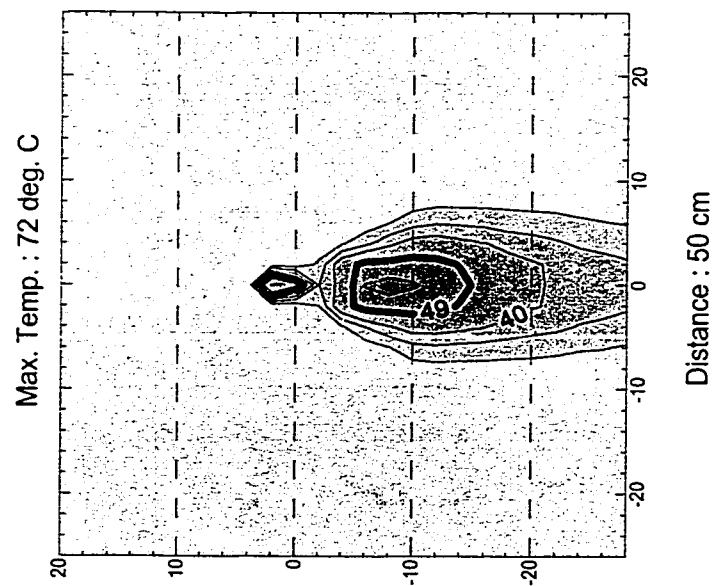- X and Y axis in cm relatively to the stack exit.
- Thick line shows 50% temperature contour.

$d_s = 1.67$ cm; $V_j = 0.5$ m/s; $U_\infty = 1.5$ m/s

124

data files : S07W20E05P080.grd, S07W20E05P110.grd, S07W20E05P140.grd

Max. Temp. : 67 deg. C
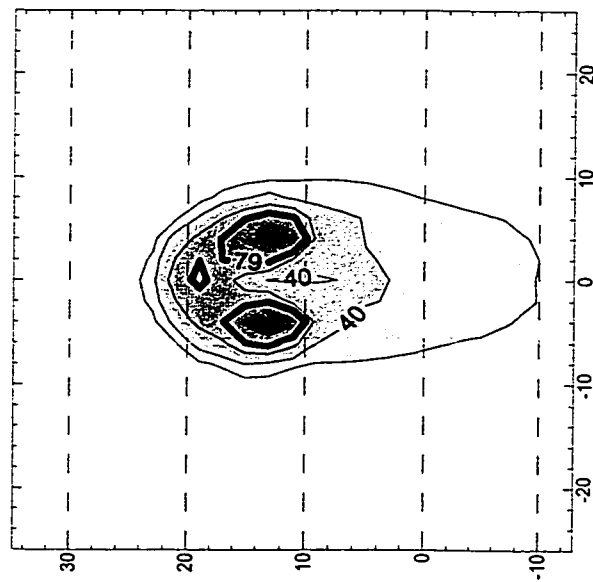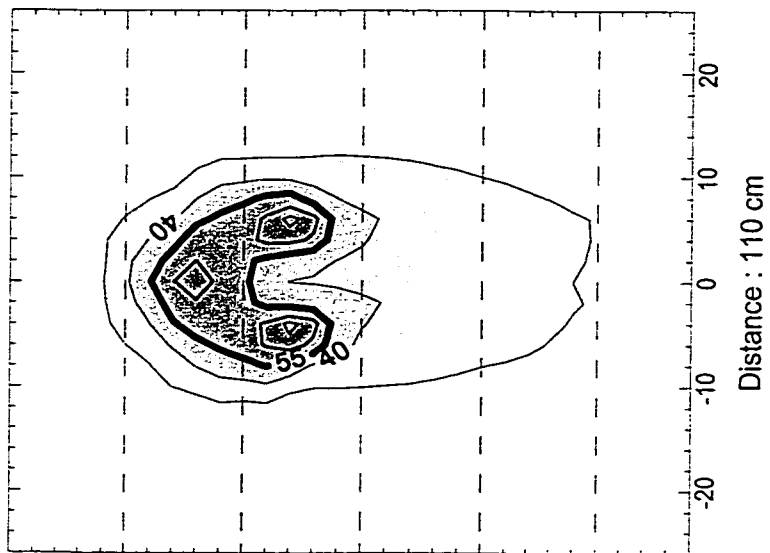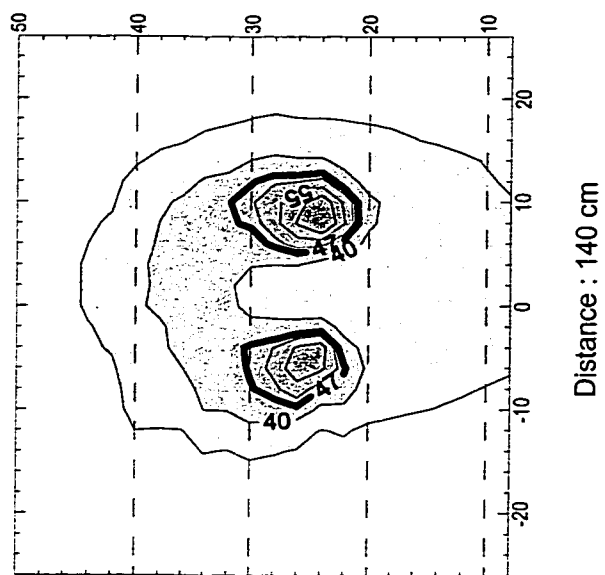
Distance : 140 cm

Max. Temp. : 83 deg. C

Distance : 110 cm

Max. Temp. : 134 deg. C

Distance : 80 cm

Temperature scale (deg. C)

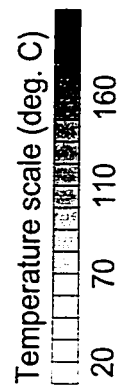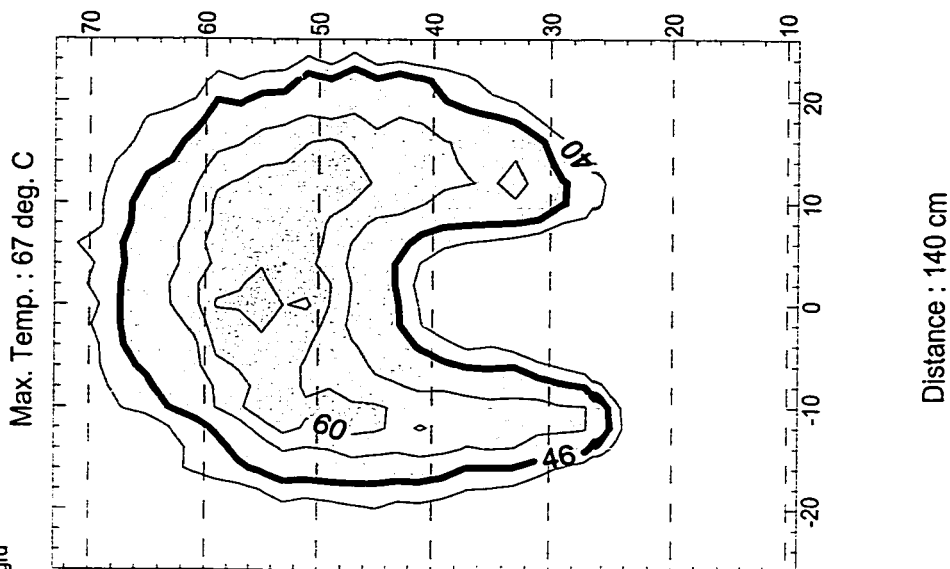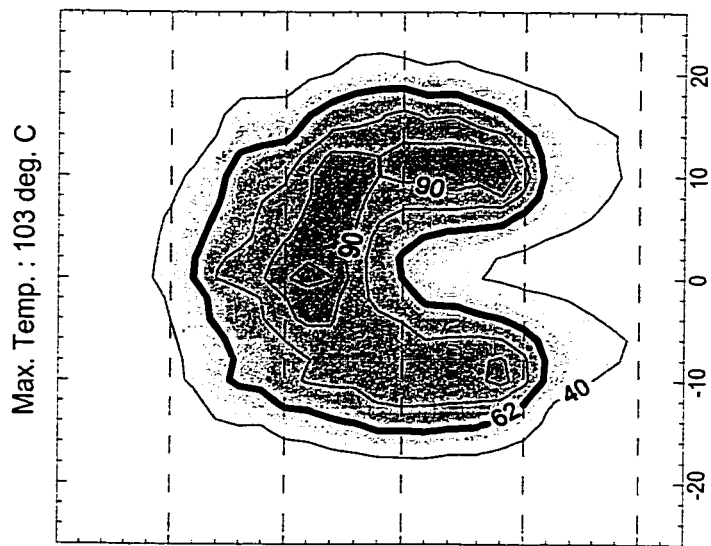d_s = 1.67 cm; V_j = 0.5 m/s; U_∞ = 2 m/s

Notes:
- X and Y axis in cm relatively to the stack exit.
- Thick line shows 50% temperature contour.

125

data files : S07W30E05P080.grd, S07W30E05P110.grd, S07W30E05P140.grd

Max. Temp. : 73 deg. C
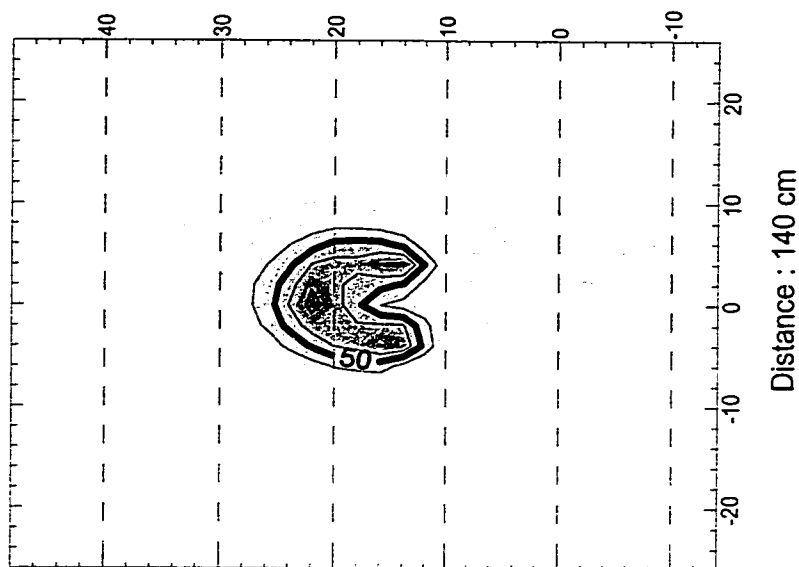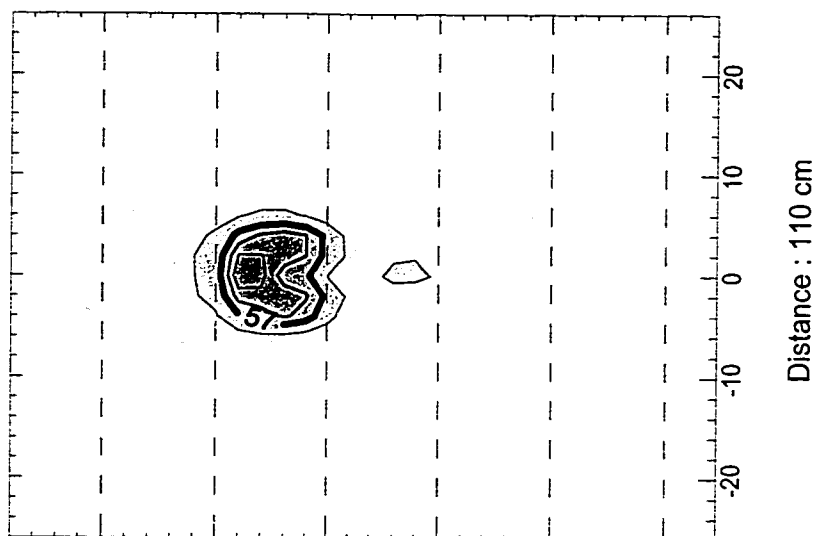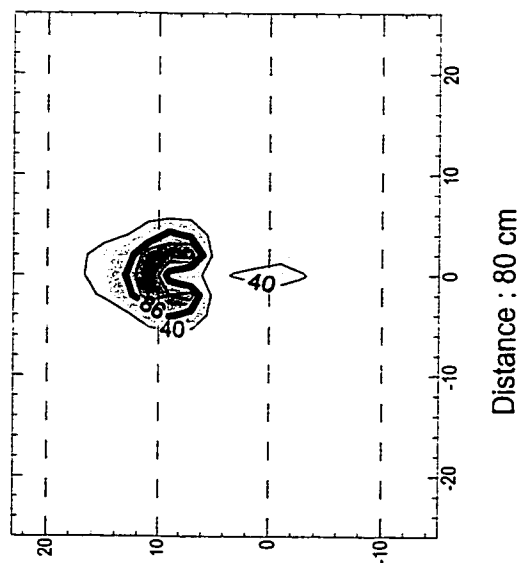
Distance : 140 cm

Max. Temp. : 88 deg. C

Distance : 110 cm

Max. Temp. : 148 deg. C

Distance : 80 cm

Temperature scale (deg. C)

d_s = 1.67 cm; V_j = 0.5 m/s; U_∞ = 3 m/s

Notes:
- X and Y axis in cm relatively to the stack exit.
- Thick line shows 50% temperature contour.

126

data files : S07W15E10P080.grd, S07W15E10P110.grd, S07W15E10P140.grd
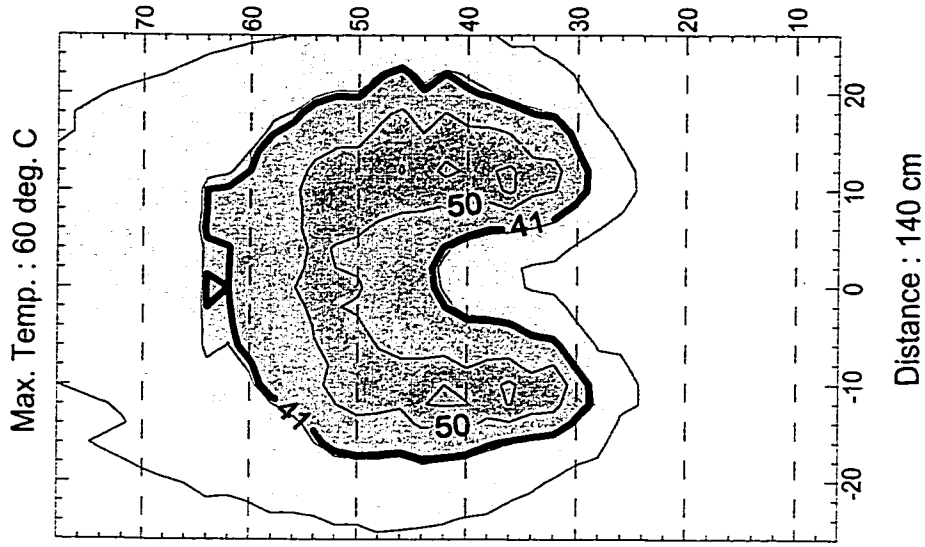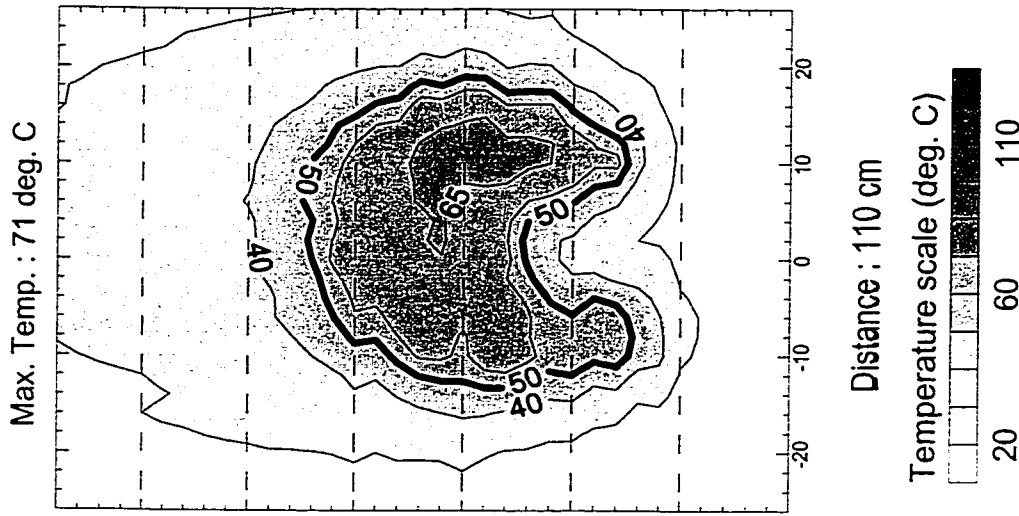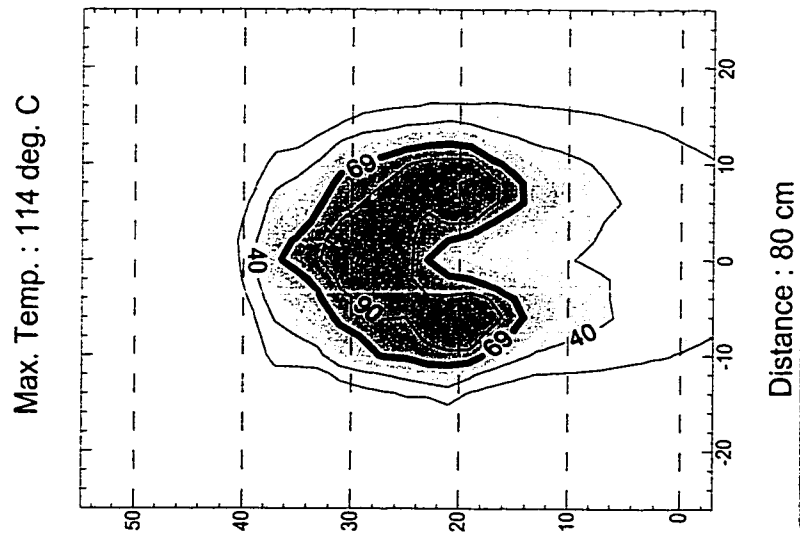
Max. Temp. : 60 deg. C

Distance : 140 cm

Max. Temp. : 71 deg. C

Distance : 110 cm

Max. Temp. : 114 deg. C

Distance : 80 cm

Temperature scale (deg. C)

d_s = 1.67 cm; V_j = 1 m/s; U_∞ = 1.5 m/s

Notes:
- X and Y axis in cm relatively to the stack exit.
- Thick line shows 50% temperature contour.

127

data files : S07W20E10P080.grd, S07W20E10P110.grd, S07W20E10P140.grd

Max. Temp. : 60 deg. C
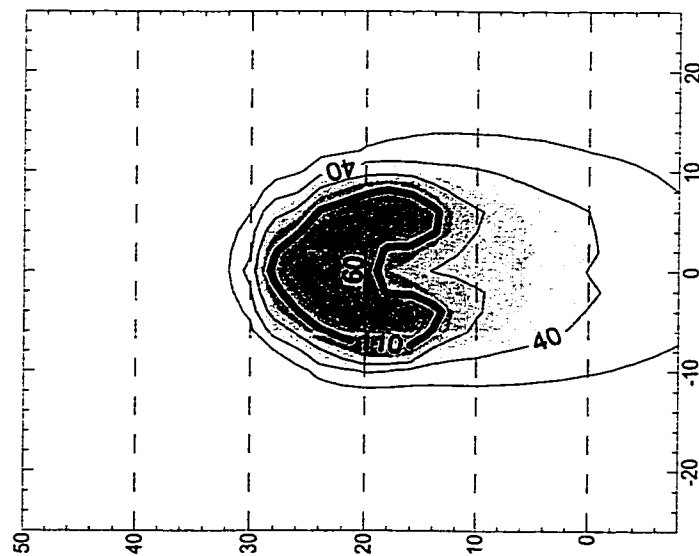
Distance : 140 cm

Max. Temp. : 95 deg. C
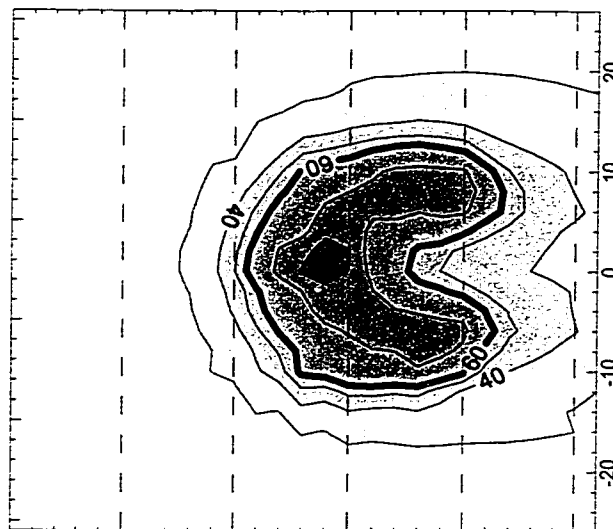
Distance : 110 cm
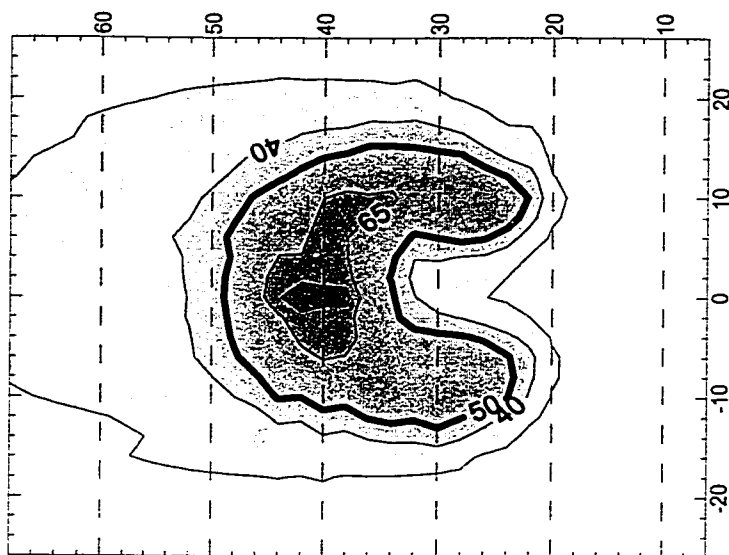
Max. Temp. : 196 deg. C

Distance : 80 cm

Temperature scale (deg. C)

20   60   120   200

d_s= 1.67 cm; V_j =1 m/s; U_∞ = 2 m/s

Notes:
- X and Y axis in cm relatively to the stack exit.
- Thick line shows 50% temperature contour.

128

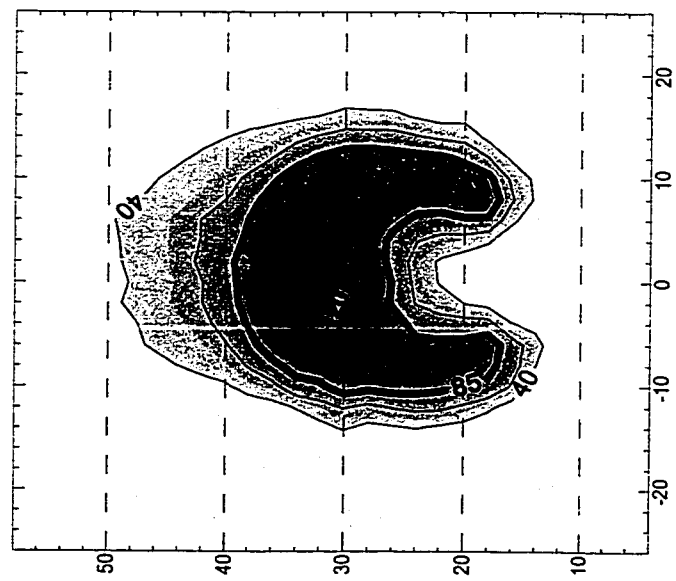data files : S07W30E10P080.grd, S07W30E10P110.grd, S07W30E10P140.grd

Max. Temp. : 299 deg. C
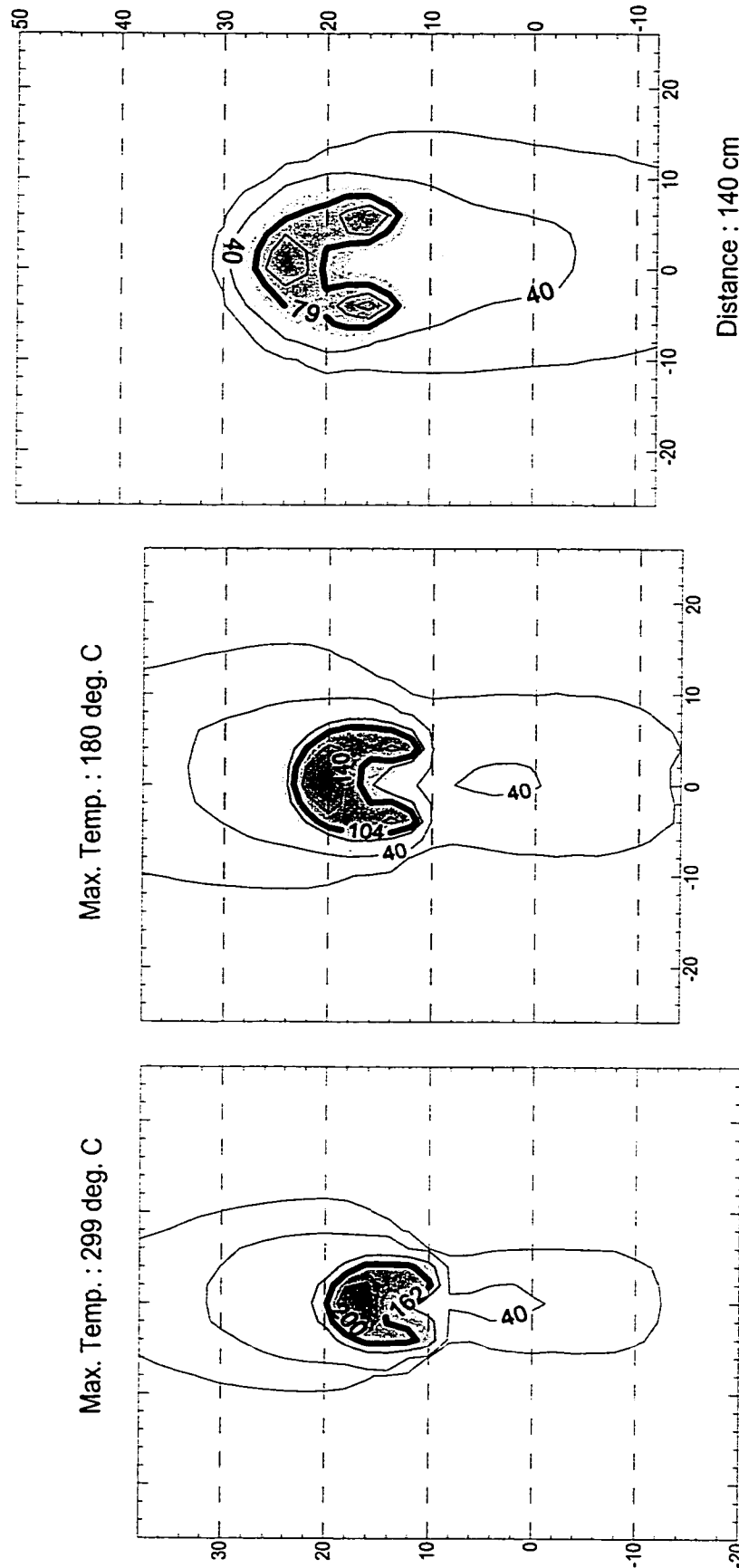
Max. Temp. : 180 deg. C
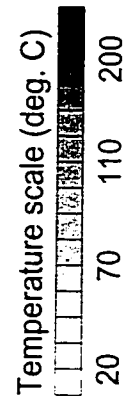
Max. Temp. : 79 deg. C

Distance : 80 cm

Distance : 110 cm

Distance : 140 cm

Temperature scale (deg. C)

20   60   162   300

d_s = 1.67 cm; V_j = 1 m/s; U_∞ = 3 m/s

Notes:
- X and Y axis in cm relatively to the stack exit.
- Thick line shows 50% temperature contour.

data files : S07W40E10P080.grd, S07W40E10P110.grd, S07W40E10P140.grd

Max. Temp. : 317 deg. C   Max. Temp. : 181 deg. C   Max. Temp. : 139 deg. C
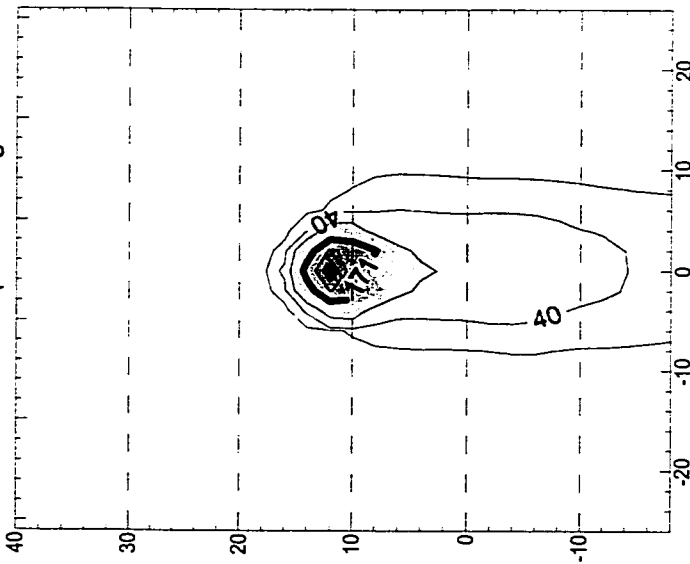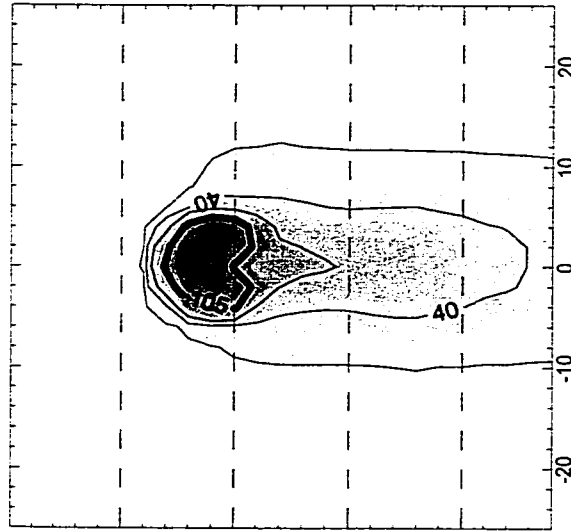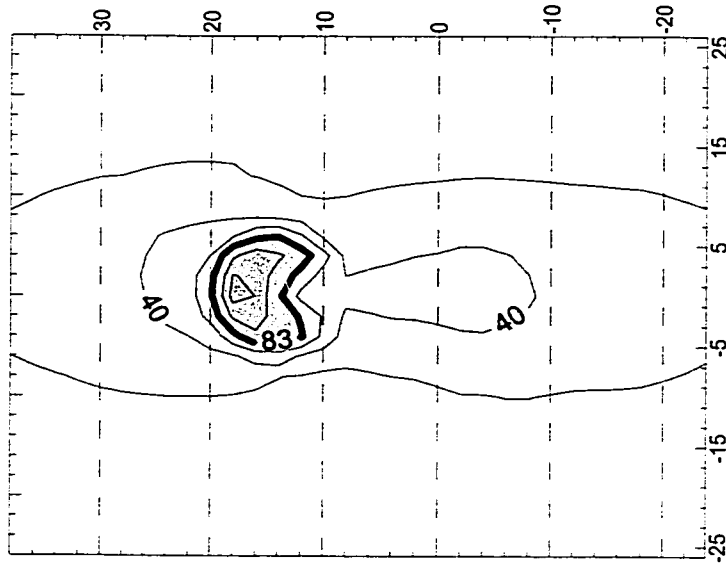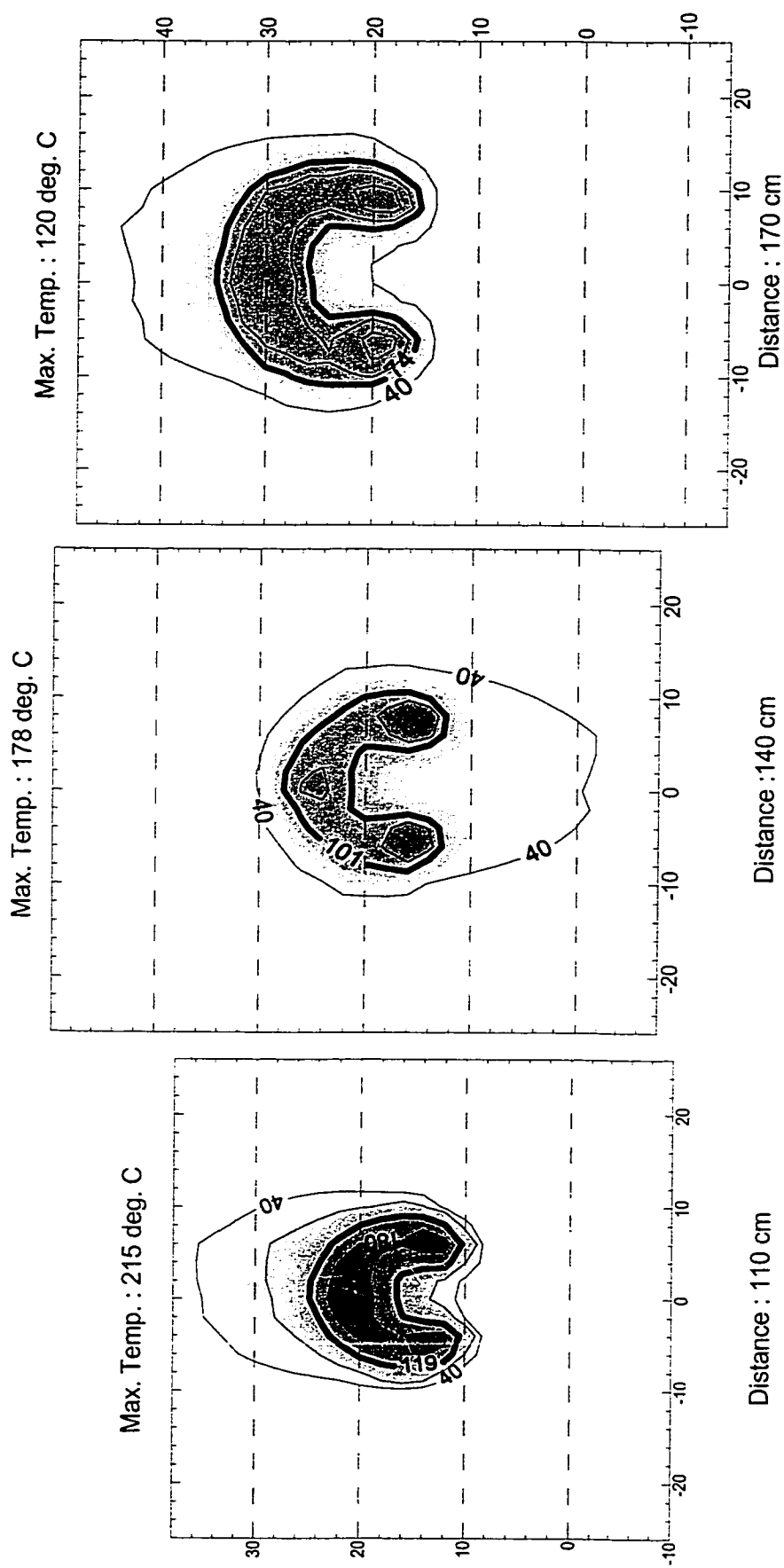
Distance : 80 cm   Distance : 110 cm   Distance : 140 cm

Temperature scale (deg. C)

20   50   140   280

$d_s = 1.67$ cm; $V_j = 1$ m/s; $U_\infty = 4$ m/s

Notes:
- X and Y axis in cm relatively to the stack exit.
- Thick line shows 50% temperature contour.

130
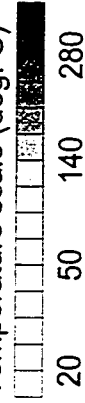
data files : S07W60E10P080.grd, S07W60E10P110.grd, S07W60E10P140.grd

Max. Temp. : 175 deg. C
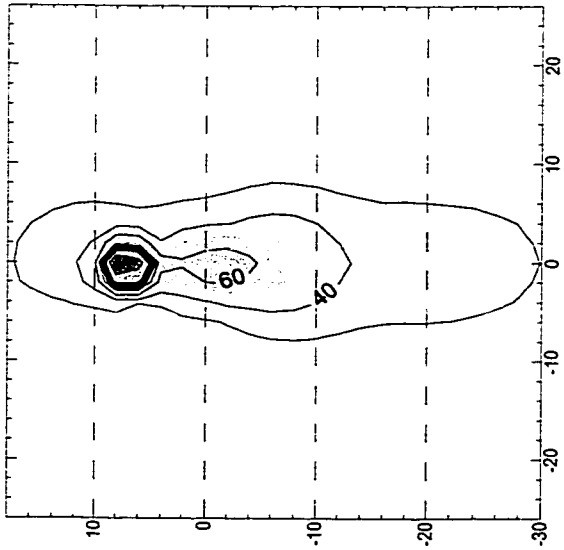
Distance : 80 cm

Max. Temp. : 109 deg. C
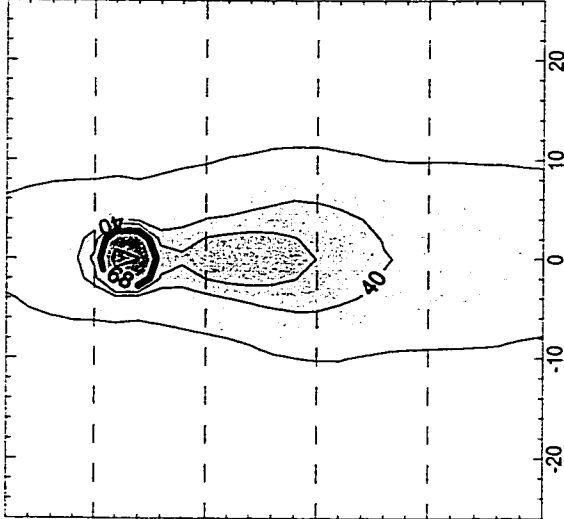
Distance : 110 cm

Max. Temp. : 87 deg. C
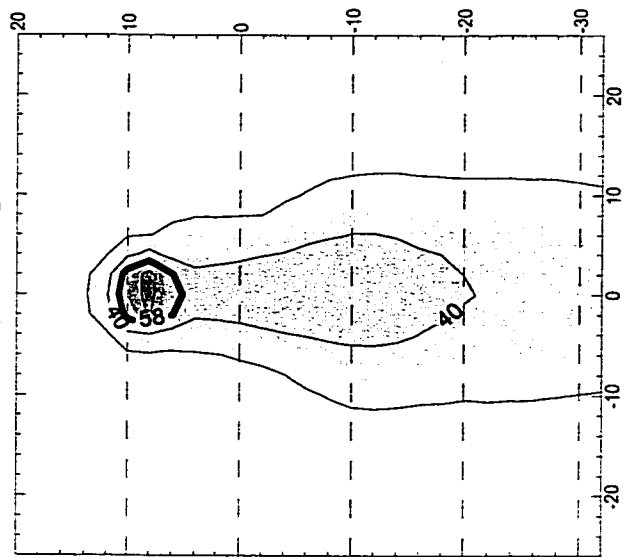
Distance : 140 cm
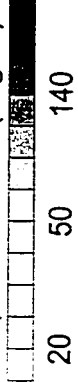
Temperature scale (deg. C)

d_s = 1.67 cm; V_j = 1 m/s; U_∞ = 6 m/s

Notes:
- X and Y axis in cm relatively to the stack exit.
- Thick line shows 50% temperature contour.

131

data files : S07W80E10P050.grd, S07W80E10P080.grd, S07W80E10P110.grd

Max. Temp. : 72 deg. C
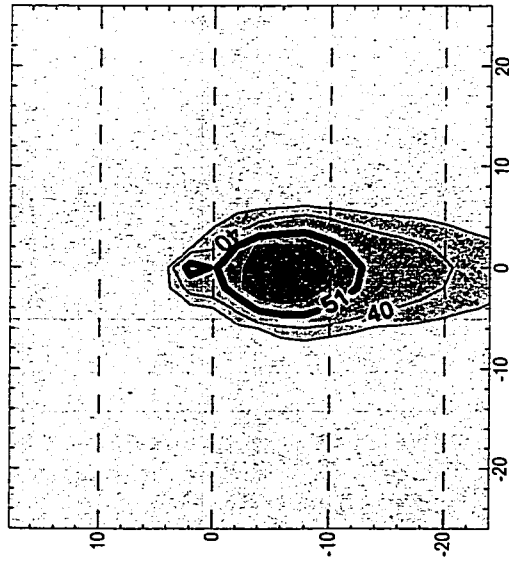
Distance : 50 cm

Max. Temp. :51 deg. C
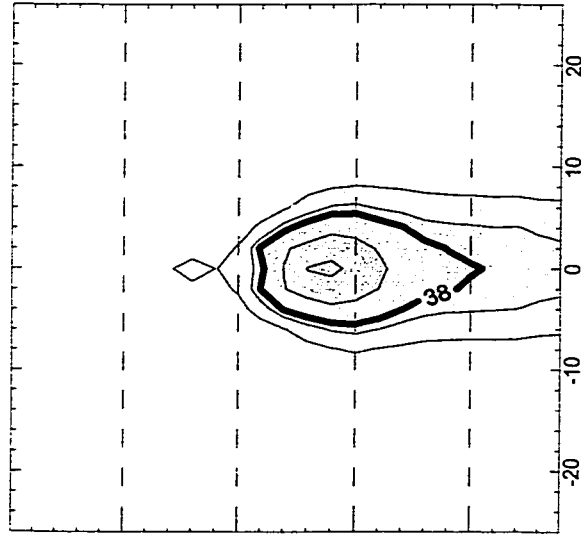
Distance :80 cm

Max. Temp. :47 deg. C
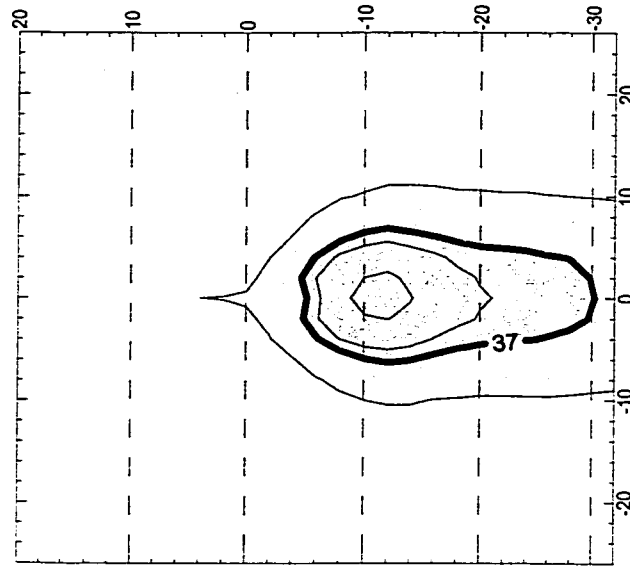
Distance : 110 cm

Temperature scale (deg. C)

20   60

d_s=1.67 cm; V_j = 1 m/s; U_∞ = 8 m/s

Notes:
- X and Y axis in cm relatively to the stack exit.
- Thick line shows 50% temperature contour.

132

data files : S07W15E20P110.grd, S07W15E20P140.grd, S07W15E20P170.grd
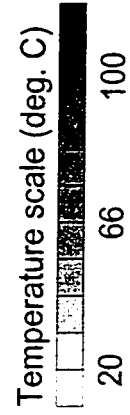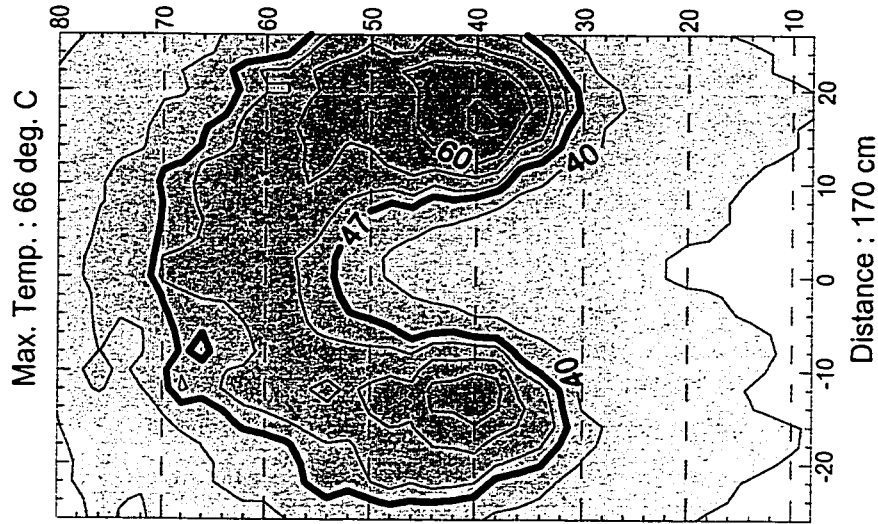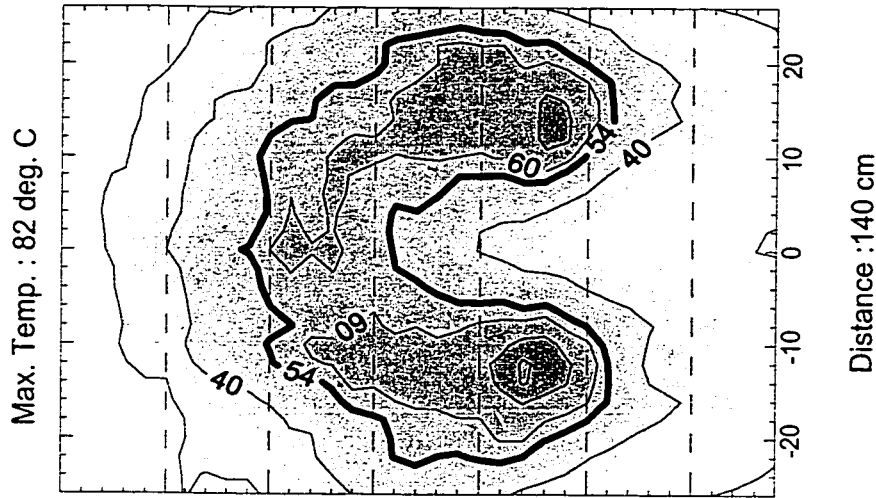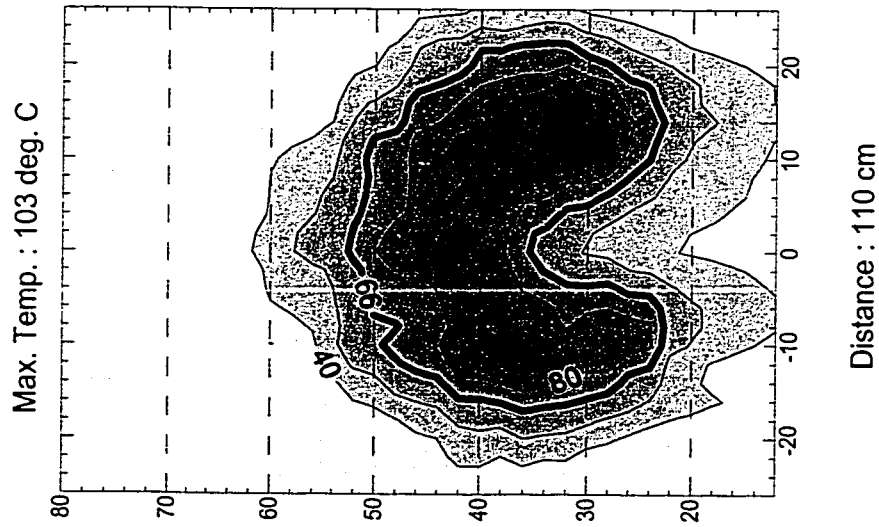
Max. Temp. : 103 deg. C

Max. Temp. : 82 deg. C

Max. Temp. : 66 deg. C

Distance : 110 cm

Distance :140 cm
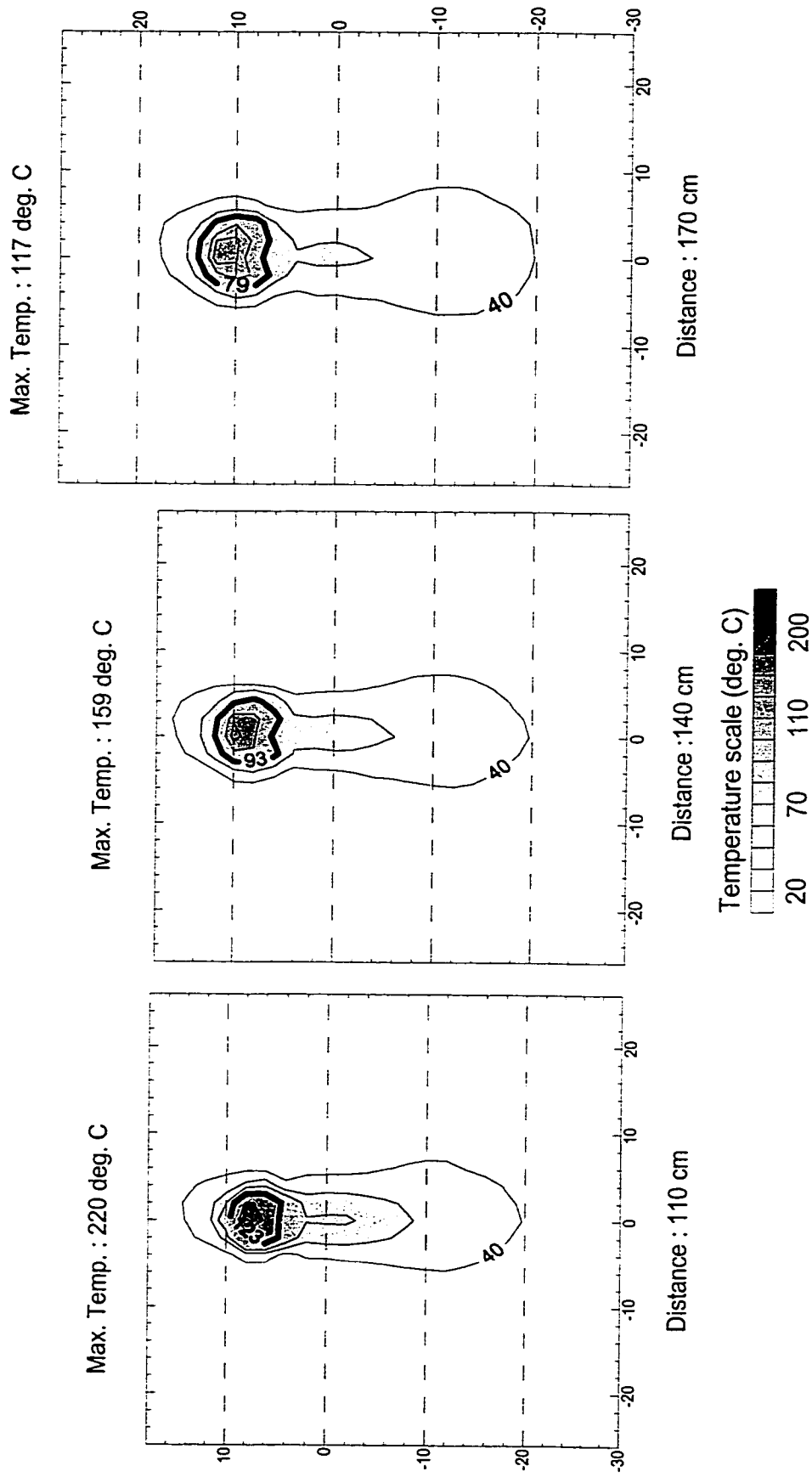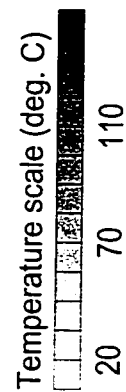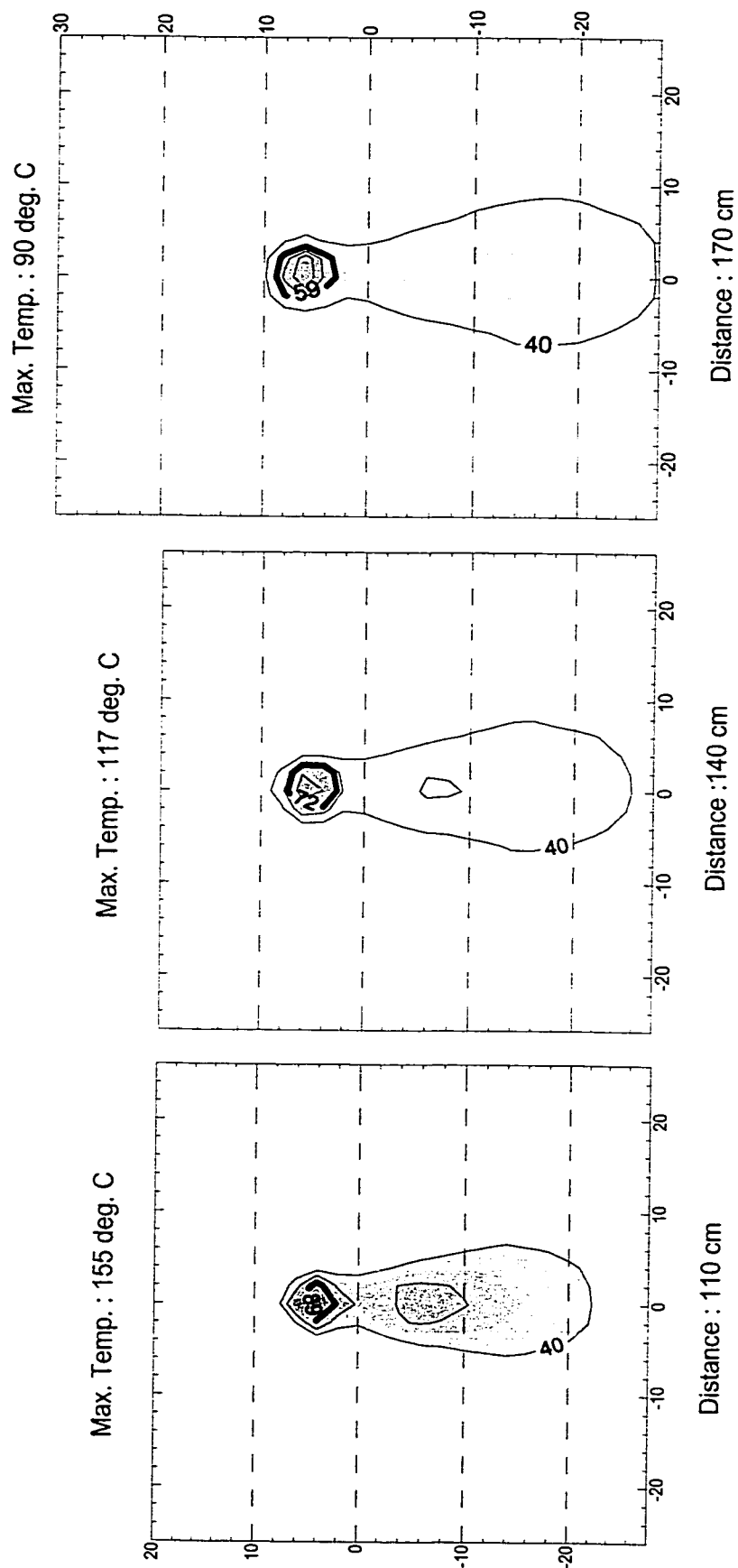
Distance : 170 cm

Temperature scale (deg. C)

20   66   100

Notes:
- X and Y axis in cm relatively to the stack exit.
- Thick line shows 50% temperature contour.

d_s = 1.67 cm; V_j = 2 m/s; U_∞ = 1.5 m/s

133

data files : S07W20E20P110.grd, S07W20E20P140.grd, S07W20E20P170.grd

Max. Temp. : 76 deg. C
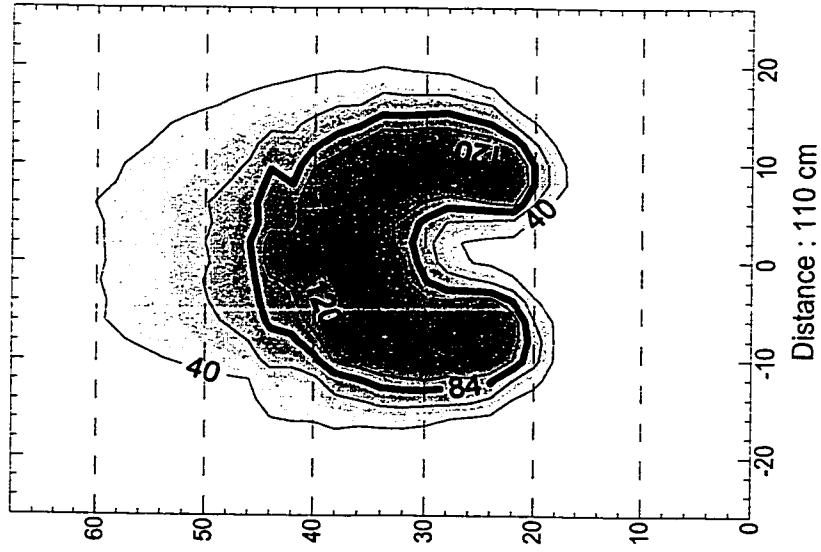
Max. Temp. : 94 deg. C
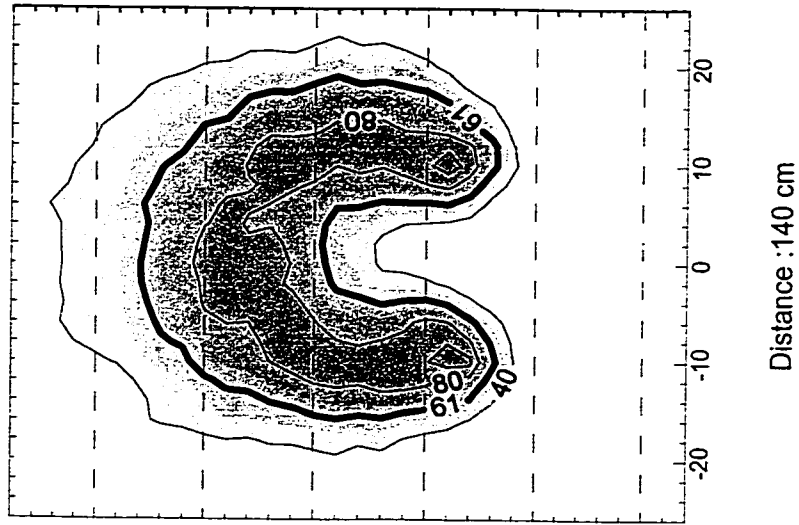
Max. Temp. : 140 deg. C
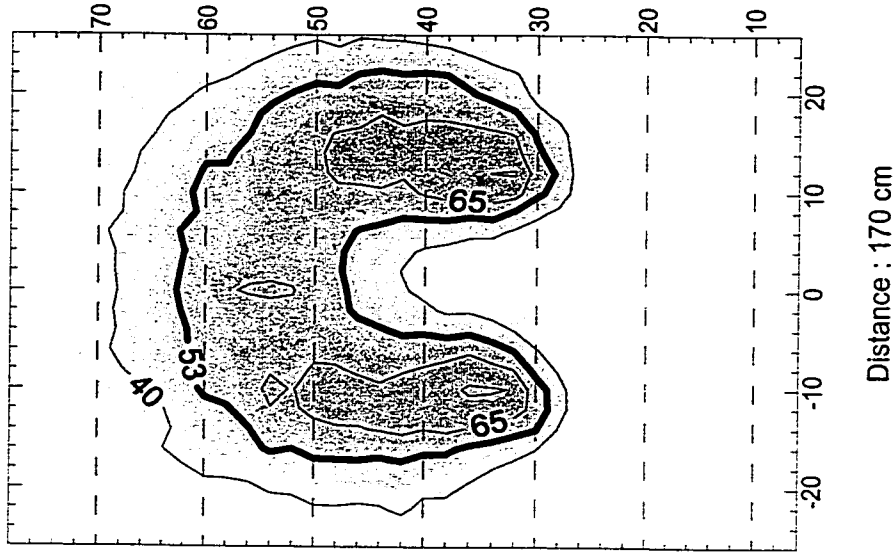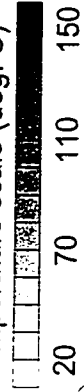
Distance : 170 cm

Distance :140 cm

Distance : 110 cm

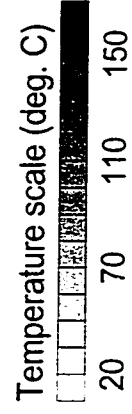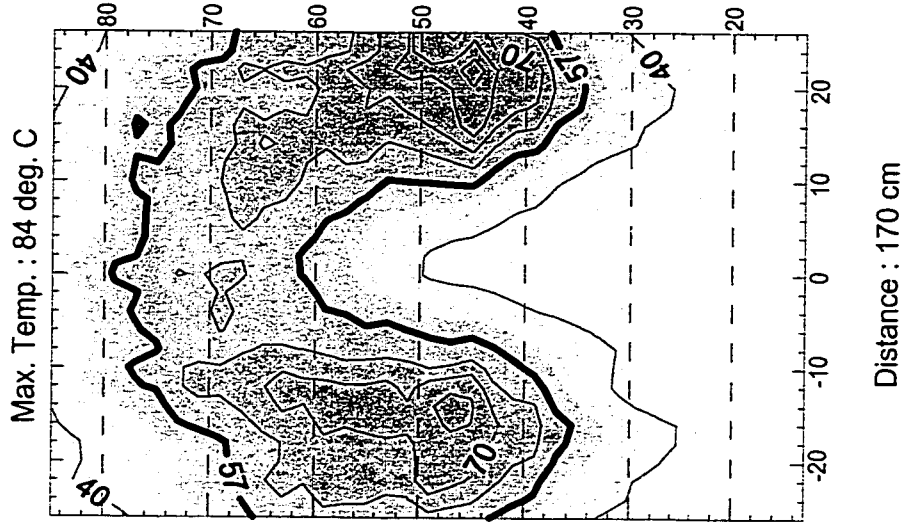Temperature scale (deg. C)
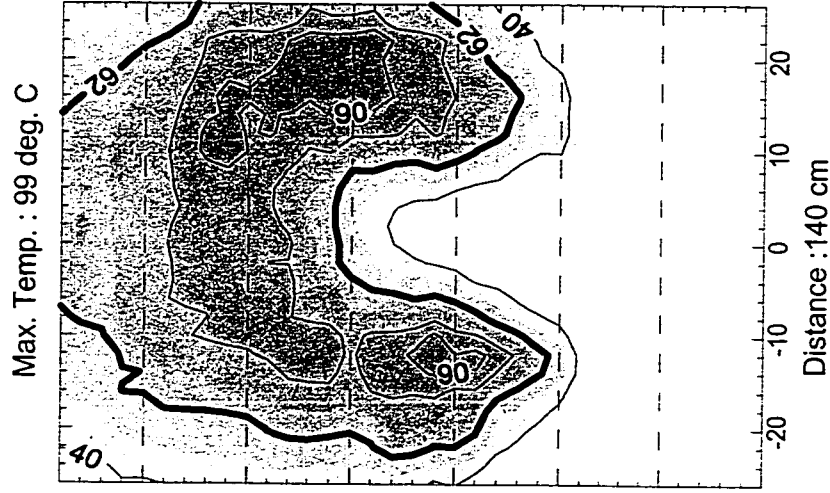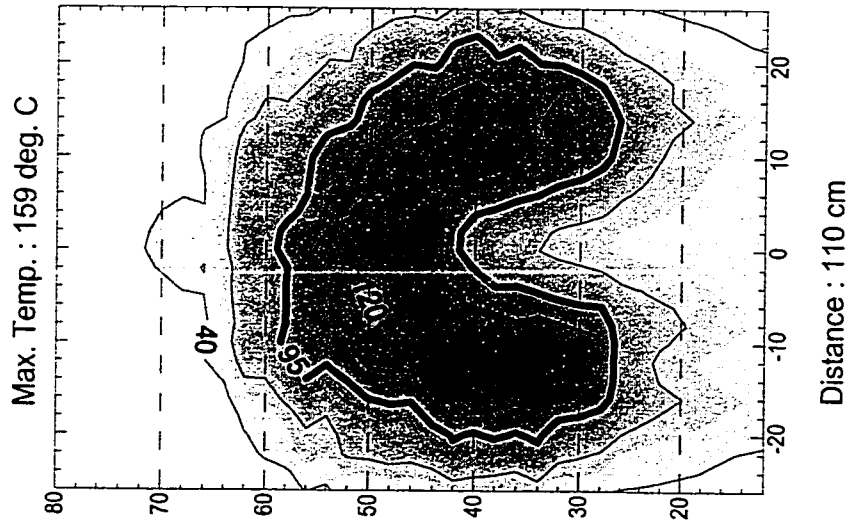
20   70   110   150

Notes:
- X and Y axis in cm relatively to the stack exit.
- Thick line shows 50% temperature contour.

d_s = 1.67 cm; V_j = 2 m/s; U_∞ = 2 m/s

134

Max. Temp. : 138 deg. C

Distance : 170 cm

Max. Temp. : 176 deg. C

Distance : 140 cm

Max. Temp. : 253 deg. C

Distance : 110 cm

data files : S07W30E20P110.grd, S07W30E20P140.grd, S07W30E20P170.grd
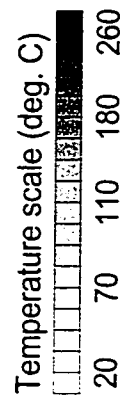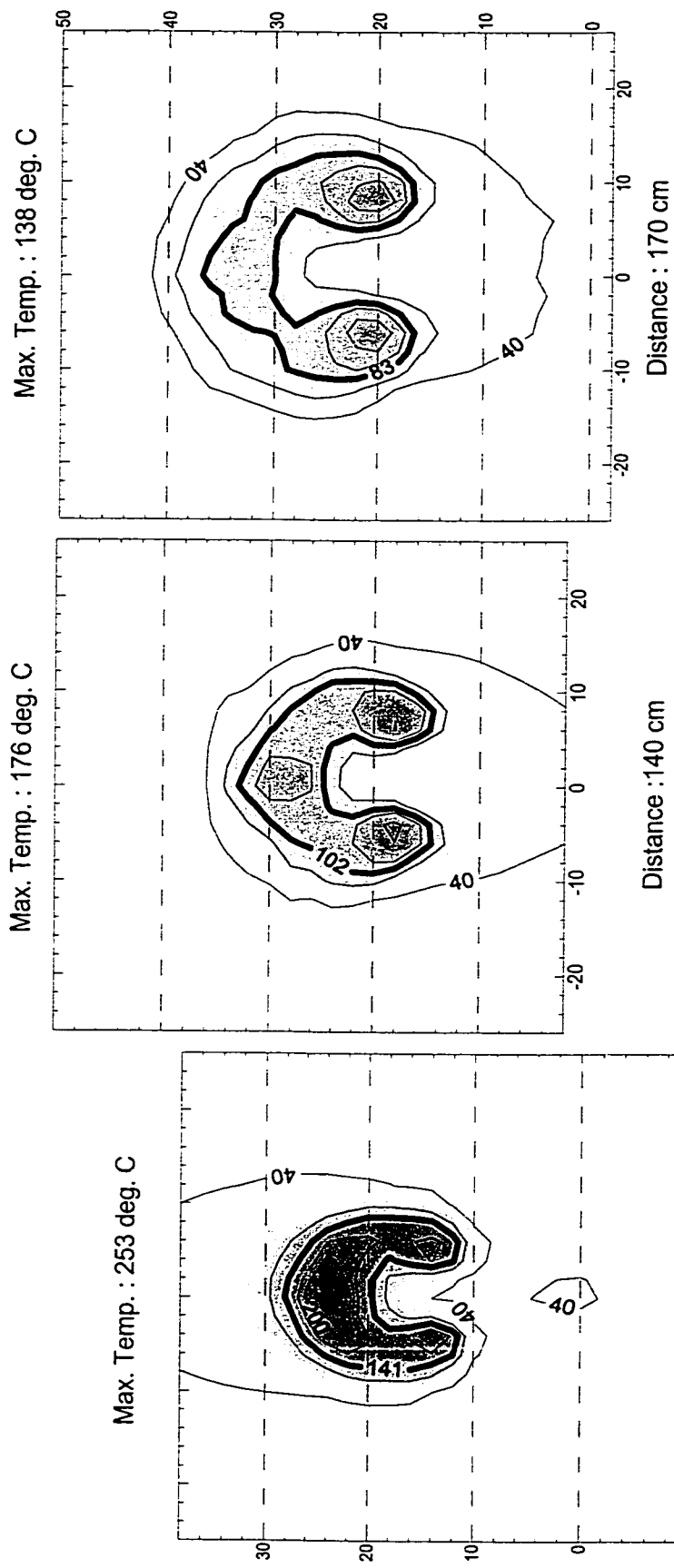
Temperature scale (deg. C)

20   70   110   180   260

d_s = 1.67 cm; V_j = 2 m/s; U_∞ = 3 m/s

Notes:
- X and Y axis in cm relatively to the stack exit.
- Thick line shows 50% temperature contour.

135

Max. Temp. : 130 deg. C

Distance : 170 cm

Max. Temp. : 183 deg. C

Distance :140 cm

Max. Temp. : 311 deg. C

Distance : 110 cm

data files : S07W40E20P110.grd, S07W40E20P140.grd, S07W40E20P170.grd
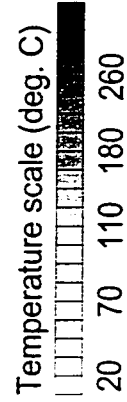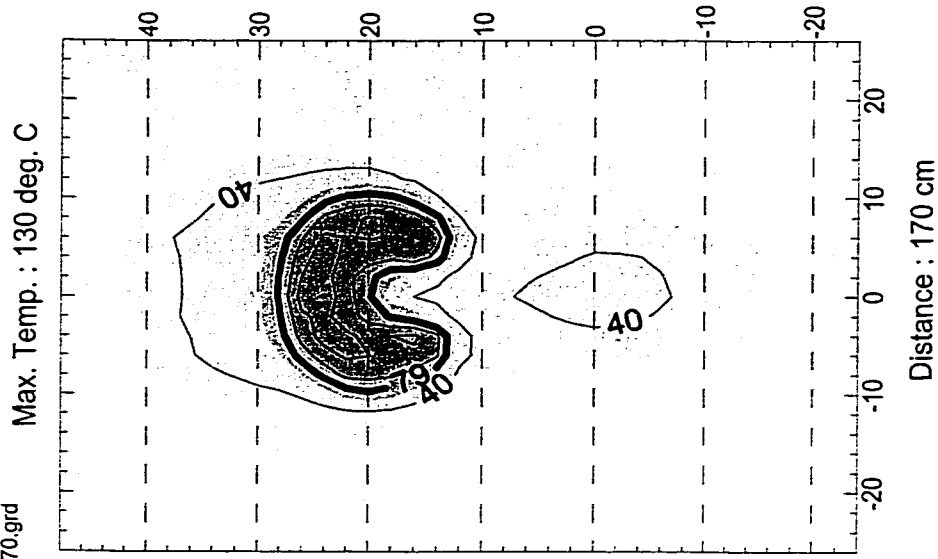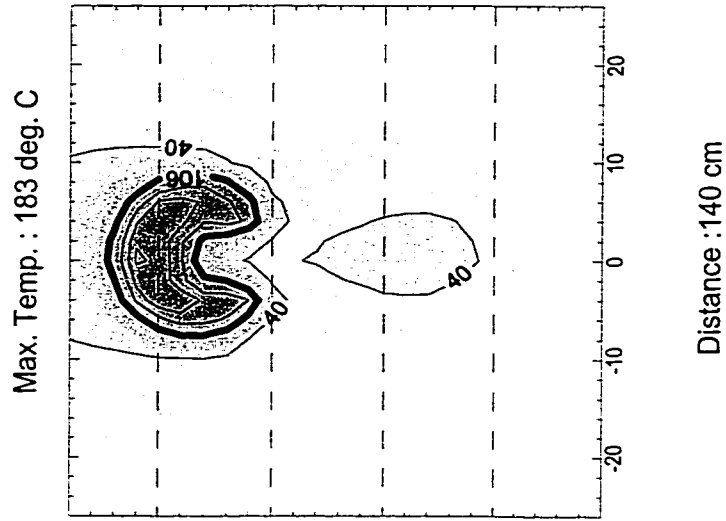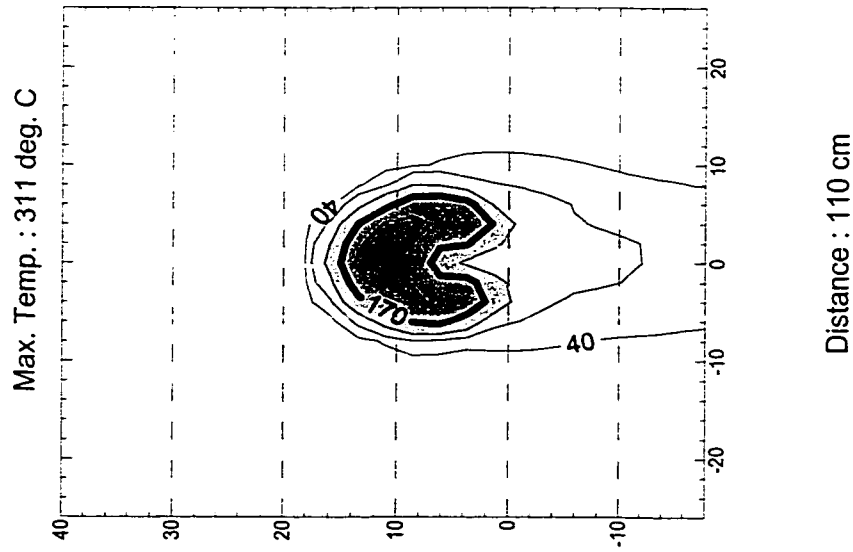
Temperature scale (deg. C)

20   70   110   180   260

$d_s = 1.67$ cm; $V_j = 2$ m/s; $U_\infty = 4$ m/s

Notes:
- X and Y axis in cm relatively to the stack exit.
- Thick line shows 50% temperature contour.

136

data files : S07W60E20P110.grd, S07W60E20P140.grd, S07W60E20P170.grd

Max. Temp. : 309 deg. C
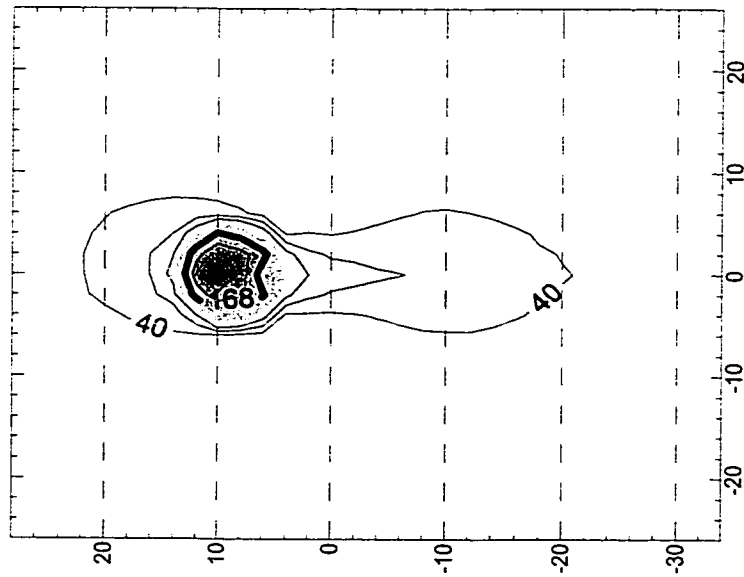
Distance : 110 cm

Max. Temp. : 205 deg. C
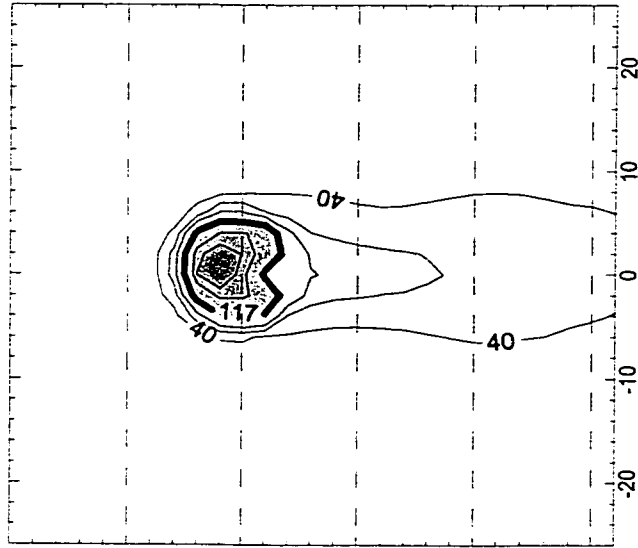
Distance :140 cm

Max. Temp. : 130 deg. C
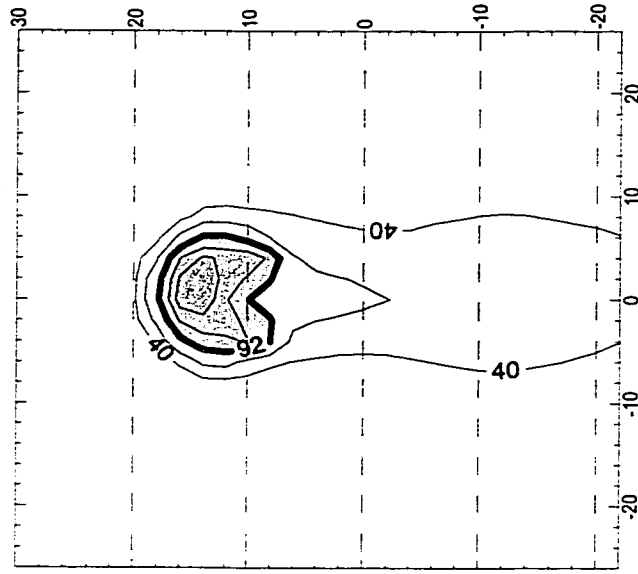
Distance : 170 cm
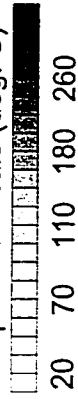
Temperature scale (deg. C)

20   70   110   180   260

d_s = 1.67 cm; V_j = 2 m/s; U_∞ = 6 m/s

Notes:
- X and Y axis in cm relatively to the stack exit.
- Thick line shows 50% temperature contour.

137

data files : S07W80E20P080.grd, S07W80E20P110.grd, S07W80E20P140.grd

Max. Temp. : 313 deg. C
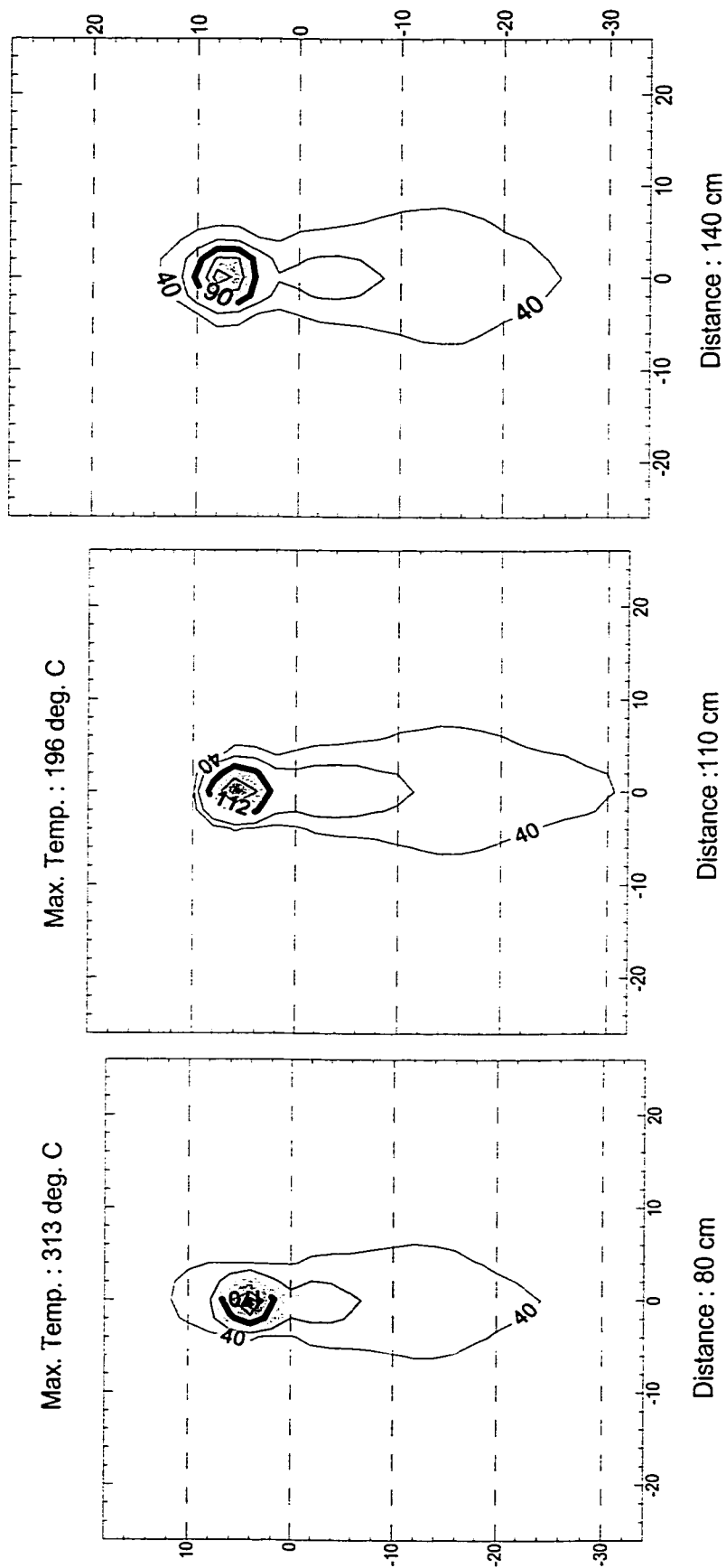
Distance : 80 cm

Max. Temp. : 196 deg. C

Distance :110 cm

Max. Temp. : 151 deg. C

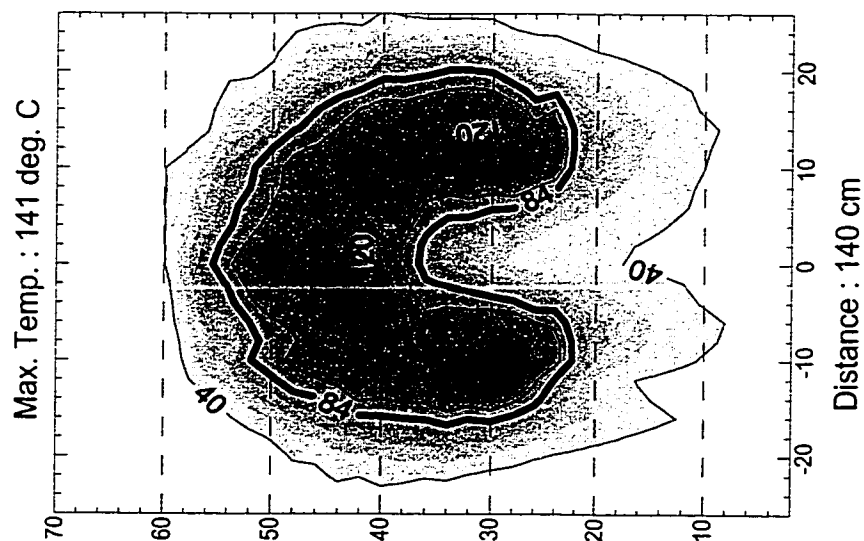Distance : 140 cm

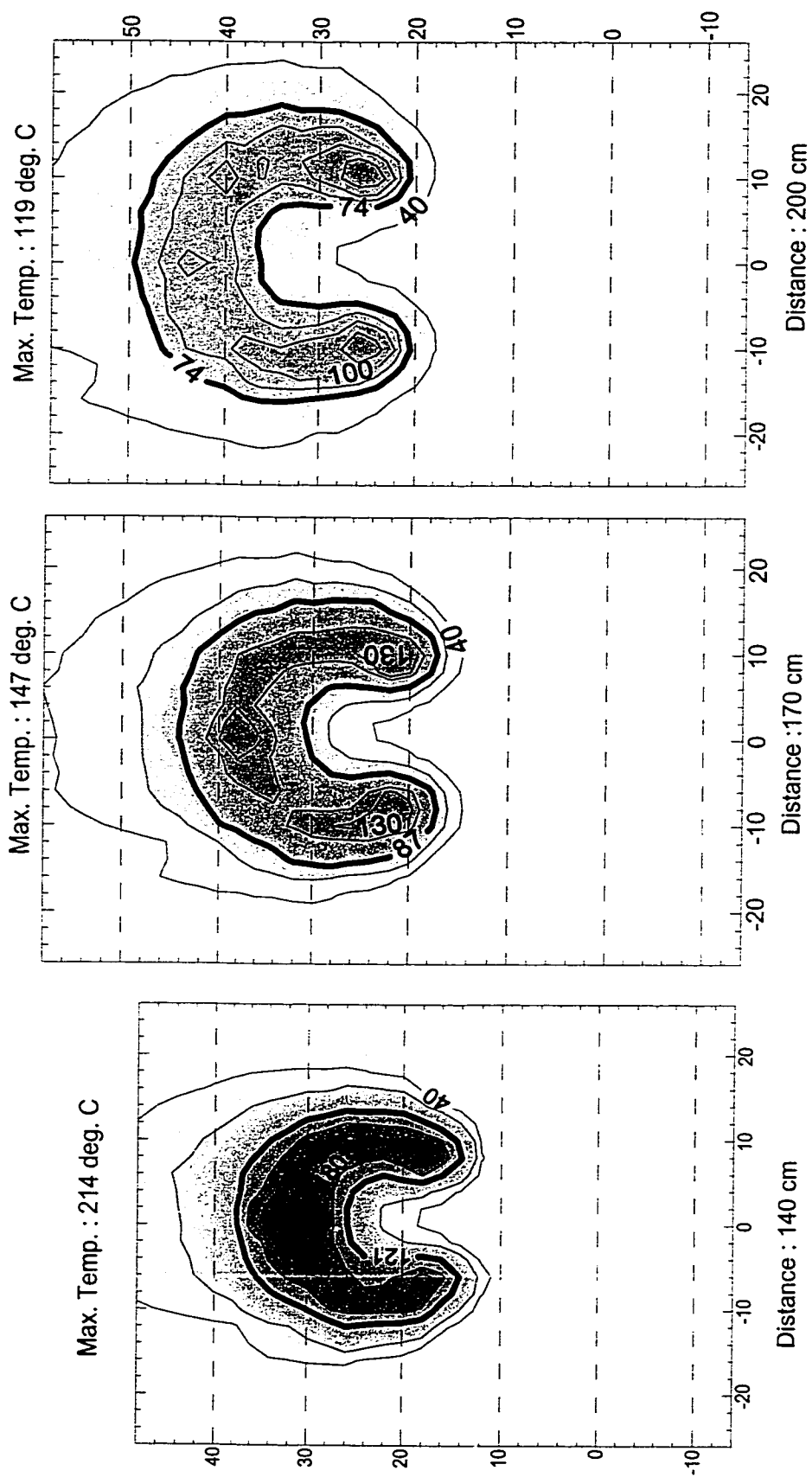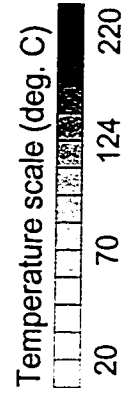Temperature scale (deg. C)

20   70   110   180   260

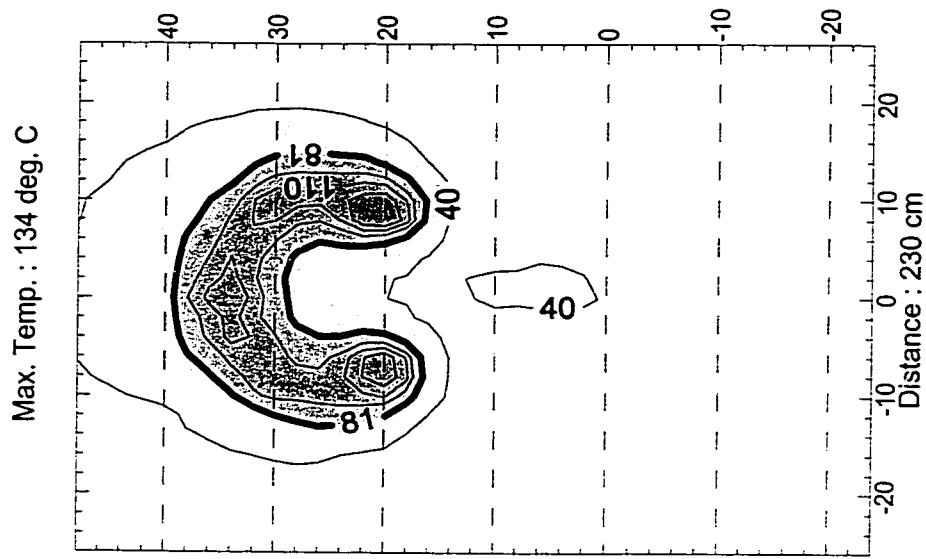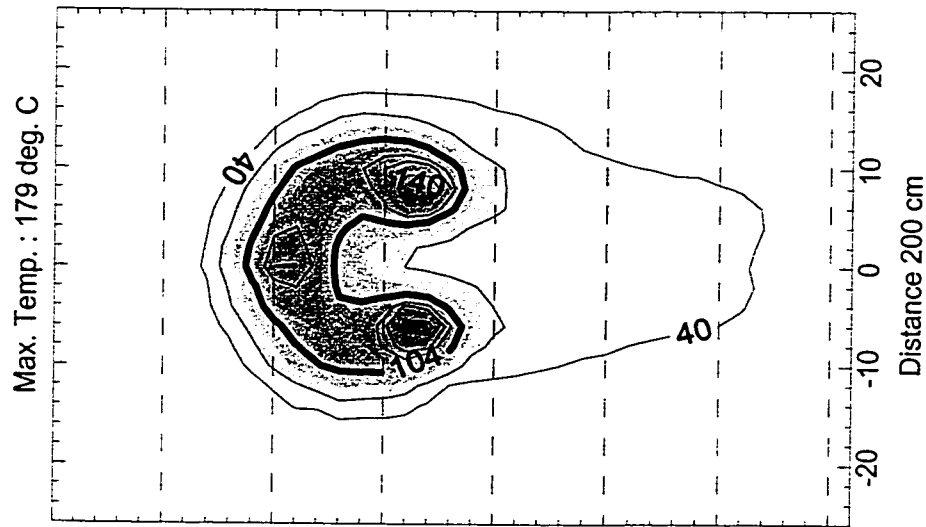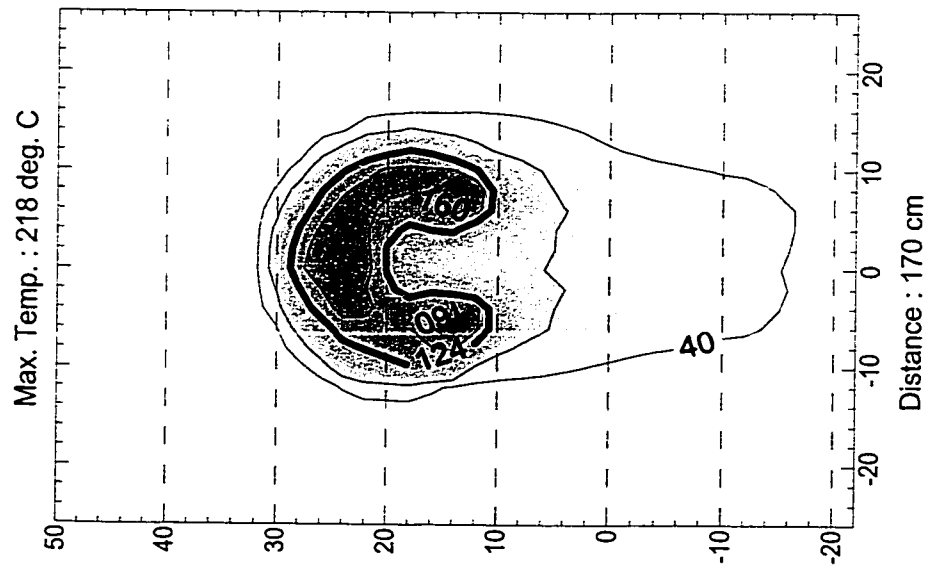Notes:
- X and Y axis in cm relatively to the stack exit.
- Thick line shows 50% temperature contour.

d_s = 1.67 cm; V_j = 2 m/s; U_∞ = 8 m/s

138

data files : S10W15E05P050.grd, S10W15E05P080.grd, S10W15E05P110.grd
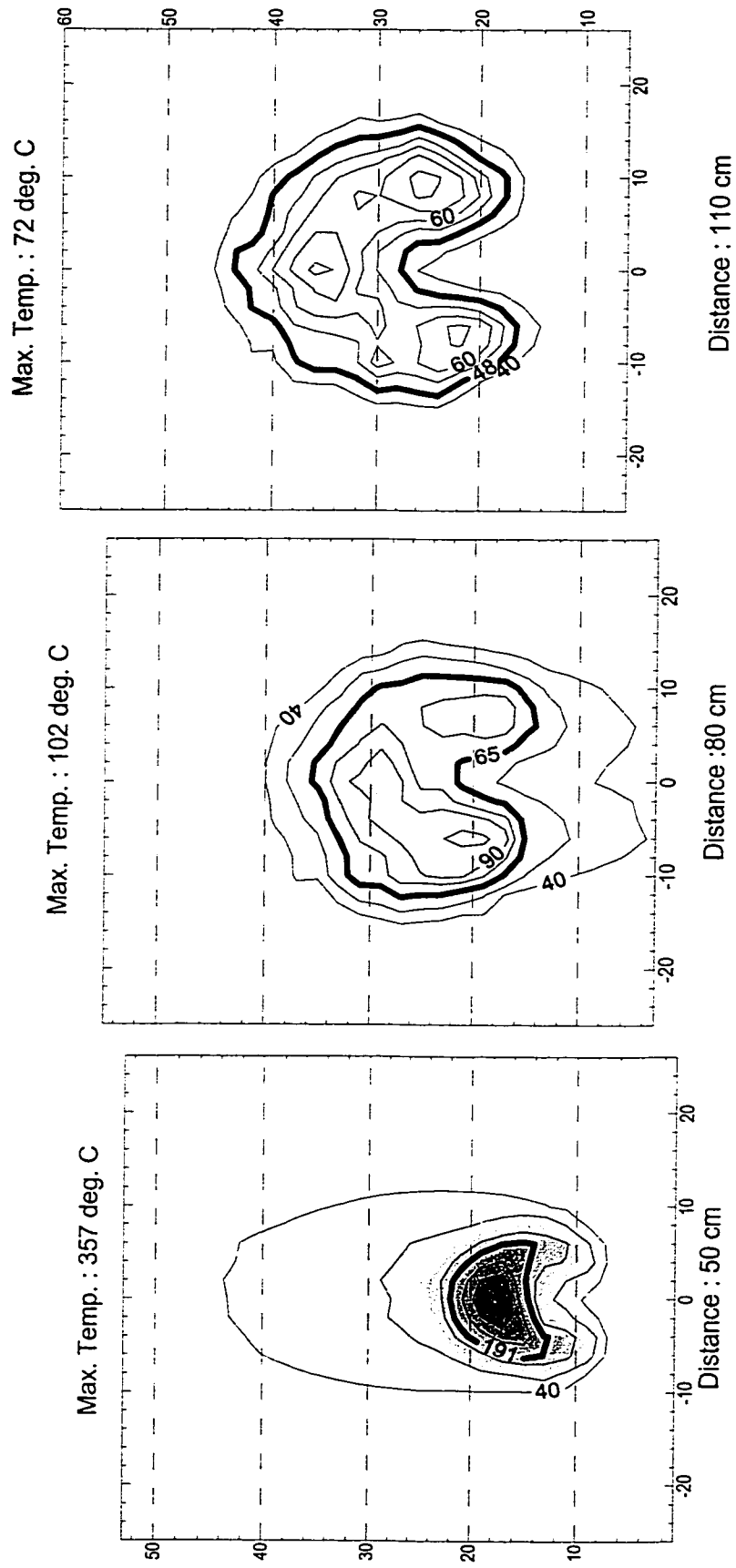
Max. Temp. : 357 deg. C

Max. Temp. : 102 deg. C

Max. Temp. : 72 deg. C

Distance : 50 cm

Distance :80 cm

Distance : 110 cm

Temperature scale (deg. C)

20   70   110   191   250

d_s = 2.21 cm; V_j = 0.5 m/s; U_∞ = 1.5 m/s

Notes:
- X and Y axis in cm relatively to the stack exit.
- Thick line shows 50% temperature contour.

139

Max. Temp. : 73 deg. C

Distance : 140 cm

Max. Temp. : 110 deg. C

Distance :110 cm

Max. Temp. : 183 deg. C

Distance : 80 cm

data files : S10W20E05P080.grd, S10W20E05P110.grd, S10W20E05P140.grd
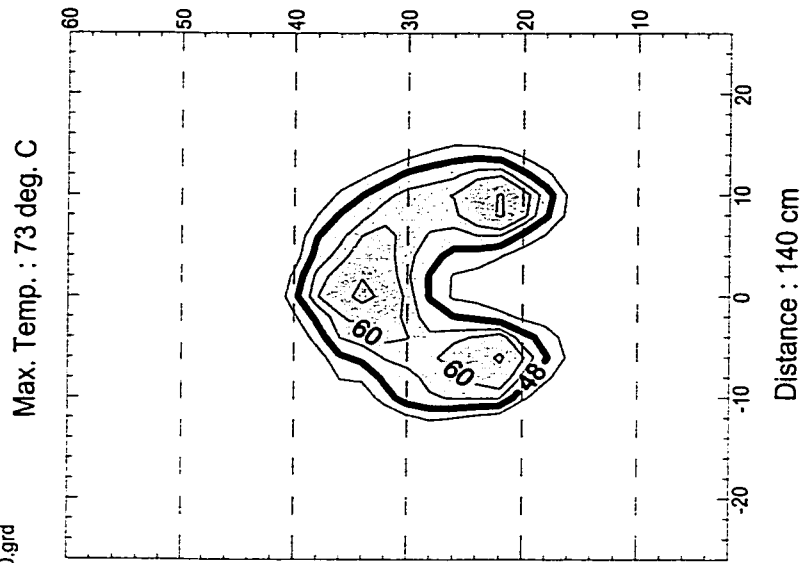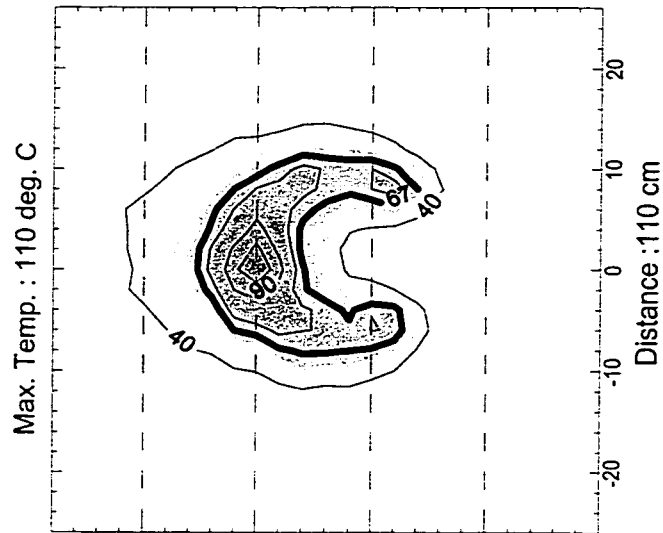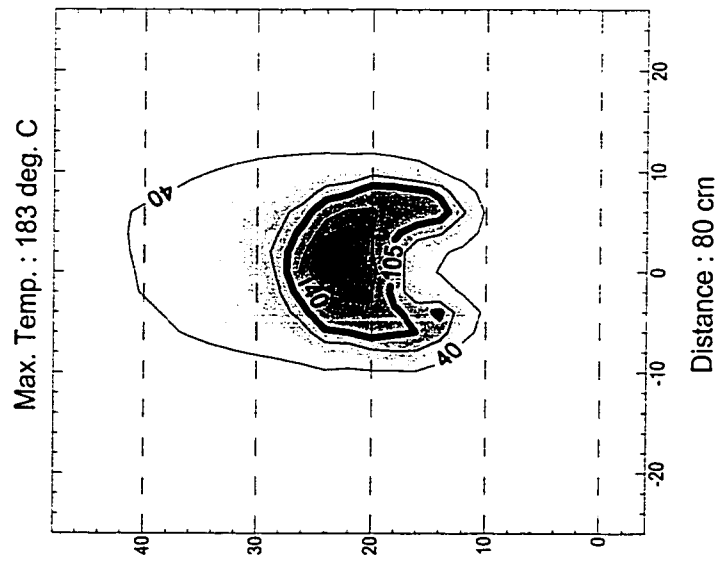
Temperature scale (deg. C)
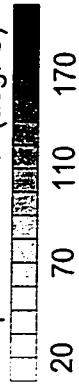
20   70   110   170

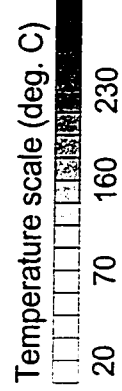d_s= 2.21 cm; V_j =0.5 m/s; U_∞ = 2 m/s

Notes:
- X and Y axis in cm relatively to the stack exit.
- Thick line shows 50% temperature contour.

140

data files : S10W30E05P110.grd, S10W30E05P140.grd, S10W30E05P170.grd
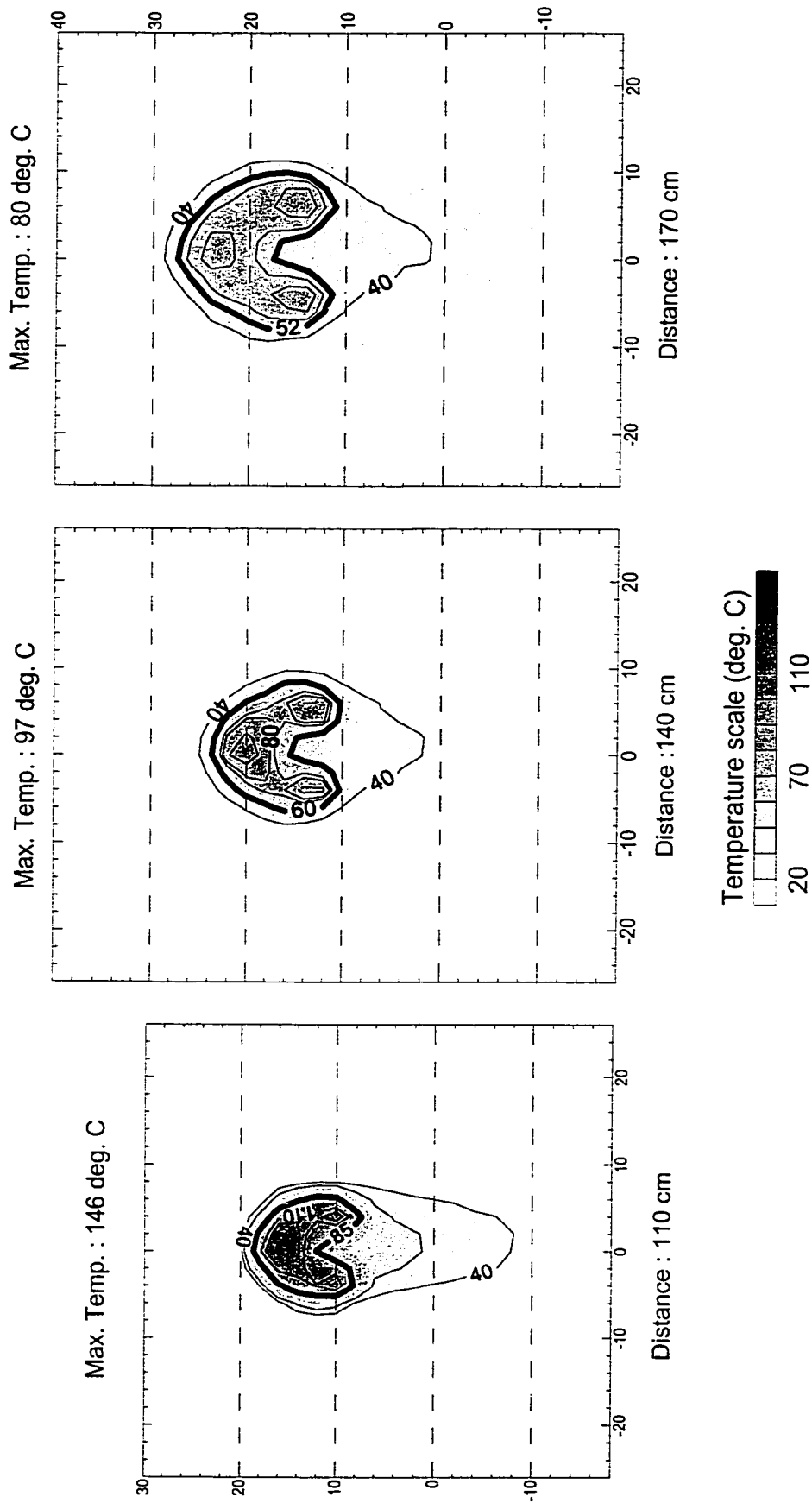
Max. Temp. : 80 deg. C

Distance : 170 cm

Max. Temp. : 97 deg. C

Distance :140 cm

Max. Temp. : 146 deg. C

Distance : 110 cm

Temperature scale (deg. C)

d_s = 2.21 cm; V_j =0.5 m/s; U_∞ = 3 m/s

Notes:
- X and Y axis in cm relatively to the stack exit.
- Thick line shows 50% temperature contour.

141

data files : S10W40E05P110.grd, S10W40E05P140.grd, S10W40E05P170.grd

Max. Temp. : 156 deg. C

Distance : 110 cm

Max. Temp. : 110 deg. C

Distance :140 cm

Max. Temp. : 90 deg. C

Distance : 170 cm

Temperature scale (deg. C)

20   70   110

d_s = 2.21 cm; V_j = 0.5 m/s; U_∞ = 4 m/s

Notes:
- X and Y axis in cm relatively to the stack exit.
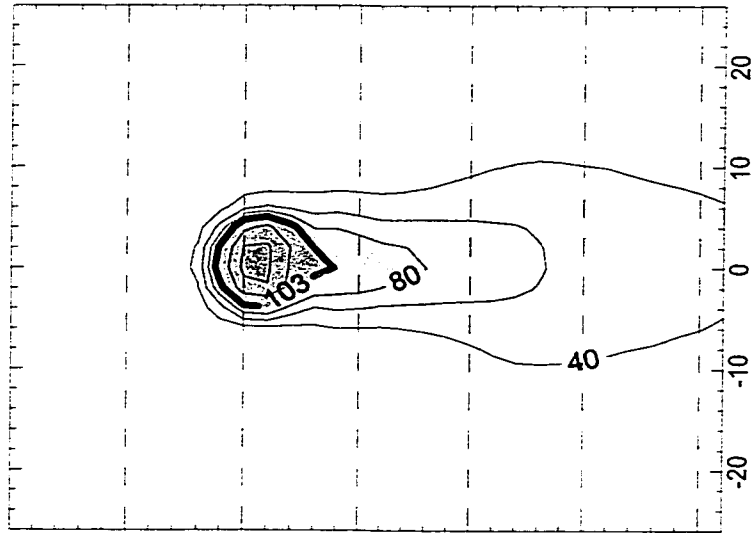- Thick line shows 50% temperature contour.

142

data files : S10W60E05P080.grd, S10W60E05P110.grd, S10W60E05P140.grd

Max. Temp. : 166 deg. C

Distance : 80 cm

Max. Temp. : 92 deg. C

Distance :110 cm

Max. Temp. : 67 deg. C

Distance : 140 cm

Temperature scale (deg. C)
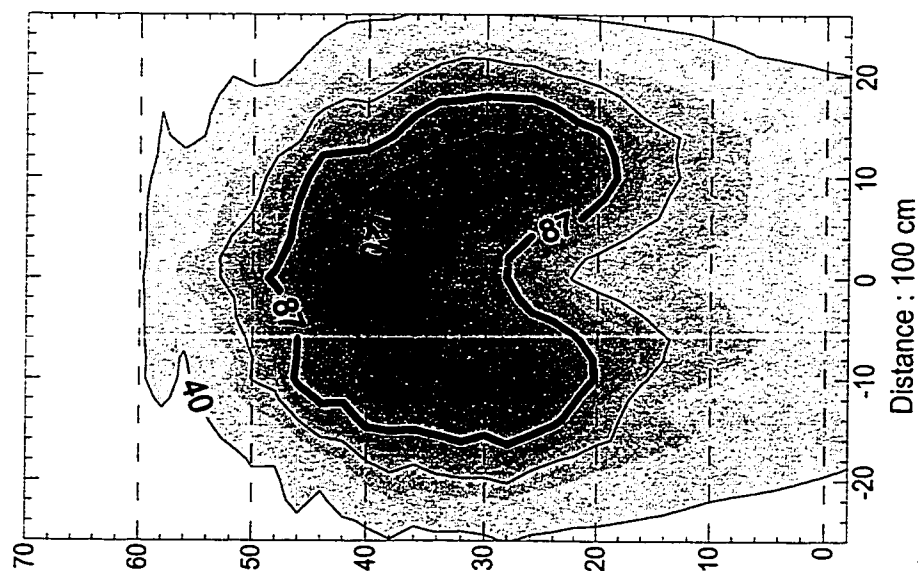
20   70   110   160

d_s= 2.21 cm; V_j =0.5 m/s; U_∞ = 6 m/s

Notes:
- X and Y axis in cm relatively to the stack exit.
- Thick line shows 50% temperature contour.

143

data files : S10W80E05P050.grd, S10W60E05P080.grd, S10W60E05P110.grd

Max. Temp. : 72 deg. C

Distance : 50 cm

Max. Temp. : 46 deg. C

Distance : 80 cm

Temperature scale (deg. C)

20   45   80

Max. Temp. : 40 deg. C

Distance : 110 cm

d_s = 2.21 cm; V_j = 0.5 m/s; U_∞ = 8 m/s

Notes:
- X and Y axis in cm relatively to the stack exit.
- Thick line shows 50% temperature contour.

data files : S10W15E10P080.grd, S10W15E10P110.grd, S10W15E10P140.grd
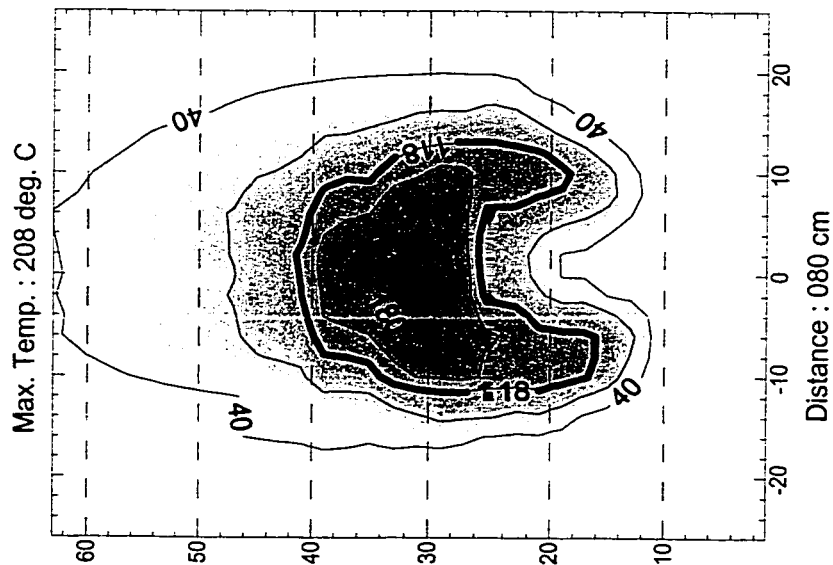
Max. Temp. : 67 deg. C

Max. Temp. : 103 deg. C
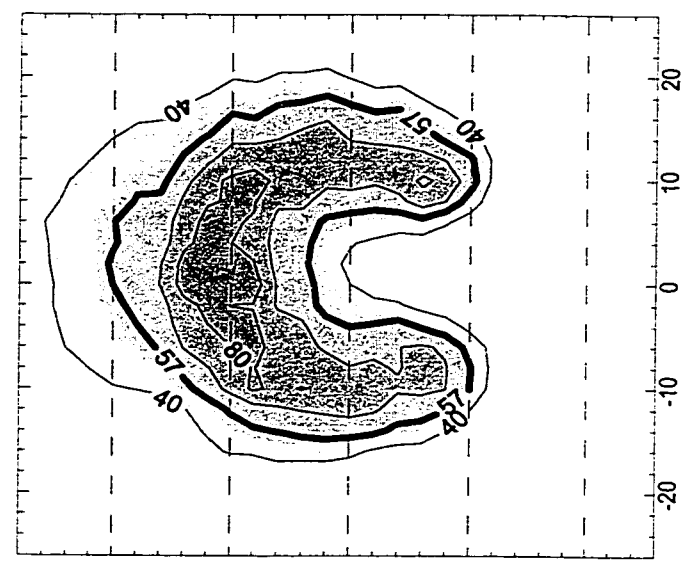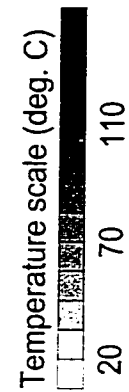
Max. Temp. : 208 deg. C

Distance : 140 cm

Distance :110 cm

Distance : 080 cm

Temperature scale (deg. C)

20   70   110   160

d_s = 2.21 cm; V_j = 1 m/s; U_∞ = 1.5 m/s

Notes:
- X and Y axis in cm relatively to the stack exit.
- Thick line shows 50% temperature contour.

145

Max. Temp. : 67 deg. C

Distance : 170 cm

Max. Temp. : 89 deg. C

Distance :140 cm

Max. Temp. : 148 deg. C

Distance : 110 cm

data files : S10W20E10P110.grd, S10W20E10P140.grd, S10W20E10P170.grd

Temperature scale (deg. C)

20   70   110

d_s= 2.21 cm; V_j = 1 m/s; U_∞ = 2 m/s

Notes:
- X and Y axis in cm relatively to the stack exit.
- Thick line shows 50% temperature contour.

146

data files : S10W30E10P110.grd, S10W30E10P140.grd, S10W30E10P170.grd

Max. Temp. : 120 deg. C

Distance : 170 cm

Max. Temp. : 178 deg. C

Distance : 140 cm

Max. Temp. : 215 deg. C

Distance : 110 cm

Temperature scale (deg. C)

20   70   110   200

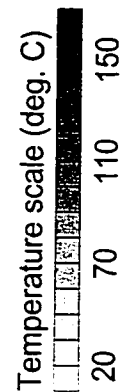d_s= 2.21 cm; V_j = 1 m/s; U_∞ = 3 m/s

Notes:
- X and Y axis in cm relatively to the stack exit.
- Thick line shows 50% temperature contour.

147

data files : S10W40E10P110.grd, S10W40E10P140.grd, S10W40E10P170.grd

Max. Temp. : 129 deg. C
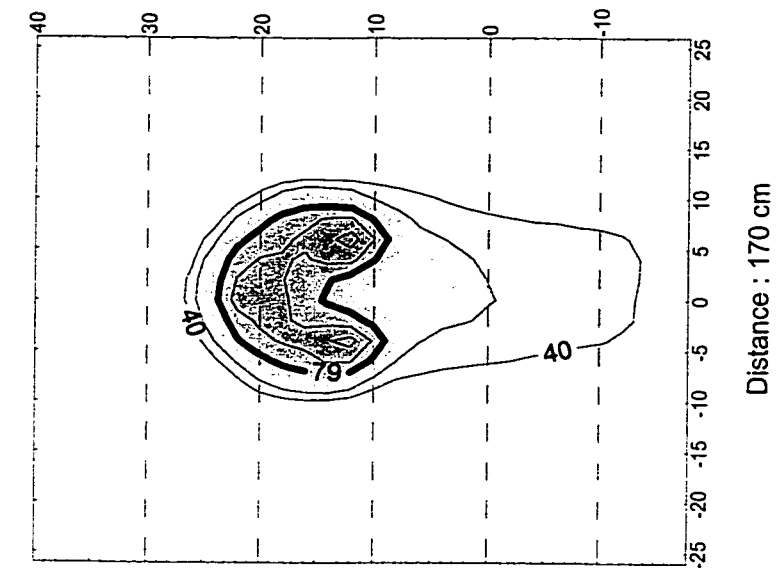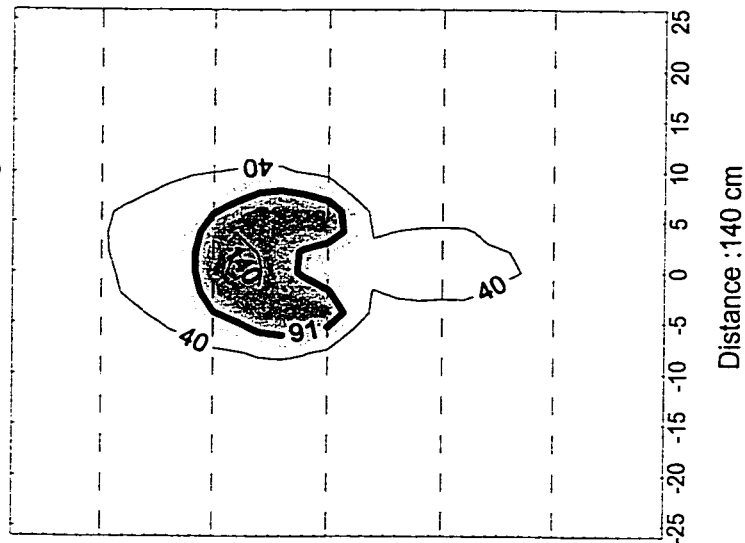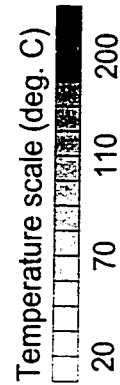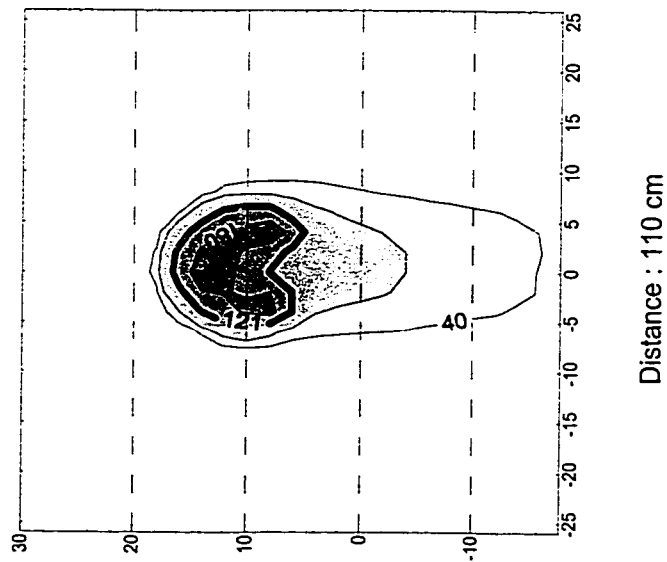
Distance : 170 cm

Max. Temp. : 157 deg. C

Distance :140 cm

Max. Temp. : 218 deg. C

Distance : 110 cm

Temperature scale (deg. C)

20   70   110   200

d_s= 2.21 cm; V_j = 1 m/s; U_∞ = 4 m/s

Notes:
- X and Y axis in cm relatively to the stack exit.
- Thick line shows 50% temperature contour.

148

data files : S10W60E10P110.grd, S10W60E10P140.grd, S10W60E10P170.grd

Max. Temp. : 220 deg. C

Distance : 110 cm

Max. Temp. : 159 deg. C

Distance :140 cm

Max. Temp. : 117 deg. C
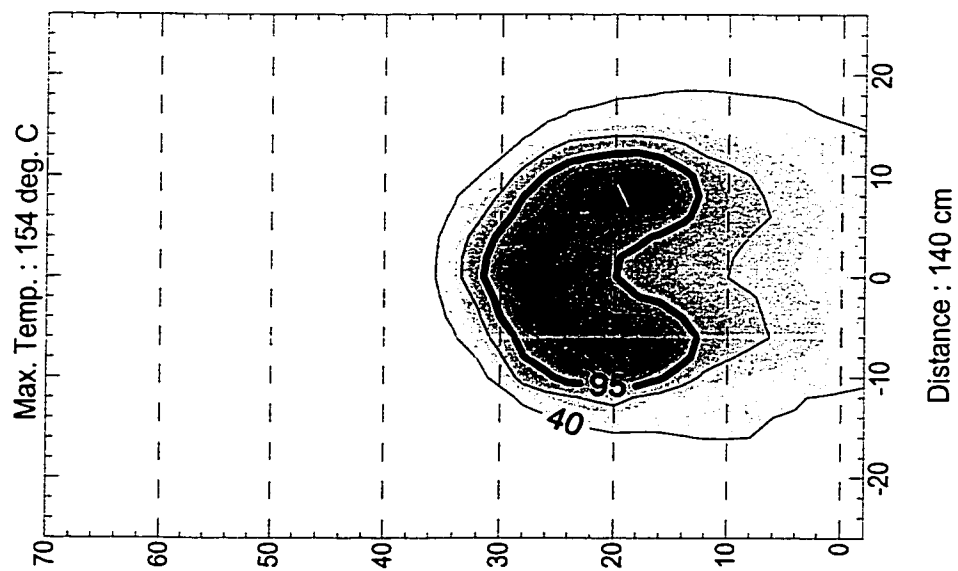
Distance : 170 cm
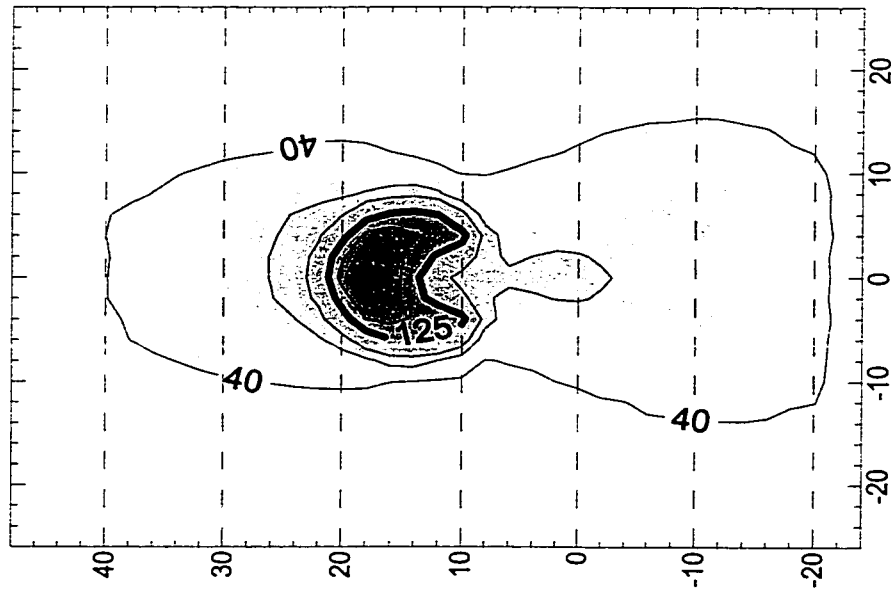
Temperature scale (deg. C)

20   70   110   200

Notes:
- X and Y axis in cm relatively to the stack exit.
- Thick line shows 50% temperature contour.

d_s= 2.21 cm; V_j = 1 m/s; U_∞ = 6 m/s

149

Max. Temp. : 90 deg. C

Distance : 170 cm

Max. Temp. : 117 deg. C

Distance :140 cm

Max. Temp. : 155 deg. C

Distance : 110 cm

data files : S10W80E10P110.grd, S10W80E10P140.grd, S10W80E10P170.grd

Temperature scale (deg. C)

20   70   110

d_s= 2.21 cm; V_j = 1 m/s; U_∞ = 8 m/s

Notes:
- X and Y axis in cm relatively to the stack exit.
- Thick line shows 50% temperature contour.

150

data files : S10W15E20P110.grd, S10W15E20P140.grd, S10W15E20P170.grd

Max. Temp. : 159 deg. C

Distance : 110 cm

Max. Temp. : 99 deg. C

Distance :140 cm

Max. Temp. : 84 deg. C

Distance : 170 cm

Temperature scale (deg. C)

20   70   110   150

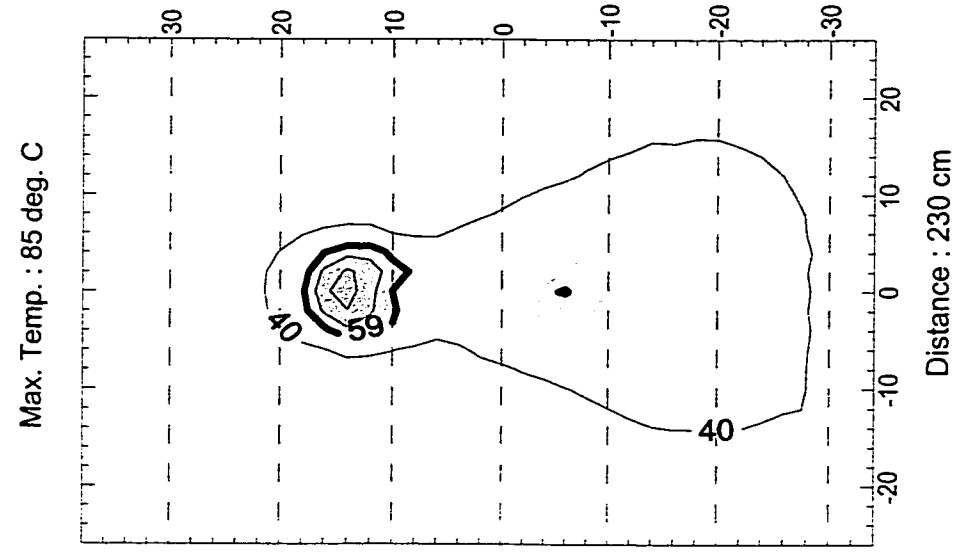d_s = 2.21 cm; V_j = 2 m/s; U_∞ = 1.5 m/s

Notes:
- X and Y axis in cm relatively to the stack exit.
- Thick line shows 50% temperature contour.

151

Max. Temp. : 141 deg. C

Distance : 140 cm

Max. Temp. : 99 deg. C

Distance :170 cm

Max. Temp. : 81 deg. C

Distance : 200 cm

data files : S10W20E20P140.grd, S10W20E20P170.grd, S10W20E20P200.grd
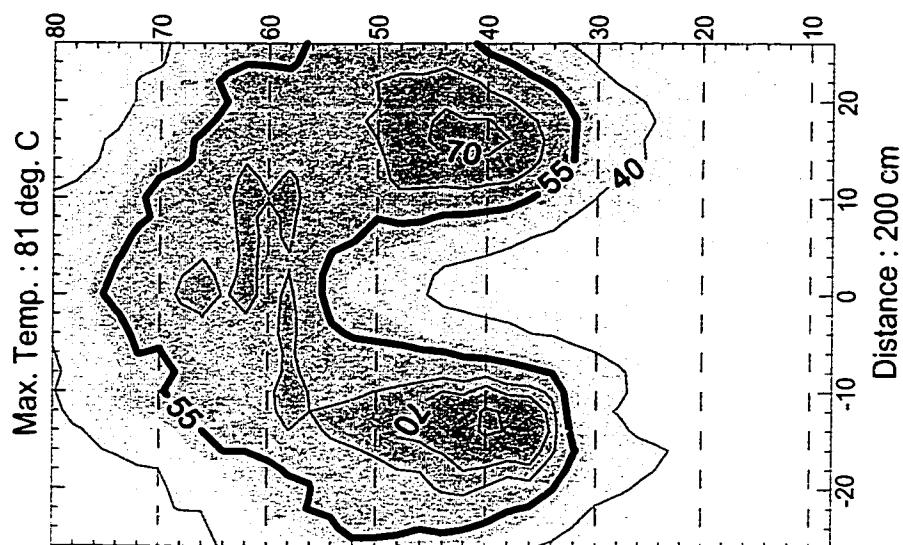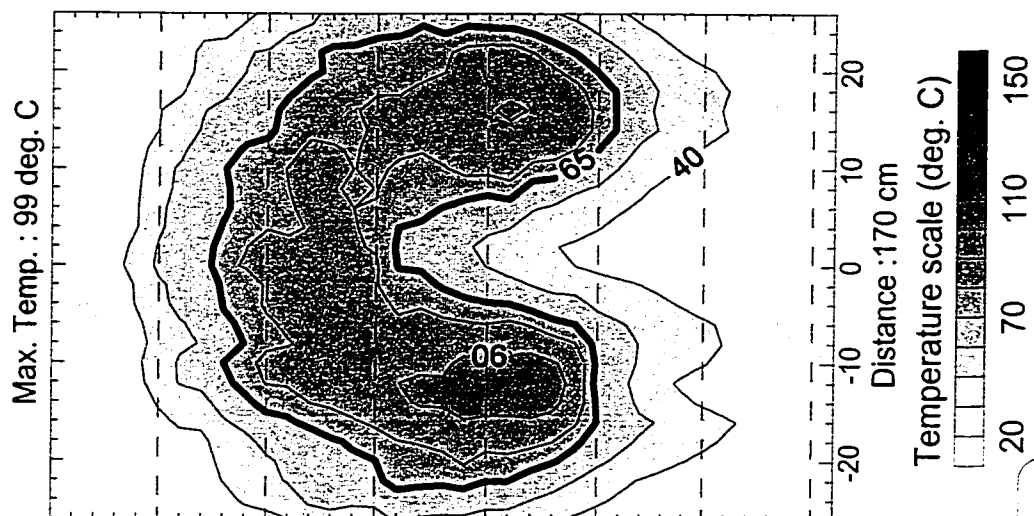
Temperature scale (deg. C)

20   70   110   150

d_s = 2.21 cm; V_j = 2 m/s; U_∞ = 2 m/s

Notes:
- X and Y axis in cm relatively to the stack exit.
- Thick line shows 50% temperature contour.

152

data files : S10W30E20P140.grd, S10W30E20P170.grd, S10W30E20P200.grd

Max. Temp. : 214 deg. C

Max. Temp. : 147 deg. C

Max. Temp. : 119 deg. C

Distance : 140 cm

Distance :170 cm

Distance : 200 cm

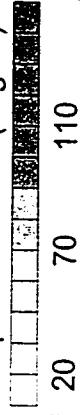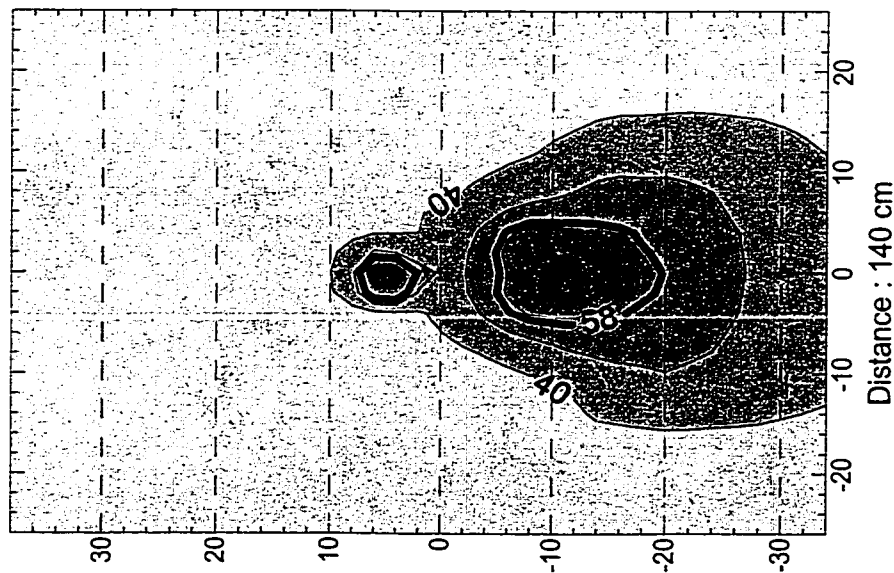Temperature scale (deg. C)

20   70   121   220

Notes:
- X and Y axis in cm relatively to the stack exit.
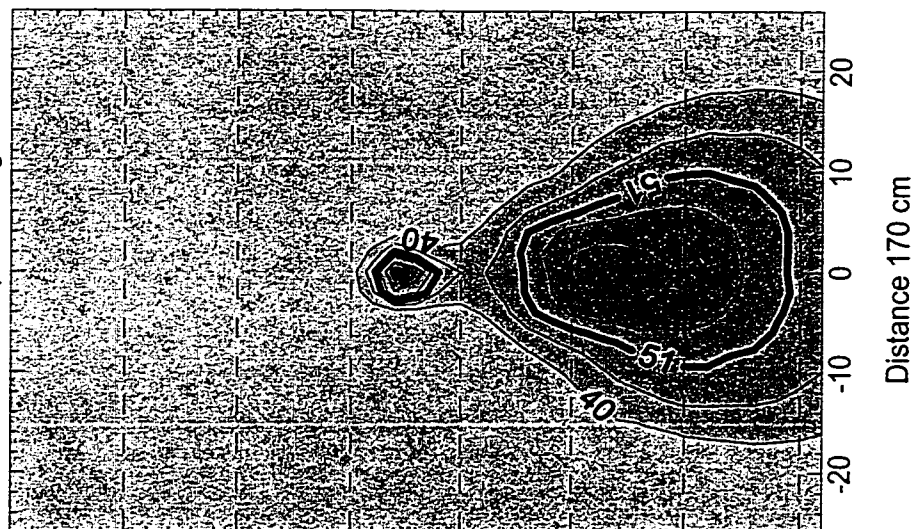- Thick line shows 50% temperature contour.

d_s = 2.21 cm; V_j = 2 m/s; U_∞ = 3 m/s

data files : S10W40E20P170.grd, S10W40E20P200.grd, S10W40E20P230.grd

Max. Temp. : 218 deg. C

Max. Temp. : 179 deg. C

Max. Temp. : 134 deg. C

Distance : 170 cm

Distance 200 cm
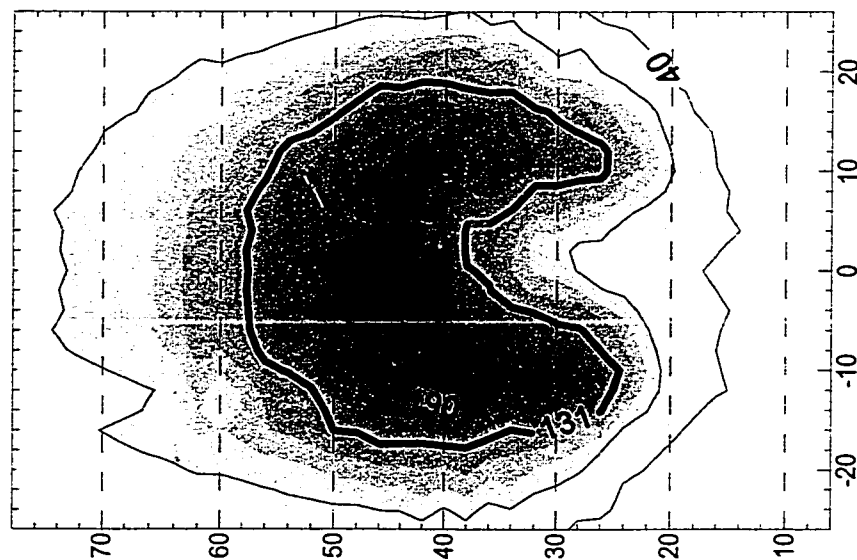
Distance : 230 cm

Temperature scale (deg. C)

20   70   124   220

Notes:
- X and Y axis in cm relatively to the stack exit.
- Thick line shows 50% temperature contour.

d_s= 2.21 cm; V_j = 2 m/s; U_∞ = 4 m/s

154

Max. Temp. : 177 deg. C

Distance : 200 cm

Max. Temp. : 235 deg. C

Distance 170 cm

Max. Temp. : 309 deg. C

Distance : 140 cm

Temperature scale (deg. C)

20   70   160   230

d_s = 2.21 cm; V_j = 2 m/s; U_∞ = 6 m/s

Notes:
- X and Y axis in cm relatively to the stack exit.
- Thick line shows 50% temperature contour.

155

Max. Temp. : 151 deg. C

Distance : 200 cm
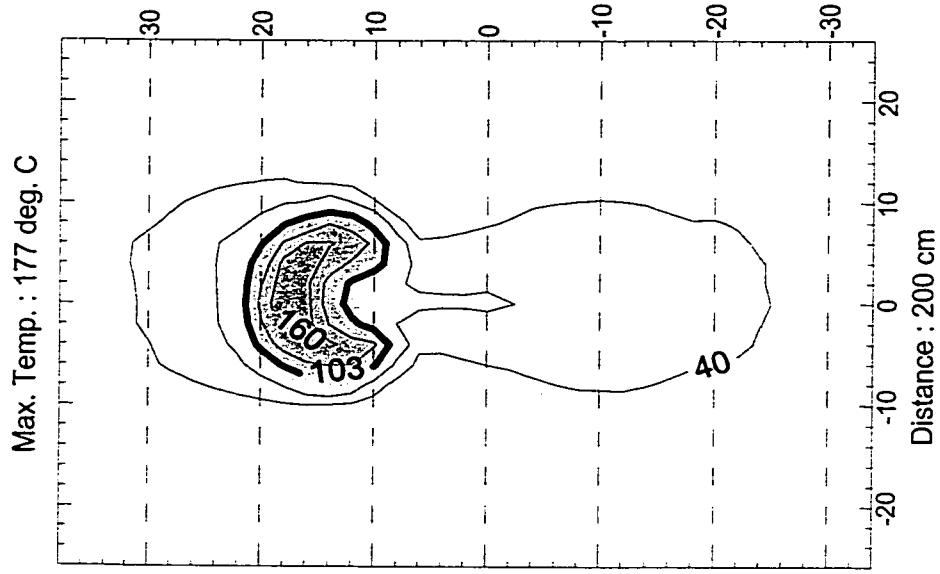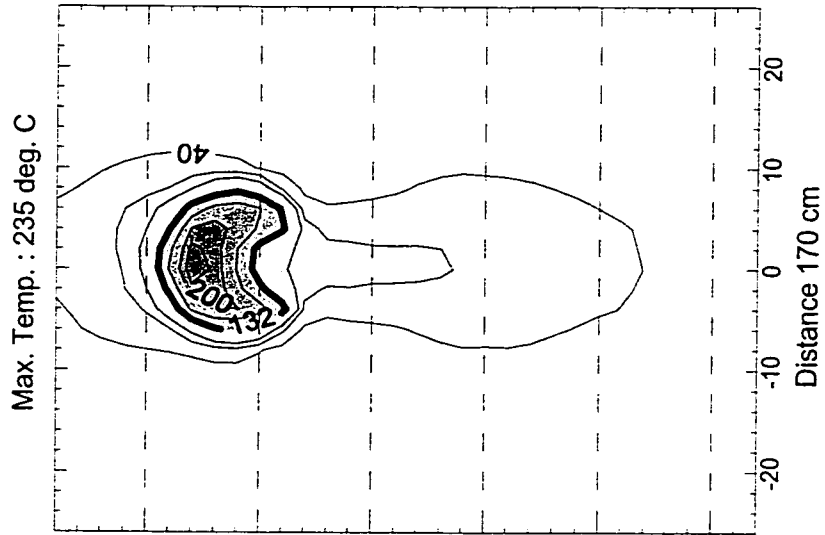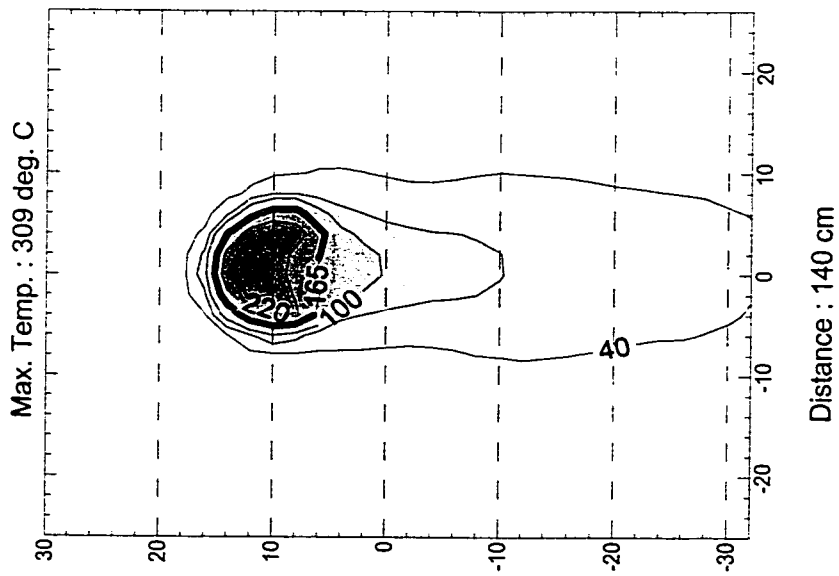
Max. Temp. : 179 deg. C

Distance 170 cm
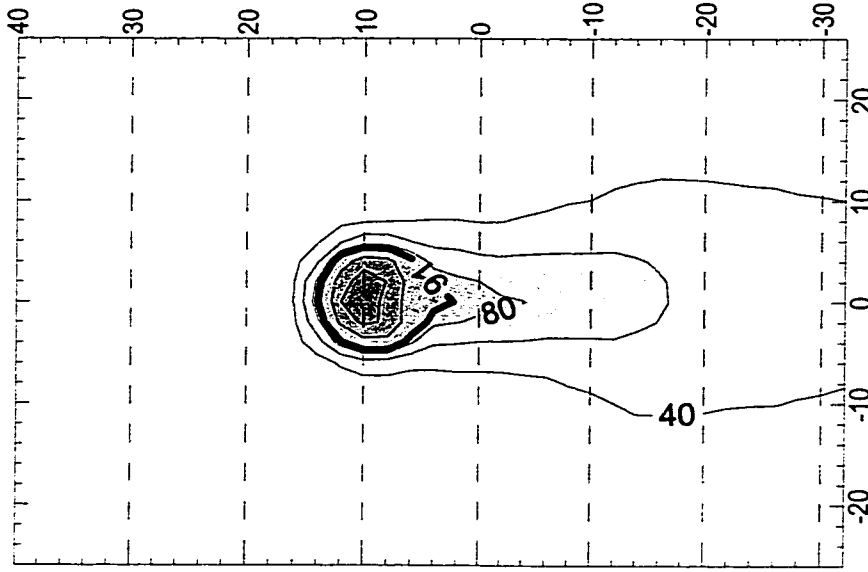
Max. Temp. : 250 deg. C

Distance : 140 cm

data files : S10W80E20P140.grd, S10W80E20P170.grd, S10W80E20P200.grd

Temperature scale (deg. C)

20   70   137   220

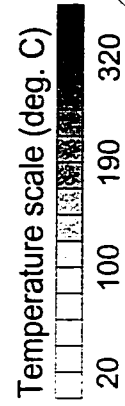$d_s = 2.21$ cm; $V_j = 2$ m/s; $U_\infty = 8$ m/s

Notes:
- X and Y axis in cm relatively to the stack exit.
- Thick line shows 50% temperature contour.

156

data files : S15W15E05P100.grd, S15W15E05P110.grd, S15W15E05P120.grd

Max. Temp. : 136 deg. C

Max. Temp. : 112 deg. C
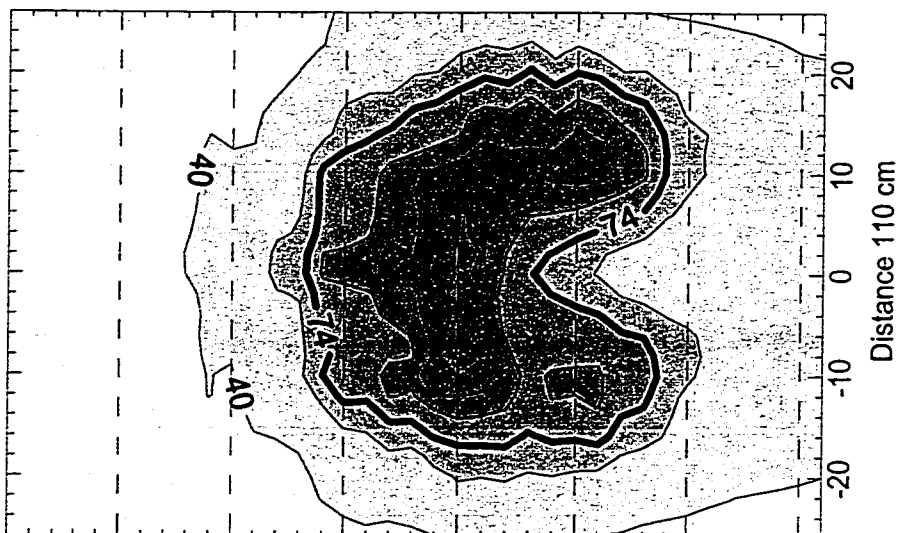
Max. Temp. : 101 deg. C
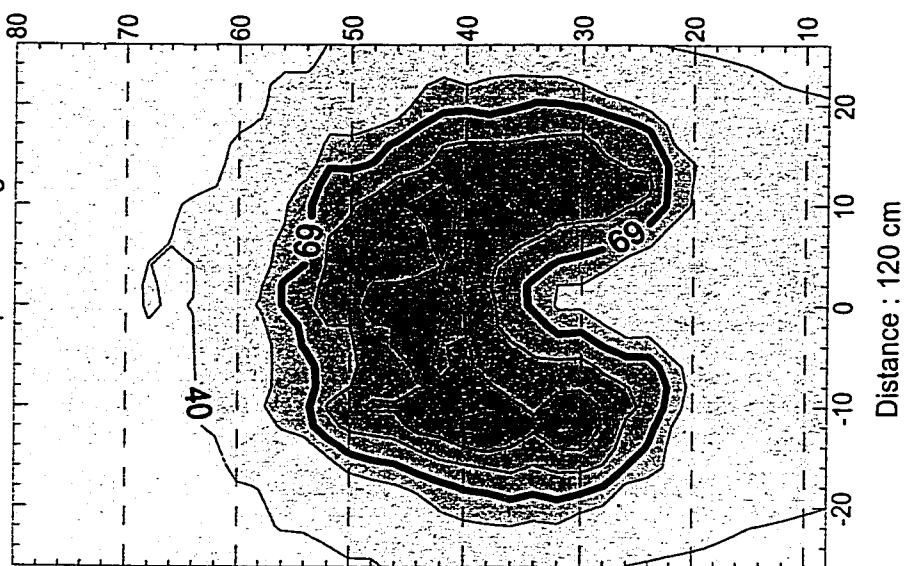
Distance : 100 cm

Distance 110 cm

Distance : 120 cm

Temperature scale (deg. C)

d_s = 3.33 cm; V_j = 0.5 m/s; U_∞ = 1.5 m/s

Notes:
- X and Y axis in cm relatively to the stack exit.
- Thick line shows 50% temperature contour.

157

data files : S15W20E05P100.grd, S15W20E05P110.grd

Max. Temp. : 152 deg. C
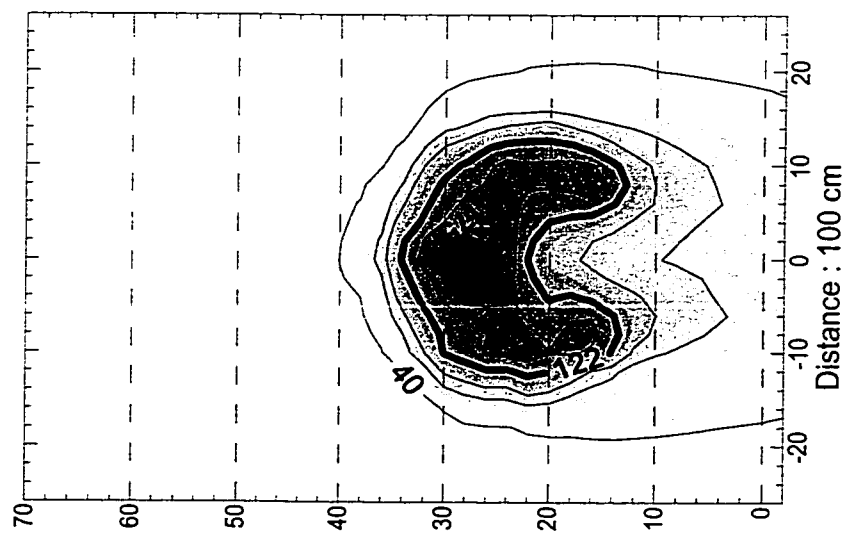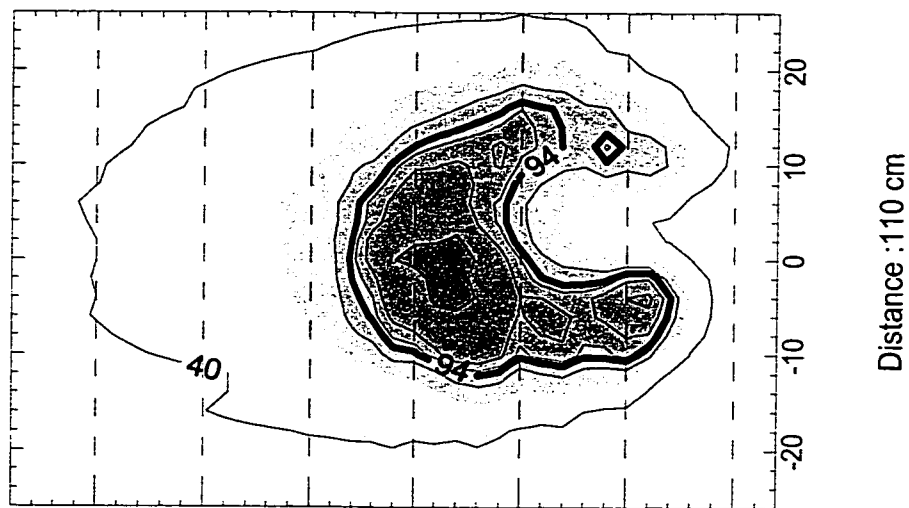
Max. Temp. : 209 deg. C

Distance :110 cm

Distance : 100 cm

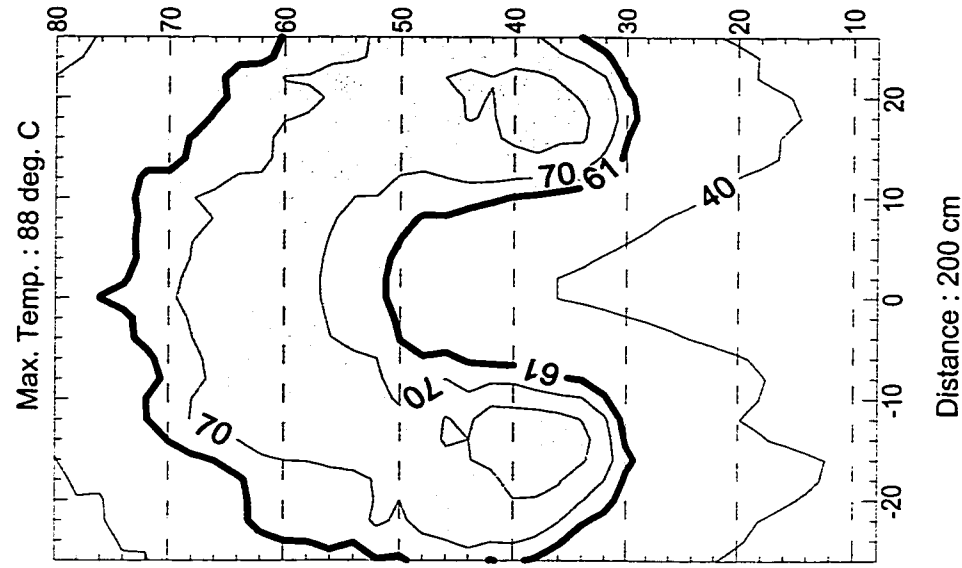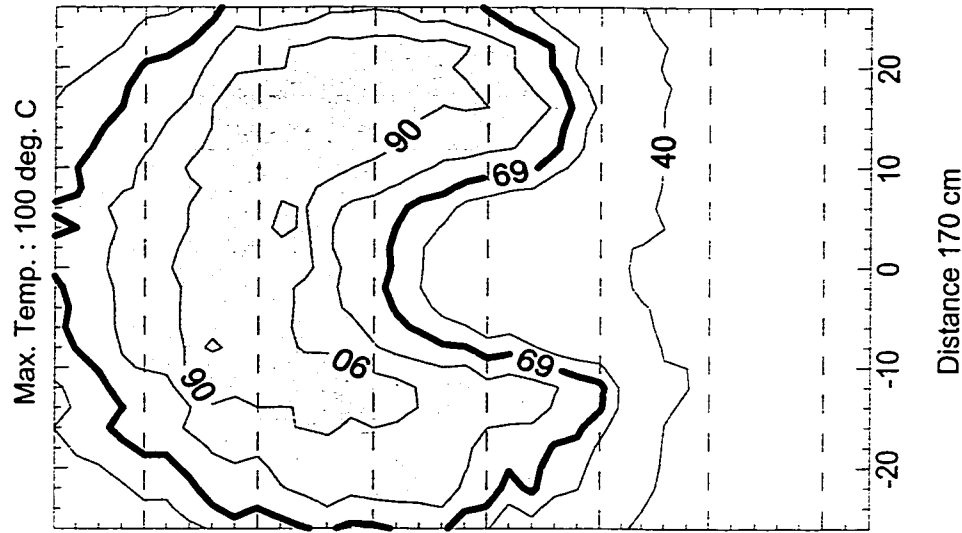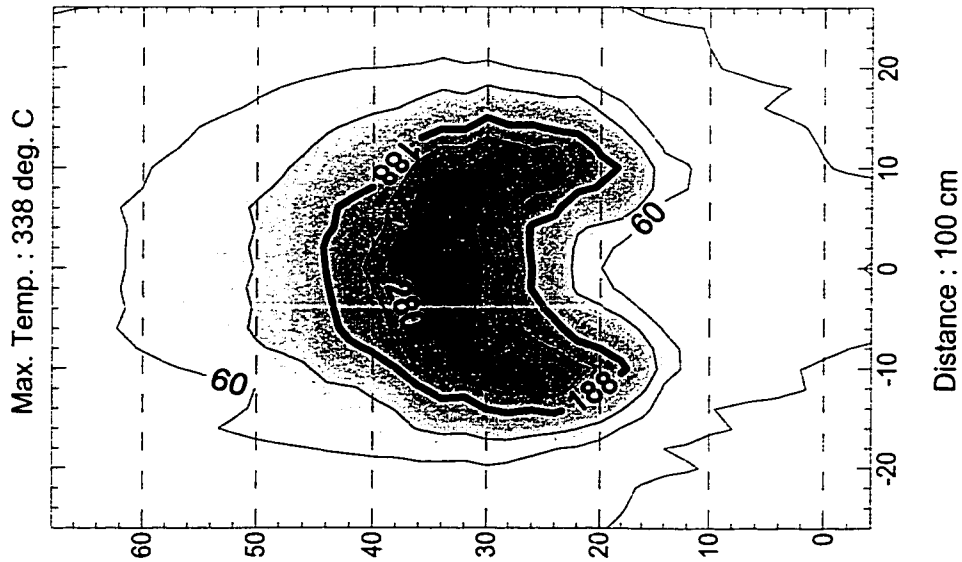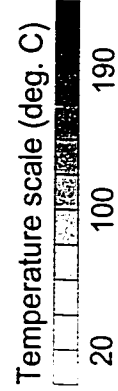Temperature scale (deg. C)

20   70   130   210
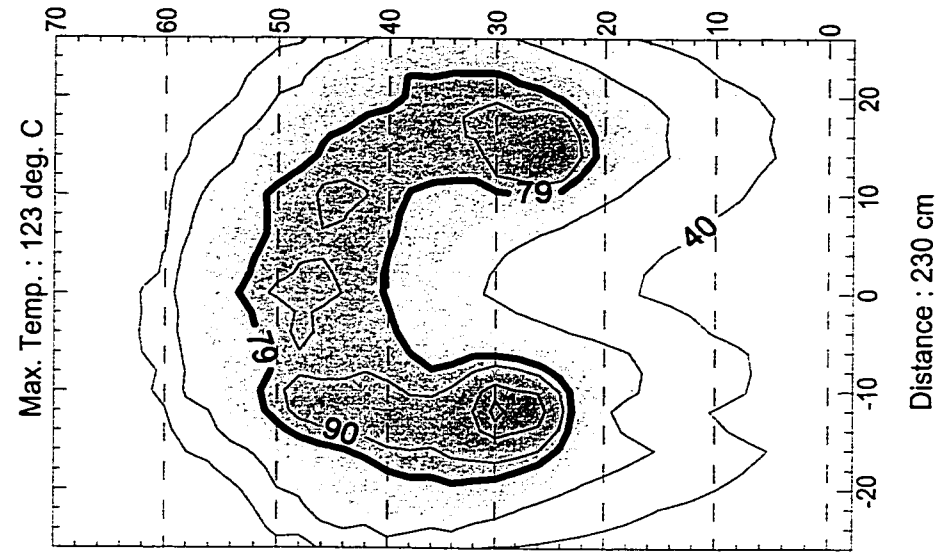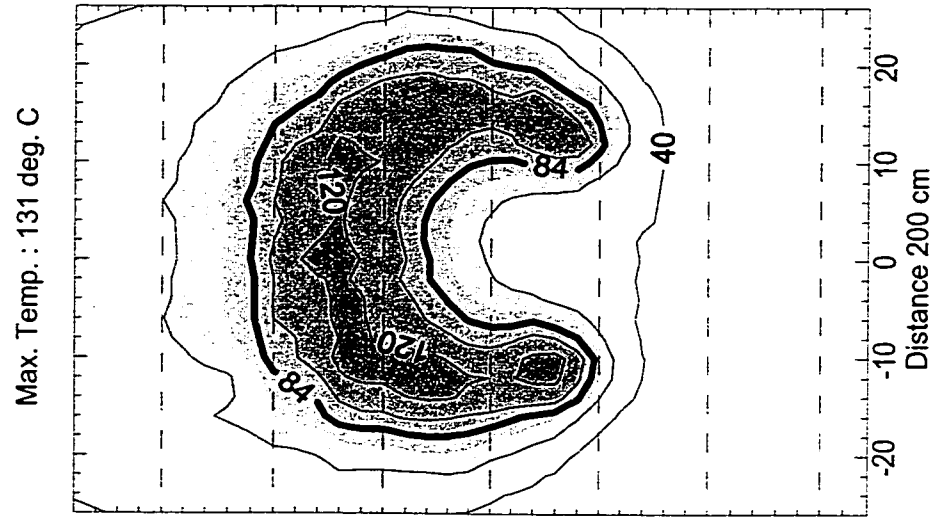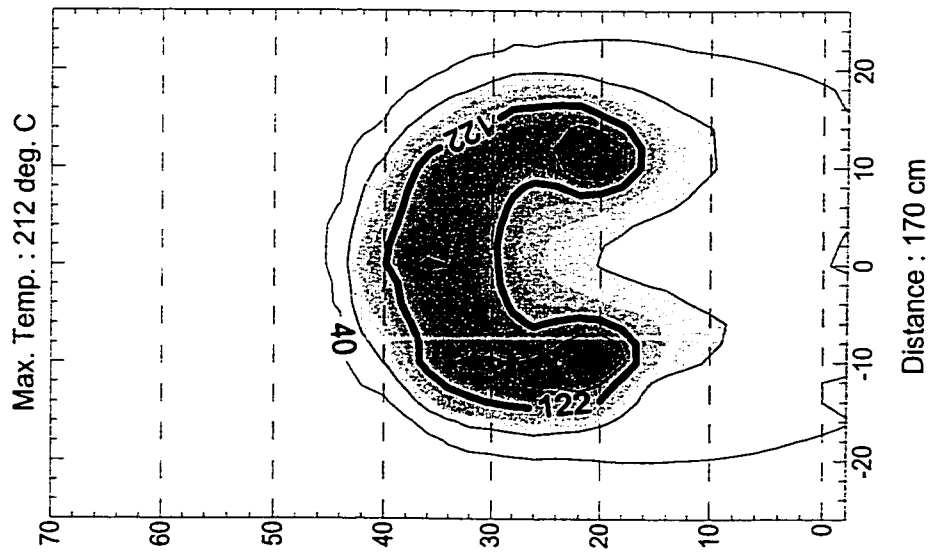
Notes:
- X and Y axis in cm relatively to the stack exit.
- Thick line shows 50% temperature contour.

d_s = 3.33 cm; V_j = 0.5 m/s; U_∞ = 2 m/s

158

Max. Temp. : 154 deg. C

Distance : 140 cm

Max. Temp. : 116 deg. C

Distance 170 cm

Max. Temp. : 89 deg. C

Distance : 230 cm

data files : S15W30E05P140.grd, S15W30E05P170.grd, S15W30E05P230.grd
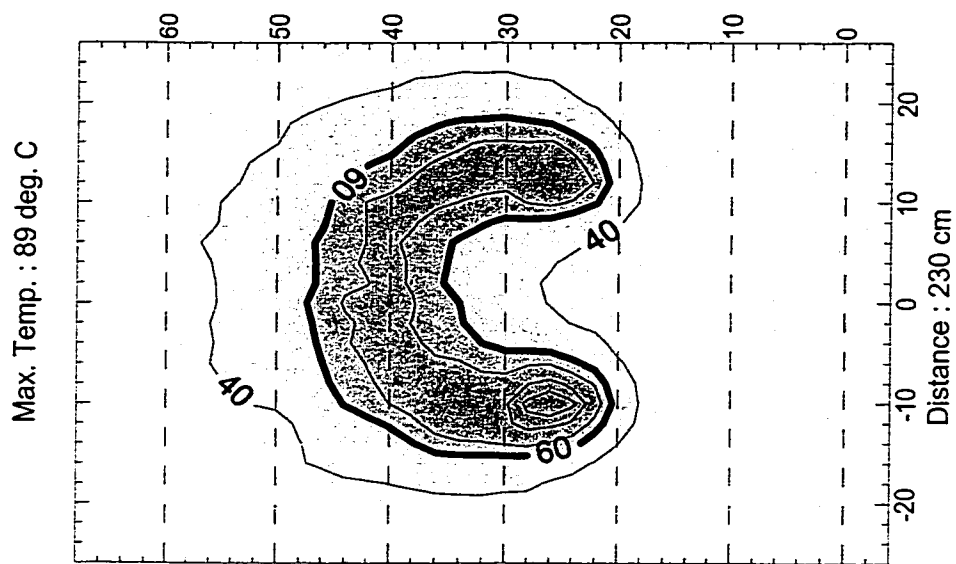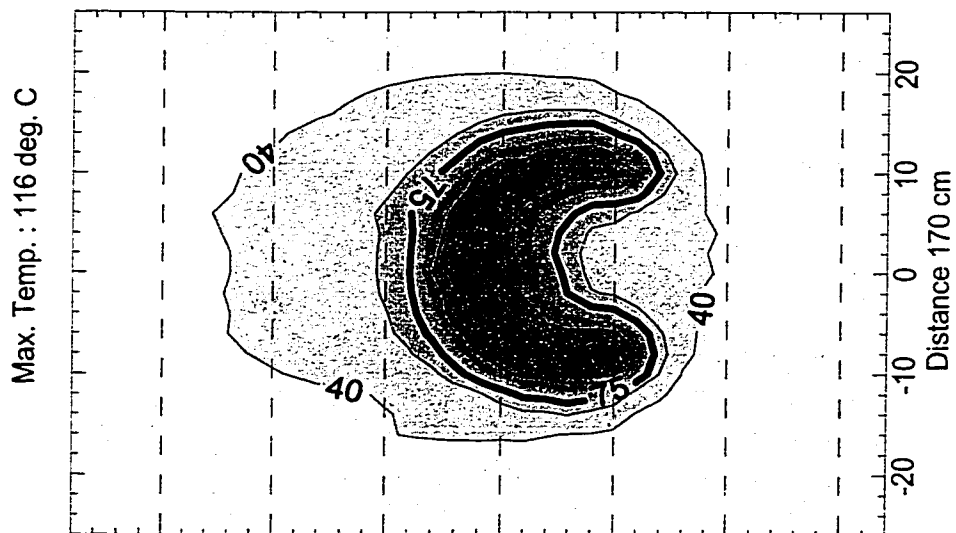
Temperature scale (deg. C)

20 70 110 150

d_s = 3.33 cm; V_j = 0.5 m/s; U_∞ = 3 m/s

Notes:
- X and Y axis in cm relatively to the stack exit.
- Thick line shows 50% temperature contour.

159

Max. Temp. : 99 deg. C

Distance : 230 cm

Max. Temp. : 156 deg. C

Distance 170 cm

Max. Temp. : 215 deg. C

Distance : 140 cm

data files : S15W40E05P140.grd, S15W40E05P170.grd, S15W40E05P230.grd
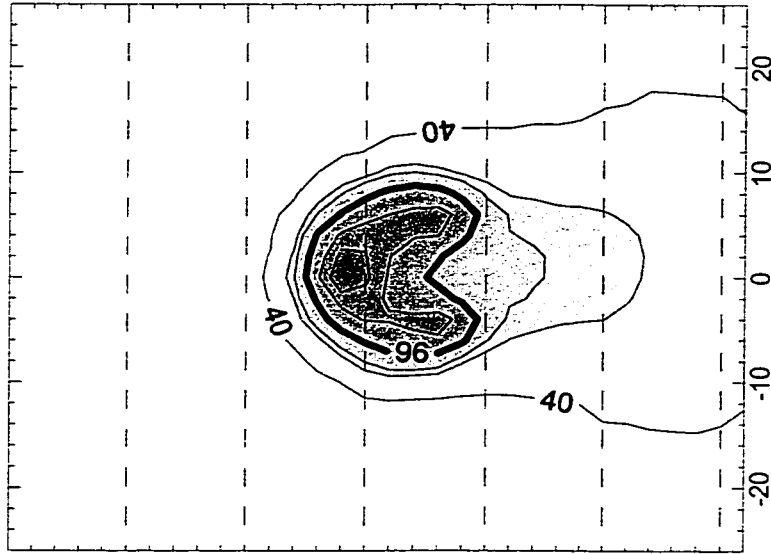
Temperature scale (deg. C)

$d_s = 3.33$ cm; $V_j = 0.5$ m/s; $U_\infty = 4$ m/s

Notes:
- X and Y axis in cm relatively to the stack exit.
- Thick line shows 50% temperature contour.

160
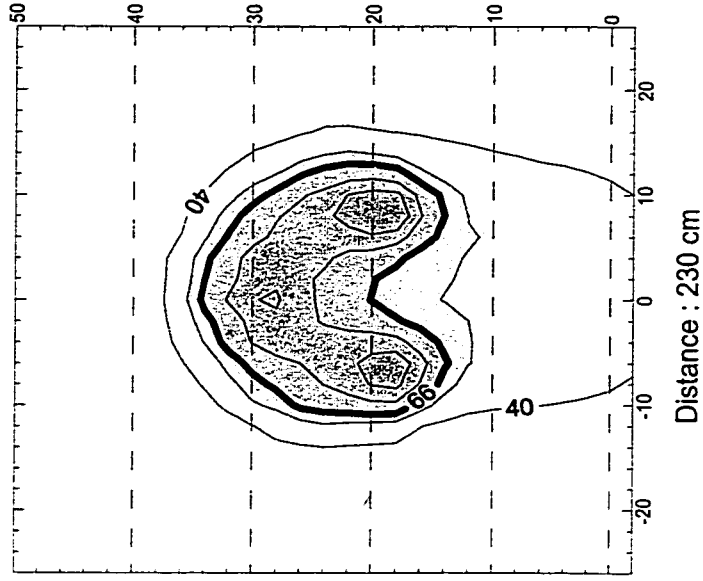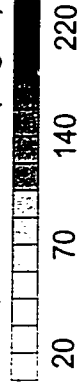
data files : S15W60E05P140.grd, S15W60E05P170.grd, S15W60E05P230.grd
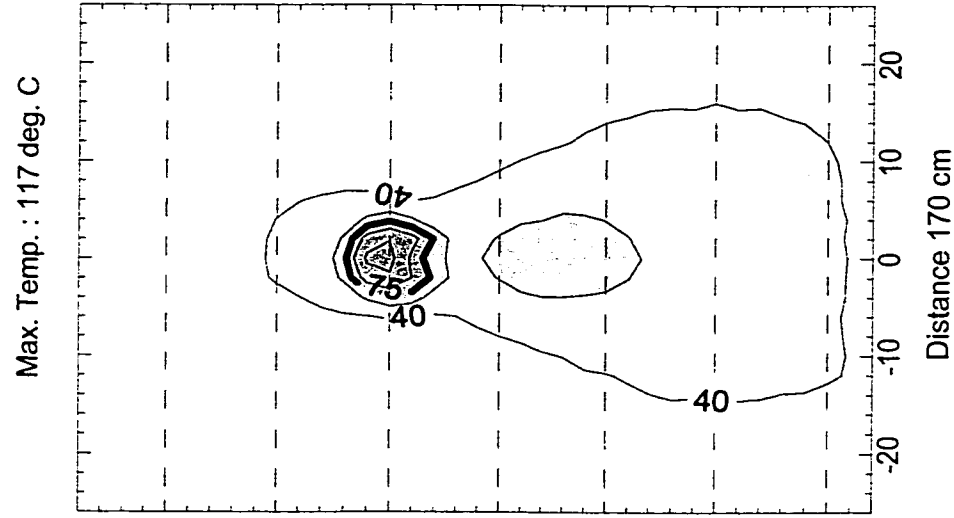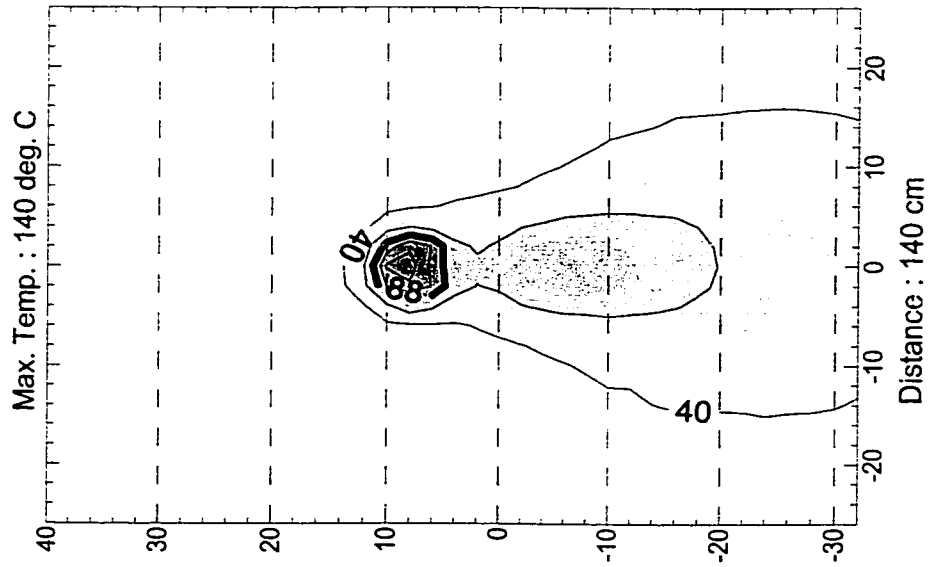
Max. Temp. : 140 deg. C

Max. Temp. : 117 deg. C

Max. Temp. : 85 deg. C

Distance : 140 cm

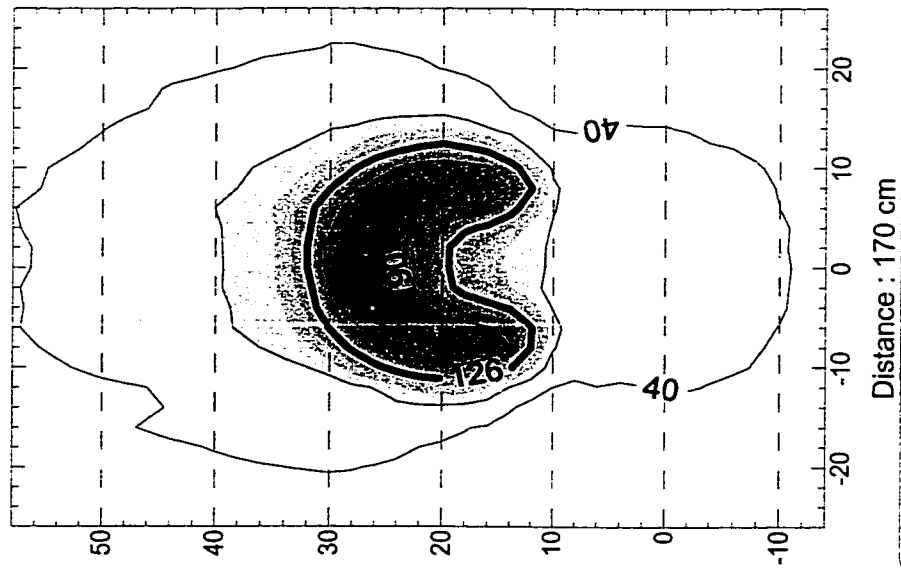Distance 170 cm

Distance : 230 cm

Temperature scale (deg. C)

20   70   110

Notes:
- X and Y axis in cm relatively to the stack exit.
- Thick line shows 50% temperature contour.

d_s= 3.33 cm; V_j = 0.5 m/s; U_∞ = 6 m/s
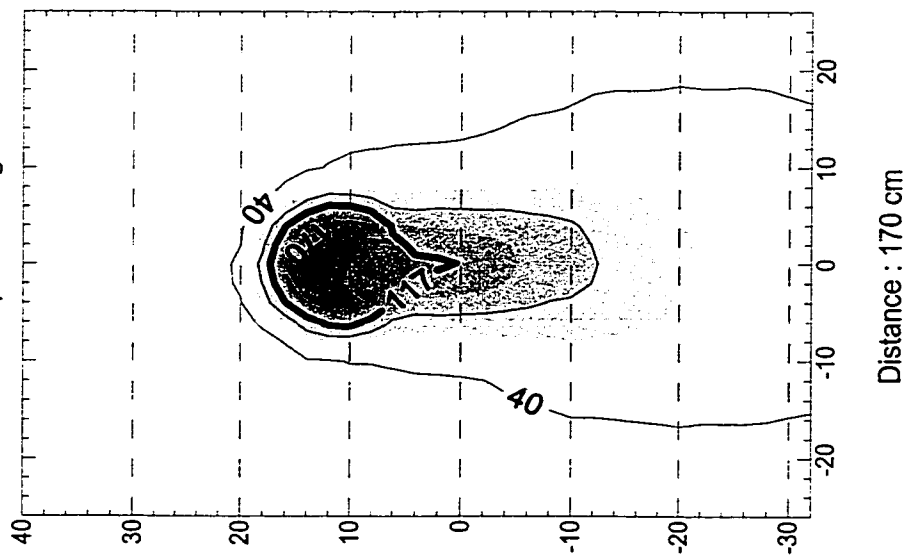
161

Max. Temp. : 53 deg. C

Distance : 230 cm

Max. Temp. : 68 deg. C

Distance 170 cm

Max. Temp. : 80 deg. C

Distance : 140 cm

data files : S15W80E05P140.grd, S15W80E05P170.grd, S15W80E05P230.grd
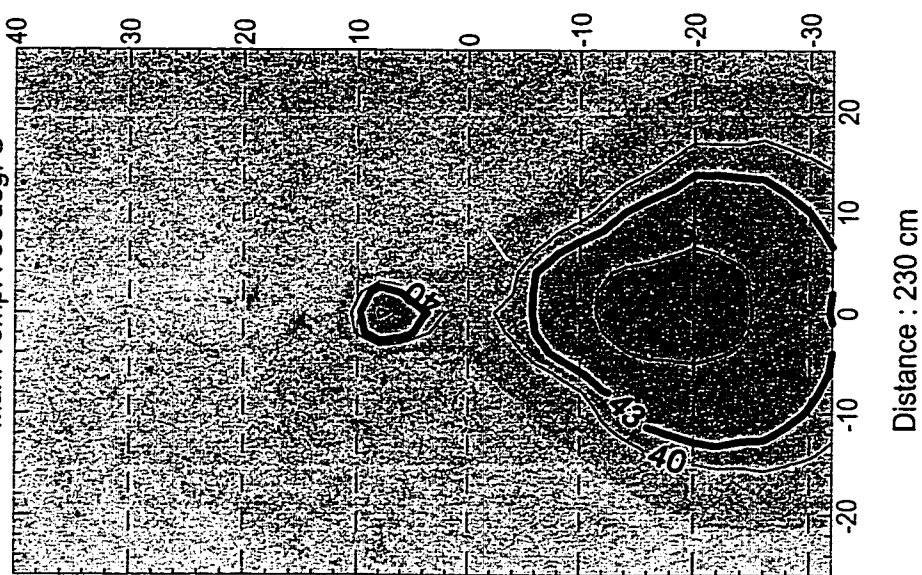
Temperature scale (deg. C)

20   60

d_s= 3.33 cm; V_j = 0.5 m/s; U_∞ = 8 m/s

Notes:
- X and Y axis in cm relatively to the stack exit.
- Thick line shows 50% temperature contour.

162

data files : S15W15E10P100.grd, S15W15E10P110.grd, S15W15E10P120.grd

Max. Temp. : 226 deg. C

Distance : 100 cm

Max. Temp. : 189 deg. C
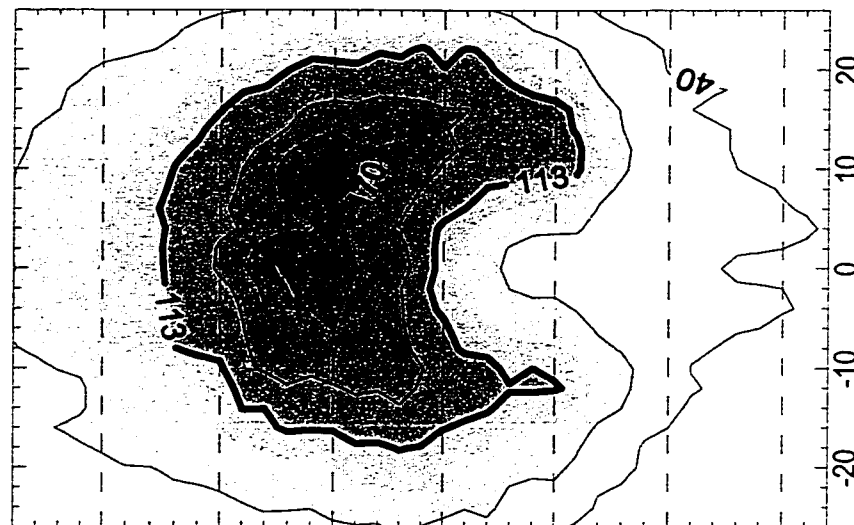
Distance 110 cm
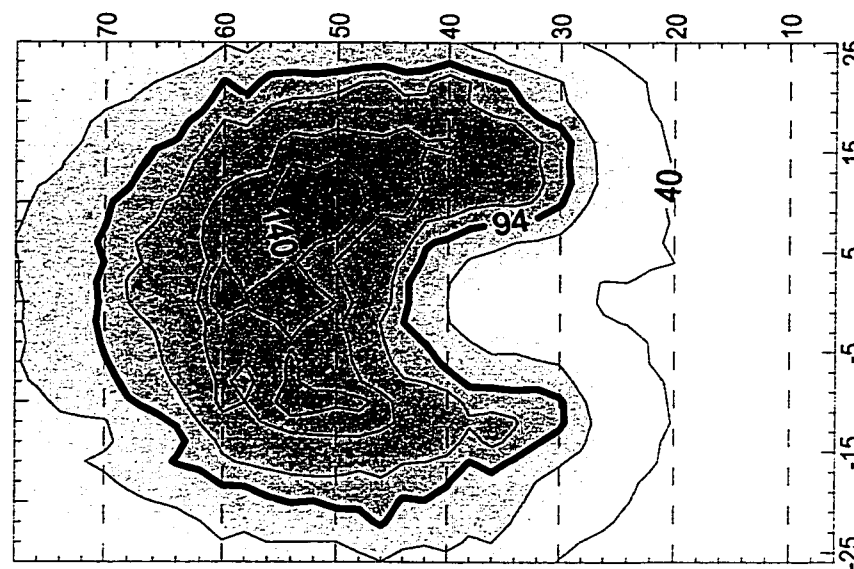
Max. Temp. : 151 deg. C

Distance : 120 cm

Temperature scale (deg. C)

20   100   170

d_s = 3.33 cm; V_j = 1 m/s; U_∞ = 1.5 m/s

Notes:
- X and Y axis in cm relatively to the stack exit.
- Thick line shows 50% temperature contour.

163

data files : S15W20E10P100.grd, S15W20E10P170.grd, S15W20E10P200.grd

Max. Temp. : 338 deg. C

Distance : 100 cm

Max. Temp. : 100 deg. C

Distance 170 cm

Max. Temp. : 88 deg. C

Distance : 200 cm

Temperature scale (deg. C)

20   100   190   320

Notes:
- X and Y axis in cm relatively to the stack exit.
- Thick line shows 50% temperature contour.

$d_s = 3.33$ cm; $V_j = 1$ m/s; $U_\infty = 2$ m/s

164

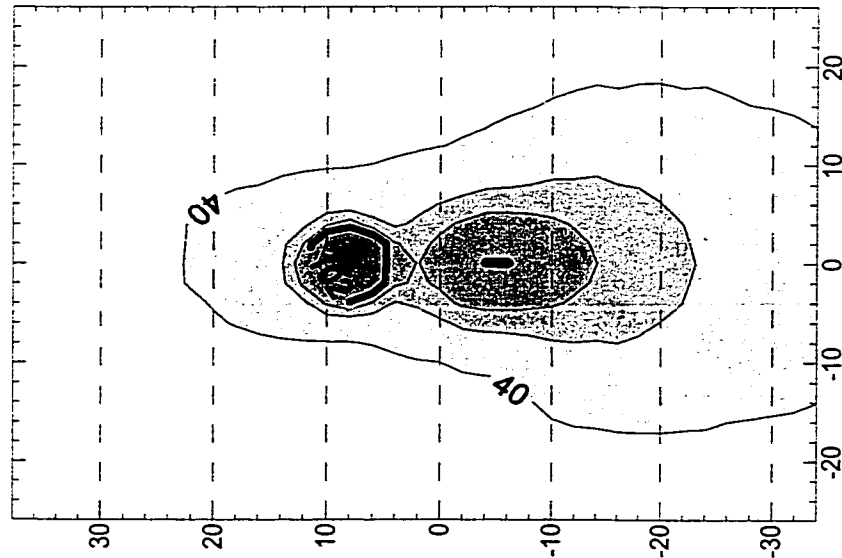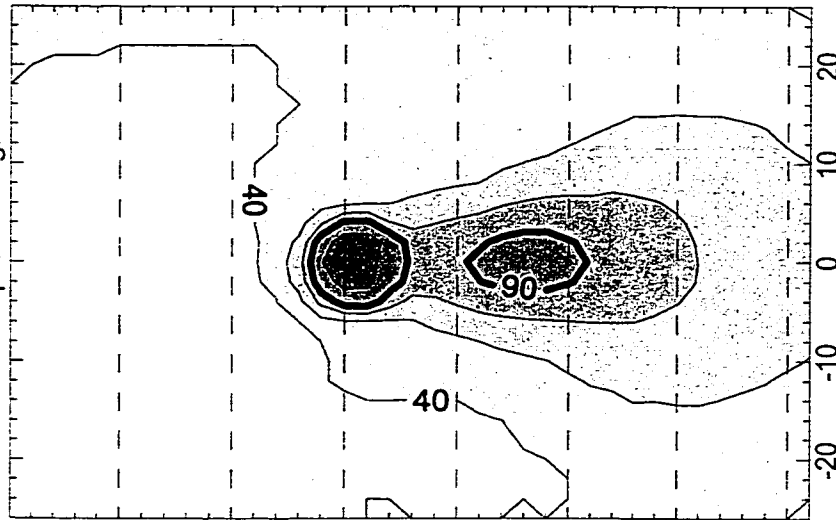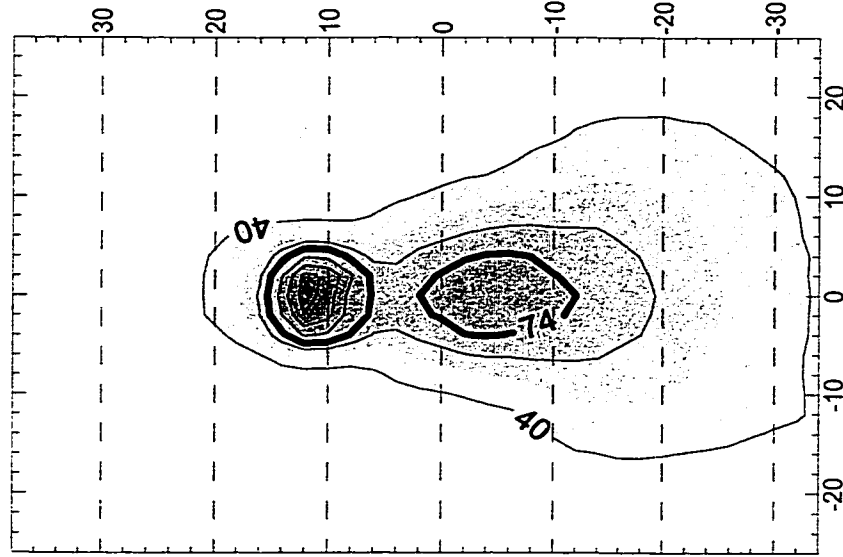data files : S15W30E10P170.grd, S15W30E10P200.grd, S15W30E10P230.grd

Max. Temp. : 212 deg. C

Max. Temp. : 131 deg. C

Max. Temp. : 123 deg. C

Distance : 170 cm

Distance 200 cm

Distance : 230 cm

Temperature scale (deg. C)

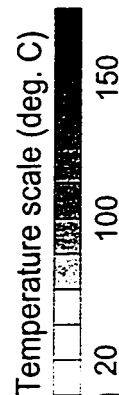d_s= 3.33 cm; V_j = 1 m/s; U_∞ = 3 m/s

Notes:
- X and Y axis in cm relatively to the stack exit.
- Thick line shows 50% temperature contour.

165

data files : S15W40E10P170.grd, S15W40E10P200.grd, S15W40E10P230.grd

Max. Temp. : 218 deg. C

Max. Temp. : 176 deg. C

Max. Temp. : 129 deg. C

Distance : 170 cm

Distance 200 cm

Distance : 230 cm

Temperature scale (deg. C)

d_s = 3.33 cm; V_j = 1 m/s; U_∞ = 4 m/s

Notes:
- X and Y axis in cm relatively to the stack exit.
- Thick line shows 50% temperature contour.

166

Max. Temp. : 200 deg. C
Distance : 170 cm

Max. Temp. : 181 deg. C
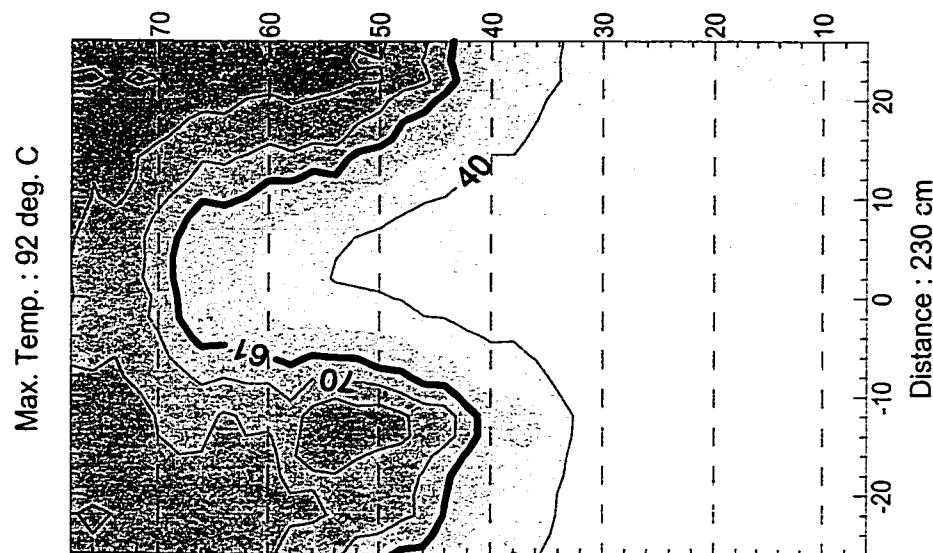Distance 200 cm

Max. Temp. : 131 deg. C
Distance : 230 cm

data files : S15W60E10P170.grd, S15W60E10P200.grd, S15W60E10P230.grd
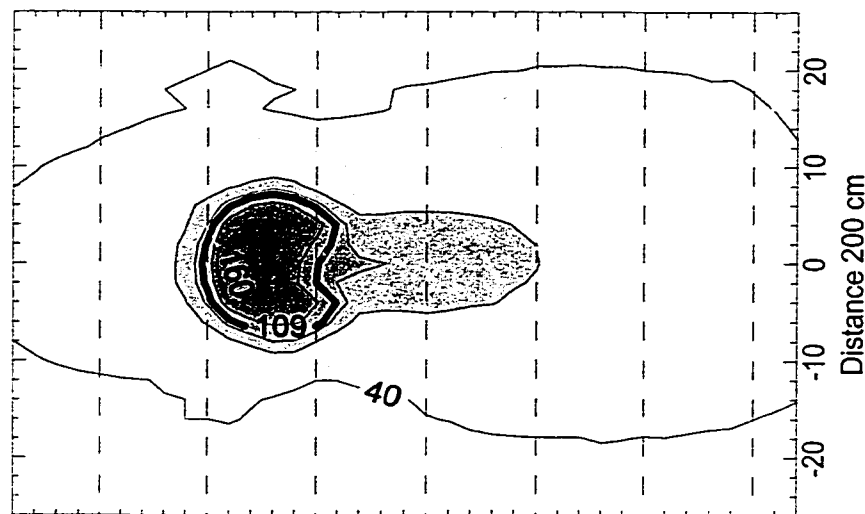
Temperature scale (deg. C)

20   100   190

d_s = 3.33 cm; V_j = 1 m/s; U_∞ = 6 m/s

Notes:
- X and Y axis in cm relatively to the stack exit.
- Thick line shows 50% temperature contour.

167

data files : S15W80E10P170.grd, S15W80E10P200.grd, S15W80E10P230.grd

Max. Temp. : 168 deg. C

Max. Temp. : 140 deg. C

Max. Temp. : 115 deg. C

Distance : 170 cm

Distance 200 cm

Distance : 230 cm

Temperature scale (deg. C)

20   102   170

d_s= 3.33 cm; V_j = 1 m/s; U_∞ = 8 m/s

Notes:
- X and Y axis in cm relatively to the stack exit.
- Thick line shows 50% temperature contour.

168

data files : S15W20E20P170.grd, S15W20E20P200.grd, S15W20E20P230.grd
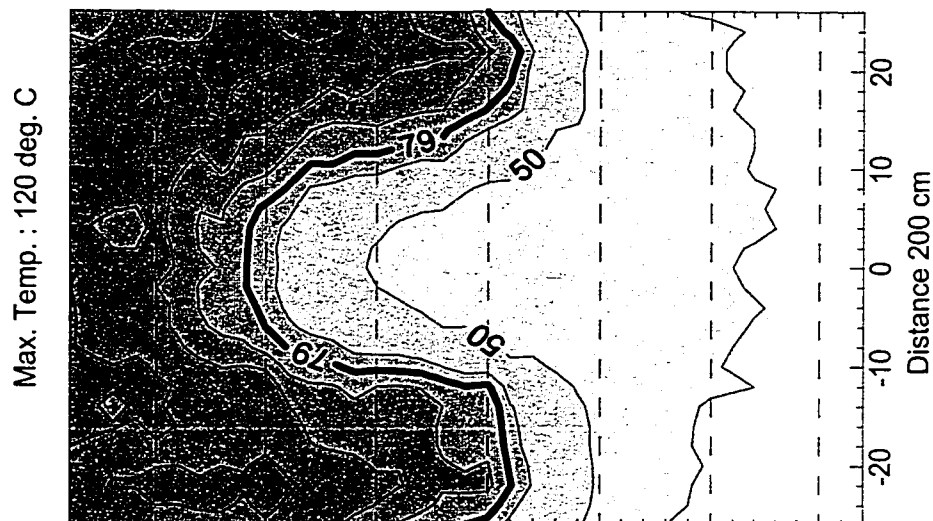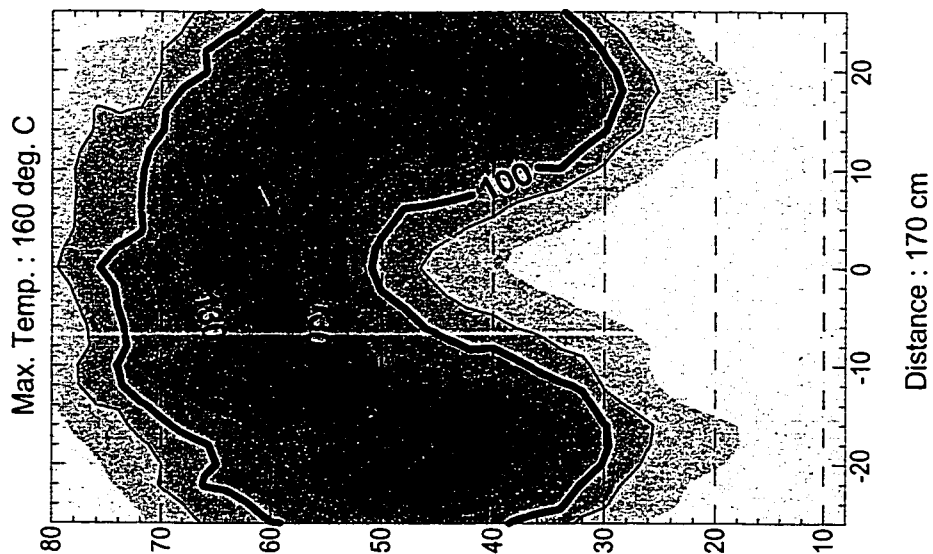
Max. Temp. : 92 deg. C

Max. Temp. : 120 deg. C

Max. Temp. : 160 deg. C

Distance : 230 cm

Distance 200 cm

Distance : 170 cm

Temperature scale (deg. C)

20   100   150

d_s = 3.33 cm; V_j =2 m/s; U_∞ = 2 m/s

Notes:
- X and Y axis in cm relatively to the stack exit.
- Thick line shows 50% temperature contour.

data files : S15W30E20P170.grd, S15W30E20P200.grd, S15W30E20P230.grd

Max. Temp. : 286 deg. C
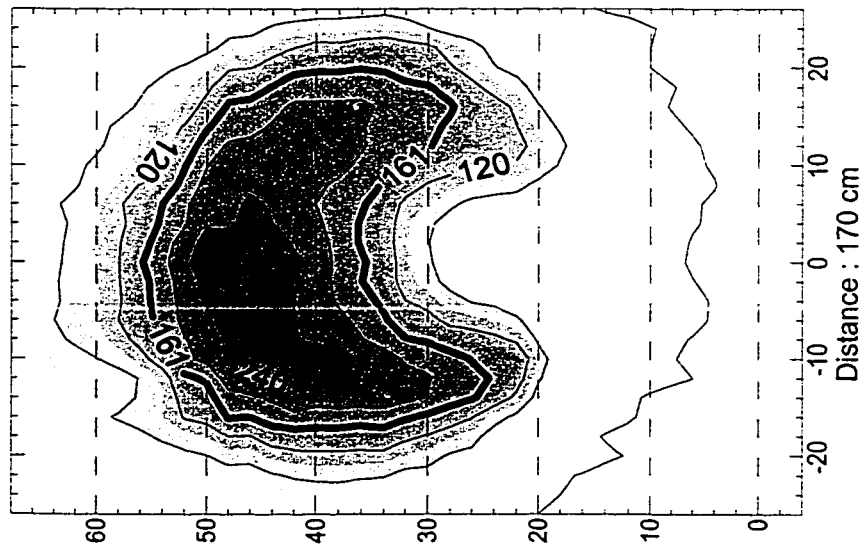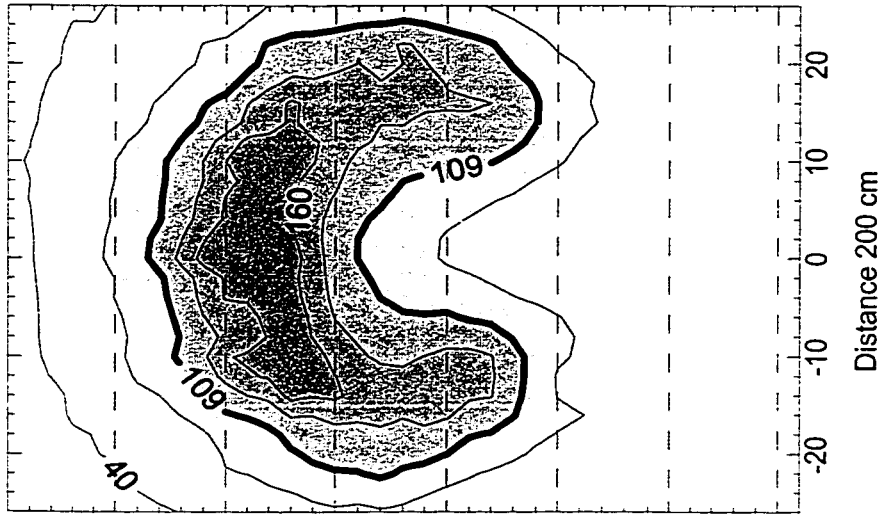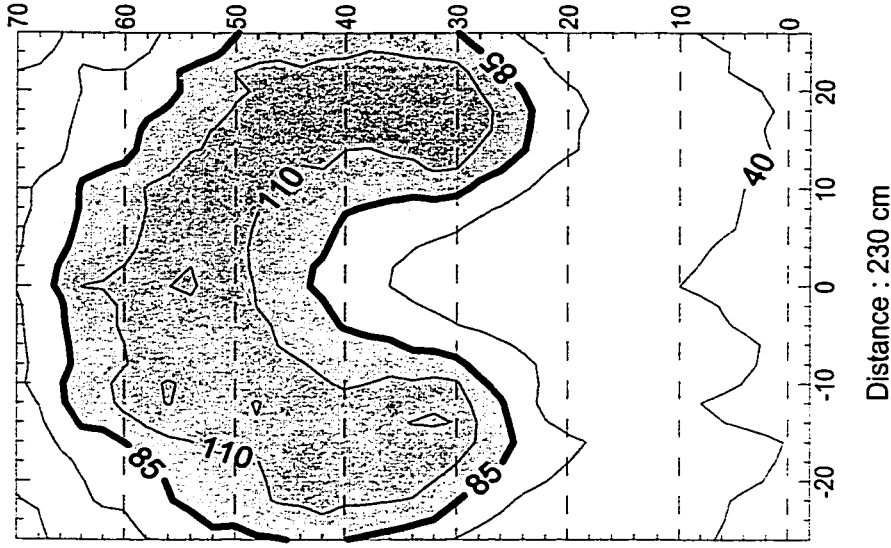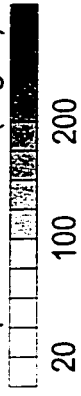
Distance : 170 cm

Max. Temp. : 181 deg. C

Distance 200 cm

Max. Temp. : 133 deg. C

Distance : 230 cm

Temperature scale (deg. C)

d_s = 3.33 cm; V_j = 2 m/s; U_∞ = 3 m/s

Notes:
- X and Y axis in cm relatively to the stack exit.
- Thick line shows 50% temperature contour.

170

data files : S15W40E20P230.grd, S15W40E20P260.grd, S15W40E20P290.grd
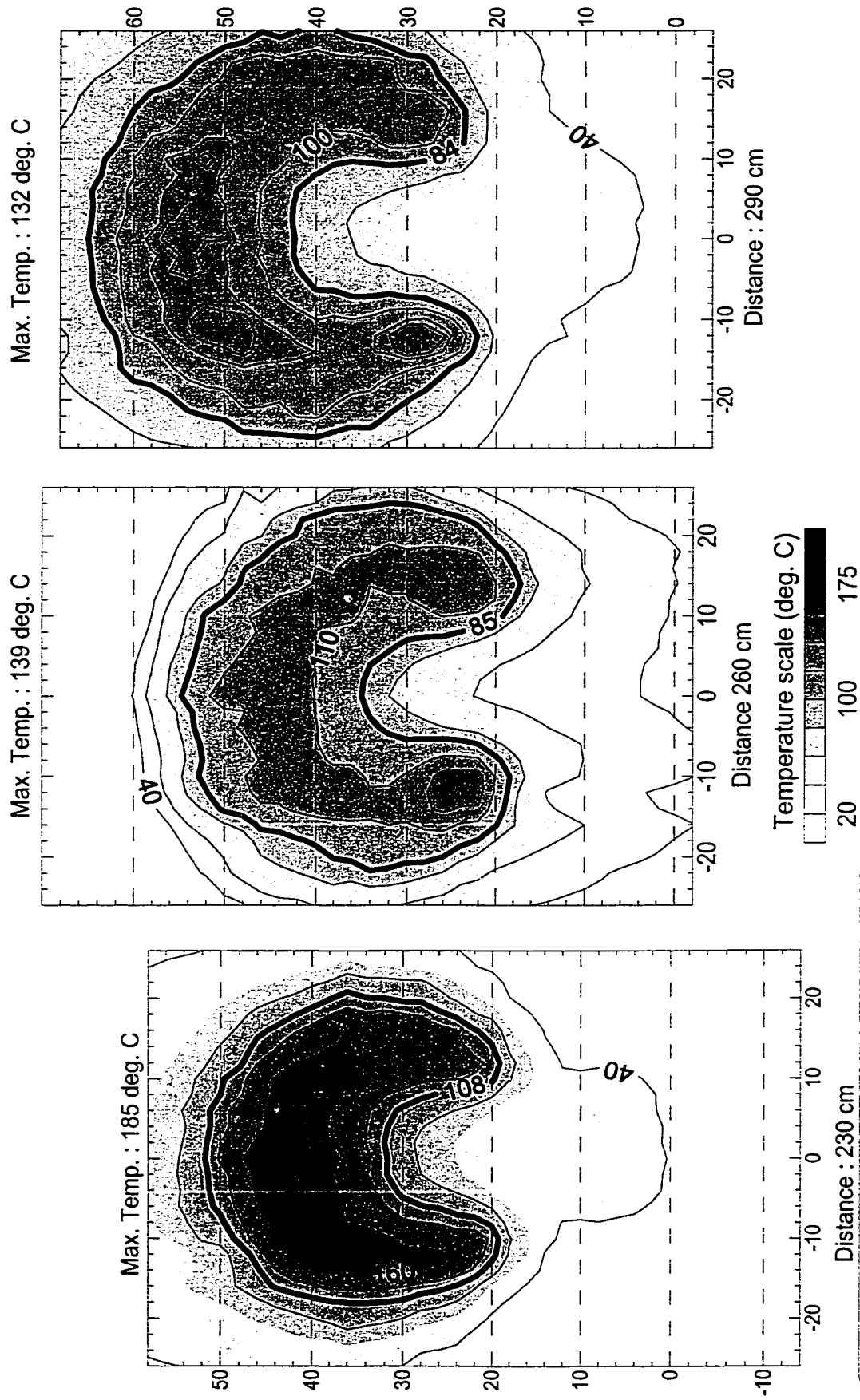
Max. Temp. : 132 deg. C

Distance : 290 cm

Max. Temp. : 139 deg. C

Distance 260 cm

Temperature scale (deg. C)

175

100

20

Max. Temp. : 185 deg. C

Distance : 230 cm

d_s = 3.33 cm; V_j = 2 m/s; U_∞ = 4 m/s

Notes:
- X and Y axis in cm relatively to the stack exit.
- Thick line shows 50% temperature contour.

171

data files : S15W60E20P230.grd, S15W60E20P260.grd, S15W60E20P290.grd
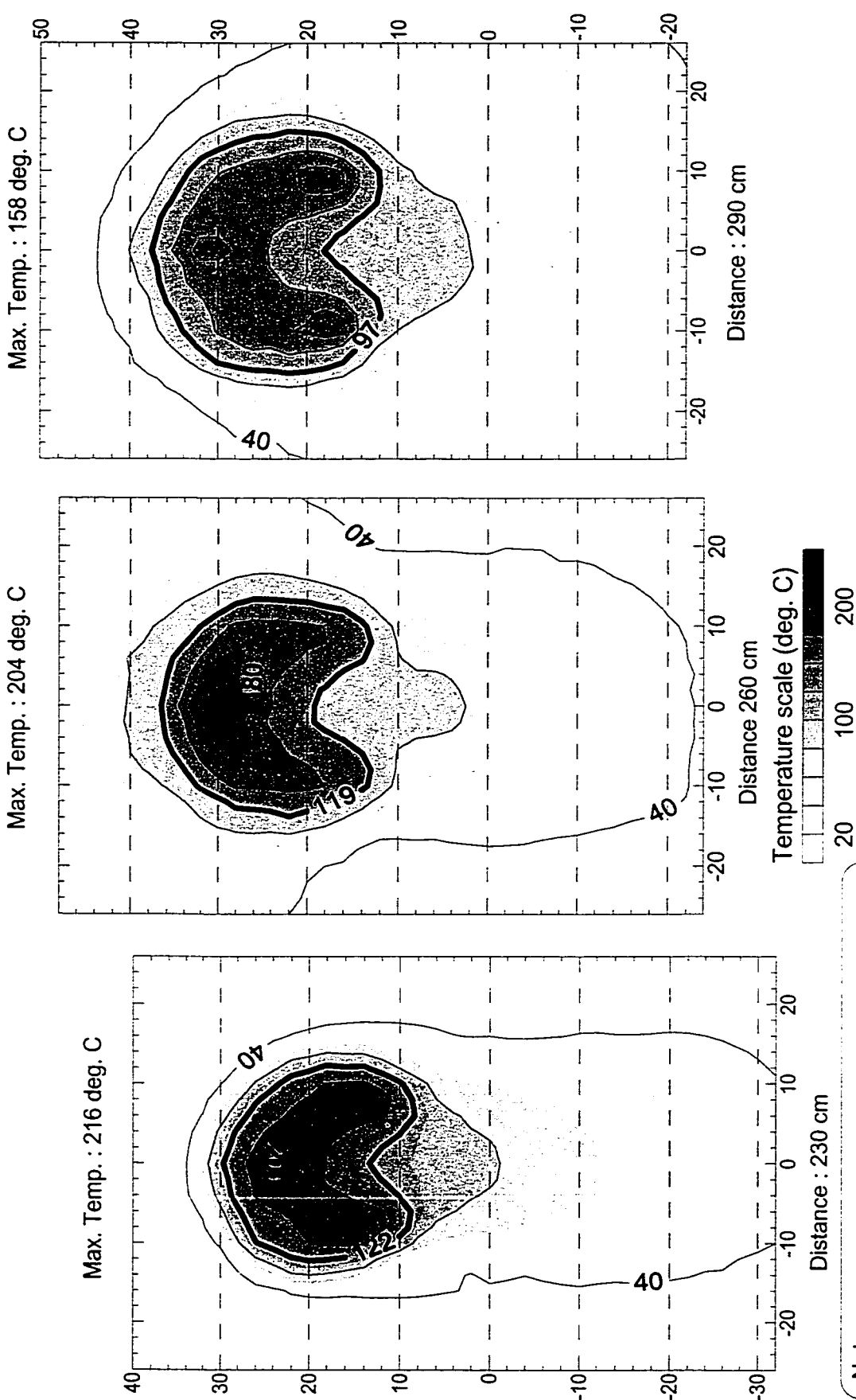
Max. Temp. : 216 deg. C

Max. Temp. : 204 deg. C

Max. Temp. : 158 deg. C

Distance : 230 cm

Distance 260 cm

Distance : 290 cm

Temperature scale (deg. C)

d_s = 3.33 cm; V_j = 2 m/s; U_∞ = 6 m/s

Notes:
- X and Y axis in cm relatively to the stack exit.
- Thick line shows 50% temperature contour.

172

data files : S15W80E20P230.grd, S15W80E20P260.grd, S15W80E20P290.grd
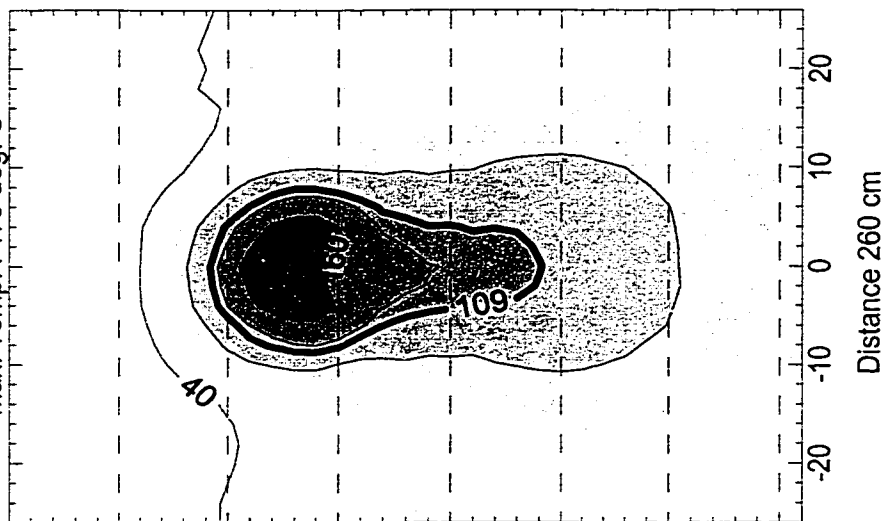
Max. Temp. : 189 deg. C

Max. Temp. : 179 deg. C

Max. Temp. : 169 deg. C

Distance : 230 cm

Distance 260 cm

Distance : 290 cm

Temperature scale (deg. C)

d_s = 3.33 cm; V_j = 2 m/s; U_∞ = 8 m/s

Notes:
- X and Y axis in cm relatively to the stack exit.
- Thick line shows 50% temperature contour.

173